UNIVERSITY OF CALIFORNIA SAN DIEGO

Simulation-based analyses of turbulent wakes: coherent structures, wake generator shape and buoyancy effects

A dissertation submitted in partial satisfaction of the
requirements for the degree
Doctor of Philosophy

in

Engineering Sciences (Mechanical Engineering)

by

Sheel Nidhan

Committee in charge:

Professor Sutanu Sarkar, Chair
Professor Eugene R. Pawlak
Professor Daniel L. Rudnick
Professor Antonio L. Sanchez
Professor Oliver T. Schmidt

2023

The dissertation of Sheel Nidhan is approved, and it is acceptable in quality and form for publication on microfilm and electronically.

University of California San Diego

2023

DEDICATION

I dedicate this dissertation to my parents

for all their help, support and sacrifices.

EPIGRAPH

A new scientific truth does not triumph by convincing its opponents and making them see the light, but rather because its opponents eventually die, and a new generation grows up that is familiar with it.

– Max Planck

TABLE OF CONTENTS

LIST OF FIGURES

LIST OF TABLES

ACKNOWLEDGEMENTS

I would like to thank Prof. Sutanu Sarkar for his help and support during my PhD. I am thankful to him for allowing me to freely pursue my research ideas and helping me grow as a researcher, while also providing constant feedback and help whenever needed. I have learned a lot about turbulence, scientific research, and technical writing from him. I would also like to acknowledge the support of my dissertation committee members: Prof. Pawlak, Prof. Rudnick, Prof. Sanchez, and Prof. Schmidt. I express my gratitude to the UCSD MAE personnel and the HPCMP support for resolving many administrative and technical issues over the last five years.

Thanks to all the present and past members of the CFD Lab for their camaraderie during the last five years. In particular, I am grateful to my mentors in the wake project, Dr. Karu Chongsiripinyo and Dr. Jose L. Ortiz-Tarin, for all their help. The numerous hours spent discussing research as well as non-research topics with them, especially during my initial years, were very fruitful and extremely crucial to my PhD journey. I would also like to thank Divyanshu, Pranav, and Vicky for their friendship, support, and help. A big thanks to the pseudo-CFD lab member, Akhil, for being a great friend and an excellent sounding board for a lot of my ideas. I am thankful to my friends: Mustafa, Aditya, Rohan, Sukanya, Govind, Arijit, Orion, Billy, Archit for making my stay in the sunny La Jolla memorable and fun. I am also grateful to Rishabh and Jashan for constantly supporting me from afar. I would also like to thank my teachers and friends from IIT Bombay for their instrumental role in shaping my technical foundations and interpersonal skills.

A very special thank is due to Aashi for believing in me and supporting me throughout this journey. She has made me a better and more grounded person. Finally, none of this would have been possible without the selfless love and unwavering support of my parents. I am indebted to them for teaching me the importance of hard work, persistence, and character through their actions and way of life.

I acknowledge the technical help and support of my co-authors. I also thank them for allowing me to use the following manuscripts for my dissertation.

Chapter 2 is a reprint of the material in the article: S. Nidhan, K. Chongsiripinyo, O. T. Schmidt, and S. Sarkar, "Spectral proper orthogonal decomposition analysis of the turbulent wake of a disk at Re = 50 000", Physical Review Fluids 5 (12), 124606 (2020). The dissertation author was the primary investigator and author of this work.

Chapter 3 is a reprint of the material in the article: S. Nidhan, O. T. Schmidt, and S. Sarkar, "Analysis of coherence in turbulent stratified wakes using spectral proper orthogonal decomposition", Journal of Fluid Mechanics, 934:A12 (2022). The dissertation author was the primary investigator and author of this work.

Chapter 4 is a reprint of the material in the article: J. L. Ortiz-Tarin, S. Nidhan, and S. Sarkar, "The high–Re stratified wake of a slender body and its comparison with a bluff body wake", accepted in Journal of Fluid Mechanics. The dissertation author was the co-primary investigator and co-first author of this work.

Chapter 5 is being prepared for publication titled: S. Nidhan, J. L. Ortiz-Tarin, and S. Sarkar, "Wake of a slender body at a moderate angle of attack in stratified and homogeneous environments". Parts of chapter 5, with slight modifications, also appear in the conference proceeding titled: S. Nidhan, J. L. Ortiz-Tarin, and S. Sarkar, " Flow past an inclined spheroid in homogeneous and stratified environments", 12th International Symposium on Turbulence and Shear Flow Phenomena, Osaka, Japan (Virtual). The dissertation author is the primary investigator and author of this work.

VITA

2017	Bachelor of Technology with Honors, Mechanical Engineering, Indian Institute of Technology Bombay, India
2018	Master of Science in Engineering Sciences (Mechanical Engineering), University of California San Diego, CA, USA
2023	Doctor of Philosophy in Engineering Sciences (Mechanical Engineering), University of California San Diego, CA, USA

PUBLICATIONS

JOURNAL PUBLICATIONS

S. Nidhan, J. L. Ortiz-Tarin, and S. Sarkar, "Wake of a slender body at a moderate angle of attack in stratified and homogeneous environments", *in preparation*.

A. Nekkanti*, **S. Nidhan***, O. Schmidt, and S. Sarkar, "Numerical evidence of streaks in a turbulent bluff body wake", *in preparation*, *equal contributions.

D. Wilde, **S. Nidhan**, H. T. Pham, H. Foysi, D. Reith, and S. Sarkar, "Stratified Taylor-Green vortex by lattice Boltzmann methods: influence of stencils, forcing schemes, and collision models", *under revision*.

J. L. Ortiz-Tarin*, **S. Nidhan***, and S. Sarkar, "The high–Re stratified wake of a slender body and its comparison with a bluff body wake", *accepted in Journal of Fluid Mechanics*, *equal contributions.

D. Gola, **S. Nidhan**, J. L. Ortiz-Tarin, H. Pham, and S. Sarkar, "Disk wakes in nonlinear stratification", *accepted in Journal of Fluid Mechanics*.

S. Nidhan, O. T. Schmidt, and S. Sarkar, "Analysis of coherence in turbulent stratified wakes using spectral proper orthogonal decomposition", *Journal of Fluid Mechanics*, 934:A12 (2022).

J. L. Ortiz-Tarin, **S. Nidhan**, and S. Sarkar, "High-Reynolds-number wake of a slender body", *Journal of Fluid Mechanics*, 918:A30 (2021).

S. Nidhan, K. Chongsiripinyo, O. T. Schmidt, and S. Sarkar, "Spectral proper orthogonal decomposition analysis of the turbulent wake of a disk at Re = 50 000", *Physical Review Fluids* 5 (12), 124606 (2020).

J. T. Ravi, **S. Nidhan**, N. Muthu, S. K. Maiti, "Analytical and experimental studies on detection of longitudinal, L and inverted T cracks in isotropic and bi-material beams based on changes in natural frequencies", *Mechanical Systems and Signal Processing* 101, 67-96 (2018).

CONFERENCE PROCEEDINGS

S. Nidhan, J. L. Ortiz-Tarin, and S. Sarkar, "Flow past an inclined spheroid in homogeneous and stratified environments", *12th International Symposium on Turbulence and Shear Flow Phenomena*, Osaka, Japan (Virtual).

S. Nidhan, D. Gola, S. Sarkar, "Modal analysis of bluff body wakes", *34th Symposium on Naval Hydrodynamics, Washington, DC*.

J. L. Ortiz-Tarin, **S. Nidhan**, S. Sarkar, "The high-Re wake of a slender body and the effects of density stratification", *34th Symposium on Naval Hydrodynamics, Washington, DC*.

S. Nidhan, J. L. Ortiz-Tarin, K. Chongsiripinyo, S. Sarkar, and P. J. Schmid (2019), "Dynamic mode decomposition of stratified wakes", *AIAA Aviation 2019 Forum*, 3330.

ABSTRACT OF THE DISSERTATION

Simulation-based analyses of turbulent wakes:
coherent structures, wake generator shape and buoyancy effects

by

Sheel Nidhan

Doctor of Philosophy in Engineering Sciences (Mechanical Engineering)

University of California San Diego, 2023

Professor Sutanu Sarkar, Chair

Turbulent wakes are pervasive in man-made and natural environments. In the ocean and the atmosphere, these wakes interact with the background ambient stratification to give rise to a myriad of interesting phenomena, e.g., multistage decay of mean and turbulence, long-lived coherent structures, and the appearance of internal gravity waves, to name a few. With the rise in supercomputing power, high-fidelity numerical simulations have become an increasingly feasible way to investigate the phenomenology of these wakes. As these simulations become commonplace in research, there is an increased focus on the use of data-driven techniques to uncover the rich dynamics from the obtained datasets. This dissertation is an examination of

turbulent wakes using data-driven techniques and numerical simulations.

In the first part, spectral proper orthogonal decomposition is used to investigate a turbulent disk wake database at $Re = 5 \times 10^4$ and $Fr = \infty$, 10, 2. We first study the evolution of the vortex shedding mode and double helix mode in the unstratified wake ($Fr = \infty$), building on and refining the previous experimental studies. Thereafter, the SPOD analysis of the stratified wakes is performed that uncovers two new results: (a) coherence originating at the body gets stronger and lives longer with progressively increasing stratification levels and (b) for $Fr \gtrsim 2$, vortex shedding is the dominant mechanism of internal gravity wave generation.

In the second part of the work, large eddy simulations (LES) are used to investigate the flow past a prolate 6:1 spheroid. Firstly, high-resolution hybrid simulation is used to simulate the far wake of a 6:1 spheroid at 0-degree angle of attack and $Re = 10^5$, $Fr = 2$ and 10. The far wake is compared to the above-mentioned disk database. The spheroid wakes show differences in locations at which mean wake transitions take place. These differences are explained in light of energy budgets. Secondly, large eddy simulations of flow past a 6:1 spheroid at $Re = 5000$, $Fr = \infty, 6, 1.9$, 1, and a moderate angle of attack $\alpha = 10^\circ$ are carried out. Body forces, mean wake and vorticity dynamics, and flow spectra are analyzed in detail and presented in the dissertation.

Chapter 1

Introduction

1.1 Phenomenology of turbulent wakes

A wake is the region of disturbance left behind when an object moves through a fluid medium or equivalently if there is a flow past an object at rest. Due to their ubiquity in nature as well as man-made environments, the phenomenology of wake has been extensively studied throughout the course of last 50 years, e.g., Bearman (1984), Lin and Pao (1979), Oertel Jr (1990), Reed and Milgram (2002), Thompson et al. (2021). In an incompressible medium, this phenomenology is controlled by the Reynolds number $Re = U_\infty D/\nu$. The Reynolds number is a measure of the relative dominance of convective term ($O(\rho U_\infty^2/D)$) to the viscous forces ($O(\mu U_\infty/D^2)$) in a flow. This dissertation focuses on the wakes in the limit of $Re >> 1$, i.e., turbulent wakes. Turbulent wakes are one of the most commonly occurring classes of flow in the nature, e.g., flow past vehicles (Grandemange et al., 2015, 2013), geophysical features (Puthan et al., 2021), urban flows (Tseng et al., 2006), to name a few. Similar to other classes of turbulent flows (e.g., jets, shear layers, boundary layers), the academic research on the investigation of the phenomenology of turbulent wakes have predominantly focused on two broad themes: (a) investigation of self-similarity and scaling laws in the far wake and (b) characterizing the coherent

structures in the flow using various statistical and visualization techniques. Both the scaling laws and coherent structures have a strong dependence of the initial and boundary conditions, i.e., Reynolds number of the incoming flow and features of the wake generator, which lasts far from the body.

1.1.1 Self-similarity and scalings in turbulent wakes

Under the framework of self-similarity for an axisymmetric wake, it has been traditionally assumed that the mean wake dynamics at any downstream distance x is controlled by two quantities: (a) mean wake defect velocity $U_d(x)$ ($<< U_\infty$, the free stream velocity) and (b) mean wake lengthscale $L(x)$ (Pope, 2000, Tennekes and Lumley, 1972). Thereafter, the Reynolds averaged Navier-Stokes (RANS) equations and continuity equations are simplified under the boundary layer assumption of slow development in the x direction compared to the lateral direction, i.e., $\partial\langle\cdot\rangle/\partial x << \partial\langle\cdot\rangle/\partial y$. After simplifications, for turbulent wakes of axisymmetric bodies, one arrives at the following scalings: (a) $U_d \sim x^{-2/3}$ and (b) $L \sim x^{1/3}$. Note that $U_d L^2 \sim$ constant comes from conservation of momentum. Earlier experimental works (Chevray, 1968, Uberoi and Freymuth, 1970) lent support to these scaling laws in the far wake of axisymmetric bodies.

However as turbulent flow research developed, it came to light that the wake evolution is not as simple as the foregoing self-similar evolution. George (1989) postulated that a turbulent flow can exist in the state of partial self-similarity where only a certain range of flow scales evolve self-similarly. In his work, George (1989) relaxed the assumption that the Reynolds stresses evolve as $R_s \sim U_d^2$ and instead invoked the TKE transport equation along with high-*Re* dissipation scaling $\varepsilon \sim C_\varepsilon K^{3/2}/L$, where C_ε is a constant, to arrive at the same scaling laws. Moreover, this way of looking at the self-similar evolution naturally reproduces the low *Re* scaling of the wakes ($U_d \sim x^{-1}$ and $L \sim x^{1/2}$) when $\varepsilon \sim \nu K^{1/2}/L^2$. In the last twenty years, there have been numerous experimental (Johansson and George, 2006a) and numerical (Dairay et al., 2015, Obligado et al., 2016) confirming George (1989) hypothesis that the Reynolds shear stress does not always evolve

in conjunction with U_d, i.e., $R_s \sim U_d^2$ need not hold. In recent years, an alternative non-equilibrium dissipation scaling (Vassilicos, 2015) has amounted evidence in various shear flows. Under this scaling, C_ε is not a constant but instead varies with the global inlet Reynolds number Re_I and local Reynolds number Re_L as $C_\varepsilon \sim Re_I^m / Re_L^n$ where m and n are constants. In turbulent axisymmetric wakes, numerical simulations (Chongsiripinyo and Sarkar, 2020, Dairay et al., 2015, Ortiz-Tarin et al., 2021, Pal et al., 2017) have found this non-equilibrium dissipation scaling to hold over large distances from the body and U_d decaying close to x^{-1} instead of $x^{-2/3}$.

1.1.2 Coherent structures in turbulent wakes

Besides wake scaling laws, analysis and characterization of coherent structures have also constituted one of the cornerstones in turbulent wake research. In the era before high-resolution numerical simulations, the characterization was carried out primarily through experimental visualization and hot-wire anemometry. The experiments of Taneda (1978) revealed the existence of large-scale wavelike structures in the sphere wake below the supercritical regime. These structures are reminiscent of the famous vortex shedding mechanism that is present across a wide range of wake generators and Reynolds number. Besides visualizations, researchers have extensively made use of spectra and two-point correlations to quantify the features of these structures in the near and far field of the wake (Achenbach, 1974, Berger et al., 1990, Fuchs et al., 1979). For a sphere, the most common bluff body prototype, these experimental studies have established that at higher Re (but still in the sub-critical regime of $Re < 3 \times 10^5$), there exist two dominant frequencies in the pointwise spectra: (a) a low-frequency mode associated with the vortex shedding in the bodies and (b) a high-frequency mode associated with the instability of the separating shear layer.

The advent of supercomputers in the 1990s ushered in a new era in the study of turbulent wakes as well. With numerical simulations, access to high-quality full spatiotemporal datasets became feasible. Tomboulides and Orszag (2000) carried out direct numerical simulations of

flow past a sphere in the range of $Re \leq 1000$ focusing on the transition between the different wake regimes as the Re is changed and discussing them in the light of linear stability studies of Natarajan and Acrivos (1993) and Kim and Pearlstein (1990). Thereafter, there have been several numerical studies studying the vortex shedding mode and its characteristics using flow visualization of numerical data (Constantinescu and Squires, 2003, Rodriguez et al., 2011, Yun et al., 2006).

While other common flow configurations like turbulent jets (Nekkanti and Schmidt, 2020, 2021, Nogueira et al., 2019, Schmidt et al., 2018) and wall-bounded flows (Abreu et al., 2020, Muralidhar et al., 2019) have seen significant development with regards to the application of data-driven techniques for coherence characterization and low-order modeling, studies using rigorous data-driven methods to discern these coherent structures in a turbulent wake are scarce. Hence, this endeavor has been one of the main focuses of this dissertation. Redford et al. (2012) found that varying the structures and features of the initial seeding structures in their temporal simulations led to a change in the decay rates of the subsequent wake evolution. However, due to the absence of the wake generator, there was no vortex shedding structure in their flow. Likewise, Bevilaqua and Lykoudis (1978) found that different wake generators showed different spreading rates despite the decay rate of the defect velocity being the same for the corresponding wakes. These studies hint towards a strong link between self-similarity and coherent structures. In the view of the author, the statistical characterization of coherent structures in turbulent wake will be a stepping stone towards merging the evolution of coherent structures and the self-similarity framework, in the context of turbulent wakes.

1.2 Stratification effects on wake evolution

The turbulent wake evolution in a homogeneous medium is in itself a challenging problem. The idea of universality in the far wake, the establishment of a direct link between the coherent

structures and the self-similar decay rates, and ultimately controlling the wake remain difficult problems to study. When we add stratification to the mix, the picture of wake evolution becomes even more complex.

In the presence of stratification, the mean deficit in the turbulent wake decays in three stages (Spedding, 1997): (a) 3D stage where the mean wake defect velocity, U_d, the decay rate is similar to the unstratified wake corresponding to that specific wake generator, (b) NEQ or non-equilibrium stage where the decay of U_d slows down compared to the unstratified wake, with $U_d \sim x^{-1/4}$, and (c) Q2D or quasi-two-dimensional stage when the stratification strongly inhibits the motions in the vertical direction and the decay rate accelerates again and $U_d \sim x^{-3/4}$. It is worth noting that a clear distinction between these three regimes is observed only for $Fr \gtrsim O(10)$ or above and most of the work has been limited to either sphere wakes or body-exclusive, temporal models of the wake. At lower Fr, the flow over the body itself gets strongly modulated by the buoyancy, especially for long bodies with aspect ratio $> O(1)$ (Ortiz-Tarin et al., 2019). In terms of non-dimensional buoyancy time (Nt), Spedding (1997) found that these regimes lasted as follows: (a) 3D regime for $Nt < 1$, (b) NEQ regime for $2 < Nt < 50$, and (c) Q2D regime for $Nt > 50$. Further numerical simulations of Brucker and Sarkar (2010) and Diamessis et al. (2011) showed that the span of the NEQ regime increases with increasing Re. In recent years, researchers have also attempted to characterize the multistage decay of turbulence in the stratified wake at high Reynolds numbers. Zhou and Diamessis (2019) and Chongsiripinyo and Sarkar (2020) borrowed this idea from the stratified homogeneous turbulence community (Brethouwer et al., 2007, de Bruyn Kops and Riley, 2019) and presented the traversal of stratified wakes through different regimes of stratified turbulence namely, weakly stratified turbulence (WST), intermediately stratified turbulence (IST) and strongly stratified turbulence (SST). The demarcation among these different stages is provided using a proxy of the local horizontal buoyancy Reynolds number ($Re_h Fr_h^2$) and the local horizontal Froude number (Fr_h).

The majority of the experimental and numerical studies of turbulent stratified wakes

have been concerned with wake scalings and flow energetics. In the early 90s, there were few experimental studies investigating the existence/absence of the three-dimensional vortex shedding mode in a stratified wake (Bonneton et al., 1993, Chomaz et al., 1993, Lin et al., 1992a). However, these studies were at low Reynolds number, focused on the near wake using a few points for quantitative analysis, and could not characterize the contribution of the discerned coherent structures to the overall wake energetics. The simulations that followed the advent of supercomputing were primarily temporal (Brucker and Sarkar, 2010, Diamessis et al., 2011, Dommermuth et al., 2002, Gourlay et al., 2001) that could not resolve the wake generator. Hence they missed the physics related to the peculiarities of the wake generator, e.g., steady lee waves, flow separation, and vortex shedding. These studies also miss the causal link, if any, between near-body flow structures and internal gravity wave generation. It is only recently that body-inclusive simulations are being performed and used to study the stratified wake dynamics at moderate to high Reynolds numbers (Chongsiripinyo and Sarkar, 2017, 2020, Ortiz-Tarin et al., 2019, Pal et al., 2017). Similar to its unstratified counterpart, it remains to be seen how the mean wake scalings relate to presence or absence of different types of coherent structures at high Reynolds numbers.

Within the stratified wake research community, much emphasis has been placed on the wake of bluff bodies, in particular, the sphere (Bonneton et al., 1993, Chomaz et al., 1993, Orr et al., 2015, Pal et al., 2016, 2017, Spedding, 1997, 2002a). Despite its widespread use in hydrodynamic applications, the stratified wake of a slender body has not received much attention. In numerical simulations, resolving the boundary layer over a slender body becomes very expensive. Coupled with the challenge of resolving until a far downstream location (x) to properly uncover the effects of stratification (particularly at large Fr), the high-fidelity simulation of a slender body wake becomes a very stiff computational problem. To the best of our knowledge, Ortiz-Tarin et al. (2019) was the first study of flow past a spheroid under the effect of stratification. Ortiz-Tarin et al. (2021) employed the hybrid method of VanDine et al. (2018) to study the far

wake of an unstratified turbulent wake of a prolate 6:1 spheroid for the first time in the literature. In the view of the author, there remain a lot of open questions in the literature on the stratified wake of a slender body, some of which are answered in this dissertation.

1.3 Modal analyses for studying turbulent flows

With the rise in computational power has come an immense increase in the quantity and quality of data available for analyses across a variety of engineering fields. The community of turbulence researchers is no exception. As we get our hands on an ever-increasing amount of data, the field is seeing a paradigm shift in the way these datasets are analyzed. Besides the classical statistical analyses, data-driven techniques are becoming commonplace in turbulence research. A lot of these techniques are based on the idea of decomposing the flow field into different modes under a certain set of assumptions, hence the name modal analysis, e.g., Taira et al. (2017, 2020). It is beyond the scope of this dissertation to discuss the many modal analysis techniques being used today to study turbulent flows. Here, we limit ourselves to a brief overview of two famous methods, proper orthogonal decomposition (POD) and dynamic mode decomposition (DMD).

Proper orthogonal decomposition (POD), in the context of turbulent flows analysis, was first put forward by Lumley (Lumley, 1967, 1970). In POD, spatiotemporal fluctuations in a flow are decomposed into an ordered set of eigenmodes and eigenvalues that capture a predefined norm optimally. The norm can be fluctuation energy, fluctuation enstrophy, or any other semi-definite positive quantity. The energy contained in a specific mode is represented by the eigenvalue corresponding to that mode. In its original form, homogeneous directions of the flow are first separated using Fourier transform and then the inhomogeneous direction is decomposed using POD. However, this way of performing POD requires a large number of ensembles which is often infeasible, both in terms of running simulations for a long time horizon and saving the huge amount of data on the storage disk, for high fidelity simulations. Hence, the more common

variant of POD used for the analysis of simulation data has been the snapshot POD variant of Sirovich (1987). Snapshot POD treats the individual flow fields at different time instants as statistically independent samples. Thereafter, the spatial correlation tensor is decomposed into modes. Hence the snapshot POD modes retain spatial coherence, but their temporal coefficients are not guaranteed to evolve coherently, unlike the original POD modes. In the recent literature, Towne et al. (2018) revisited the original POD formulation of Lumley and employed Welch's method (Welch, 1967) to overcome the issue of convergence for numerical datasets. Since its reformulation, spectral POD (SPOD), as named by Towne et al. (2018), has been used extensively in distilling coherent structures across a wide variety of flow configurations.

Another famous data-driven method of modal analysis is dynamic mode decomposition or DMD (Schmid, 2010). In DMD, the underlying operator stepping the flow from one time step to the next is assumed to be linear. Thereafter, the eigenvalue decomposition of the similarity matrix of this operator provides us with DMD eigenmodes and DMD eigenvalues. Different from the POD eigenvalues, DMD eigenvalues provide the frequency at which the modes oscillate. Unlike POD (or SPOD), there is not a strict hierarchy among the modes, i.e., one can not infer the dominance of a particular mode from its eigenvalue alone. There have been different variants of DMD thereafter building on the original algorithm, e.g., Jovanović et al. (2014). Readers are referred to a recent review by Schmid (2022) on the recent developments of DMD.

Besides these two techniques, there are other methods that lie somewhere between the purely data-driven and the purely operator-driven approach (e.g., linear stability analysis). One such popular method is the resolvent analysis (McKeon and Sharma, 2010) for analyzing turbulent channel flow. Resolvent analysis approaches the problem at hand from an input-output framework whereby one obtains the forcing modes, the response modes, and the corresponding amplification factor. Similar to SPOD, resolvent analysis has gained a lot of traction in recent times for turbulent flow physics analysis and flow modeling (Pickering et al., 2021, Schmidt et al., 2018, Thomareis and Papadakis, 2018, Yeh and Taira, 2019). Readers are referred to Rowley and Dawson (2017),

Taira et al. (2017, 2020) for an in-depth survey of a wide variety of data-driven and operator-driven analyses.

1.4 Organization and contributions of the dissertation

The contributions and organization of the two major themes of this dissertation, i.e., (a) modal analyses of turbulent disk wake and (b) large eddy simulations (LES) of the prolate 6:1 spheroid wake, to delineate differences of a slender-body stratified wake from its bluff-body counterpart, are outlined below. Readers are referred to the individual chapters for an in-depth exposition of these contributions.

1.4.1 Modal analyses of the turbulent disk wakes

In chapter 2 (Nidhan et al., 2020), the coherent structures in the turbulent wake of a disk at a moderately high Reynolds number (Re) of 5×10^4 are examined using spectral proper orthogonal decomposition (SPOD) which considers all three velocity components in a numerical database. The SPOD eigenvalues at a given streamwise (x) location are functions of azimuthal wavenumber (m), frequency (St), and SPOD index (n). By $x/D = 10$, two specific modes dominate the fluctuation energy: (i) the vortex shedding (VS) mode with $m = 1, St = 0.135, n = 1$, and (ii) the double helix (DH) mode with $m = 2, St \to 0, n = 1$. The VS mode is more energetic than the DH mode in the near wake but, in the far wake, it is the DH mode which is dominant. The DH mode, when scaled with local turbulent velocity and length scales, shows self-similarity in eigenvalues and eigenmodes while the VS mode, which is a global mode, does not exhibit strict self-similarity. Modes $m = 0$, 3 and 4, although subdominant, also make a significant net contribution to the fluctuation energy, and their eigenspectra are evaluated. The reconstruction of TKE and Reynolds shear stress, $\langle u'_x u'_r \rangle$, is evaluated by varying (m, St, n) combinations. Higher SPOD modes contribute significantly to the TKE, especially near the centerline. In contrast,

reconstruction of $\langle u'_x u'_r \rangle$ requires far fewer modes: $|m| \leq 4$, $|St| \leq 1$ and $n \leq 3$. Among azimuthal modes, $m = 1$ and 2 are the leading contributors to both TKE and $\langle u'_x u'_r \rangle$. While $m = 1$ captures the slope of the shear-stress profile near the centerline, $m = 2$ is important to capture $\langle u'_x u'_r \rangle$ at and near its peak. SPOD is also performed in the vicinity of the disk to describe the modal transition to the principal contributors in the wake. The leading SPOD modes shows a high-frequency shear-layer peak close to the disk and the vortex shedding mode commences its initial dominance of the wake at the end of the recirculation region.

In chapter 3 (Nidhan et al., 2022b), we use spectral proper orthogonal decomposition (SPOD) to extract and analyze coherent structures in the turbulent wake of a disk at Reynolds number $Re = 5 \times 10^4$ and Froude numbers $Fr = 2, 10$. We find that the SPOD eigenspectra of both wakes exhibit a low-rank behavior and the relative contribution of low-rank modes to total fluctuation energy increases with x/D. The vortex shedding (VS) mechanism, which corresponds to $St \approx 0.11 - 0.13$ in both wakes, is active and dominant throughout the domain in both wakes. The continual downstream decay of the SPOD eigenspectrum peak at the VS mode, which is a prominent feature of the unstratified wake, is inhibited by buoyancy, particularly for $Fr = 2$. The energy at and near the VS frequency is found to appear in the outer region of the wake when the downstream distance exceeds $Nt = Nx/U = 6 - 8$. Visualizations show that unsteady internal gravity waves (IGWs) emerge at the same $Nt = 6 - 8$. A causal link between the VS mechanism and the unsteady IGW generation is also established using the SPOD-based reconstruction and analysis of the pressure-transport term. These IGWs are also picked up in SPOD analysis as a structural change in the shape of the leading SPOD eigenmode. The $Fr = 2$ wake shows layering in the wake core at $Nt > 15$ which is captured by the leading SPOD eigenmodes of the VS frequency at downstream locations $x/D > 30$. The VS mode of the $Fr = 2$ wake is streamwise-coherent, consisting of V-shaped structures at $x/D \gtrsim 30$. Overall, we find that the coherence of wakes, initiated by the VS mode at the body, is prolonged by buoyancy to far downstream. Also, this coherence is spatially modified by buoyancy into horizontal layers and IGWs. Low-order

truncations of SPOD modes are shown to efficiently reconstruct important second-order statistics.

1.4.2 Large eddy simulations of the prolate 6:1 spheroid wakes

In chapter 4, the high-Reynolds number stratified wake of a slender body is studied using a high-resolution hybrid simulation. The focus is on identifying differences with a bluff-body wake (specifically, a disk wake) and explaining said differences. The wake generator is a 6:1 prolate spheroid with a tripped boundary layer, the diameter-based body Reynolds number is $Re = U_\infty D/\nu = 10^5$, and the body Froude numbers are $Fr = U_\infty/ND = \{2, 10, \infty\}$. The wake defect velocity (U_d) decays following three stages with different wake decay rates (Spedding, 1997) as for a bluff body. However, the transition points among stages do not follow the expected $Nt = Nx/U_\infty$ values. Comparison with the wake of a circular disk in similar conditions (Chongsiripinyo and Sarkar, 2020) quantifies the influence of the wake generator - bluff versus slender - in stratified flow. The strongly stratified $Fr = 2$ wake is in a resonant state for the 6:1 spheroid and not for the disk. Under the resonant condition, the half wavelength $\lambda/2$ of the steady lee waves coincides with the body length, i.e., $\lambda/2 = L$. This leads to the resonant $Fr = L/\pi D$. The steady lee waves strongly modulate the mean flow and, relative to the disk, the 6:1 spheroid (a high aspect ratio shape) wake at $Fr = 2$ shows an earlier transition from the non-equilibrium (NEQ) stage to the quasi two-dimensional (Q2D) stage. The NEQ-Q2D transition is followed by a sharp increase in the turbulent kinetic energy and horizontal wake meanders. At $Fr = 10$, the start of the NEQ stage is delayed for the spheroid. Transfers between kinetic energy and potential energy reservoirs (both mean and turbulence) are analyzed and the flows are compared in phase space (local Froude and Reynolds number as coordinates). Overall, the results of this study point to the difficulty of finding a universal framework for stratified wake evolution, independent of the features of the body, and provide insights into how buoyancy effects depend on the wake generator.

In chapter 5 (Nidhan et al., 2022a), large eddy simulations (LES) are performed to study

the flow past a 6:1 prolate spheroid placed at an angle of attack of $\alpha = 10^{\circ}$. The diameter-based Reynolds number ($Re = U_{\infty}D/\nu$) is set to a value of 5000 and four values of diameter-based Froude numbers ($Fr = U_{\infty}/ND$) are analyzed: $Fr = \infty, 6, 1.9$, and 1. Visualizations of the coefficient of pressure (C_p) and friction (C_f) contours reveal asymmetry in the $Fr = \infty$ and 6 flows while, at $Fr = 1$ and $Fr = 1.9$, the flow over the body does not have any visible asymmetry. This finding is further corroborated through the analysis of force coefficients on the body. The changes in the pressure coefficients (C_p), friction coefficients (C_f), and drag coefficients (C_d) with the Froude number are described in detail for $\alpha = 10^{\circ}$. We also present the analyses of forces on the body at $\alpha = 0^{\circ}$ angle of attack for comparison with the $\alpha = 10^{\circ}$ cases. After analyzing the flow over the body, wakes of $\alpha = 10^{\circ}$ cases are analyzed in detail through the means of turbulence statistics, flow visualizations, and spectra. The distinct flow separation patterns at different Fr have a lasting impact on the dynamics of the mean wake, mean streamwise vorticity, and the flow structures in the wake.

Chapter 2

Spectral POD analysis of the turbulent wake of a disk at $Re = 5 \times 10^4$

2.1 Introduction

The turbulent wake is a widely prevalent class of free shear flows that occurs whenever a flow encounters an obstacle in its path or, equivalently, an obstacle moves in a surrounding fluid. Like other types of free shear flows, turbulent wakes are assumed to evolve self-similarly far away from their generators in classical analysis Tennekes and Lumley (1972). Often, wakes contain large-scale anisotropic coherent structures Cannon et al. (1993), Taneda (1978) which feed on the energy of the mean flow, and in turn modify the statistical descriptors of the flow. The characteristics of these coherent structures are strongly influenced by the geometry of wake generators and by boundary conditions. Hence, the study of turbulent wakes has revolved around two major themes: (i) discerning the scaling laws of statistical mean and turbulent quantities, and (ii) extracting and analyzing coherent structures.

Townsend (1976) hypothesized that free shear flows forget their initial conditions and eventually asymptote towards a form that is both self-similar and universal. However, the study

of Bevilaqua and Lykoudis (1978) showed that initial conditions significantly influence the subsequent evolution of turbulent wakes. They compared the wakes of a sphere and a porous disk, both of which produced the same drag, and found that, although both wakes exhibited a self-similar regime with the same power laws, their spread rates were different. They attributed this difference to the distinct nature of coherent structures in these flows, thus pointing towards a link between the evolution of flow statistics and the nature of coherent structures. Decades later, Redford et al. (2012) simulated a temporally evolving wake with two different types of initial conditions: (i) an array of vortex rings, and (ii) small-amplitude broadband velocity fluctuations. Both initial conditions led to a self-similarly evolving wake with the classical $U_d \sim x^{-2/3}$ decay of the wake deficit velocity (U_d) but the magnitude of spread rates were different. Furthermore, it was only after a very long time that the spread rates converged to a common value and a universal self-similar form with $U_d \sim x^{-2/3}$ was achieved. Thus, it is possible that the imprint of coherent structures generated due to initial and boundary conditions persist for a long time (or distance) in the wake. A detailed understanding of the statistical behavior of low-dimensional coherent structures is hence crucial to construct a complete picture of the wake evolution.

Early efforts to objectively study coherent structures in the context of wakes utilized laboratory experiments. Fuchs et al. (1979) pioneered the use of two-point cross spectral analysis to investigate the coherent structures in axisymmetric shear flows. They showed the dominance of specific azimuthal modes, $m = 1$ and $m = 2$, in the wake of a disk. The azimuthal $m = 1$ mode dominated at the vortex shedding frequency of the wake $St = Uf/D = 0.135$ while the $m = 2$ mode peaked at a very low frequency of $St \approx 0.005$ in their experiments. However, the analysis was conducted at only two near-body stations, $x/D = 3$ and $x/D = 9$, and was limited to the fluctuating streamwise velocity (u'_x) and pressure (p'). Around the same time, flow visualizations of Taneda (1978) revealed a wavelike structure in sphere wakes in the regime of subcritical Re. Berger et al. (1990) investigated the near-wake ($x/D \leq 9$) structure of a sphere and a disk using cross-spectral analysis and smoke visualization. Three frequencies dominated the near wake of

a disk: a low-frequency ($St = 0.05$) axisymmetric ($m = 0$) pumping of the recirculation bubble, the vortex shedding frequency ($St = 0.135$) dominated by the helical $m = 1$ mode, and a high frequency of ($St = 1.62$) related to the instability of the separated shear layer. The wake of a sphere at subcritical Re was found to be similar to that of a disk. Cannon et al. (1993) found that these large-scale helical $m = 1$ structures persisted even further downstream until $x/D = 29$. Later, Johansson et al. (2002) analyzed the wake of disk at $Re = 26,400$ using hot-wire measurements of u'_x and proper orthogonal decomposition (POD) (Lumley, 1967, 1970). Two distinct peaks were present in their POD spectra: (i) $m = 1$, $St = 0.126$ associated with vortex shedding from the disk, and (ii) $m = 2$, $St \approx 0$. They found that the $m = 2$ mode eventually dominated the energy content of the wake by $x/D = 50$, where D is the diameter of disk. This study was later extended by Johansson and George (2006a) who performed measurements until $x/D = 150$. They found the dominance of $m = 2$ appeared at $x/D \approx 30$ beyond which the turbulence statistics also started exhibiting self-similar behavior.

Different from experiments, attempts to study the evolution of coherent structures in turbulent wakes using numerical simulations have mainly relied on flow visualizations. Constantinescu and Squires (2003) used the vortex identification method proposed by Jeong and Hussain (1995) to visualize the coherent structures in the wake of sphere at $Re = 10,000$. They observed that the main coherent structure shed patches of vorticity which then rotated irregularly while being convected downstream. Yun et al. (2006) used the method of Jeong and Hussain (1995) in conjunction with particle tracking to study the vortex structure of sphere wake at $Re = 3700$ and $10,000$. At lower $Re = 3700$, the separated shear layer formed a cylindrical vortex sheet becoming unstable at $x/D \approx 2$. At $Re = 10,000$, the separated shear layer became unstable immediately behind the body and formed vortex rings. Using particle tracking, they showed that the helical structure of the wake was not due to the rotation of vortical structures in the azimuthal direction but was due to a helical mode that translated downstream without rotation. This finding was further confirmed in later studies of Rodriguez et al. (2011) at $Re = 3700$ and Chongsiripinyo

and Sarkar (2017) at $Re = 10,000$.

In the classical formulation of POD proposed by (Lumley, 1967, 1970), the homogeneous directions are first separated using the Fourier transform and then the cross-spectral tensor is decomposed in the non-homogeneous directions to give POD eigenvalues and eigenmodes. Thus, for statistically stationary flows, each POD mode is characterized by a single frequency. Since its introduction to the fluid dynamics community, this original formulation of POD has been extensively used by experimentalists to educe coherent structures in different types of turbulent flows. In the context of free shear flows, Leib et al. (1984), Glauser et al. (1987), and Glauser and George (1987) applied the classical POD to the near-field measurements of a turbulent axisymmetric jet. Thereafter, there have been several experimental studies employing the classical form of POD to study coherent structures in a variety of flow configurations: (i) turbulent jets (Arndt et al., 1997, Bonnet et al., 1994, Citriniti and George, 2000, Davoust et al., 2012, Gordeyev and Thomas, 2000, 2002, Iqbal and Thomas, 2007), (ii) mixing layers (Bonnet et al., 1994, Delville et al., 1999, Ukeiley et al., 2001), and (iv) wakes (Johansson and George, 2006b, Johansson et al., 2002, Tutkun et al., 2008).

There have been some POD studies of simulation data from various flows but POD analysis of turbulent wake simulations is lacking. Simulation-based POD been dominated by its 'snapshot'-type variant introduced by Sirovich (1987). In snapshot POD Sirovich (1987), the spatial correlation tensor is decomposed and the modes possess spatial coherence while evolving randomly in time. As a result, the snapshot POD modes are generally not coherent in time. On the other hand, application of classical POD for numerical simulations require long time integration making its application challenging for large-scale computations. Recently Towne et al. (2018) revisited a form of POD that leverages the temporal symmetry of statistically stationary flows termed spectral POD (SPOD). SPOD has been extensively used to study the coherent structures in compressible jets and their link to noise generation (Lesshafft et al., 2019, Nogueira et al., 2019, Schmidt et al., 2017, 2018).

The main objective of the present study is to improve upon our previous understanding of the coherent structures in the wake of a disk. This is achieved by conducting an extensive SPOD analysis of data from flow past a disk simulated at $Re = 50,000$ by Chongsiripinyo and Sarkar (2020), specifically their case of the wake in a homogeneous, unstratified fluid. We improve on previous experimental studies by including all three velocity components instead of solely u_x, by employing the high spatial resolution and coverage possible with simulation data, by analyzing the flow field at several downstream locations from near the body to the far wake, and by considering a higher Re. The ability of SPOD to separate temporal and spatial scales makes it a desirable candidate to study the coherent structures in turbulent flows. It is hoped that the qualitative findings of this study will be applicable to the wakes of other bluff bodies too, e.g., a sphere.

While the previous experimental studies of the wake of a disk using POD have developed our understanding of the role of the $m = 1$ vortex shedding mode and the dominance of the $m = 2$ double helix mode away from the body, a more complete analysis of the eigenspectrum and eigenmodes of the azimuthal modes including their relative importance is missing. We bridge this gap by analyzing the SPOD eigenmodes and eigenspectra of different azimuthal modes in detail. Specifically, we consider the following questions. How is the energy distributed among SPOD modes of different azimuthal wave numbers (m) and frequencies (St), both in the near as well as the far wake? Does the turbulent wake of a disk at a higher Re, as in the present case, show the dominance of the $m = 2$ azimuthal mode akin to the experimental investigations of the past? Do the SPOD eigenvalues and eigenmodes of the different dominant modes exhibit self-similarity indicating their connection to the local turbulence structure instead of being global modes?

We also explore the reconstruction of the turbulent kinetic energy (TKE) and $\langle u'_x u'_r \rangle$ to further clarify the role of modal decomposition. In particular, we address the following questions. What is the distribution of TKE and $\langle u'_x u'_r \rangle$ in the leading SPOD modes of the dominant azimuthal wave numbers and frequencies? How does the reconstruction of both TKE and $\langle u'_x u'_r \rangle$ change

when we systematically change the reconstruction parameters by varying m, St and the number of SPOD modes?

The remainder of the paper is organized as follows. In section 2.2 and 2.3, we present the numerical methodology and a brief description of SPOD, respectively. Some visualizations of the flow follow in section 2.4. Section 2.5 is a presentation of some single-point statistics obtained from ensemble-averaging (averaging in time and in the azimuthal direction) of the numerical data. Section 2.6 and 2.7 is a description of SPOD eigenvalues and eigenmodes at locations $x/D \geq 20$. The sensitivity of the reconstruction of TKE and $\langle u'_x u'_r \rangle$ to the selection of SPOD modes is discussed in section 2.8. Finally, we report the SPOD analysis at a few locations near the body in Section 2.9 and present conclusions in section 2.10.

2.2 Governing equations and numerical scheme

The flow past a disk in a homogeneous fluid was simulated at $Re = 50,000$. As reported by Chongsiripinyo and Sarkar (2020), a large eddy simulation (LES) approach was adopted and the simulation was conducted with high resolution. The non-dimensional filtered Navier-Stokes equations governing the flow are as follows:

continuity:

$$\frac{\partial u_i}{\partial x_i} = 0, \tag{2.1}$$

momentum:

$$\frac{\partial u_i}{\partial t} + \frac{\partial (u_i u_j)}{\partial x_j} = -\frac{\partial p}{\partial x_i} + \frac{1}{Re}\frac{\partial}{\partial x_j}\Big[\Big(1 + \frac{\nu_s}{\nu}\Big)\frac{\partial u_i}{\partial x_j}\Big], \tag{2.2}$$

where u_i corresponding to $i = 1,2$, and 3 refers to filtered fluid velocities in streamwise (x_1), lateral (x_2), and vertical (x_3) directions, respectively. In Eq. (3.2), ν_s and ν refer to the kinematic subgrid viscosity obtained from the LES formulation and the kinematic viscosity of the fluid,

respectively. The governing equations are non-dimensionalized using the following parameters: free-stream velocity (U_∞) for velocity, diameter of disk (D) for spatial locations (x_i), dynamic pressure ($\rho_o U_\infty^2$) for pressure (p), and advection time (D/U_∞) for time (t). The Reynolds number is denoted by $Re = U_\infty D/\nu$.

The filtered Navier-Stokes equations given by Eq. (3.1) and Eq. (3.2) are solved in a cylindrical coordinate system for the streamwise axial velocity (u_x), radial velocity (u_r), azimuthal velocity (u_θ) and pressure (p). The field variables are functions of streamwise location (x), radial distance from the axis (r), and azimuthal location (θ). The disk is centered at $(x_1, x_2, x_3) = (0, 0, 0)$ in the computational domain, and is represented by the immersed boundary method of Balaras (2004); Yang and Balaras (2006). Spatial derivatives are computed using second-order accurate finite central differences. The temporal marching is performed using the fractional step method which combines the low-storage Runge-Kutta-Wray (RKW3) scheme with the second-order Crank-Nicolson scheme. Taking the divergence of velocity in the predictor step, a pressure Poisson equation is formed which, after taking account of periodicity in the azimuthal direction, transforms to a linear system of equations for Fourier pressure modes. The linear system involves a pentadiagonal matrix which is inverted using a direct solver Rossi and Toivanen (1999). The kinematic subgrid viscosity (ν_s) is obtained using the dynamic eddy viscosity model of Germano et al. (1991). At the inlet boundary, a uniform stream of velocity (U_∞) is imposed while an Orlanski-type convective boundary condition is used for the outflow Orlanski (1976). Neumann boundary condition is imposed at the radial boundary of the domain for all three velocity components.

The computational domain for the present simulation extends until $x/D = 125$ in the streamwise and $r/D = 15$ in the radial direction. The number of grids points used to discretize the domain is as follows: $N_r = 364$ in the radial direction, $N_\theta = 256$ in the azimuthal direction, and $N_x = 4608$ in the axial direction. This choice results in approximately 430 million elements. The conducted LES has high resolution. At $x/D = 10$, $\Delta x/\eta$ is smaller than 10, decreasing to

below 6 by $x/D = 125$. The resolution in the other directions is similarly good. Chongsiripinyo and Sarkar (2020) can be referred for more details regarding the numerics.

2.3 Description of spectral proper orthogonal decomposition (SPOD)

2.3.1 Overview of POD for statistically stationary flows

Let us consider a zero-mean stochastic process $\boldsymbol{u}(\mathbf{x},t)$ in a finite spatial domain Ω. In the context of turbulent flows, $\boldsymbol{u}(\mathbf{x},t)$ can be considered as the fluctuating component of the full velocity field. POD proposed by (Lumley, 1967, 1970) aims at obtaining deterministic functions $\boldsymbol{\Psi}(\boldsymbol{x},t)$ on which $\boldsymbol{u}(\mathbf{x},t)$ has the maximum ensemble-averaged projection. Analytically, this maximization is expressed as,

$$\max_{\boldsymbol{\Psi}} \frac{\langle \{\boldsymbol{u}(\boldsymbol{x},t), \boldsymbol{\Psi}(\boldsymbol{x},t)\}\rangle}{||\boldsymbol{\Psi}(\boldsymbol{x},t)||^2}, \tag{2.3}$$

where $\langle . \rangle$ represents the ensemble average and the inner product $\{\boldsymbol{u}(\boldsymbol{x},t), \boldsymbol{v}(\boldsymbol{x},t)\}$ is defined as

$$\{\boldsymbol{u}(\boldsymbol{x},t), \boldsymbol{v}(\boldsymbol{x},t)\} = \int_{-\infty}^{\infty}\int_{\Omega} \boldsymbol{v}^*(\boldsymbol{x},t)\boldsymbol{W}(\boldsymbol{x})\boldsymbol{u}(\boldsymbol{x},t)\,\mathrm{d}\boldsymbol{x}\,\mathrm{d}t. \tag{2.4}$$

Here, $\boldsymbol{W}(\boldsymbol{x})$ is a positive-definite Hermitian matrix and the asterisk denotes the complex conjugate of the vector field. Using the calculus of variation Holmes, P. and Lumley, J. L. and Berkooz, G. and Rowley, C. W. (2012), the minimization of the expression in Eq. (2.3) reduces to a Fredholm-type integral eigenvalue equation given by

$$\int_{-\infty}^{\infty}\int_{\Omega} R_{ij}(\boldsymbol{x},\boldsymbol{x}',t,t')\boldsymbol{W}(\boldsymbol{x}')\Psi_j^{(n)}(\boldsymbol{x}',t')\,\mathrm{d}\boldsymbol{x}'\,\mathrm{d}t' = \lambda^{(n)}\Psi_i^{(n)}(\boldsymbol{x},t), \tag{2.5}$$

where $\lambda^{(n)}$ and $\Psi_i^{(n)}(\boldsymbol{x},t)$ are the n^{th} eigenvalue and the component of the corresponding eigenmode in the i^{th} direction, respectively. In Eq. (2.5), $R_{ij}(\boldsymbol{x},\boldsymbol{x'},t,t') = \langle u_i(\boldsymbol{x},t)u_j^*(\boldsymbol{x'},t')\rangle$ corresponds to the space-time cross-correlation tensor.

Since time (t) is a homogeneous direction in statistically stationary flows, $R_{ij}(\boldsymbol{x},\boldsymbol{x'},t,t')$ for such flows can be written as,

$$R_{ij}(\boldsymbol{x},\boldsymbol{x'},t,t') = R_{ij}(\boldsymbol{x},\boldsymbol{x'},\tau) = \int_{-\infty}^{\infty} S_{ij}(\boldsymbol{x},\boldsymbol{x'},f)e^{-i2\pi f\tau}\,\mathrm{d}f, \tag{2.6}$$

where $\tau = t - t'$ and $S_{ij}(\boldsymbol{x},\boldsymbol{x'},f)$ is the Fourier transform of $R_{ij}(\boldsymbol{x},\boldsymbol{x'},\tau)$. Using Eq. (2.6), the eigenvalue problem given by Eq. (2.5) can be recast as the following equivalent problem Towne et al. (2018),

$$\int_\Omega S_{ij}(\boldsymbol{x},\boldsymbol{x}',f)\boldsymbol{W}(\boldsymbol{x}')\Phi_j^{(n)}(\boldsymbol{x}',f)\,\mathrm{d}\boldsymbol{x}' = \lambda^{(n)}(f)\Phi_i^{(n)}(\boldsymbol{x},f), \tag{2.7}$$

which can be solved at each frequency f. The modified eigenmodes are then given by $\Phi_i^{(n)}(\boldsymbol{x},f) = \Psi_i^{(n)}(\boldsymbol{x},t)e^{-i2\pi ft}$. By virtue of the Hilbert-Schmidt theorem, the eigenvalues are sorted such that $\lambda^{(1)}(f) \geq \lambda^{(2)}(f) \geq \ldots \geq \lambda^{(n)}(f)$ where $\lambda^{(n)}(f)$ represents the energy content of the n^{th} mode at the frequency f. The eigenmodes are orthonormal to each other, i.e.,

$$\int_\Omega \boldsymbol{\Phi}^{*(n)}(\boldsymbol{x},f)\boldsymbol{W}(\boldsymbol{x})\boldsymbol{\Phi}^{(m)}(\boldsymbol{x},f)\,\mathrm{d}\boldsymbol{x} = \delta_{mn}, \tag{2.8}$$

where δ_{mn} is the Dirac-delta function. These eigenmodes also provide a complete basis for the Fourier realization of the turbulent velocity field $\boldsymbol{u}(\boldsymbol{x},t)$ at frequency f, i.e.,

$$\hat{\boldsymbol{u}}(\boldsymbol{x},f) = \sum_{n=1}^{\infty} a^{(n)}(f)\boldsymbol{\Phi}^{(n)}(\boldsymbol{x},f), \tag{2.9}$$

where $a^{(n)}(f) = \{\hat{\boldsymbol{u}}(\boldsymbol{x},f), \boldsymbol{\Phi}^{(n)}(\boldsymbol{x},f)\}$ is the inner product of the Fourier transform of $\boldsymbol{u}(\boldsymbol{x},t)$ and the n^{th} eigenmode at frequency f.

2.3.2 Numerical implementation of SPOD

In the present work, SPOD is applied to two-dimensional (2D) cross-stream slices of the three-dimensional (3D) velocity field sampled at different streamwise locations from the numerical simulation. Downstream locations, ranging from $x/D = 5$ to 100, are sampled at a spacing of approximately $5D$. Two additional locations at $x/D = 110$ and 120 are also sampled. Besides these locations, SPOD is also performed at $x/D = 0.1, 1, 2$, and 5 to analyze the modal distribution of fluctuation energy near the disk.

The turbulent wake behind a disk is homogeneous-periodic in the azimuthal direction. It can be shown that the SPOD eigenfunctions in the azimuthal direction (or any other homogeneous direction for that matter) are harmonic functions (Lumley, 1970, Towne et al., 2018). Owing to the statistically stationary nature of the wake, the azimuthally decomposed velocity field can be further decomposed into the temporal Fourier modes such that

$$\boldsymbol{u}(x;r,\theta,t) = \sum_m \tilde{\boldsymbol{u}}_m(x;r,t)e^{im\theta} = \sum_f \sum_m \hat{\boldsymbol{u}}_{mf}(x;r)e^{im\theta}e^{i2\pi ft}, \tag{2.10}$$

where $\hat{\boldsymbol{u}}_{mf}$ is the double Fourier decomposed velocity field for a given (m, f) pair and $\tilde{\boldsymbol{u}}_m$ is the azimuthally decomposed instantaneous snapshot at a time instant t .

For the numerical implementation of the SPOD, the velocity field is first decomposed in the azimuthal direction and the data for each azimuthal mode is collected into a snapshot matrix $\boldsymbol{U}_m$ as

$$\boldsymbol{U}_m = [\tilde{\boldsymbol{u}}_m^{(1)}, \tilde{\boldsymbol{u}}_m^{(2)}, \cdots \tilde{\boldsymbol{u}}_m^{(N)}], \tag{2.11}$$

where N is the total number of time snapshots used for the SPOD. Subsequently, $\boldsymbol{U}_m$ is divided into N_{blk} overlapping blocks, each containing N_{freq} entries, as follows:

$$\boldsymbol{U}_m^{(l)} = [\tilde{\boldsymbol{u}}_m^{(l)(1)}, \tilde{\boldsymbol{u}}_m^{(l)(2)}, \cdots \tilde{\boldsymbol{u}}_m^{(l)(N_{freq})}], \tag{2.12}$$

where $\boldsymbol{U}_m^{(l)}$ is the l^{th} block consisting of N_{freq} time snapshots. Each block is then Fourier transformed in the temporal direction and all realizations at a given frequency f are collected into a matrix $\hat{\boldsymbol{U}}_{mf}$ as

$$\hat{\boldsymbol{U}}_{mf} = [\hat{\boldsymbol{u}}_{mf}^{(1)}, \hat{\boldsymbol{u}}_{mf}^{(2)}, \cdots \hat{\boldsymbol{u}}_{mf}^{(N_{blk})}]. \tag{2.13}$$

At this stage, the (r, θ, t) simulation data at each of the chosen streamwise planes has been represented as a collection of N_{blk} independent realizations of the (r, m, f) dependence of the three velocity components. From this form of the data, eigenvectors and eigenvalues are obtained by the eigenvalue decomposition of the weighted cross-spectral density matrix:

$$\hat{\boldsymbol{U}}_{mf}^{*} \boldsymbol{W} \hat{\boldsymbol{U}}_{mf} \boldsymbol{\Gamma}_{mf} = \boldsymbol{\Lambda}_{mf} \boldsymbol{\Gamma}_{mf}. \tag{2.14}$$

Here, $\boldsymbol{W}$ is a $3N_r \times 3N_r$ diagonal matrix which contains the quadrature weights of radial grid points for all three velocity components, accounting for the numerical area-integration of TKE on the discrete grid. This ensures that the obtained SPOD modes optimally capture the area-integrated TKE at any x/D location. The SPOD modes for a given (m, f) can then be obtained from the eigenvectors $\boldsymbol{\Gamma}_{mf}$ as $\boldsymbol{\Phi}_{mf} = \hat{\boldsymbol{U}}_{mf} \boldsymbol{\Gamma}_{mf} \boldsymbol{\Lambda}_{mf}^{-1/2}$. The obtained eigenmodes are orthogonal and the eigenvalues are ordered with respect to their contribution to area-integrated fluctuation kinetic energy as described in the previous section.

For the present analysis, $N = 7200$ snapshots are used for the analysis. Consecutive snapshots are separated by non-dimensional time $\Delta t D/U_\infty \approx 0.07$. N_{freq} (size of each block) and N_{blk} (overlap between two consecutive blocks) are set as 512 and 256 respectively, resulting in total of $N_{blk} = 27$ SPOD modes for each pair of (m, f). Thus, in the present application of SPOD, $\hat{\boldsymbol{U}}_{mf}$ is a matrix of dimension $3N_r \times N_{blk}$. It is worth noting that one block, consisting of $N_{freq} = 512$ snapshots, spans a time window $T_{block} = 36.91 D/U_\infty$. The integral timescale at $r/D = 0.5$, evaluated by integrating the auto-correlation function of streamwise fluctuation velocity (u_x') from a zero value of time lag (τ) to the first zero crossing (Katul and Parlange, 1995,

O'Neill et al., 2004), varies from $\gamma = 0.6045D/U_\infty$ at $x/D = 10$ to $\gamma = 1.6529D/U_\infty$ at $x/D = 120$. Thus, at $x/D = 10$, one block of 512 snapshots spans approximately 61 integral timescales which decreases to approximately 22 integral timescales by $x/D = 120$. Readers are referred to Towne et al. (2018) for more details regarding SPOD and its connection to different modal decomposition techniques (e.g., DMD, resolvent analysis, etc.) and to Schmidt and Colonius (2020) for an introduction to the method.

2.4 Visualizations

Figure 2.1 shows three-dimensional instantaneous visualizations of Q-criterion Hunt et al. (1988), which is used to identify vorticity-dominated regions in a flow field. Q is the second invariant of the velocity gradient tensor, defined as

$$Q = \frac{1}{2}(|\Omega^2| - |\boldsymbol{S}|^2), \tag{2.15}$$

where

$$\Omega_{ij} = \frac{1}{2}\Big(\frac{\partial u_i}{\partial x_j} - \frac{\partial u_j}{\partial x_i}\Big), \quad S_{ij} = \frac{1}{2}\Big(\frac{\partial u_i}{\partial x_j} + \frac{\partial u_j}{\partial x_i}\Big) \tag{2.16}$$

are the rotation tensor and strain-rate tensor respectively. Regions with $Q > 0$ are dominated by vorticity signifying that the fluid motion is primarily rotational in those regions.

At the high *Re* of the present study, velocity gradients are found to be dominated by small-scale turbulent fluctuations. To focus on the large-scale coherent structures, the instantaneous velocity field is filtered using a Gaussian low-pass filter, an in-built SciPy function named *gaussian_filter*. In the inputs for the function *gaussian_filter*, the standard deviation (σ) of the Gaussian kernel was varied systematically from $\sigma = 2$ to 30. Subsequently, based on visual inspection, a Gaussian low-pass filter with $\sigma = 10$ was used for the present visualizations. Higher σ values led to the smearing of large-scale coherent structures while visualizations with lower

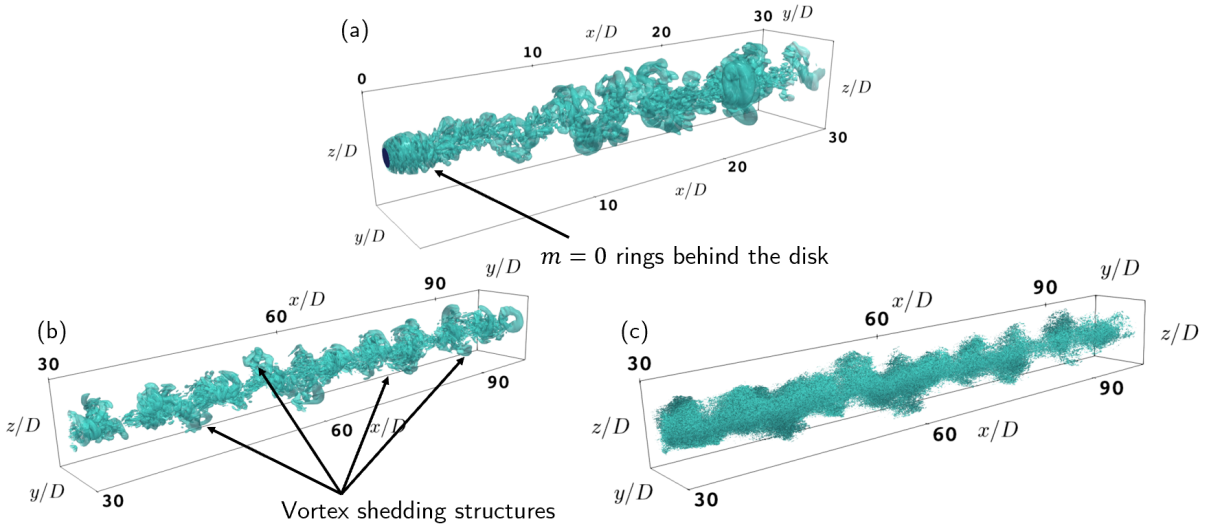

Figure 2.1: Isosurfaces of Q-criterion. $Q = 0.001$ of the filtered velocity for (a) $0 < x/D < 30$ and for (b) $30 < x/D < 100$ at a given time instant; (c) $Q = 0.05$ of the residual field for $30 < x/D < 100$.

σ still had significant imprints of the small-scale turbulence obscuring the large-scale coherent structures. The width of the Gaussian kernel is set such that the Q of the filtered velocity field elucidates coherent structures without much distortion and, at the same time, is not completely dominated by the small-scale fluctuations.

In Fig. 2.1(a), it can be observed that vortex rings are shed in the immediate downstream of the disk. These vortex rings represent the axisymmetric $m = 0$ mode. As the flow evolves spatially, these rings become unstable and give way to a complex distribution of vorticity in the wake. Instantaneous two-dimensional contours of Q in the vicinity of the disk (see Fig. 2.2) shows higher azimuthal modes with $m > 0$ (see Fig. 2.2(a)) that emerge close to the disk and distort the $m = 0$ vortex rings. At $x/D = 0.5$ and 1.05, the presence of $m = 1$ and $m = 2$ modes can be seen in Fig. 2.2(b) and 2.2(c), respectively.

Despite the entangled arrangement of vortices, a helical orientation of coherent structures in the wake can be discerned from the 3D visualizations of Fig. 2.1. These coherent structures are the vortex shedding structures that originate near the disk from instabilities in $m = 0$ and

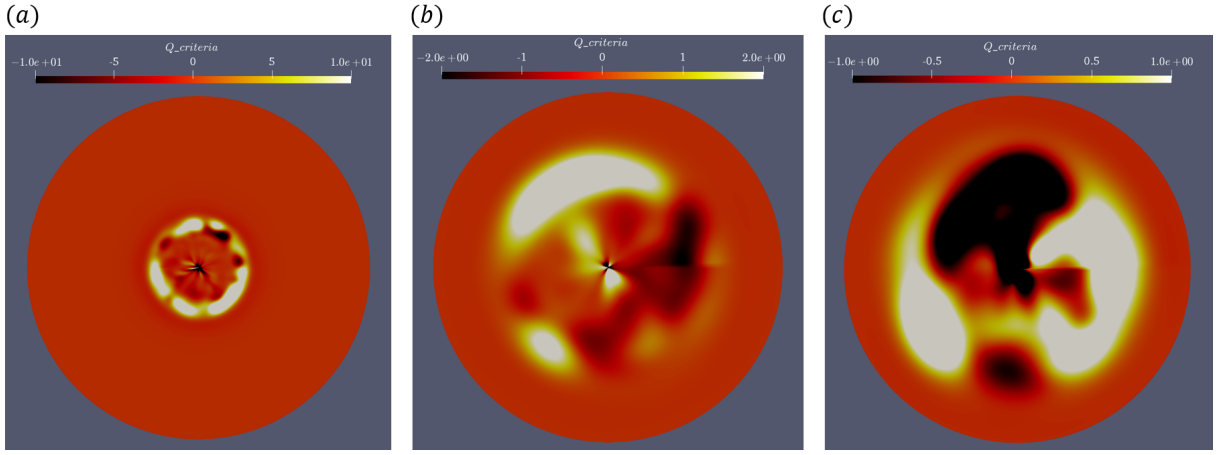

Figure 2.2: Two-dimensional contours of Q-criterion of the filtered velocity fields at the same time instant as in Fig. 2.1 at various streamwise locations: (a) $x/D = 0.05$, (b) $x/D = 0.5$, and (c) $x/D = 1.05$.

advect downstream. Visual inspection of Fig. 2.1(a) and (b) reveal the following points. First, the vortex shedding structures are separated approximately by $\lambda_{VS}/D = 1/St$ where $St = 0.135$ (identified formally by the modal decomposition, as will be seen) is the vortex shedding frequency of the disk wake at hand. Second, these structures meander away from the wake centerline as the flow evolves downstream. For completeness, Q-criterion of the residual velocity field, obtained by subtracting the filtered velocity from the original velocity, is presented in Fig. 2.1(c) for $30 < x/D < 100$. The residual field also shows a helical-like orientation similar to the filtered field observed in Fig. 2.1(b). It is worth noting that the above-mentioned procedure of obtaining the residual field does not ensure the absence of an imprint of the large-scale features on the residual field. It is also possible that this imprint can be physical (rather than the imperfection of scale separation by a physical-space filter) in the sense that the structure of the fine-scale turbulence is dependent on the coherent structures.

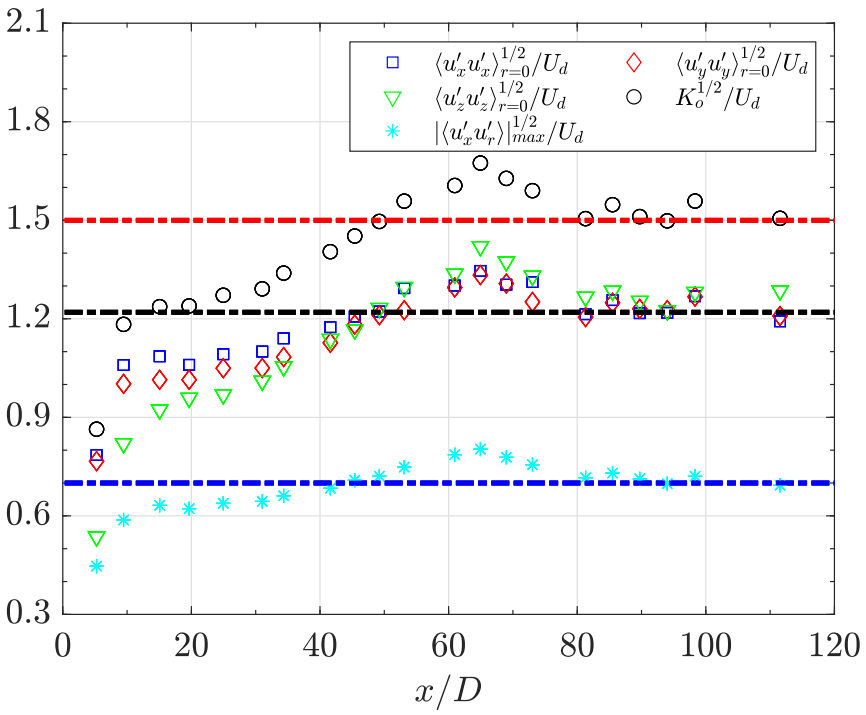

Figure 2.3: Ratio of centerline turbulent intensities and $|\langle u'_x u'_r \rangle|^{1/2}_{max}$ to U_d as a function of x/D.

2.5 Evolution of turbulence statistics in the wake

Figure 2.3 shows the streamwise evolution of the centerline r.m.s. velocity fluctuations and the maximum value of $\langle -u'_x u'_r \rangle^{1/2}(r)$, each normalized by the centerline defect velocity (U_d). The normalized turbulent velocity scale ($K_o^{1/2}$), derived from the centerline TKE ($K_o = \langle u'_i u'_i \rangle_{r=0}/2$), is also shown. Chongsiripinyo and Sarkar (2020) found, using the same simulation, that the mean velocity scale (U_d) and the turbulence velocity scale ($K_o^{1/2}$) did not follow the same decay rates for $10 < x/D < 65$; U_d was $\propto x^{-0.9}$ while $K_o^{1/2}$ was $\propto x^{-0.7}$. After $x/D \approx 65$, the decay rates of both U_d and $K_o^{1/2}$ became similar and close to the classical decay exponent of $-2/3$ for the axisymmetric turbulent wake. The consequences of this difference in the initial decay rates can be observed in Fig. 2.3 where the ratio of each r.m.s. velocity fluctuation to U_d keeps increasing until $x/D \approx 65$. Beyond $x/D = 65$, the ratios drop down and asymptote to approximately 1.2 for the individual r.m.s. fluctuations and 1.5 for $K_o^{1/2}$. It can also be seen that the near-wake turbulence ($x/D < 40$) is more anisotropic with the streamwise component dominating over

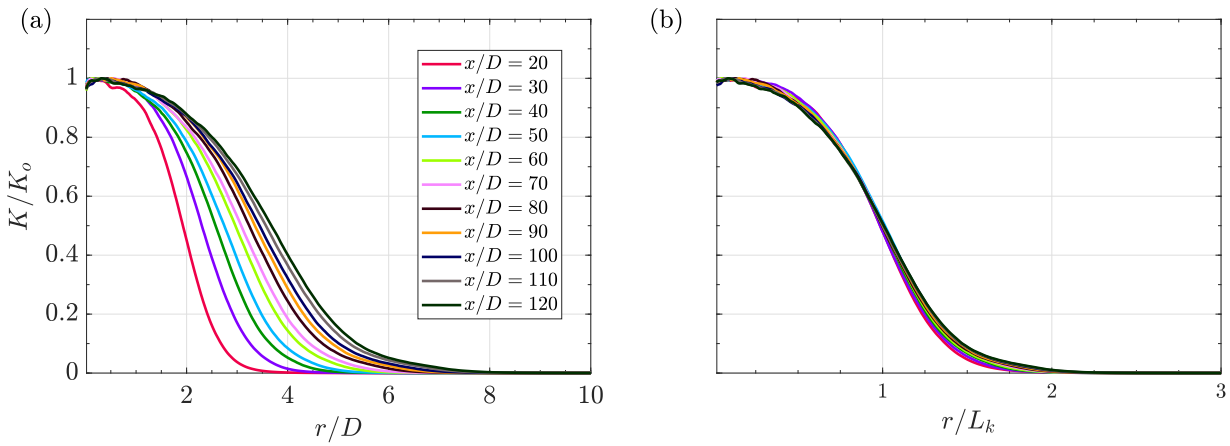

Figure 2.4: TKE profiles scaled with K_o at different streamwise locations ($20 < x/D < 120$) with radial direction scaled by: (a) D and (b) L_k.

the other two. It is beyond $x/D = 40$ that the r.m.s. velocity fluctuations become more or less isotropic. Figure 2.3 also shows the ratio of square-root of the maximum value of $\langle -u'_x u'_r \rangle(r)$ to U_d. This ratio also increases for $x/D < 65$, albeit slowly, compared to the ratios of the r.m.s. fluctuations. After $x/D \approx 80$, the value of $\langle -u'_x u'_r \rangle^{1/2}_{\max}/U_d$ asymptotes to ≈ 0.7. Compared to the previous experimental studies of flow past a disk (Johansson et al. (2003), Table 5.3 in Pope (2000)), the ratios of turbulent intensities to the defect velocity are slightly higher in the present case (an asymptotic value of 1.2 instead of approximately $0.9-1.1$ found in the previous studies), which may be due to the relatively high *Re* of the current study.

Figure 2.4 shows radial profiles of TKE at different downstream locations spanning $20 < x/D < 100$. Normalization of r by the disk diameter (D) in part (a) is compared with normalization by the local wake width (L_k) in part (b). Here, L_k is the half-width of the TKE profile defined by $K(x; r = L_k) = \frac{1}{2}K_o(x)$. The downstream growth of wake thickness is seen in Fig. 2.4(a) where the radial spread of K/K_o monotonically increases with increasing x/D. When the radial direction is scaled by L_k, these profiles collapse onto a single profile implying self-similar evolution of TKE beyond $x/D \approx 20$. It is worth noting that the TKE becomes approximately zero by $r/L_k = 2$.

In Fig. 2.5 we plot the scaled profiles of normal stresses along with $\langle u'_x u'_r \rangle$, the component

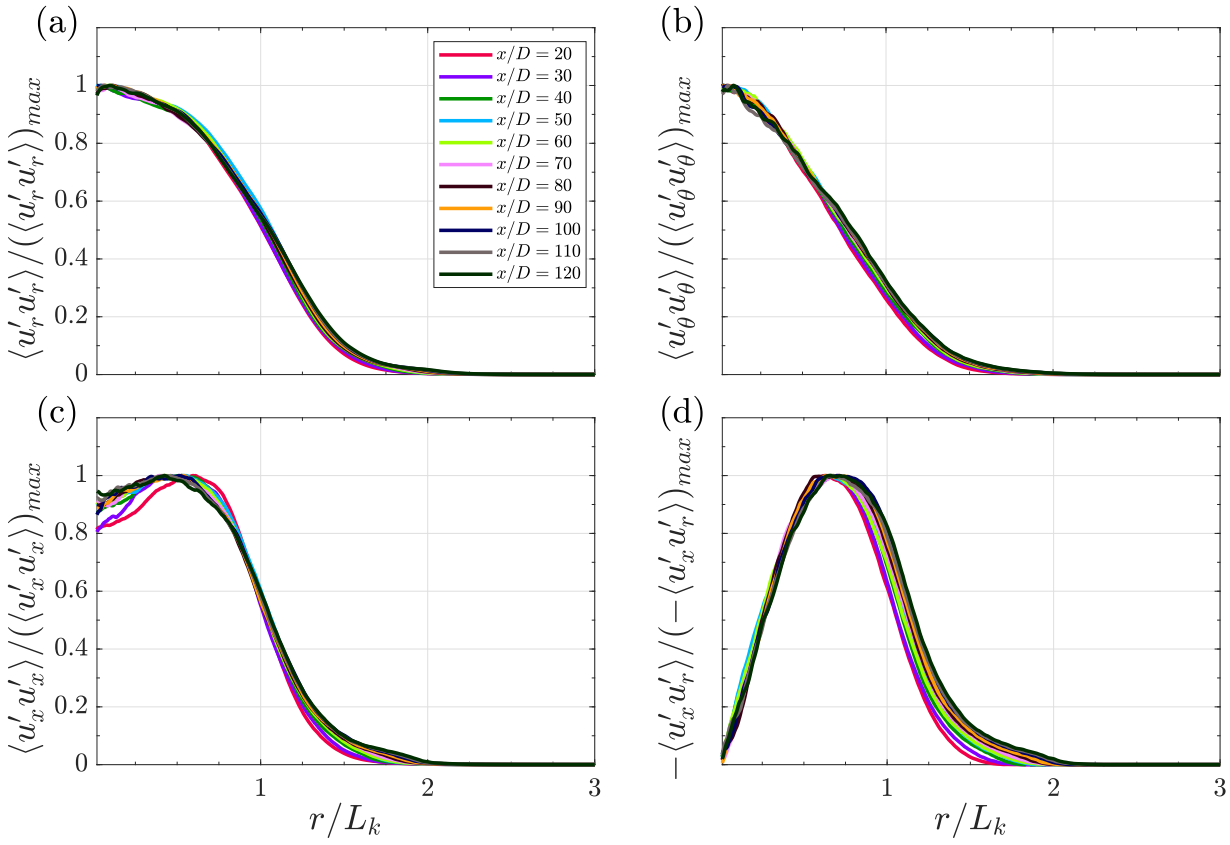

Figure 2.5: Normal turbulent stresses (a, b, c) and $\langle u'_x u'_r \rangle$ (d) profiles at different streamwise locations ($20 < x/D < 120$) scaled by their maximum values at the respective locations. The radial direction is scaled by TKE-based wake width L_k.

of Reynolds stress tensor that appears in the simplified Reynolds-averaged streamwise momentum equation of the turbulent axisymmetric wake,

$$U_\infty \frac{\partial}{\partial x}(U - U_\infty) = -\frac{1}{r}\frac{\partial}{\partial r}(r\langle u'_x u'_r \rangle). \tag{2.17}$$

All the turbulent stresses in Fig. 2.5 have been scaled by their maximum values at the corresponding x/D locations, and the the radial direction has been scaled by the TKE-based wake width L_k. All the three normal turbulent stresses plotted in Fig. 2.5 collapse beyond $x/D \approx 40$. Until $x/D \approx 40$, the profile of the streamwise component shows the largest deviation among different locations. Besides $\langle u'_x u'_x \rangle$, which peaks between $r/L_k = 0.5 - 0.75$, the other two normal turbulent stresses peak near the centerline and decay with increasing r. All three normal stresses approach zero by $r/L_k \approx 2$ as was also seen for the TKE profiles.

The profiles of $\langle u'_x u'_r \rangle$ collapse well for $r/L_k < 0.75$ when scaled with L_k. Beyond the peak location of $\langle -u'_x u'_r \rangle$, which occurs near the peak of $\langle u'_x u'_x \rangle$, there is some spread in the normalized profiles. The radial extent of the scaled profiles increases with increasing x/D. At $x/D = 20$, the scaled Reynolds stress profile decays to zero by $r/L_k \approx 1.6$. By $x/D = 100$, the radial extent of the scaled profiles has increased to $r/L_k \approx 2$.

2.6 SPOD eigenvalues and eigenspectra

Figure 2.6 shows the distribution of energy in the leading SPOD (or the most energetic SPOD) eigenvalue $\lambda^{(1)}$ as a function of azimuthal mode (m) and non-dimensional frequency (St) at four downstream locations: $x/D = 20$, 40, 80, and 100. At all locations, the energy in $\lambda^{(1)}$ among all (m, St) pairs is predominantly contained in modes that satisfy $m \leq 4$ and $St < 0.4$.

There are two distinct peaks in Fig. 2.6: (i) $m = 1$, $St = 0.135$ (vortex shedding (VS) structure), and (ii) $m = 2$, $St = 0$ (double helix (DH) structure). The former has long been known to be the vortex shedding structure in the turbulent wake of a disk (Berger et al., 1990, Cannon

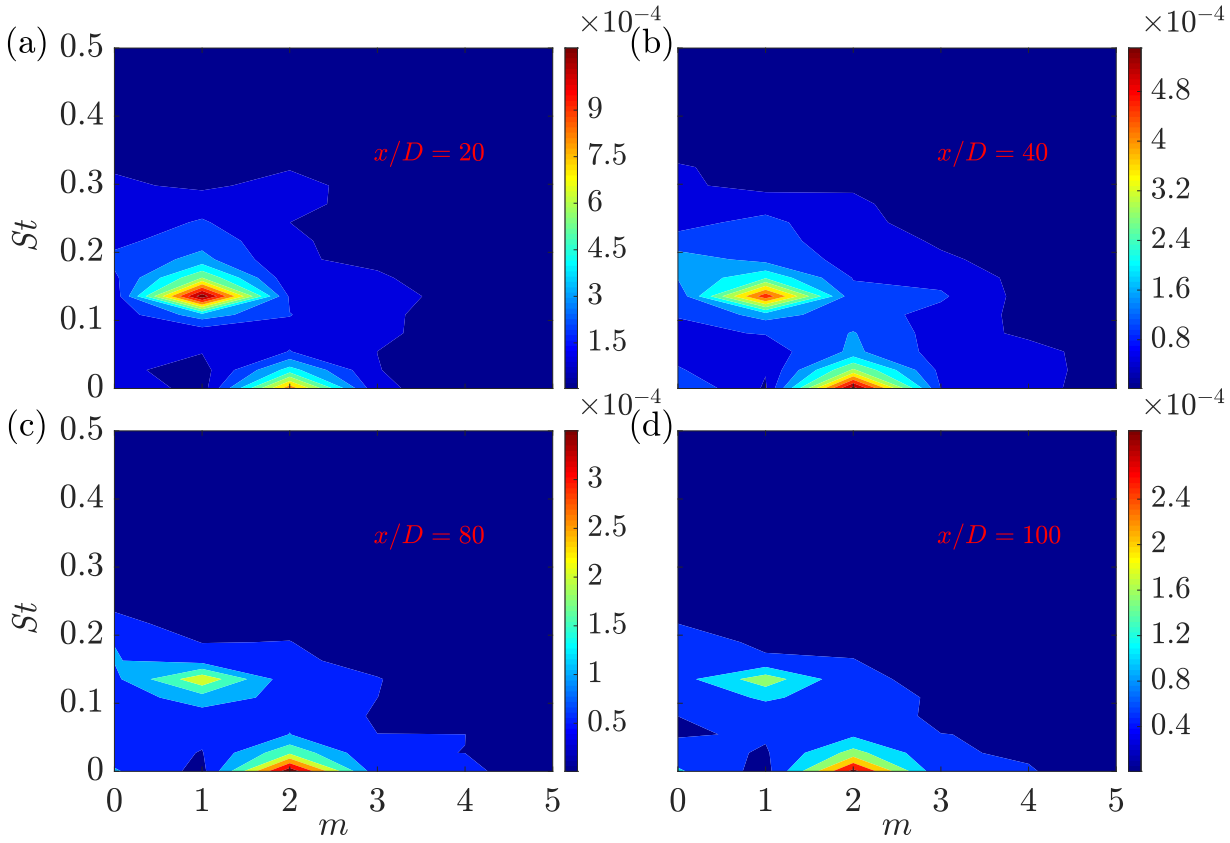

Figure 2.6: SPOD contour maps showing energy contained in leading SPOD mode, $\lambda^{(1)}$, as a function of azimuthal wavenumber m and frequency St at different locations: (a) $x/D = 20$, (b) $x/D = 40$, (c) $x/D = 80$, and (d) $x/D = 100$.

et al., 1993, Fuchs et al., 1979, Johansson and George, 2006b, Johansson et al., 2002). The existence of the latter in the high-*Re* wake of disk was first reported by Fuchs et al. (1979) and its importance was expanded upon later by Johansson and George (2006b). The prominent peak at $St = 0$ should be interpreted as a quasi-steady structure in the limit of $St \to 0$ Nogueira et al. (2019). The discrete nature of the Fourier transform and the limited temporal runtime ($T \approx 504D/U_\infty$, which is approximately four flow-through times) of these computationally intensive simulations make it difficult to resolve very small frequencies in the limit of $St \to 0$, leading to the energy of very low frequencies being captured in $St = 0$. In the rest of the paper, $St = 0$ will be replaced with $St \to 0$ in the context of $m = 2$ to avoid misinterpreting it as a temporally stationary mode.

Figure 2.6 has two important implications. First, the peak associated with vortex shedding persists far downstream, being still present at $x/D = 100$. Second, the leading SPOD mode of the VS structure clearly dominates the near wake (at $x/D = 20$) and gradually declines in importance relative to the DH structure which eventually dominates the energy content in $\lambda^{(1)}$ by $x/D = 100$. This observation is consistent with the previous findings of Johansson and George (2006b) who found that the DH structure dominated in the wake beyond $x/D = 30$.

To further analyze the contribution of different azimuthal modes to the area-integrated TKE, the eigenspectrum of each m has been summed over all resolved frequencies and normalized with $E_k^T(x/D)$ to obtain the percentage contribution of each m as follows:

$$\xi^{(i)}(m;x/D) = \frac{\sum_{St} \lambda^{(i)}(m,St;x/D)}{E_k^T(x/D)} \times 100, \tag{2.18}$$

where the index i corresponds to the i^{th} SPOD mode and $E_k^T(x/D)$ is the area-integrated TKE at that x/D location. The resulting frequency-integrated eigenspectrum has been plotted for four locations $x/D = 20, 40, 80$, and 100 in Fig. 2.7. From Fig. 2.7 it can be ascertained that a major contribution to TKE comes from the first five azimuthal modes in the near as well as far wake. Another observation is the overall low-rank behavior of azimuthal modes $m \leq 4$ in the

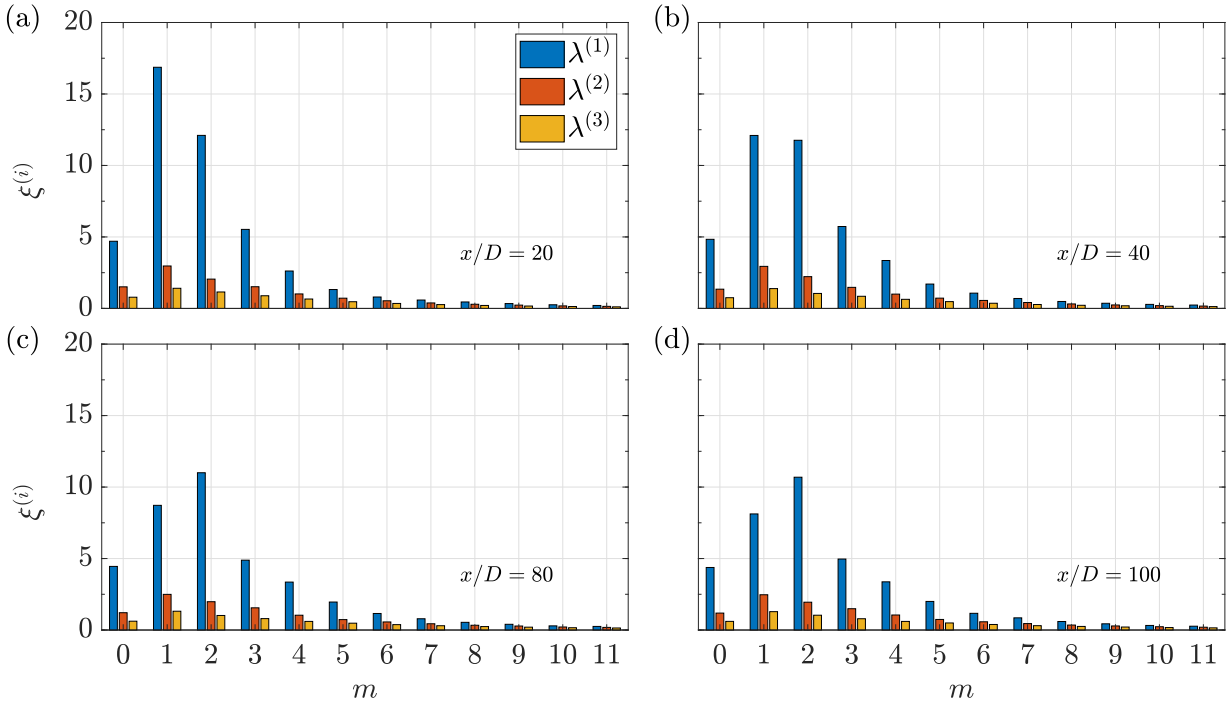

Figure 2.7: Frequency-integrated eigenspectrum as a function of azimuthal mode number m at different locations: (a) $x/D = 20$, (b) $x/D = 40$, (c) $x/D = 80$, and (d) $x/D = 100$. Three leading SPOD modes ($\lambda^{(1)}$, $\lambda^{(2)}$, and $\lambda^{(3)}$) at each m are shown in terms of their percentage contributions to the area-integrated TKE.

sense that there is a significant difference between the contributions of $\lambda^{(1)}$ and $\lambda^{(2)}$ for these m. At $x/D = 20$ in Fig. 2.7(a), $m = 1$ dominates the integrated eigenspectra followed by $m = 2, 3$, and 0 respectively. As x/D increases, the relative contribution of $m = 2$ starts increasing while that of $m = 1$ starts declining. By $x/D = 40$ (Fig. 2.7(b)), both $m = 1$ and $m = 2$ have similar contribution and eventually $m = 2$ starts dominating the integrated eigenspectra as seen in Fig. 2.7(c) and Fig. 2.7(d). Beyond $m = 2$, the energy content of $\lambda^{(i)}$ decreases monotonically with increasing m.

The results of Johansson and George (2006b) showed the eventual dominance of the $m = 2$ mode beyond $x/D = 40$. In the present analysis, the $m = 2$ mode emerges as the dominant mode at a farther downstream distance $x/D = 60$. It is worth noting that all three velocity components are included in the SPOD kernel as opposed to the previous analysis Johansson and George (2006b) which only included the streamwise velocity component. Besides this difference, the present results show that the axisymmetric mode $m = 0$ is always significantly less dominant than $m = 1$ and is of comparable magnitude to the $m = 3$ mode. In the previous results Johansson and George (2006b), the axisymmetric mode was of comparable magnitude to $m = 1$ and was significantly more dominant than $m = 3$ for all measurement stations at $30 \leq x/D \leq 150$ (see Fig. 7 in their paper). It is also worth noting that $Re = 50,000$ is almost twice that of the previous study.

The findings of Fig. 2.6 and 2.7 warrant a detailed investigation of the VS and DH mode. In what follows, we investigate the $m = 1$ and $m = 2$ modes in more detail, particularly in the context of the VS and DH modes. We also present some results on the eigenvalues and eigenspectra of $m = 0, 3$, and 4 modes since Fig. 2.7 shows that these modes, although not dominant, also make appreciable contributions to the area-integrated TKE.

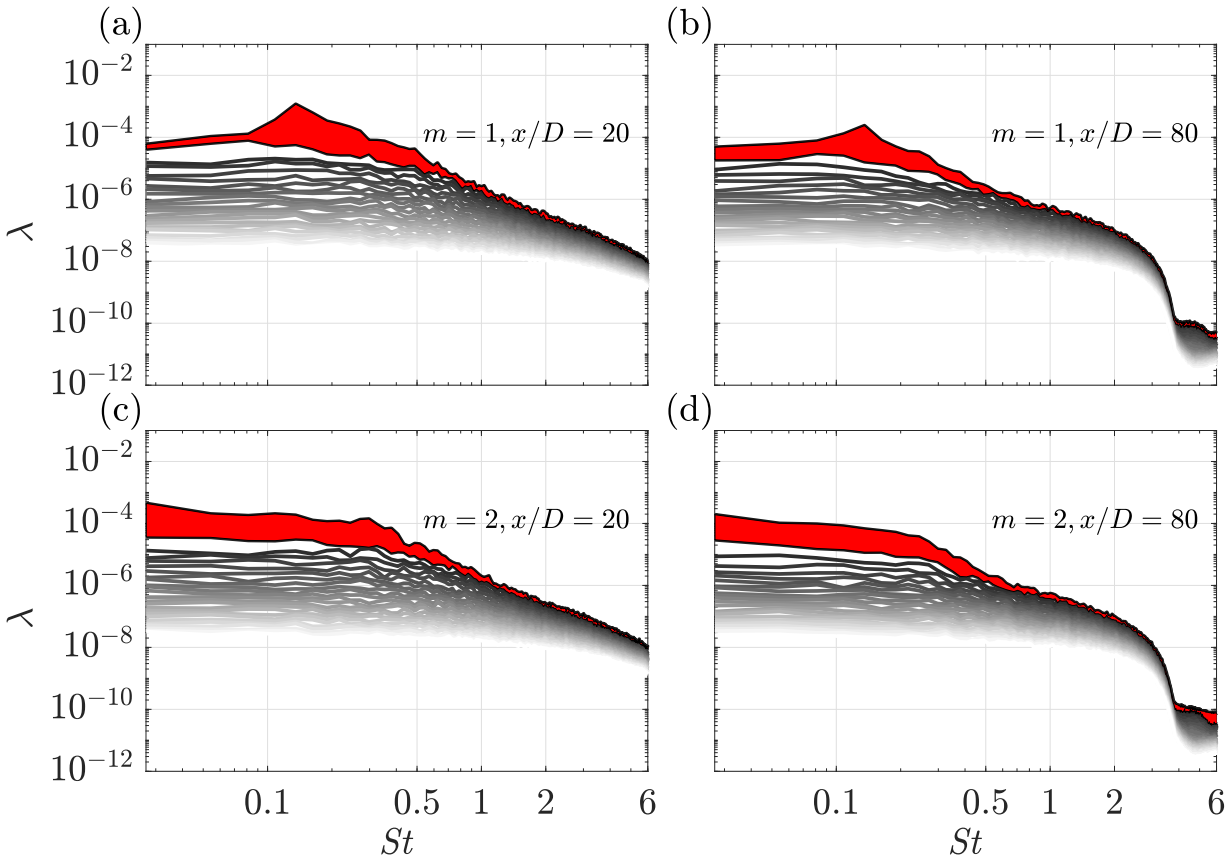

Figure 2.8: SPOD eigenspectra of 25 modes (dark to light shade corresponds to high to low energy eigenvalues): (a) $m = 1$, $x/D = 20$; (b) $m = 1$, $x/D = 80$; (c) $m = 2$, $x/D = 20$; (d) $m = 2$, $x/D = 80$.

2.6.1 Eigenspectra of $m = 1$ and $m = 2$ modes

As observed in Fig. 2.7, azimuthal modes $m = 1$ and $m = 2$ dominate the energy distribution of the leading SPOD mode in the near as well as far wake. To further clarify the energy distribution among different frequencies for these two azimuthal modes, Fig. 2.8 shows the SPOD eigenspectra of the $m = 1$ and $m = 2$ modes at two representative locations in the near ($x/D = 20$) and far ($x/D = 80$) wake. The area shaded by red denotes the difference between the energy content of the first and second SPOD modes. For the $m = 1$ mode in Fig. 2.8(a) and (b), the distinct peak at $St = 0.135$ is still clearly visible in the leading SPOD mode at $x/D = 80$. This is in contrast to the results of Johansson and George (2006b) in which the VS structure was almost undetectable in the eigenvalue spectra by $x/D = 70$ (see Fig. 2 of that paper). Interestingly the peak at $St = 0.135$ is not visible in the subsequent SPOD modes. Besides, there is a significant gap between the first and second SPOD modes at $St \approx 0.135$, more so at $x/D = 20$ than at $x/D = 80$. This large gap implies that vortex shedding contributes significantly to the dynamics of the overall behavior of the $m = 1$ mode.

Contrary to the $m = 1$ mode, the eigenspectra of the $m = 2$ mode shown in Fig. 2.8(c) and (d) peaks near $St \to 0$ and decays monotonically with increasing St. This decay rate is observed to increase for frequencies with $St > 0.5$ at both the locations. Like the $m = 1$ mode, the $m = 2$ mode also exhibits a prominent gap between $\lambda^{(1)}$ and $\lambda^{(2)}$ at low frequencies with $St < 0.3$. SPOD eigenspectra of $m = 1$ and 2 analyzed at other locations (not shown here) qualitatively exhibit features similar to the locations shown in Fig. 2.8.

Figure 2.6 established that the energy in the leading SPOD mode is dominated by the DH structure ($m = 2$ and $St \to 0$) in the far wake. To further quantify this observation, the evolution of $\lambda^{(1)}$ of the VS and DH structure is plotted in Fig. 2.9. Both SPOD modes exhibit a monotonic decay which is in accordance with the decaying nature of wake turbulence. However, there are salient differences in the nature of their decay. The leading SPOD mode of the VS structure decays as $\lambda^{(1)} \propto x^{-1.14}$ from $10 < x/D < 120$. On the other hand, $\lambda^{(1)}$ of the DH structure decays

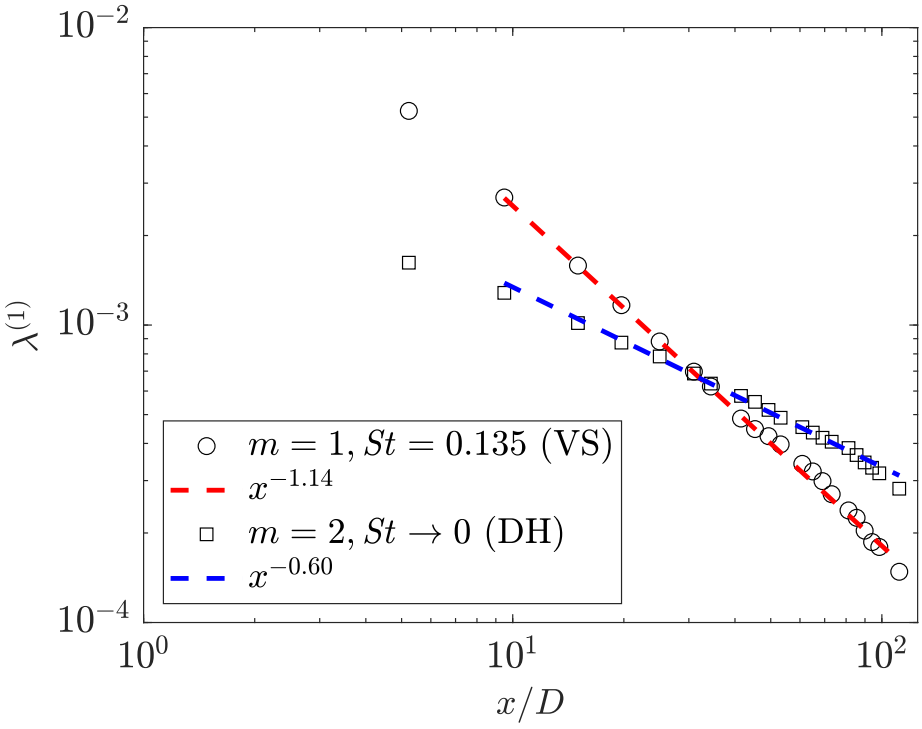

Figure 2.9: Evolution of leading SPOD mode of $m = 1$, $St = 0.135$ and $m = 2$, $St \to 0$ as x/D.

at a slower rate as $\lambda^{(1)} \propto x^{-0.60}$ so that it eventually exceeds the VS mode in terms of energy content beyond $x/D = 35$.

We now explore the self-similarity of $\lambda^{(1)}$ of the $m = 1$ and $m = 2$ modes. Figure 2.10 shows $\lambda^{(1)}$ for these two modes after scaling by $(K_o^{1/2} L_k)^2$, a quantity representative of area-integrated TKE in the wake. For $m = 2$, the eigenvalues collapse well when scaled by $(K_o^{1/2} L_k)^2$ throughout $20 < x/D < 100$ as seen in Fig. 2.10(b). The unscaled eigenvalues (not presented here) for $m = 2$ show a variability of $50\% - 60\%$ for lower frequencies. The eigenspectra of $\lambda^{(1)}$ for $m = 2$ always peaks at $St \to 0$ for all downstream locations. The local timescale (ζ) of an axisymmetric wake scales as $x^{3m/2}$ if we assume: (i) $U_d \propto x^{-m}$, and (ii) $\zeta \sim L_d/U_d$. Thus, the local frequency $f \propto x^{-3m/2}$ decays as x/D increases since m is a positive real number. The conclusion that f decays with x/D is unchanged even if local turbulent velocity ($K_o^{1/2}$) and TKE-based wake width (L_k) is used to form ζ. For the present case, f starts off as $f \sim O(10^{-2})$ and decays to $f \sim O(10^{-3})$ by the end of the domain. The collapse of the $m = 2$ energy content

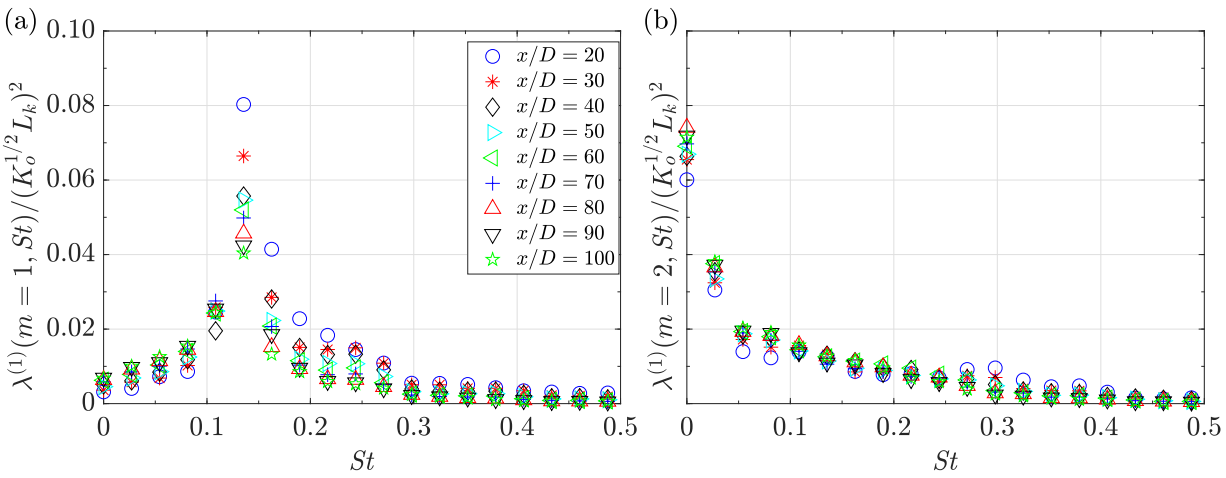

Figure 2.10: $\lambda^{(1)}$ of: (a) $m=1$ and (b) $m=2$, scaled by $(K_o^{1/2}L_k)^2$ for $20<x/D<100$. Here K_o is the centerline value of TKE and L_k is the TKE-based wake width.

by local shear variables, particularly in the limit of $St \to 0$, suggests a possible link of this mode to the local shear structure of the wake.

Figure 2.10(a) shows the eigenspectrum of the $m=1$ mode scaled with $(K_o^{1/2}L_k)^2$ for $20<x/D<100$. There is a significant spread in the scaled eigenvalues around the vortex shedding frequency $St=0.135$. It is clear from the plot that the leading SPOD mode of the vortex shedding structure does not collapse in local shear variables. This is a global mode which originates near the disk and convects downstream. As St increases beyond 0.3, the collapse improves indicating that the high frequency components in $m=1$ might be linked to the local turbulence structure. However their energy is small and hence the non-similar contribution of the vortex shedding frequency dominates the overall behavior of $m=1$.

POD is a statistical technique. Thus, although the obtained mode optimally capture the fluctuation energy in an ensemble-averaged sense, these modes do not necessarily represent the structures of instantaneous eddies in the flow. However, it is the case that these modes possess the imprints of coherent structures found in instantaneous snapshots. To assess whether different azimuthal modes which are found to be dominant from SPOD analysis are distinctly visible in the flow field, u'_x at three different downstream locations $x/D=10,40$, and 80 and at some selected

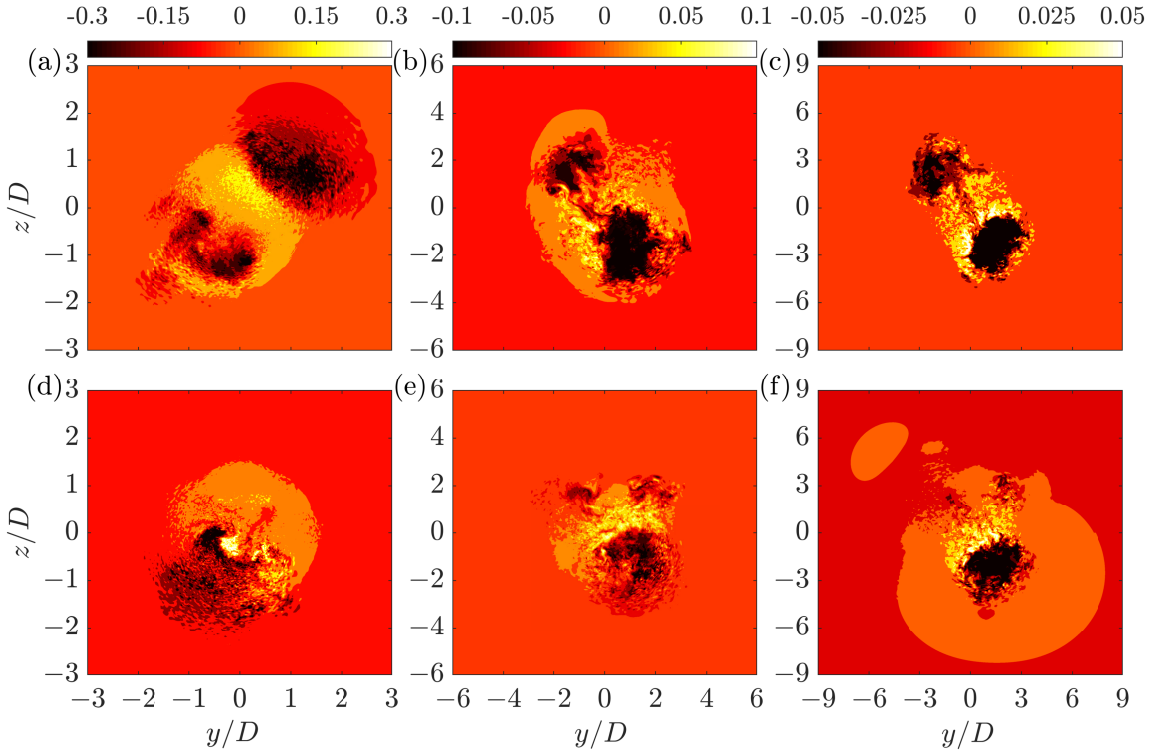

Figure 2.11: Instantaneous snapshots of the u'_x field showing the imprint of the $m = 1$ (bottom row) and $m = 2$ (top row) modes: (a,d) at $x/D = 10$, (b, e) at $x/D = 40$, and (c, f) at $x/D = 80$.

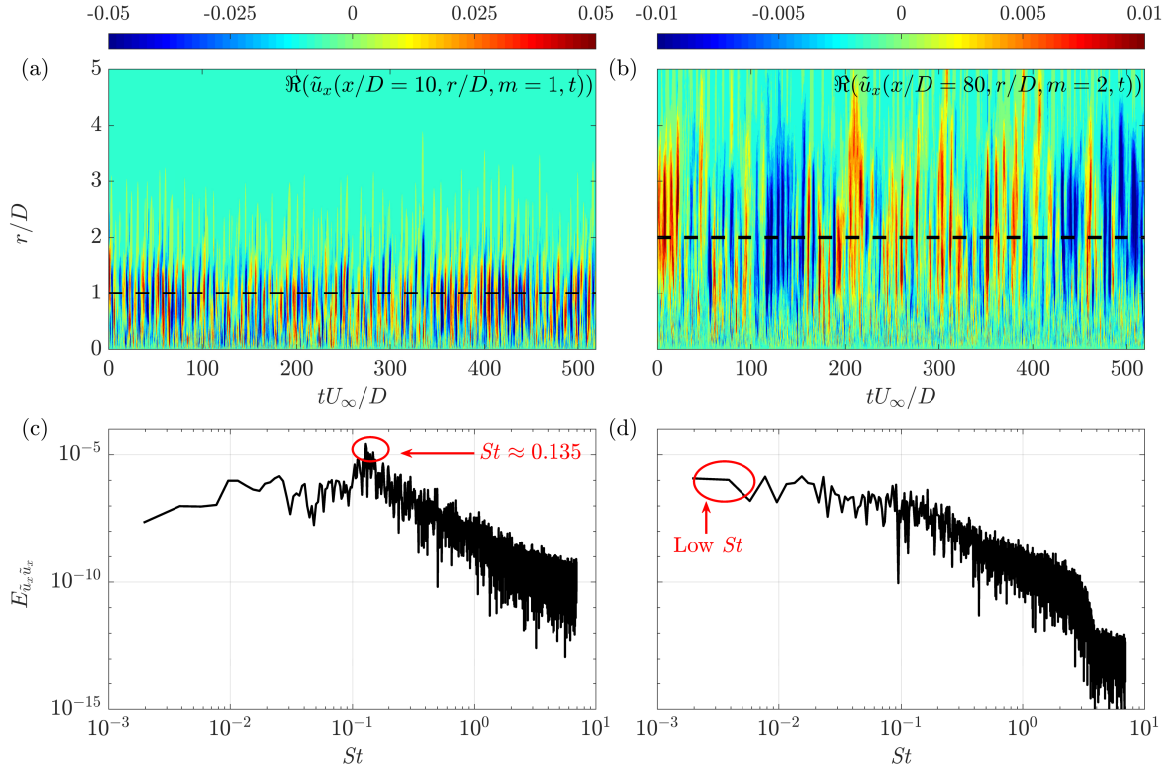

Figure 2.12: *r-t* plot of the real part of the azimuthally decomposed velocity field: (a) $m = 1$ at $x/D = 10$, and (b) $m = 2$ at $x/D = 80$. Power spectra of time series: (c) $r/D = 1$, $x/D = 10$ for $m = 1$, and (d) $r/D = 2$, $x/D = 80$ for $m = 2$, with the r/D locations shown by dashed black lines in (a) and (b), respectively.

time instants is plotted in Fig. 2.11. These snapshots were selected by projecting instantaneous u'_x to leading SPOD modes of the VS and DH structures and requiring large values of projection coefficient (similar to the approach of Hellstrom et al. (2016)). In the top row (Fig. 2.11(a,b,c)), the instantaneous u'_x has the imprint of the $m = 2$ velocity field at all three locations. Likewise the bottom row shows the time instants at which the velocity field exhibits evidence of the $m = 1$ mode. Although these snapshots do not exactly mimic the mode shapes (inset contour maps of Fig. 2.15) to be discussed later, they imply that aspects of the $m = 1$ and 2 modes can be found in individual flow realizations. Both of these azimuthal modes are observed in the instantaneous flow snapshots throughout the wake evolution from near ($x/D = 10$) to far wake ($x/D = 80$) consistent with the eigenspectra analysis.

The two most dominant SPOD frequencies, $St = 0.135$ and $St \to 0$, are apparent in the space-time history of the $m = 1$ and $m = 2$ modes as demonstrated by the r - t plot of these modes of u'_x in Fig. 2.12. The near-wake location of $x/D = 10$ (Fig. 2.12 a) has a clear periodicity in the time series which corresponds to a peak at $St \approx 0.135$ of the power spectrum of this signal at $r/D = 1$ (Fig. 2.12 b). The SPOD spectrum, by exploiting correlation in space along with time, makes this frequency for $m = 1$ more distinctive as was seen in Fig. 2.8(a). While discussing Fig. 2.6, it was noted that the $St = 0$ peak in the SPOD spectrum of $m = 2$ is likely related to a very low-frequency signal. Figure 2.12(b) substantiates this hypothesis since a signal with a very large time period, shown by wide (in the $t-$axis) patches of blue and red, can be discerned. These patches span the entire radial extent of the wake. The power spectrum calculated at $r/D = 2$ (Fig. 2.12 d) indeed peaks at low $St \approx 10^{-3}$.

2.6.2 Eigenspectra of $m = 0, 3,$ and 4 modes

The $m = 0, 3,$ and 4 modes are energetically the three important azimuthal modes after the $m = 1$ and 2 modes. Therefore, it is of interest to characterize their eigenspectra and assess the applicability of local similarity scaling of their magnitude.

Fig. 2.13 shows eigenspectra of the $m = 0, 3,$ and 4 modes at two locations $x/D = 20$ and $x/D = 80$. Similar to the $m = 1$ and 2 modes, these azimuthal modes also exhibit a significant gap between $\lambda^{(1)}$ and $\lambda^{(2)}$ SPOD modes for $St < 0.5$ shown by the red-shaded area. The eigenspectra of the $m = 0$ mode shown in Fig. 2.13(a) and (d) exhibit a peak at $St = 0.189$ for $\lambda^{(1)}$. This peak is evident even in the far wake location at $x/D = 80$. This peak is also found close to the disk as will be discussed in more detail in Section 2.9. The other two azimuthal modes, $m = 3$ and $m = 4$, exhibit features similar to the $m = 1$ and $m = 2$ modes, respectively. The eigenspectrum of $\lambda^{(1)}$ for the $m = 3$ mode shows a peak at the vortex shedding frequency $St = 0.135$, although the peak is much less pronounced than for the $m = 1$ case. Like the $m = 2$ mode, the eigenspectra of the $m = 4$ mode peak at $St \to 0$ and decay thereafter. An increased rate of decay with increasing

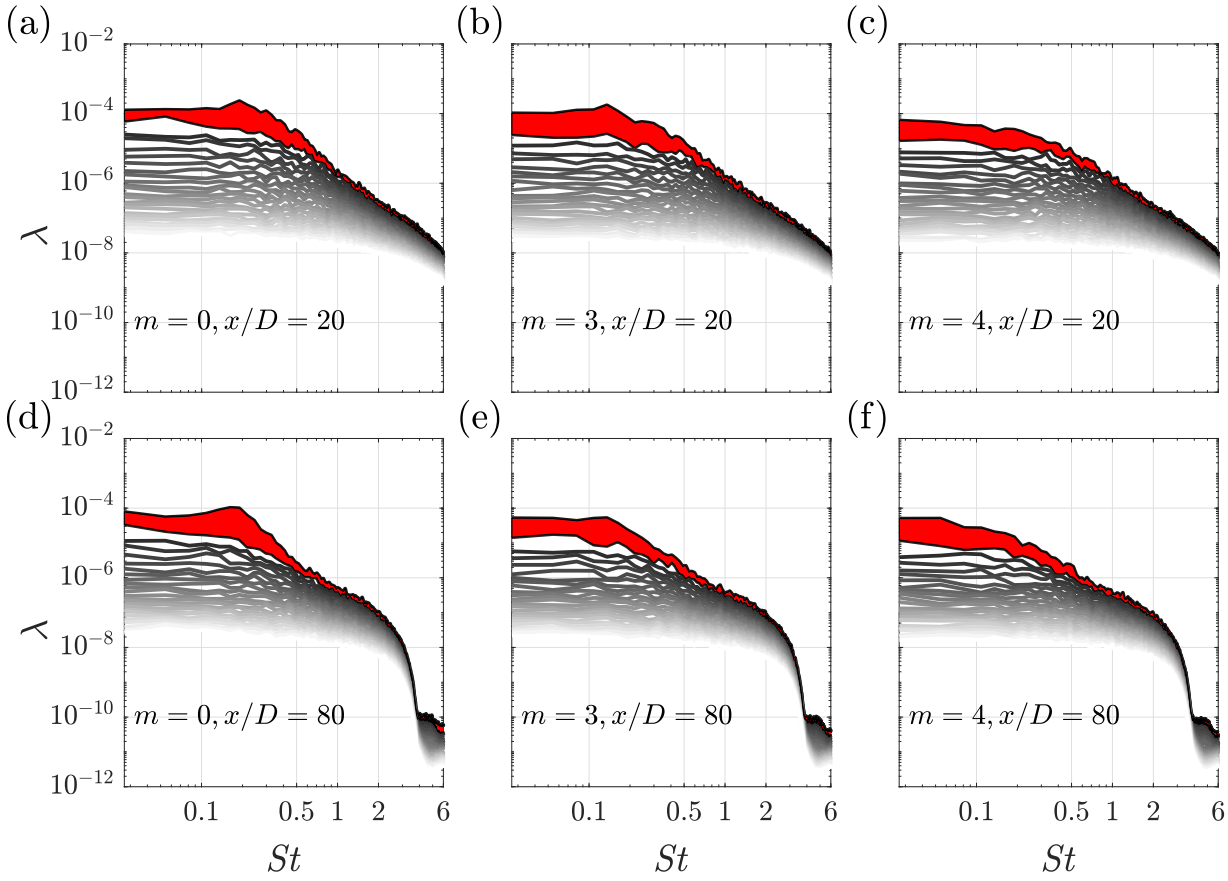

Figure 2.13: SPOD eigenspectra of 25 modes (dark to light shade corresponds to high to low energy eigenvalues) for $m = 0$ (left), $m = 3$ (middle) and $m = 4$ (right). Top row shows $x/D = 20$ and bottom row shows $x/D = 80$.

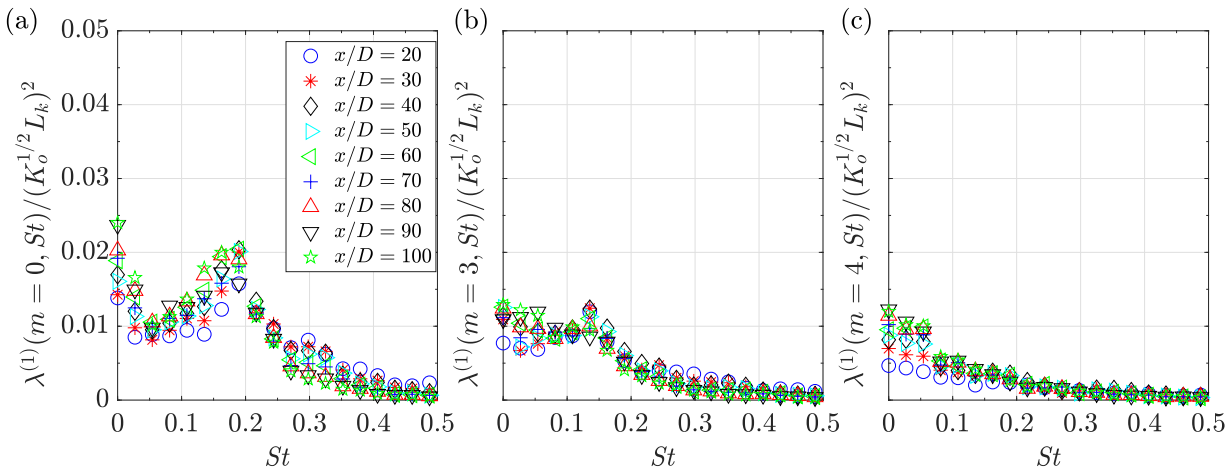

Figure 2.14: Leading SPOD eigenvalue ($\lambda^{(1)}$), scaled by $(K_o^{1/2}L_k)^2$, are plotted over $20 < x/D < 100$ for the following modes: (a) $m = 0$, (b) $m = 3$, and (c) $m = 4$, Here K_o is the centerline value of TKE and L_k is the TKE-based wake width.

frequency is also observed beyond $St = 0.3$, similar to the $m = 2$ case.

Figure 2.14 shows the eigenspectra of $\lambda^{(1)}$ for the $m = 0, 3$, and 4 modes spanning $20 \leq x/D \leq 100$ and scaled by $(K_o^{1/2}L_k)^2$, to explore the presence of similarity as was done with $m = 1$ and 2 in Fig. 2.10. There are two distinct peaks, $St = 0$ and 0.189, in the scaled eigenspectra of the $m = 0$ mode presented in Fig. 2.14. The scaled eigenspectra show significant spread for $St \leq 0.2$ indicating that the low-frequency content in the $m = 0$ mode might have its origin near the wake generator rather than being local. A proper collapse of scaled eigenvalues is observed only beyond $St > 0.35$ for the $m = 0$ azimuthal mode. As discussed in the context of Fig. 2.13(b) and (e), the scaled eigenspectra of $m = 3$ plotted in Fig. 2.14(b) show a peak at the vortex shedding frequency $St = 0.135$, the magnitude of which, relative to $(K_o^{1/2}L_k)^2$, decays with increasing x/D. Somewhat similar to the scaled eigenspectra plot of the $m = 0$ mode in Fig. 2.14(a), the scaled eigenspectra of the $m = 1$ mode also show some spread for lower frequencies $St < 0.2$ and collapse only beyond $St \approx 0.2$. Finally the scaled eigenspectra of the $m = 4$ mode peak at $St \to 0$ and collapse well for $St > 0.1$. For $St < 0.1$, after $x/D \approx 50$, the scaled eigenvalues do collapse. The scaled eigenspectra of the $m = 4$ mode are quite similar to that of the $m = 2$ mode, apart from the lower magnitudes.

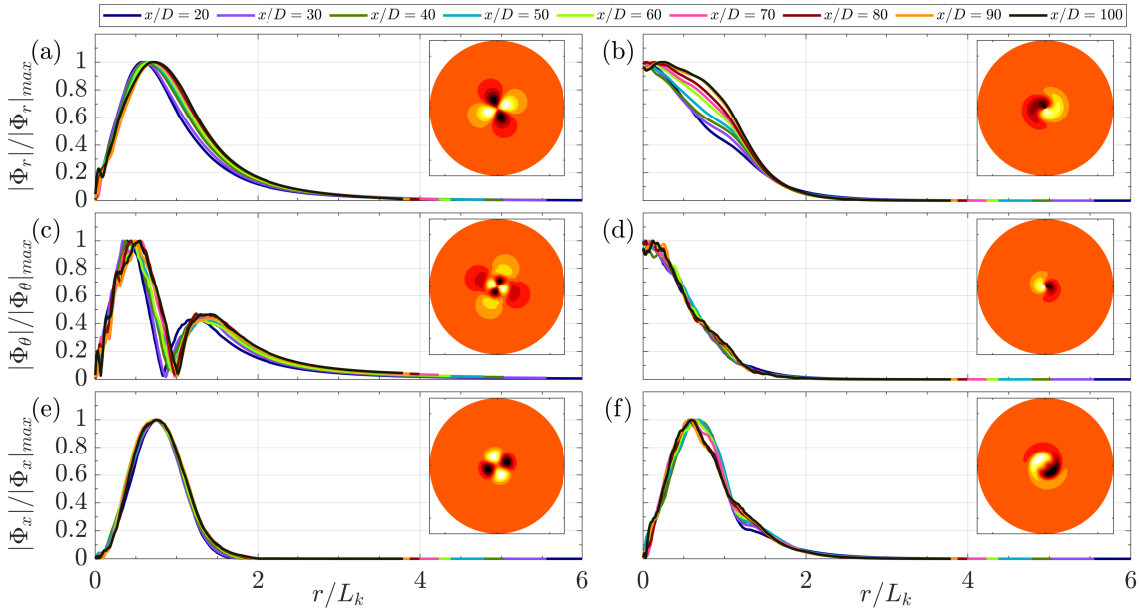

Figure 2.15: Modulus of eigenmode shapes for all three velocity components corresponding to $\lambda^{(1)}$ of the DH and VS structures: (a), (c), (e) correspond to u_r, u_θ, u_x eigenmodes respectively of the DH structure and (b), (d), (f) correspond to u_r, u_θ, u_x eigenmodes respectively of the VS structure.

The $m = 0, 3$, and 4 modes, although suboptimal relative to the $m = 1$ and 2 modes dominate over the remaining modes in terms of energy content. Based on the findings of Fig. 2.13 and 2.14, it can be concluded that the wake generator (disk in the present case) can have a profound impact on the characteristics of the suboptimal modes too which can last for large downstream distances, at least up to $O(x/D = 100)$.

2.7 Eigenmodes of the dominant vortex shedding and double helix modes

The shape of the eigenmodes for each velocity component is contrasted between the dominant VS and DH modes in this section. The applicability of similarity scaling to these modes is also assessed.

Figure 2.15 shows the shapes of leading SPOD modes of the VS and DH structures. For

this purpose, moduli of eigenmodes scaled by their respective maximum values ($|\Phi_i^{(1)}(r)|/|\Phi_i^{(1)}(r)|_{max}$) are plotted as a function of the radial similarity coordinate. Figure 2.15 (a), (c), and (e) show the u_r, u_θ, and u_x components of the leading SPOD eigenmode of the DH structure at different x/D locations. The u_r and u_x modes have single global peak at nearby locations, $\Phi_r^{(1)}$ at at $r/L_k \approx 0.7$ and $\Phi_x^{(1)}$ at $r/L_k \approx 0.75$, throughout $20 < x/D < 100$. It will be shown later that their cross-correlation $\langle -u_x' u_r' \rangle$ also peaks at $r/L_k \approx 0.7$. The radial shape of $\Phi_x^{(1)}$ starts exhibiting self-similarity from $x/D = 20$ onward while $\Phi_r^{(1)}$ exhibits collapse beyond $x/D = 40$. Furthermore, for the DH mode, $\Phi_x^{(1)}$ decays faster with increasing r relative to $\Phi_r^{(1)}$. The shape of the $\Phi_\theta^{(1)}$ mode is qualitatively different with respect to its counterparts for radial and axial velocity. At all downstream locations, $|\Phi_\theta^{(1)}|$ exhibits two maxima, at $r/L_k \approx 0.50$ and 1.35, respectively, and a minimum at $r/L_k \approx 1$. The minimum in the plot of $|\Phi_\theta^{(1)}|$ is evident as a zero-crossing at $r/L_k \approx 1$ for $\Phi_\theta^{(1)}$ in the two-dimensional inset plot for this mode in Fig. 2.15 (c). Similar to the other two components, $\Phi_\theta^{(1)}$ eventually becomes self-similar, beyond $x/D \approx 30$. Fig. 2.15 suggests that the leading SPOD mode of the DH structure eventually becomes self-similar for all three velocity components beyond $x/D \approx 40$.

The inset figures in Fig. 2.15(a), (c), and (e) show the two-dimensional contour plots of the real part of the corresponding velocity components of the leading SPOD mode of the DH structure at $x/D = 50$. The characteristic 4-lobe structure of the $m = 2$ mode can be seen in these contour maps. From the contour maps, it can be inferred that $\Phi_r^{(1)}$ and $\Phi_x^{(1)}$ are negatively correlated at $x/D = 50$. It turns out that the imaginary parts of radial and axial components are also negatively correlated (not shown here) resulting in an overall positive contribution from the leading SPOD mode of the DH structure to $\langle -u_x' u_r' \rangle$, the most dominant Reynolds shear stress term in axisymmetric turbulent shear flows. This positive contribution to $\langle -u_x' u_r' \rangle$ is found at all other downstream locations sampled for SPOD analysis in the present study and will be discussed with more detail in a later section.

Figure 2.15(b), (d), and (f) show the moduli of the leading SPOD mode of the VS structure.

Except $\Phi_x(r)$, none of the other two components start off at zero near $r = 0$. Both $|\Phi_r(r)|$ and $|\Phi_\theta(r)|$ peak near the axis and decay monotonically to zero as r increases. On the other hand, $|\Phi_x(r)|$ peaks at $r/L_k \approx 0.66$. All three components of $\Phi_i^{(1)}$ die out to zero by $r/L_k \approx 2$ implying that the prevalence of vortex shedding is confined to $r/L_k < 2$ at all locations. An immediate observation can be made about the lack of self-similarity of the leading SPOD mode of the VS structure. Although $\Phi_x^{(1)}$ and $\Phi_\theta^{(1)}$ tend to collapse to some extent when r is scaled by L_k, there is a significant spread in $\Phi_r^{(1)}$ mode for all downstream locations.

The inset plots in Fig. 2.15(b), (d), and (f) show the two-dimensional contours of the real part of the corresponding SPOD velocity components at $x/D = 50$. Similar to the leading SPOD mode of the DH structure, the real parts of $\Phi_r^{(1)}$ and $\Phi_x^{(1)}$ are negatively correlated for the VS structure too. The imaginary parts although not explicitly shown are also negatively correlated. This implies that the VS structure also contributes positively to $\langle -u'_x u'_r \rangle$ in a similar fashion to the DH structure.

2.8 Reconstruction of the TKE and Reynolds shear stress using SPOD modes

In this section, the utility of SPOD modes for capturing the spatial distribution of TKE and $\langle u'_x u'_r \rangle$ is examined. By construction, SPOD modes in the present analysis optimally capture the area-integrated TKE at a given cross-section (refer section 2.3). However there is no guarantee that these modes will be optimal for the Reynolds shear stress $\langle u'_x u'_r \rangle$. Nevertheless it is generally the case that the energetic structures are also the ones that carry a major portion of the turbulent shear stress. In fact, as will become clear for the present example of a turbulent wake, SPOD is successful as a low-order model for the Reynolds shear stress, more so than for the TKE.

The Reynolds stress tensor can be reconstructed from a selected number ($n = 1$ to Λ) of

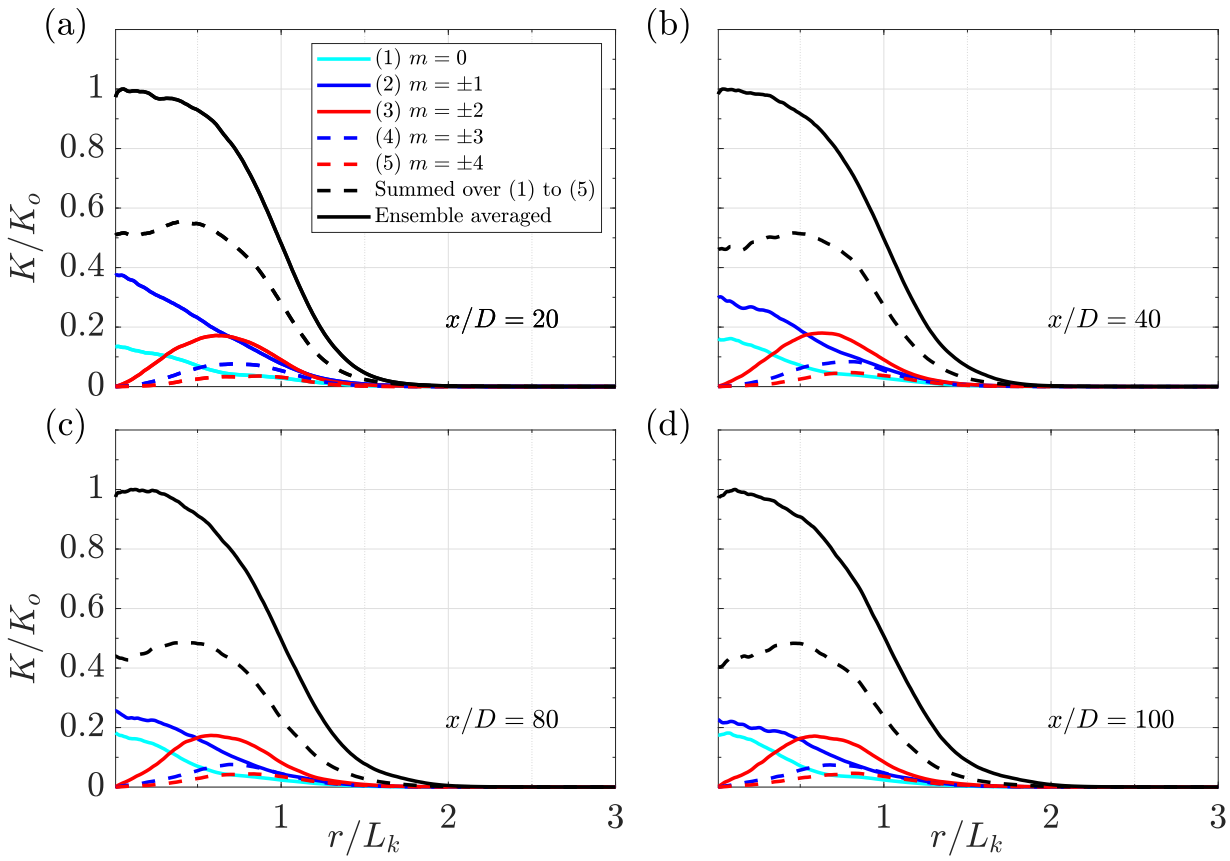

Figure 2.16: Reconstruction of TKE from a low-order truncation that comprises the leading 3 SPOD modes of azimuthal modes ($|m| \leq 4$) with energy summed over $-1 \leq St \leq 1$: (a) $x/D = 20$, (b) $x/D = 40$, (c) $x/D = 80$, and (d) $x/D = 100$.

SPOD modes as follows:

$$\langle u_i' u_j' \rangle (x;r) = \sum_{n=1}^{\Lambda} \sum_{m=-M}^{m=M} \sum_{St=-N}^{St=N} \lambda^{(n)}(x;m,St)\, \Phi_i^{(n)}(x;r,m,St)\, \Phi_j^{(n)*}(x;r,m,St), \tag{2.19}$$

where the first M azimuthal modes and the first N discrete frequencies are incorporated in the reconstruction. Setting $i = x$ and $j = r$ gives the reconstructed $\langle u_x' u_r' \rangle$ and twice the TKE is recovered when $i = j$ adopting the convention of summation over repeated indices. The reconstruction of TKE and $\langle u_x' u_r' \rangle$ is elaborated as follows.

2.8.1 TKE reconstruction from SPOD modes

Figure 2.16 shows the reconstructed TKE using a low-order truncation that includes modes with the following characteristics: $|m| \leq 4$, $|St| \leq 1$, and $n \leq 3$. The fidelity of the reconstruction is shown at four different locations $x/D = 20, 40, 80$, and 100 by comparison with the actual TKE obtained as an ensemble average of the numerical data. For the given set of (m, St, n) triplets, the qualitative nature of reconstructed TKE remains similar throughout all the locations considered in Fig. 2.16. However, a closer inspection reveals that the TKE reconstruction deteriorates slightly with increasing x/D. For instance, at $x/D = 20$, reconstructed TKE captures 50% of the actual TKE at the centerline. By $x/D = 80$, this value comes down to 40%. It is worth noting that the quality of reconstruction improves with increasing r/L_k as the flow becomes less turbulent away from the centerline and fewer modes are required to accurately capture the TKE. The implications of expanding the range of m, St, and n in the reconstruction will be discussed shortly.

The major contributors to the overall reconstructed TKE in Figure 2.16 are the $m = 0, 1$, and 2 azimuthal modes. However, only the $m = 0$ and $m = 1$ modes contribute to the centerline TKE. All the other azimuthal modes with $m \geq 2$ have zero TKE at the centerline. It can also be seen that the relative contribution of the leading $m = 1$ mode to the centerline TKE reconstruction declines progressively with increasing x/D. This decrease is linked to the declining relative importance of the $m = 1$ mode in the integrated eigenspectra as discussed in preceding sections.

The sensitivity of the TKE reconstruction to the addition of more modes (m, St, or n) has been investigated. The effect of increasing the number of modes is illustrated at one representative location $x/D = 40$ for brevity. The trends do not change qualitatively at different x/D except for a slight decrease in the energy capture at larger x/D locations pointing to an increasing importance of higher modes. From Fig. 2.17(a) to (d), the upper limits of m, St, and n are increased successively. The reconstruction of TKE shows a monotonically increasing accuracy with the inclusion of additional m, St, and n.

Comparing Fig. 2.17(b) with (a) one can see that the reconstructed TKE improves in

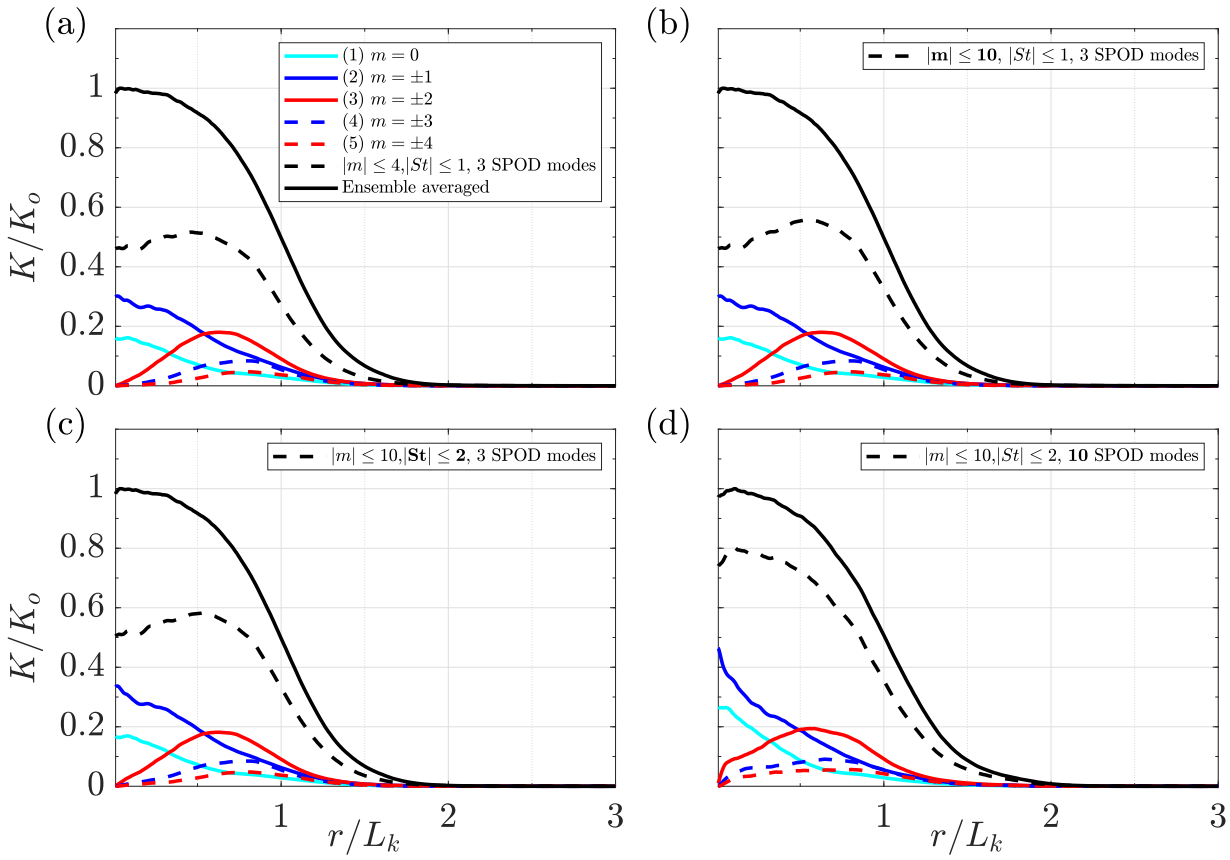

Figure 2.17: Reconstruction of TKE at $x/D = 40$ using: (a) $|m| \leq 4$, $|St| \leq 1$, $n \leq 3$, (b) $|m| \leq 10$, $|St| \leq 1$, $n \leq 3$, (c) $|m| \leq 10$, $|St| \leq 2$, $n \leq 3$, and (d) $|m| \leq 10$, $|St| \leq 2$, $n \leq 10$. Radial direction is scaled with TKE-based wake width L_k and TKE is scaled with centerline TKE K_o.

the region of $r/L_k > 0.5$ when more azimuthal modes are included keeping St and n same. This indicates that the higher azimuthal modes (modes with increasing m) do not significantly influence the TKE near the centerline and are only active beyond a certain r/L_k. This characteristic is confirmed by the TKE profiles of solely the $m = 3$ and $m = 4$ modes which start off as zero near centerline and peak at $r/L_k \approx 0.75$.

When the reconstruction is performed using more frequencies, shown in Fig. 2.17(c), there is a slight improvement in the overall reconstruction of the TKE. The individual contributions from each azimuthal modes increase leading to an overall improvement of the reconstructed profile

The inclusion of more SPOD modes leads to a significant boost in the quality of TKE reconstruction in the wake core ($r/L_k < 0.75$). The reconstructed profile captures almost 80% of the TKE at the centerline and in the wake core with 10 SPOD modes (Fig. 2.17 d) instead of about 50% with 3 SPOD modes (Fig. 2.17 c). The improvement away from the wake core is small and the reconstruction remains at about 80% of the actual value. This implies that the higher SPOD modes that are individually suboptimal, when summed together, can contribute significantly to the TKE in the wake core where the turbulence is more intense. Referring back to Fig. 2.8, these SPOD modes ($\lambda^{(3)}$ and beyond) are the ones which have almost uniform energy distribution over $St < 0.5$ and do not contain evidence of any coherent structures. They are representative of incoherent turbulence which is more prominent near the centerline.

2.8.2 Reconstruction of Reynolds shear stress with SPOD modes

In the same vein as Fig. 2.16 for the TKE, Fig. 2.18 compares the reconstruction of $\langle u'_x u'_r \rangle$ with the corresponding actual value at four locations $x/D = 20, 40, 80$, and 100. The leading 3 SPOD modes of the azimuthal modes $|m| \leq 4$ and $|St| \leq 1$ are employed. The reconstruction turns out to have higher fidelity for $\langle u'_x u'_r \rangle$ than for TKE.

Figure 2.18 shows that the two major contributors to the Reynolds stress $\langle u'_x u'_r \rangle$ are the

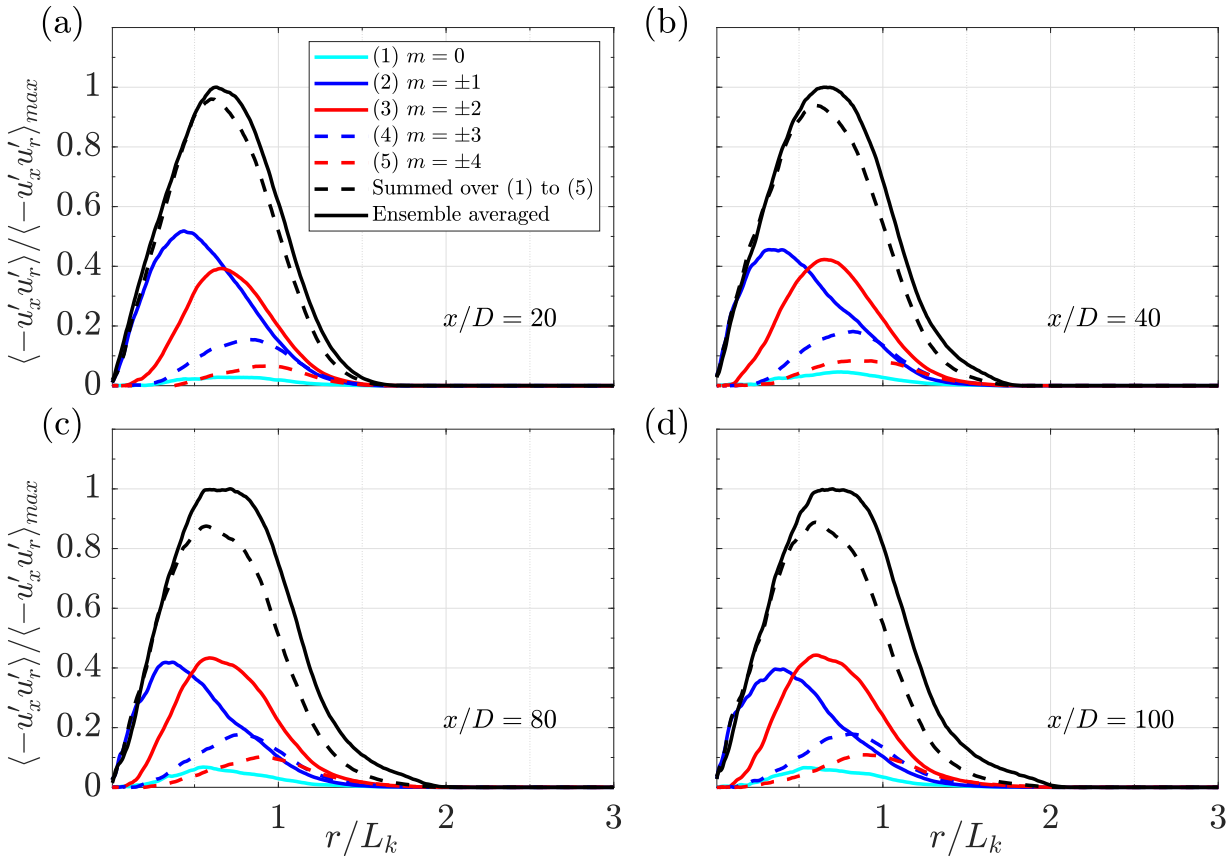

Figure 2.18: Reconstruction of $\langle u'_x u'_r \rangle$ from the leading 3 SPOD modes of various azimuthal modes ($|m| \leq 4$) summed over $-1 \leq St \leq 1$ at different streamwise locations: (a) $x/D = 20$, (b) $x/D = 40$, (c) $x/D = 80$, and (d) $x/D = 100$.

$m = 1$ and $m = 2$ modes followed by the $m = 3$ and $m = 4$ modes, respectively. Consistent with the integrated eigenspectrum in Fig. 2.7, the $m = 1$ mode contributes more than $m = 2$ to the reconstruction in the near wake, i.e., $x/D = 20$. With increasing x/D, the contribution from the $m = 2$ mode gradually exceeds the $m = 1$ contribution, except close to the centerline, say $r/L_k < 0.25$. The $m = 0$ mode carries negligible shear stress although it carries significant TKE as seen in the previous subsection. It is worth noting that the accuracy of reconstruction of $\langle u'_x u'_r \rangle$ is significantly better at $x/D = 20$ and 40 than at the far wake locations of $x/D = 80$ and 100. With increasing x/D, more azimuthal modes have to be included for the far wake so as to get the same quality of reconstruction as in the near wake.

As pointed out, the two major contributors to $\langle u'_x u'_r \rangle$ are the azimuthal modes $m = 1$ and $m = 2$. Interestingly, these two azimuthal modes capture different characteristics of the radial variation of Reynolds shear stress. The $m = 1$ mode accurately captures the actual $\langle u'_x u'_r \rangle$ in the central region with $r/L_k < 0.25$ including the slope at the axis ($r/D = 0$). Thereafter, its contribution peaks between $r/L_k = 0.25$ and $r/L_k = 0.5$, and decays faster than the contribution from the azimuthal mode $m = 2$. Contributions from the $m = 2$ and higher azimuthal modes start off with zero slope at $r/D = 0$ and they do not contribute near to the centerline.

While the $m = 1$ mode dominates for $r/L_k < 0.25$, the $m = 2$ mode plays an increasing important role in the reconstruction of $\langle u'_x u'_r \rangle$ at larger r/L_k. For instance, the maximum of the $m = 2$ contribution coincides with the peak of actual $\langle u'_x u'_r \rangle$ at $r/L_k \approx 0.75$.

The profiles of $\langle u'_x u'_r \rangle$, which were shown in Section 2.5, tend to flatten at the peak location with increasing x/D. This flattening at the peak is also observed for the $m = 2$ contribution. Compared to the $m = 1$ mode, the Reynolds stress in the $m = 2$ mode decays slowly with r and dominates over the $m = 1$ contribution beyond $r/L_k > 0.5$ from $x/D = 40$ onward.

At $x/D = 40$, the error in reconstruction of $\langle -u'_x u'_r \rangle_{max}$ is already small, not more than 10 %. It is found that increasing the azimuthal mode count to $|m| = 10$ is sufficient to obtain complete reconstruction (not shown). It is not necessary to increase the SPOD number beyond

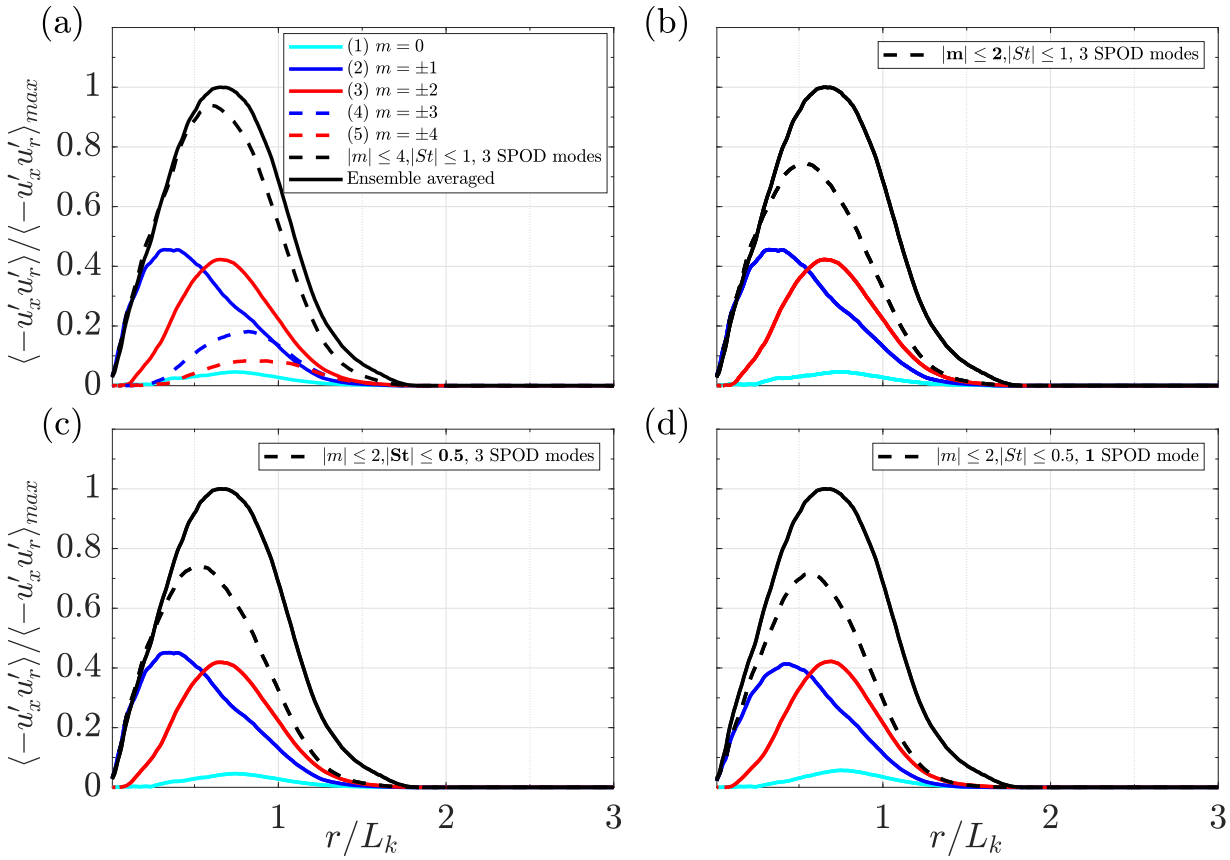

Figure 2.19: Reconstruction of $\langle u'_x u'_r \rangle$ at $x/D = 40$ using: (a) $|m| \leq 4$, $|St| \leq 1$, $n \leq 3$, (b) $|m| \leq 2$, $|St| \leq 1$, $n \leq 3$, (c) $|m| \leq 2$, $|St| \leq 0.5$, $n \leq 3$, and (d) $|m| \leq 2$, $|St| \leq 0.5$, $n = 1$. Radial direction is scaled with TKE-based wake width L_k and $\langle u'_x u'_r \rangle$ is scaled with $\langle -u'_x u'_r \rangle_{max}$.

$n = 3$ and the frequency above $St = 1$.

The influence of decreasing the number of retained modes on the reconstruction of $\langle -u'_x u'_r \rangle$ has also been explored. Figure 2.19 illustrates the results for one representative location, $x/D = 40$, noting that the same procedure at other locations results in the same qualitative conclusions. In Fig. 2.19(b), the total number of azimuthal modes included for reconstruction is decreased to $m = 2$ keeping St and the number of SPOD modes unchanged. The reconstruction quality is reduced with the reconstructed $\langle u'_x u'_r \rangle$ capturing around 75% of the peak $\langle u'_x u'_r \rangle$ in Fig. 2.19(b). The location of the peak at $r/L_k \approx 0.5$ is shifted erroneously closer to the centerline since the higher-m modes, which peak at $r/L_k \approx 0.75$, are now excluded from the reconstruction. An additional decrease in the number of frequencies (Fig. 2.19 c) does not lead to any noticeable difference in the reconstruction. Finally, the effect of further limiting the modal content to solely the leading SPOD mode is shown in Fig. 2.19 (d). Although the change in the peak of $\langle -u'_x u'_r \rangle$ is negligible, the reconstruction accuracy in the region $r/L_k < 0.25$ suffers. Thus, the inclusion of a small number of additional SPOD modes (up to $n = 3$ in the present example) beyond $\lambda^{(1)}$ is needed to accurately capture the trends in $\langle u'_x u'_r \rangle$ near the centerline. This is somewhat analogous to the TKE reconstruction, where inclusion of more SPOD modes improved the accuracy at the centerline. A notable difference is that, in the case of $\langle u'_x u'_r \rangle$, it is not necessary to include higher SPOD modes beyond $n = 3$ unlike in the TKE reconstruction where they significantly improved the accuracy.

For high Re axisymmetric shear flows, $\langle u'_x u'_r \rangle$ is the dominant off-diagonal Reynolds stress. $\langle u'_x u'_r \rangle$ extracts energy from the mean flow through turbulent production and transfers it to the TKE. Reconstructions shown in Fig. 2.19 indicate that the majority of $\langle u'_x u'_r \rangle$ is contained in the first few leading SPOD modes of low m and low St. This is in stark contrast to the reconstruction of TKE. The same set of modes which captured 50% of the centerline TKE, capture about 90% of the peak $\langle -u'_x u'_r \rangle$. The reconstruction of TKE using varying sets of modes presented in Fig. 2.17 showed that the higher modes (modes having large m, large St and higher SPOD index) can

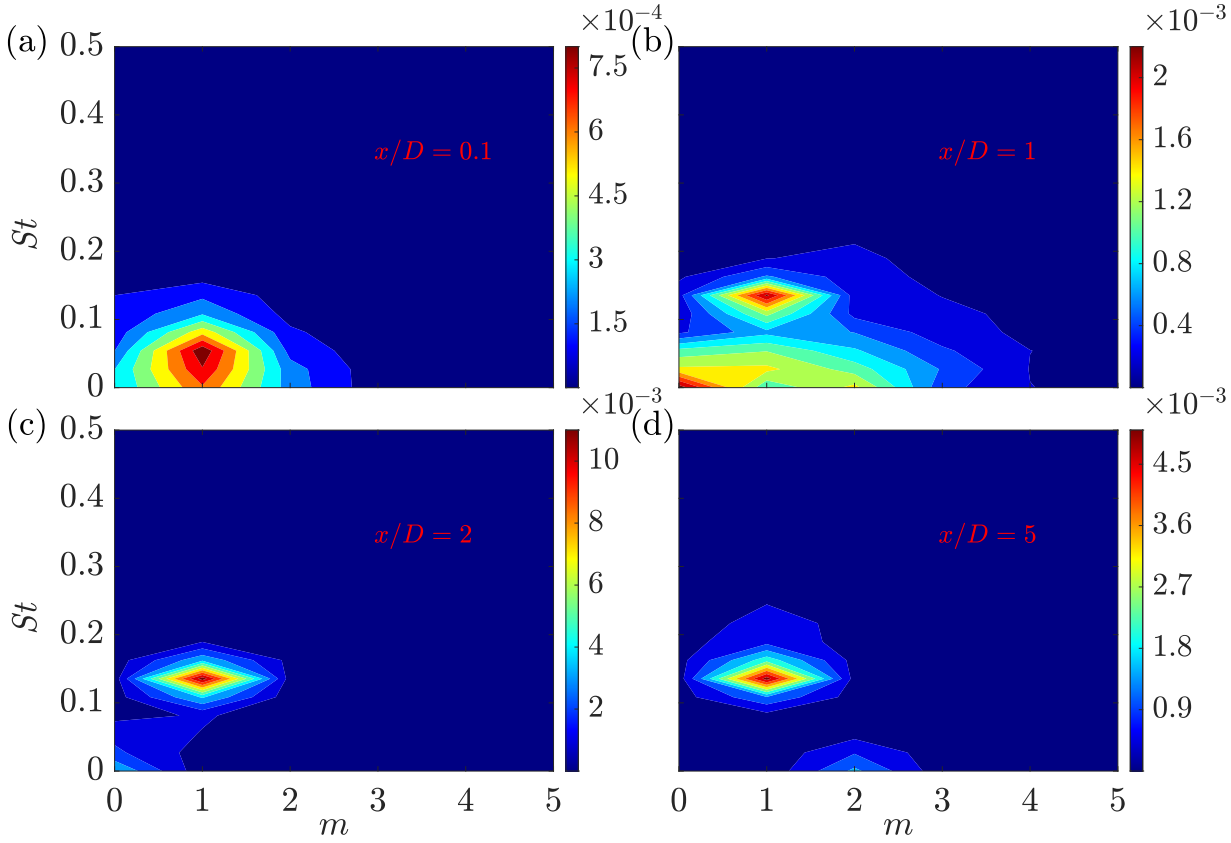

Figure 2.20: SPOD contour maps showing energy contained in leading SPOD mode, $\lambda^{(1)}$, as a function of azimuthal wavenumber m and frequency St at different locations near the disk: (a) $x/D = 0.1$, (b) $x/D = 1$, (c) $x/D = 2$, and (d) $x/D = 5$.

also contribute significantly to TKE when summed together. On the other hand, including more SPOD modes does not significantly improve the Reynolds stress reconstruction. This leads to the conclusion that the interaction between the mean flow and turbulence occurs primarily through more energetic SPOD modes of low m and St. These modes then transfer the TKE to the less energetic modes as the flow evolves.

2.9 SPOD analysis of locations near the disk

To conclude the results, we present a brief analysis of SPOD spectra at additional locations, $x/D = 0.1, 1, 2$, and 5, so as to shed light on the modal energy distribution close to the disk and

its transition to the wake.

Figure 2.20 shows the distribution of energy in the $\lambda^{(1)}$ constituent as a function of m and St at four streamwise locations: $x/D = 0.1, 1, 2$ and 5. At $x/D = 0.1$ shown in Fig. 2.20(a), most of the energy is concentrated in a narrow range: $St \leq 0.1$ and $m \leq 2$. The azimuthal $m = 1$ mode shows a distinctive peak at $St = 0.054$. In their study of flow past a disk, Berger et al. (1990) found a spectral peak at $St \approx 0.05$ in the axisymmetric mode $m = 0$, not $m = 1$. They attributed this frequency to pumping of the recirculation bubble. As will be seen later, the spectral peak at $St \approx 0.05$ does appear in the $m = 0$ SPOD eigenspectra at larger x/D.

The $x/D = 1$ location lies approximately in the middle of the recirculation region and has a complex distribution of energy among different m and St. By $x/D = 1$ (Fig. 2.20 b), the dominant $St = 0.054$, $m = 1$ peak has disappeared and a new peak at the vortex shedding frequency, $St = 0.135$, appears. This location marks the initial appearance of the vortex shedding structure which dominates the SPOD eigenspectra until $x/D \approx 40$ (Fig. 2.6 and 2.7). Besides the peak at the VS structure, a major portion of energy in the $\lambda^{(1)}$ constituent is also contained in the region of $St \leq 0.05$ distributed over $0 \leq m \leq 3$. At $x/D = 2$ (Fig. 2.20 c), the contour map of $\lambda^{(1)}$ is found to be dominated by the VS structure with $m = 1, St = 0.135$. The location of $x/D \approx 2$ also marks the end of the turbulent recirculation region behind the disk and the contribution from its high-m modes. The DH structure ($m = 2, St \to 0$) which dominates the far wake is absent from the energy distribution map of $\lambda^{(1)}$ at $x/D \leq 2$, but appears as a local peak by $x/D = 5$ (Fig. 2.20 d).

The frequency-integrated eigenspectra, at the same four locations of $x/D = 0.1, 1, 2$ and 5, are shown in Fig. 2.21, to contrast the relative importance of different azimuthal modes near the disk. The procedure for obtaining the frequency integrated eigenspectrum is same as that used for Fig. 2.7. At all four locations, the $m = 1$ mode dominates the frequency-integrated eigenspectrum, followed by $m = 2$. At $x/D = 2$, the relative energy content in the $m = 1$ mode becomes almost twice that at $x/D = 1$. This sudden increase in the relative importance of the $m = 1$ mode is also

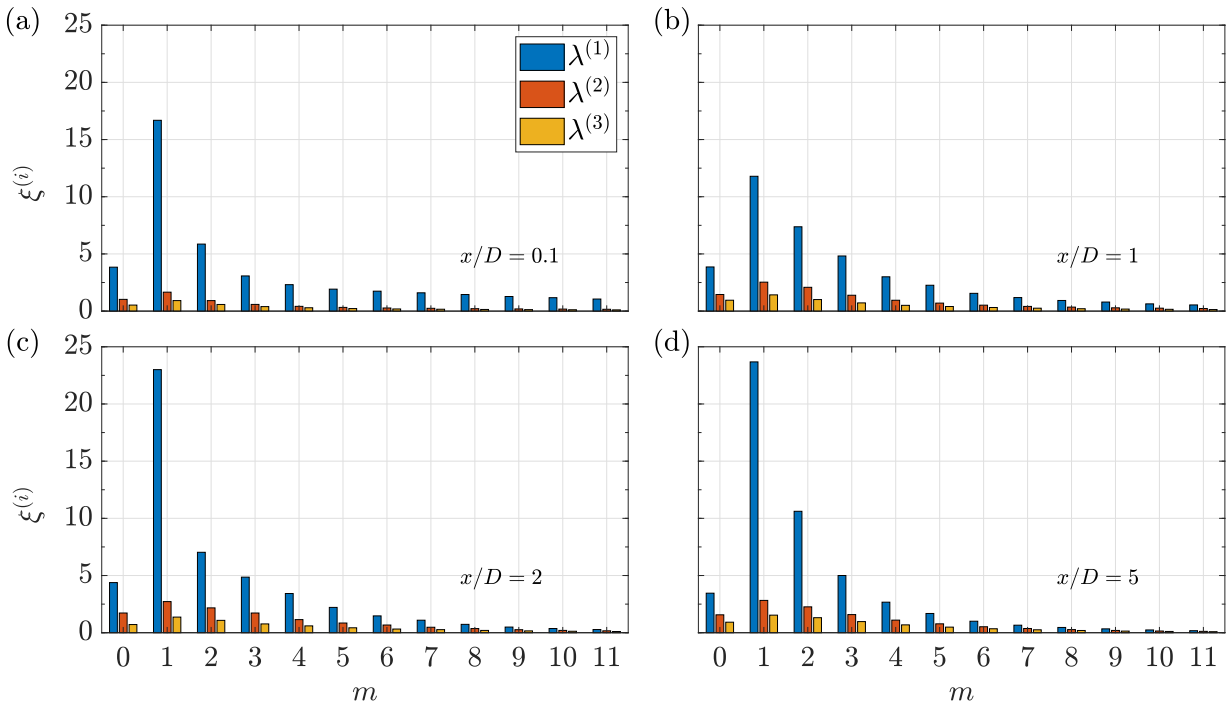

.

Figure 2.21: Frequency-integrated eigenspectrum as a function of azimuthal mode number m at different locations in the near wake: (a) $x/D = 0.1$, (b) $x/D = 1$, (c) $x/D = 2$, and (d) $x/D = 5$.

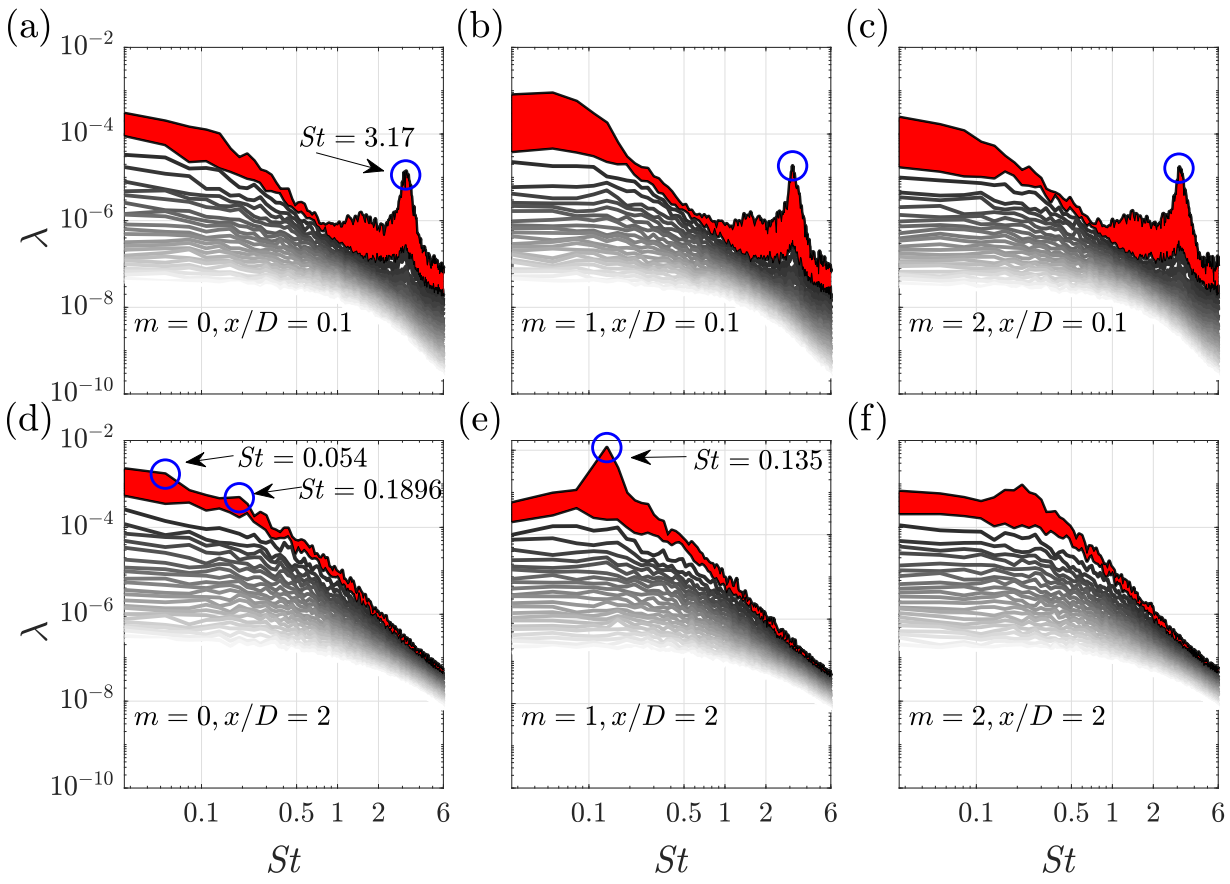

Figure 2.22: SPOD eigenspectra of 25 modes (dark to light shade corresponds to high to low energy eigenvalues): (a) $m = 0$, $x/D = 0.1$; (b) $m = 1$, $x/D = 0.1$; (c) $m = 2$, $x/D = 0.1$; (d) $m = 0$, $x/D = 2$; (e) $m = 1$, $x/D = 2$; (f) $m = 2$, $x/D = 2$.

seen in the energy distribution of $\lambda^{(1)}$ (Fig. 2.20) where the broadband distribution of energy at $x/D = 1$ gives way to a single dominant peak at $m = 1, St = 0.135$ at $x/D = 2$. By $x/D = 5$, the $m = 2$ mode starts gaining relative importance although $m = 1$ is still dominant. Besides the $m = 1$ and 2 modes, the major contributors to the frequency-integrated eigenspectra are the $m = 0, 3$ and 4 modes, similar to the previously shown far-wake locations.

Figure 2.22 shows the SPOD eigenspectra of $m = 0, 1$, and 2 azimuthal modes at two locations: $x/D = 0.1$ (very close to the disk) and $x/D = 2$ (end of the recirculation region). At $x/D = 0.1$ shown in the top row of Fig. 2.22, a distinct peak at the high frequency of $St = 3.17$ is visible in the $\lambda^{(1)}$ eigenspectrum at all three values of m. This high-frequency peak is associated

with the shear layer instability in the vicinity of the disk, arising from the instability of the boundary layer which separates from the disk. It is also worth mentioning that the SPOD eigenspectra of all three azimuthal modes $m = 0, 1$, and 2 show a prominent gap between the $\lambda^{(1)}$ and $\lambda^{(2)}$ SPOD modes at and near the frequency of $St = 3.17$. The study by Berger et al. (1990) at $Re = 15,000$ identified $St = 1.62$ as the frequency related to the shear layer instability, dominated by the $m = 0$ mode, and followed by $m = 1$ and 2 modes with equal contributions. The higher St identified in the near-disk SPOD eigenspectra here is likely a consequence of the higher $Re = 50,000$ of the current study. Fig. 2.22(b) shows the eigenspectra of the $m = 1$ mode at $x/D = 0.1$. At this location, a broad peak around $St = 0.05$ is found as was was also seen in the $\lambda^{(1)}$ contour map at $x/D = 0.1$ in Fig. 2.20(a).

Figure 2.22(d) shows the SPOD eigenspectra of the $m = 0$ mode at $x/D = 2$. At this location, two small peaks can be found in the $\lambda^{(1)}$ constituent at $St = 0.054$ and $St = 0.189$, respectively. The first of these frequencies is the axisymmetric pumping of the recirculation bubble identified in previous studies (Berger et al., 1990, Yang et al., 2014) of flow past a disk. The axisymmetric pumping is found to persist, albeit with decreasing strength, until $x/D = 10$. The second of these frequencies, $St = 0.189$ has not been discussed in the existing literature of flow past a disk. However, a peak at approximately this frequency does exist in the study of Berger et al. (1990) (see Fig. 12 of their paper) although the authors do not discuss it. This peak at $St = 0.189$ in the $m = 0$ mode is found to persist for long downstream distances as seen in Fig. 2.13(a) and (d) indicating that it is a global mode similar to the VS structure.

By $x/D = 2$, a distinct peak at $St = 0.135$ appears in the $\lambda^{(1)}$ eigenspectrum of the $m = 1$ azimuthal mode (Figure 2.22 e). A large gap between the $\lambda^{(1)}$ and $\lambda^{(2)}$ spectra at the vortex shedding frequency also appears by $x/D = 2$ implying that the vortex shedding structure dominates the dynamics of the $m = 1$ mode from early on. The SPOD eigenspectra of the $m = 2$ mode, shown in Fig. 2.22(f), shows a peak at $St \approx 0.20$. However, it is found that this peak disappears in the eigenspectra of the $m = 2$ mode by $x/D = 5$ (not shown here).

2.10 Summary and Conclusions

In the present study, we elucidate the characteristics of the coherent structures in the turbulent wake of a disk at $Re = 50,000$ using the high-resolution LES database of Chongsiripinyo and Sarkar (2020). For this purpose, we decompose the flow snapshots into azimuthal modes m followed by SPOD analysis to further decompose the modes into non-dimensional frequencies St and energy content. The eigenvalue ($\lambda^{(n)}$) of the SPOD mode (n) of a given (m, St) pair represents the fraction of area-integrated TKE contained in that mode, thus providing an objective framework to rank the SPOD modes based on the energy content.

SPOD eigenspectra at different streamwise locations beyond $x/D = 10$ show that the energy in the leading-order SPOD mode ($\lambda^{(1)}$) is predominantly contained in the low azimuthal modes $(m \leq 4)$ and low frequencies of $St < 0.4$. At all the streamwise locations, two distinct peaks: (i) $m = 1$, $St = 0.135$ and (ii) $m = 2$, $St \to 0$ are visible in the flow. The first peak has long been established as the vortex shedding (VS) structure in the turbulent wake of a disk. The importance of the second peak was established by the experimental studies of Johansson et al. (2002) and Johansson and George (2006b). In particular, the double helix (DH) structure with $m = 2$ and $St \to 0$ was found to dominate over the VS structure from $x/D = 30$ onward in their study. In the present case, the azimuthal mode $m = 2$ emerges as the dominant azimuthal mode at farther downstream distance, beyond $x/D = 60$. This is also the location where the wake defect law transitions from $U_d \propto x^{-0.9}$ to $U_d \propto x^{-2/3}$, and where the characteristic r.m.s turbulence scales become proportional to U_d during the wake decay.

When $\lambda^{(1)}$ corresponding to the azimuthal modes $m = 1$ and $m = 2$ are scaled by a parameter representing the area-integrated TKE, i.e., $(K_o^{1/2} L_k)^2$, it is found that the eigenspectrum of $m = 2$ at different streamwise locations beyond $x/D = 20$ collapse perfectly on to a single curve. On the other hand, the scaled eigenspectrum of $m = 1$ at different x/D show a significant spread around the vortex shedding frequency $St = 0.135$ while collapsing for higher frequencies

$St > 0.3$. It is also found that the leading eigenmode of the DH structure collapses well in the scaled radial coordinates (r/L_k), unlike the eigenmode of the VS structure. These findings, along with the FFT analysis of the $m = 2$ mode, indicate that the DH structure is connected to the local turbulence structure of the flow. On the other hand, the VS structure is a global mode which originates near the wake generator (further clarified by our near-body SPOD analyses). More studies, preferably with different wake generators, and at further higher *Re* are needed to explore the robustness of the present results regarding the VS and DH modes.

Apart from $m = 1$ and 2, the summed contribution of the azimuthal modes $m = 0, 3$, and 4 to the TKE is also found to be significant. We also characterize the eigenspectra of these sub-dominant azimuthal modes in the present work. The SPOD eigenspectra of $m = 3$ and 4 azimuthal modes show features similar to the $m = 1$ and 2 modes, respectively. The SPOD eigenspectra of the $m = 0$ mode show a peak at $St = 0.189$, in the intermediate ($x/D = 20$) as well as the far wake ($x/D = 80$). Further analysis reveals that this spectral peak is present in the SPOD eigenspectra of the $m = 0$ mode at near-body locations ($x/D = 2$) too. We speculate that the $m = 0, St = 0.189$ is a global mode (similar to the VS structure) which appears in the wake of the disk at high *Re*. Further studies using global resolvent analysis (Thomareis and Papadakis, 2018, Yeh and Taira, 2019) may help decipher the physical origin and dynamics of this particular mode.

Besides analyzing the SPOD eigenspectra and eigenmodes, we also perform reconstruction of TKE and $\langle u'_x u'_r \rangle$ using SPOD modes at different x/D locations. In the reconstruction of TKE, it is found that the first few modes of each kind (specifically $|m| < 4, |St| < 1$, and $n \leq 3$) captures approximately 50% of TKE in the central region. The contributors to the TKE at the centerline ($r = 0$) are the azimuthal modes $m = 0$ and $m = 1$. Other higher azimuthal modes start off as zero near the centerline and peak in the region, $0.5 < r/L_k < 1$. The three parameters (m, St, n) are then systematically varied to test the sensitivity of TKE reconstruction to different parameters. It is found that higher n (more SPOD eigenmodes) is necessary for accurate reconstruction of the

centerline TKE, implying that higher SPOD modes are more active near the centerline and are turbulence controlled rather than being associated with coherent motions. Inclusion of additional m and St monotonically improves the reconstruction quality of the TKE, considered over the entire wake width. It is worth noting that in the experimental study by Johansson and George (2006b) at $Re = 26,700$, the first three eigenmodes were able to capture 90% of the measured streamwise fluctuation energy. A lower fraction (approximately 50%) is captured by these modes in the present study because small-scale structures contribute more significantly at the higher $Re = 50,000$ considered here, and the significantly higher radial and azimuthal resolution possible in a simulation-based work enables accounts for the energy carried by these structures with small spatial scale.

As far as the reconstruction of $\langle u'_x u'_r \rangle$ is concerned, it is worth noting that the primary production term in the TKE equation for a turbulent axisymmetric wake is $-\langle u'_x u'_r \rangle \partial \langle U \rangle / \partial r$, where $\langle U \rangle$ is the ensemble-averaged streamwise velocity. Thus, $\langle u'_x u'_r \rangle$ is responsible for transferring energy from the mean flow to turbulence within the Reynolds-averaged framework. It is found that the same set of modes with low m, St and n, which capture only around 50% of centerline TKE, almost completely reconstruct the $\langle u'_x u'_r \rangle$ in the near wake locations. The implication is that it is only a considerably reduced set of (m, St, n) modes which directly interact with the mean flow. Another important result from the reconstruction of $\langle u'_x u'_r \rangle$ is the dominance of azimuthal modes $m = 1$ and 2, with each capturing different features of the actual profile. The azimuthal mode $m = 1$ captures the slope of the actual profiles at $r/D = 0$ while $m = 2$ captures the location of peak in the profile.

The near-body locations, $x/D = 0.1, 1, 2$ and 5 are also investigated using SPOD to characterize the transition of modal content form the immediate lee of the body to the near wake. The fluctuation energy at these near-body locations is primarily dominated by the $m = 1$ mode, which is in turn dominated by the VS mode from $x/D = 1$ onward. In the close proximity of the disk, at $x/D = 0.1$, a high frequency peak at $St \approx 3.10$ is detected in all three azimuthal modes

$m = 0, 1$, and 2. This frequency value is significantly larger than $St = 1.62$ found by Berger et al. (1990) in their study of coherent structures in the vicinity of the disk. However, the Re of the current study is more than three times the $Re = 15,000$ of the previous study Berger et al. (1990). The $St \approx 3.1$ peak in the current study is likely the shear layer instability; the reason for the comparatively higher magnitude of St is the high Re of the current study.

The VS mode appears in the SPOD eigenspectra of $m = 1$ at $x/D = 1$ (approximately in the middle of the recirculation region). Surprisingly, the $m = 1$ mode shows a peak at $St = 0.054$ in the SPOD eigenspectra at $x/D = 0.1$, which then disappears in its SPOD eigenspectra at further downstream locations. This low frequency has been associated to the axisymmetric ($m = 0$) pumping of the recirculation bubble in some previous studies (Berger et al., 1990, Yang et al., 2014). The eigenspectra of $m = 0$ mode shows small peaks at $St = 0.054$ (related to the pumping of recirculation bubble) and $St = 0.189$ at $x/D = 2$. The DH structure which dominates the far wake of the disk starts gaining importance relative to the VS structure at only $x/D = 5$.

2.11 Acknowledgments

Chapter 2 is a reprint of the material in the article: S. Nidhan, K. Chongsiripinyo, O. T. Schmidt, and S. Sarkar, "Spectral proper orthogonal decomposition analysis of the turbulent wake of a disk at Re = 50 000", Physical Review Fluids 5 (12), 124606 (2020). The dissertation author was the primary investigator and author of this work.

Chapter 3

Analysis of coherence in turbulent stratified wakes using spectral proper orthogonal decomposition

3.1 Introduction

Turbulent wakes are ubiquitous both in nature and man-made devices. From flow past moving vehicles (Grandemange et al., 2015) to flow past topographic features (Puthan et al., 2022a,b, 2021) in oceans, they play an important role in transporting momentum and energy across large distances from the wake generator. In the ocean and the atmosphere, the background density often has a stable density stratification. Buoyancy in a stable background enables the emergence of several distinctive features, e.g., suppression of vertical turbulent motions (Spedding, 2002b), multistage wake decay (Lin and Pao, 1979, Spedding, 1997), appearance of coherent structures in the late wake (Lin and Pao, 1979, Lin et al., 1992a), and formation of steady (Hunt and Snyder, 1980) and unsteady (Bonneton et al., 1993, Gilreath and Brandt, 1985) internal gravity waves, to name a few. A majority of wake studies utilize axisymmetric body shapes

(sphere, disk, spheroid, etc.) since such canonical shapes make it convenient to understand the phenomenology of turbulent stratified wakes.

The existence of coherent structures has been established to be an universal feature of both unstratified and stratified turbulent wakes. The Kárman vortex street associated with vortex shedding from the body at a specific frequency is a well known feature of unstratified bluff body wakes which arises from the global instability of the $m = 1$ azimuthal mode as was demonstrated for a sphere by Natarajan and Acrivos (1993) and Tomboulides and Orszag (2000). The Strouhal number (St) associated with vortex shedding varies with the shape of the body. Vortex shedding has been investigated in stratified wakes too. Lin et al. (1992b) conducted a detailed experimental investigation of stratified flow past a sphere of diameter D towed with speed U in a fluid with buoyancy frequency N for $5 \leq Re\ (UD/\nu) \leq 10^4$ and $0.005 \leq Fr\ (U/ND) \leq 20$. At $Fr \gtrsim 2$, they found that St in the near wake of the sphere, at $x/D \approx 3$, attained a constant value of $St \approx 0.18$, same as in the unstratified wake. For $Fr \lesssim 2$, the vortex shedding was two-dimensional and St increased with decreasing Fr in the near wake, similar to the trend in the flow past a circular cylinder. Chomaz et al. (1993) identified four regimes, differentiated by the value of Fr, in the near wake of a sphere. These regimes showed structural differences in the shed vortices and their interactions with the lee wave field.

Another distinctive feature of the stratified wakes is the generation of IGWs which are of two types: (i) body generated steady lee waves and (ii) wake generated unsteady IGWs. In their pioneering work on the wake of a self-propelled slender body, Gilreath and Brandt (1985) noted a coupling between the unsteady IGWs in the outer wake and the wake core turbulence, which suggests that the generation of the unsteady IGWs is inherently nonlinear in nature. Bonneton et al. (1993) and Bonneton et al. (1996) examined IGWs in the flow past a sphere. Lee waves were found to dominate when $Fr \lesssim 0.75$ and, for $Fr \gtrsim 2.25$, the downstream wake was dominated by the unsteady IGWs. Analysis of the density and velocity spectra in the outer wake showed a distinct peak at the vortex shedding frequency of sphere, $St \approx 0.18$. Brandt and Rottier (2015) found wake

turbulence to be a dominant source term for IGWs at $Fr \gtrsim 1$ in their experimental work on sphere wakes. However, they did not expand on the spectral characteristics of these wake-generated IGWs. Recently, Meunier et al. (2018) also conducted a theoretical and experimental study of waves generated by various wake generators, focusing primarily on the scalings of wavelengths and amplitudes across various Fr and wake generators. Various aspects of IGWs have also been studied through numerical simulations (Abdilghanie and Diamessis, 2013, Ortiz-Tarin et al., 2019, Rowe et al., 2020, Zhou and Diamessis, 2016).

In the last two decades, the rise in computing power has enabled a number of numerical studies which have improved our understanding of stratified wakes. A large body of numerical literature employs the temporal model wherein the wake generator is not included (Abdilghanie and Diamessis, 2013, Brucker and Sarkar, 2010, de Stadler and Sarkar, 2012, Diamessis et al., 2011, Dommermuth et al., 2002, Gourlay et al., 2001, Redford et al., 2015, Rowe et al., 2020, Zhou and Diamessis, 2019). Instead, these simulations are initialized with synthetic mean and turbulence profiles mimicking those of a wake. Body-inclusive simulations which resolve the flow at the wake generator and at a high enough Re that sustain turbulence are relatively recent (Chongsiripinyo and Sarkar, 2020, Orr et al., 2015, Ortiz-Tarin et al., 2019, Pal et al., 2016, 2017).

The database from the body-inclusive simulation of Chongsiripinyo and Sarkar (2020), hereafter referred to as CS2020, will be interrogated in this paper to analyze spatio-temporal coherence. CS2020 perform large eddy simulation (LES) of flow past a disk at $Re = 5 \times 10^4$ and at various values of Fr. The authors find that the wake transitions through three different regimes of stratified turbulence (provided buoyancy Reynolds number $> O(1)$), each with distinctive turbulence properties: weakly stratified turbulence (WST) which commences when the turbulent Froude number Fr_h decreases to $O(1)$, intermediately stratified turbulence (IST) when Fr_h decreases to $O(0.1)$, and strongly stratified turbulence (SST) when Fr_h reduces to to $O(0.01)$. Here $Fr_h = u'_h/Nl_v$, where u'_h, N, and l_v are r.m.s. horizontal velocity fluctuations, buoyancy frequency, and a characteristic turbulent vertical lengthscale, respectively. In the WST regime, the

turbulence is not yet appreciably affected by buoyancy effects. Anisotropy in turbulent velocity components, which is a key manifestation of stratification, has not kicked in yet (see figure 8 of CS2020). As the flow evolves downstream, turbulence anisotropy keeps increasing and the turbulence transitions to the IST regime at $Fr_h \sim O(0.1)$. The SST regime, which commences at $Fr_h \approx 0.03$, is characterized by a strong anisotropy in turbulence. An indication of arrival of this regime is the scaling of the vertical lengthscale with u_h'/N as derived by Billant and Chomaz (2001) (also see figure 12 in CS2020). In the SST regime, mean defect velocity and u_h' decay at the same rate of $x^{-0.18}$ while vertical turbulent velocity (u_z') decays at a faster rate of x^{-1}. Regime classification based on turbulence instead of mean velocity was introduced in the context of stratified homogeneous turbulence, e.g., Brethouwer et al. (2007), and was recently extended to stratified turbulent wakes by Zhou and Diamessis (2019) and CS2020.

With the huge amount of numerical and experimental data becoming available, data-driven modal decomposition techniques have also seen an unprecedented rise in their use to understand the dynamics and role of coherent structures in turbulent flows. These techniques have also been used to construct reduced-order models of these flows. One popular technique is proper orthogonal decomposition (POD), proposed by Lumley (1967, 1970) in the context of turbulent flows, which provides a set of modes ordered hierarchically in terms of energy content. Another popular technique is dynamic mode decomposition (DMD), described by Schmid (2010), which decomposes the flow into a set of spatial modes, each oscillating at a specific frequency.

However, applications of modal decomposition to stratified flows are few in number. Diamessis et al. (2010) performed snapshot POD (Sirovich (1987)) on the vorticity field from a temporal simulation at $Re = 5 \times 10^3$ and $Fr = 2$, noting a link between wake core structures and the angle of emission of IGWs in the outer wake. The layered wake core structure, which is a distinctive feature of stratified turbulent wakes, was found in the POD modes with lower modal index (corresponding to higher energy). As the modal index increased, the wake core was found to be dominated by small-scale incoherent turbulence. Xiang et al. (2017) performed spatial

and temporal DMD on the experimental data of the stratified wake of a grid showing that DMD modes successfully captured lee waves and Kelvin-Helmholtz (KH) instability in the near wake ($Nt < 10$). Nidhan et al. (2019) performed three-dimensional (3D) and planar two-dimensional (2D) DMD on the sphere wake at $Re = 500$ and 10^4, respectively. At $Re = 500$ and $Fr = 0.125$, they found that the 2D vortex shedding in the center-horizontal plane and 'surfboard' structures in the center-vertical plane corresponded to the same DMD mode oscillating at the vortex shedding frequency of $St \approx 0.19$. At the higher $Re = 10^4$, DMD modes associated with vortex shedding showed IGWs in the outer wake.

In the present work, we use spectral proper orthogonal decomposition (SPOD), originally proposed by Lumley (1967, 1970) and recently revisited by Towne et al. (2018), to identify and analyze the coherent structures in the turbulent stratified wake of a disk at $Re = 5 \times 10^4$. In its original form, POD is prohibitively expensive to apply on today's large numerical databases with high space-time resolution. The form put forward by Towne et al. (2018) leverages the temporal symmetry of statistically stationary flows to improve computational tractability. SPOD decomposes statistically stationary flows into energy-ranked modes with monochromatic frequency content, thus separating both the temporal and spatial scales in the flow, unlike the popular snapshot variant given by Sirovich (1987). SPOD has been used extensively in recent times for analysis of coherent structures and reduced-order modeling in a variety of unstratified flow configurations: (i) turbulent jets (Nekkanti and Schmidt, 2020, Nogueira et al., 2019, Schmidt et al., 2017, 2018, Semeraro et al., 2016), (ii) turbulent wakes (Nidhan et al., 2020), (iii) channel (Muralidhar et al., 2019) and pipe (Abreu et al., 2020) flows, (iv) flow reconstruction (Nekkanti and Schmidt, 2021, 2022) and low-order modeling (Chu and Schmidt, 2021), (v) wakes of actuator disks in turbulent environments (Ghate et al., 2018, 2020), etc.

The formation of coherent pancake vortices in the Q2D late wake does not necessarily require vortex shedding from the body as was demonstrated by Gourlay et al. (2001) whose temporally evolving model at $Fr = 10$ did not include the vortex shedding mode but still exhibited

Q2D-regime pancake vortices. Our interest is also in coherent structures but in a region of the far wake which is at large x/D but still not in the Q2D regime. We ask how does buoyancy affect the space-time coherence as the flow progresses from the near wake to the far wake? What are the salient differences between the unstratified ($Fr = \infty$) and stratified wakes in the context of coherent structures? We will address these questions by analyzing the LES dataset of CS2020, specifically the wakes at $Fr = 2$ and 10. We adopt SPOD for the data analysis since it is well suited to extract modes which have spatial and temporal coherence and thus track the evolution of specific modes, e.g. the vortex shedding (VS) mode, as the wake evolves downstream. The SPOD analysis also allows us to address a second set of questions: (i) are coherent modes linked to unsteady IGWs and (ii) how is the energy in dominant coherent structures distributed across the wake cross-section during downstream evolution? SPOD modes can also be useful for constructing reduced-order models prompting the third question: what is the efficacy of different SPOD modal truncations in regard to the reconstruction of various second-order turbulence statistics in turbulent stratified wakes?

The rest of the paper is organized as follows. Sections 3.2 and 3.3 give a brief overview of the numerical methodology and SPOD technique. Visualizations of $Fr = 2$ and 10 wakes are presented in section 3.4. The characteristics of SPOD eigenvalues and eigenspectrum are discussed in section 3.5. The VS mode and its link to the unsteady IGWs are discussed in detail in section 3.6. Sections sections 3.7 and 3.8 discuss the spatial structure of SPOD eigenmodes and trends in the reconstruction of second-order statistics by sets of truncated SPOD modes, respectively. Finally, the discussion and conclusions are presented in section 3.9.

3.2 Numerical methodology

We use the numerical database of the wake of a circular disk at $Re = 5 \times 10^4$ from CS2020. In particular, we analyze the datasets of stratified wakes at $Fr = 2$ and 10 from their

numerical database. CS2020 use high-resolution large eddy simulation (LES) to numerically solve the filtered Navier-Stokes equations system along with density diffusion equation under the Boussinesq approximation.

These equations are as follows:

continuity,

$$\frac{\partial u_i}{\partial x_i} = 0, \tag{3.1}$$

momentum,

$$\frac{\partial u_i}{\partial t} + \frac{\partial (u_i u_j)}{\partial x_j} = -\frac{\partial p}{\partial x_i} + \frac{1}{Re}\frac{\partial}{\partial x_j}\Big[\Big(1+\frac{\nu_s}{\nu}\Big)\frac{\partial u_i}{\partial x_j}\Big] - \frac{1}{Fr^2}\rho'\delta_{i3}, \tag{3.2}$$

and density diffusion,

$$\frac{\partial \rho}{\partial t} + \frac{\partial (\rho u_j)}{\partial x_j} = \frac{1}{RePr}\frac{\partial}{\partial x_j}\Big[\Big(1+\frac{\kappa_s}{\kappa}\Big)\frac{\partial \rho}{\partial x_j}\Big], \tag{3.3}$$

where u_i corresponding to $i = 1, 2$, and 3 refer to velocity in the streamwise (x_1 or x), lateral (x_2 or y), and vertical (x_3 or z) directions, respectively. Gravity acts in the vertical direction (3.2). The density field is decomposed into a background profile, $\rho_b(z) = \rho_o + (\mathrm{d}\rho_b/\mathrm{d}z)z$ (where K is a constant), and density deviation (ρ'). Thus $\rho(x,y,z,t) = \rho_b(z) + \rho'(x,y,z,t)$. In (3.2), ν_s and ν refer to the subgrid kinematic viscosity obtained from LES and kinematic viscosity of the fluid, respectively. Likewise, κ_s and κ in equation (3.3) refer to the subgrid density diffusivity and density diffusivity of the fluid, respectively.

(3.1) - (3.3) are non-dimensionalized using the following parameters: (i) free stream velocity (U_∞) for velocity field, (ii) diameter of disk (D) for spatial locations x_i, (iii) dynamic pressure ($\rho_o U_\infty^2$) for pressure field, (iv) advection timescale (D/U_∞) for time t, and (iv) $-(\mathrm{d}\rho_b/\mathrm{d}z)D$ for density deviation. There are three non-dimensional parameters of interest: (1) body-based Reynolds number (Re) defined as $U_\infty D/\nu$, (2) body-based Froude number (Fr) defined as U_∞/ND where N is the buoyancy frequency, $N^2 = -g/\rho_o(\mathrm{d}\rho_b/\mathrm{d}z)$, and (3) Prandtl number (Pr) defined

as ν/κ which is set as 1 in CS2020 simulations. κ_s is also set equal to ν_s for the LES simulations.

A cylindrical coordinate system is adopted and the disk is represented using the immersed boundary method (IBM) of Balaras (2004), Yang and Balaras (2006). Spatial derivatives are computed using second-order central finite differences and temporal marching is performed using a fractional step method which combines a low-storage Runge-Kutta scheme (RKW3) with the second-order Crank-Nicolson scheme. The kinematic subgrid viscosity (ν_s) and density diffusivity (κ_s) are obtained using the dynamic eddy viscosity model of Germano et al. (1991). At the inlet and outlet, Dirichlet inflow and Orlanski-type convective (Orlanski (1976)) boundary conditions are specified, respectively. The Neumann boundary condition is used at the radial boundary for the density and velocity fields. To prevent the spurious propagation of internal waves upon reflection from the boundaries, sponge regions with Rayleigh-damping are employed at radial, inlet, and outlet boundaries.

The radial and streamwise domains span $0 \leq r/D \leq 80$ and $-30 \leq x/D \leq 125$, respectively. A large radial extent facilitates weakening of the IGWs before they hit the boundary and thereby also controls the amplitude of spurious reflected waves. The distribution of grid points are as follows: $N_r = 531$ in the radial direction, $N_\theta = 256$ in the azimuthal direction, and $N_x = 4608$ in the streamwise direction, resulting in approximately 530 million elements. The grid resolution is excellent by LES standards in all three directions. Readers may refer to Chongsiripinyo and Sarkar (2020) for more details on the grid resolution and numerical scheme.

3.3 Spectral proper orthogonal decomposition - theory and present application

In this work, we employ spectral POD (SPOD) to study the dynamics of coherent structures in stratified wakes, rather than the more commonly employed snapshot POD (Sirovich, 1987). SPOD enables the identification of dominant structures evolving coherently in both space

and time by exploiting temporal correlation among flow snapshots. This approach is particularly well-suited for flow configurations like turbulent wakes which are known to be dominated by mechanisms operating at specific frequencies, e.g., vortex shedding, pumping of recirculation bubble, shear layer breakdown, to name a few (Berger et al., 1990). On the contrary, snapshot POD assumes each snapshot of the flow to be an independent realization. As a result, the temporal coherence of POD modes is not guaranteed. Furthermore, it can be also shown that the coefficients dictating the temporal evolution of snapshot POD modes are broadband, i.e., containing contributions from a range of frequencies (Towne et al., 2018). SPOD requires a larger amount of time-resolved data compared to snapshot POD. Hence, snapshot POD has dominated the literature compared to SPOD.

3.3.1 Theory of SPOD for statistically-stationary stratified flows

For the SPOD analysis of stratified wakes, the fluctuating density fields ($\rho'(\boldsymbol{x},t)$) and velocity fields ($\boldsymbol{u}'(\boldsymbol{x},t) = [u'_r(\boldsymbol{x},t), u'_\theta(\boldsymbol{x},t), u'_x(\boldsymbol{x},t)]^T$) are taken together as a single state-space field $\boldsymbol{\Lambda}(\mathbf{x},t) = [\boldsymbol{u}'(\boldsymbol{x},t), \rho'(\boldsymbol{x},t)]^T$. Following Lumley (1970), we seek POD modes $\boldsymbol{\Psi}(\boldsymbol{x},t)$ that have maximum ensembled-average projection on $\boldsymbol{\Lambda}(\boldsymbol{x},t)$, expressed as:

$$\max_{\boldsymbol{\Psi}} \frac{\langle |\{\boldsymbol{\Lambda}(\boldsymbol{x},t), \boldsymbol{\Psi}(\boldsymbol{x},t)\}|^2 \rangle}{\{\boldsymbol{\Psi}(\boldsymbol{x},t), \boldsymbol{\Psi}(\boldsymbol{x},t)\}}, \tag{3.4}$$

where $\langle . \rangle$ denotes the ensemble average. We define the inner product $\{\boldsymbol{\Lambda}^{(1)}(\boldsymbol{x},t), \boldsymbol{\Lambda}^{(2)}(\boldsymbol{x},t)\}$ as:

$$\{\boldsymbol{\Lambda}^{(1)}(\boldsymbol{x},t), \boldsymbol{\Lambda}^{(2)}(\boldsymbol{x},t)\} = \int_{-\infty}^{\infty} \int_{\Omega} \boldsymbol{\Lambda}^{(2)*}(\boldsymbol{x},t) \mathrm{diag}\Big(1,1,1,\frac{g^2}{\rho_o^2 N^2}\Big) \boldsymbol{\Lambda}^{(1)}(\boldsymbol{x},t)\, \mathrm{d}\boldsymbol{x}\, \mathrm{d}t, \tag{3.5}$$

where $(.)^*$ denotes the Hermitian transpose. The so-defined inner-product norm ensures that the obtained POD modes are optimal in terms of capturing two-times the overall sum of turbulent kinetic energy (TKE) and turbulent potential energy (TPE), where TKE $= \langle u'_i u'_i \rangle / 2$ and

TPE=$\frac{g^2}{2\rho_o^2 N^2}\langle \rho'\rho' \rangle$.

Following Holmes, P. and Lumley, J. L. and Berkooz, G. and Rowley, C. W. (2012), (3.4) can be expressed as a Fredholm-type integral eigenvalue problem as follows:

$$\int_{-\infty}^{\infty}\int_{\Omega} R_{ij}(\boldsymbol{x},\boldsymbol{x}',t,t')\boldsymbol{W}(\boldsymbol{x}')\Psi_j^{(n)}(\boldsymbol{x}',t')\,\mathrm{d}\boldsymbol{x}'\,\mathrm{d}t' = \lambda^{(n)}\Psi_i^{(n)}(\boldsymbol{x},t), \tag{3.6}$$

where $\boldsymbol{W}(\boldsymbol{x})$ is a positive-definite Hermitian matrix accounting for the weights of each variable as defined in the (3.5). In (3.6), $\lambda^{(n)}$ and $\Psi_i^{(n)}(\boldsymbol{x},t)$ correspond to the n^{th} eigenvalue and the i^{th} component of the n^{th} eigenmode. The kernel $R_{ij}(\boldsymbol{x},\boldsymbol{x}',t,t')$ which is the two-point two-time correlation tensor, is defined as follows:

$$R_{ij}(\boldsymbol{x},\boldsymbol{x}',t,t') = \langle u_i'(\boldsymbol{x},t)u_j'(\boldsymbol{x}',t)\rangle, \quad i,j=1,2,3, \tag{3.7}$$

$$R_{i4}(\boldsymbol{x},\boldsymbol{x}',t,t') = \langle u_i'(\boldsymbol{x},t)\rho'(\boldsymbol{x}',t)\rangle, \quad i=1,2,3, \tag{3.8}$$

$$R_{4j}(\boldsymbol{x},\boldsymbol{x}',t,t') = \langle \rho'(\boldsymbol{x},t)u_j'(\boldsymbol{x}',t)\rangle, \quad j=1,2,3, \tag{3.9}$$

$$R_{44}(\boldsymbol{x},\boldsymbol{x}',t,t') = \langle \rho'(\boldsymbol{x},t)\rho'(\boldsymbol{x}',t)\rangle. \tag{3.10}$$

For statistically stationary flows, such as the turbulent stratified wake in the present case, the kernel $R_{ij}(\boldsymbol{x},\boldsymbol{x}',t,t')$ is only a function of time difference $\tau = t-t'$, $\boldsymbol{x}$, and $\boldsymbol{x}'$. Furthermore, it can be Fourier-transformed in the temporal direction as follows:

$$R_{ij}(\boldsymbol{x},\boldsymbol{x}',\tau) = \int_{-\infty}^{\infty} S_{ij}(\boldsymbol{x},\boldsymbol{x}',f)e^{i2\pi f\tau}\,\mathrm{d}f, \tag{3.11}$$

where $S_{ij}(\boldsymbol{x},\boldsymbol{x}',f)$ is the Fourier transform of the kernel $R_{ij}(\boldsymbol{x},\boldsymbol{x}',\tau)$. Using (3.11), the Fredholm-type eigenvalue problem in (3.6) can be transformed into an equivalent eigenvalue problem which

is solved at each frequency f, following Towne et al. (2018),

$$\int_{\Omega} S_{ij}(\boldsymbol{x},\boldsymbol{x}',f)\boldsymbol{W}(\boldsymbol{x}')\Phi_j^{(n)}(\boldsymbol{x}',f)\,\mathrm{d}\boldsymbol{x}' = \lambda^{(n)}(f)\,\Phi_i^{(n)}(\boldsymbol{x},f), \tag{3.12}$$

where $\lambda^{(n)}(f)$ are the eigenvalues at f and $\Phi_i^{(n)}(\boldsymbol{x},f) = \Psi_i^{(n)}(\boldsymbol{x},t)e^{-i2\pi ft}$ are the modified eigenmodes. The eigenvalues are ordered such that $\lambda^{(1)}(f) \geq \lambda^{(2)}(f) \geq \ldots \geq \lambda^{(n)}(f)$. The sum over all the eigenvalues at frequency f equates to two-times the total fluctuation energy content, i.e., $\langle u_i' u_i' \rangle + \frac{g^2}{\rho_o^2 N^2}\langle \rho'\rho' \rangle$ at that frequency. The obtained eigenmodes in the frequency space are spatially orthogonal to each other such that:

$$\int_{\Omega} \boldsymbol{\Phi}^{*(n)}(\boldsymbol{x},f)\boldsymbol{W}(\boldsymbol{x})\boldsymbol{\Phi}^{(m)}(\boldsymbol{x},f)\,\mathrm{d}\boldsymbol{x} = \delta_{mn}, \tag{3.13}$$

where δ_{mn} is the Dirac-delta function.

3.3.2 Numerical implementation of SPOD for current work

In this work, we primarily present results from SPOD on two-dimensional planes at various x/D − ranging from $x/D = 10$ to 100 − sampled at a spacing of approximately $5D$. The domain of $10 \leq x/D \leq 100$ spans: (i) $5 \leq Nt_2 \leq 50$ for $Fr = 2$ and (ii) $1 \leq Nt_{10} \leq 10$ for $Fr = 10$ in terms of buoyancy time. In the radial direction, the SPOD domain spans $0 \leq r/D \leq 10$, resulting in a total of $N_r^{SPOD} = 333$ points. In the azimuthal direction, the number of grid points $N_\theta = 256$.

For numerical implementation, the mean-subtracted data, consisting of N temporal snapshots, is divided into N_{blk} blocks with an overlap of N_{ovlp} snapshots. Each block contains N_{freq} entries: $\boldsymbol{Q} = [\boldsymbol{q}^{(1)}, \boldsymbol{q}^{(2)}, \boldsymbol{q}^{(3)}, \cdots \boldsymbol{q}^{(N_{freq})}]$. Here, $\boldsymbol{q}^{(i)} = [\boldsymbol{u'}^{(i)}, \rho'^{(i)}]^T$ where $\boldsymbol{u'}$ and ρ' are velocity and density fluctuations, respectively. Thereafter, discrete Fourier transform (DFT) of each block is performed in the temporal direction and the ensemble of N_{blk} Fourier realizations of any given

frequency, let us say f, is collected as $\hat{\boldsymbol{Q}}_f = [\boldsymbol{q}^{(1)(f)}, \boldsymbol{q}^{(2)(f)}, \boldsymbol{q}^{(3)(f)}, \cdots \boldsymbol{q}^{(N_{blk})(f)}]$. Once, $\hat{\boldsymbol{Q}}_f$ is obtained, SPOD eigenvalues and eigenvectors corresponding to f are given by the following eigenvalue decomposition:

$$\hat{\boldsymbol{Q}}_f^* \boldsymbol{W} \hat{\boldsymbol{Q}}_f \boldsymbol{\Gamma}_f = \boldsymbol{\Gamma}_f \boldsymbol{\Lambda}_f, \tag{3.14}$$

where $\boldsymbol{\Lambda}_f = diag\left(\lambda_f^{(1)}, \lambda_f^{(1)}, \cdots \lambda_f^{(N_{blk})}\right)$ is a diagonal matrix containing eigenvalues ranked in the decreasing order of energy content from $i = 1$ to N_{blk}. The corresponding spatial eigenmodes $\hat{\boldsymbol{\Phi}}_f$ can be obtained as $\hat{\boldsymbol{\Phi}}_f = \hat{\boldsymbol{Q}}_f \boldsymbol{\Gamma}_f \boldsymbol{\Lambda}_f^{-1/2}$. In (3.14), $\boldsymbol{W}$ is a diagonal matrix of size $4N_r^{SPOD} N_\theta$, containing the numerical quadrature weights multiplied by coefficients required to form the energy quantities given in (3.5).

The parameters for SPOD are set as follows: (i) total number of snapshots $N = 7168$ with consecutive snapshots separated by $\Delta t D/U_\infty \approx 0.09$ and 0.104 for $Fr = 2$ and 10, respectively, (ii) number of frequencies $N_{freq} = 512$, and (iii) overlap between blocks $N_{ovlp} = 256$, resulting in total of $N_{blk} = \frac{N - N_{ovlp}}{N_{freq} - N_{ovlp}} = 27$ SPOD modes at each frequency. Interested readers are referred to Towne et al. (2018) and Schmidt and Colonius (2020) for more details on the theoretical aspects and numerical implementation of SPOD.

Most of the results are obtained from SPOD analyses at constant x/D planes with modes maximizing the two-times sum of TKE and TPE. However, for some results, we perform additional SPOD analyses. For example, to illustrate the streamwise variation of a certain leading-order SPOD mode in section 3.7, we perform SPOD analysis on fluctuating velocity and density fields at the center-vertical plane ($y = 0$ plane) with reduced number of snapshots $N = 5376$ and half-resolution in vertical and streamwise directions. N_{freq} and N_{ovlp} are kept the same as SPOD on fixed x/D planes. The spatial resolution and N are reduced to avoid memory limitations since large matrices with complex double precision have to be stored in the intermediate steps of SPOD. Also in section 3.6, we present results from SPOD analyses of the $Fr = 2$ wake (at constant x/D planes) with (i) density fluctuations replaced by pressure fluctuations and (ii) norm defined

such as to maximize the sum of $\langle p'p' \rangle$ and $\langle u_i' u_i' \rangle$. N, N_{freq}, and N_{blk} are kept the same as in the previous paragraph. The motivation behind performing this additional set of SPOD analyses is explained in section 3.6.

3.4 Flow visualizations

Three-dimensional visualizations of the Q criterion and planar views of the vorticity and velocity fields in this section provide a first look at the vortical and unsteady IGW structure of the simulated wakes. The structure of the steady (in a frame attached to the disk) lee wave field is not discussed in this paper. To emphasize the large-scale coherent structures, the instantaneous velocity fields have been filtered using a SciPy Gaussian low-pass filter (*gaussian_filter*) in all three directions with standard deviation $\sigma = 5$ before calculating the Q criterion and vorticity fields.

Figure 3.1 shows that, in both wakes, circular vortex rings appear immediately downstream of the disk. At $Fr = 2$, the buoyancy induced anisotropy between horizontal and vertical directions commences in the near wake. The wake contracts in the vertical at $x/D \approx 5$ (visible in the side view given in figure 3.1(b)) owing to the oscillatory modulation by the lee wave. The top view (figure 3.1(a)) shows a distinct large-scale waviness in the intermediate wake, shown by the dashed black line. Its approximate wavelength is $\lambda/D \approx 1/St_{VS}$, where St_{VS} is the vortex shedding (VS) frequency. Likewise, large-scale VS structures separated approximately by $\lambda/D \approx 1/St_{VS}$ can also be identified in the $Fr = 10$ wake (figure 3.1(c)). The value of St_{VS} and the spatial behavior of the VS mode will be made precise formally using SPOD in the subsequent sections.

Figure 3.2 shows the instantaneous vertical vorticity ($\omega_z D/U_\infty$) on the central horizontal plane ($z = 0$) for the $Fr = 2$ (top) and $Fr = 10$ (bottom) wakes. Similar to figure 3.1, ω_z is calculated using filtered velocity fields to emphasize large-scale features. In both wakes, the complex spatial distribution of vorticity in the immediate downstream of the disk gives way to a

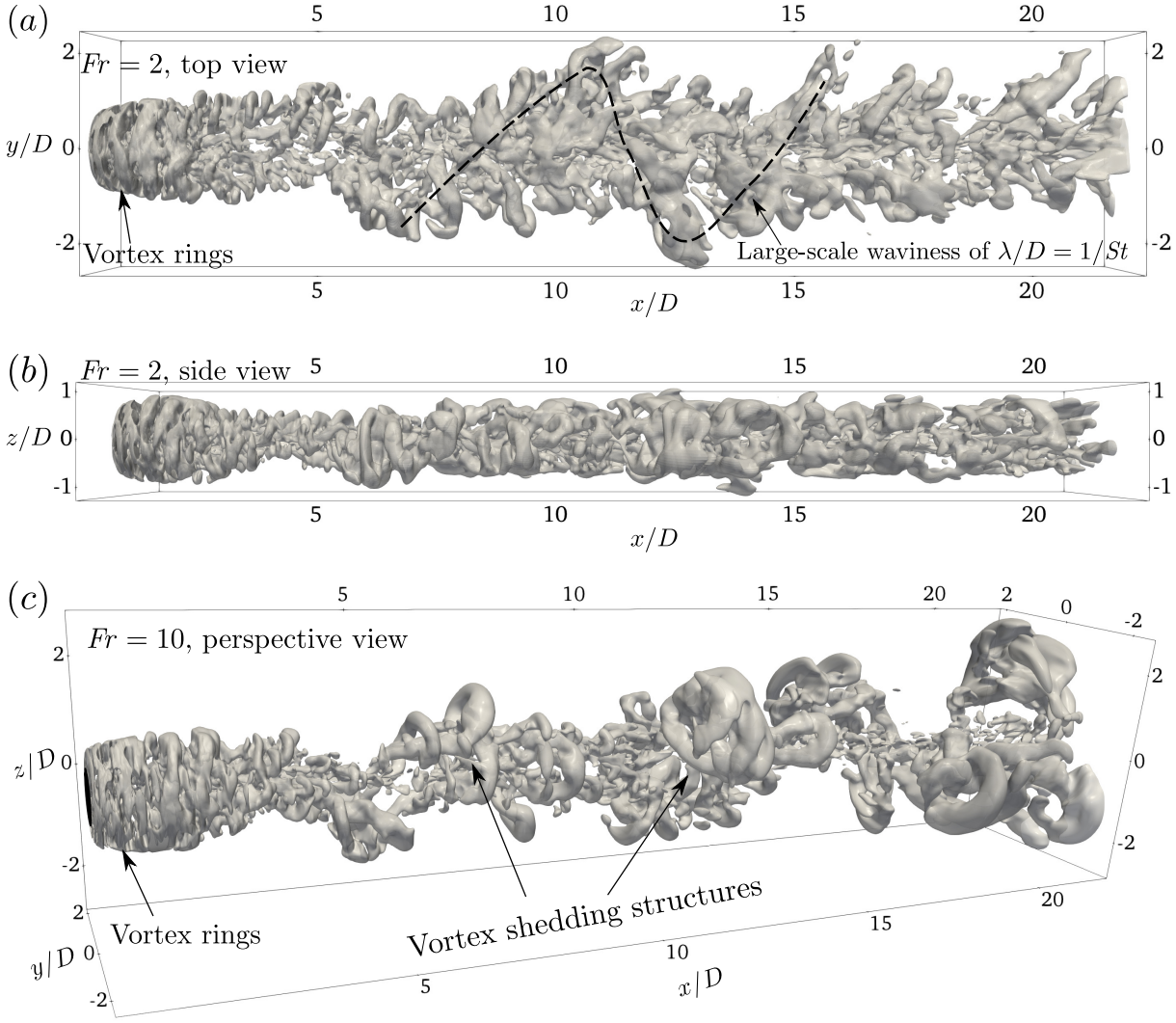

Figure 3.1: Isosurfaces of instantaneous Q criterion at $Q = 0.01$: (a,b) $Fr = 2$ and (c) $Fr = 10$. Streamwise domain is limited to $0 < x/D < 20$ for clarity.

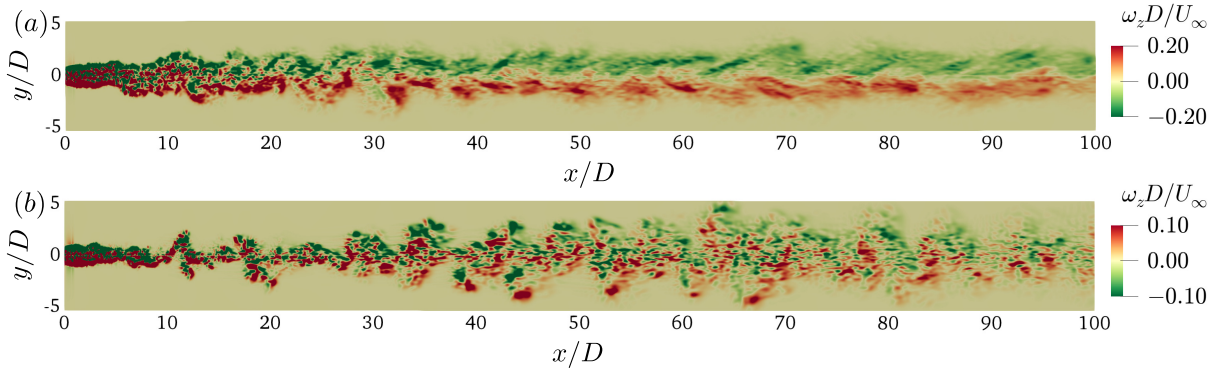

Figure 3.2: Instantaneous snapshot of vertical vorticity at the central horizontal plane ($z = 0$): (a) $Fr = 2$ and (b) $Fr = 10$.

well-defined coherent distribution of opposite signed vortices in the intermediate to late wakes. For the $Fr = 2$ wake, spatial coherence is visible as early as $x/D \approx 20$. Beyond $x/D \approx 20$, the regions of opposite-signed ω_z remain separated till the end of the domain. On closer inspection, a streamwise undulation of length $\lambda/D \approx 1/St_{VS}$ can be observed in figure 3.2(a). At this point, it is important to emphasize that the $Fr = 2$ wake remains actively turbulent throughout the computational domain as demonstrated by CS2020 through spectra and visualizations of the turbulent dissipation rate. From $x/D \approx 40$ onward, the $Fr = 2$ wake resides in the strongly stratified turbulent (SST) regime. Different regimes of stratified turbulence are discussed briefly in section 3.1. The strong signature of coherence in the $Fr = 2$ wake is not a consequence of the transition into the weakly turbulent state of the Q2D regime noted in previous works, e.g. by Spedding (1997).

The $Fr = 10$ wake also shows a distinct wavy motion with non-dimensional wavelength $\approx 1/St_{VS}$. However, the separation between the regions with opposite signed vorticity is not as well defined as in the $Fr = 2$ wake. According to CS2020, the $Fr = 10$ wake stays in the weakly stratified regime (WST) from $x/D \approx 10$ to 50 and thereafter stays in the intermediately stratified regime (IST) till the end of the domain.

To conclude this section, instantaneous snapshots of fluctuating spanwise velocity (u'_y/U_∞) are shown in figure 3.3 at locations in the near, intermediate and far wake at $Fr = 2$ (top row) and $Fr = 10$ (bottom row). An ellipse with major and minor axes equal to $2L_{Hk}$ and $2L_{Vk}$, where L_{Hk} and L_{Vk} are the TKE-based wake widths in horizontal and vertical directions, respectively, is also shown. L_{Hk} is defined by $\mathrm{TKE}(x, y = L_{Hk}, z = 0) = \mathrm{TKE}(x, r = 0)/2$ and L_{Vk} by $\mathrm{TKE}(x, y = 0, z = L_{Vk}) = \mathrm{TKE}(x, r = 0)/2$. Here, $r = 0$ denotes the disk centerline. It is worth noting that using the sum of TKE and TPE to define the wake widths (not shown here) result in values similar to L_{Hk} and L_{Vk} for both $Fr = 2$ and $Fr = 10$ wakes. Following CS2020, we use the TKE-based definitions in the rest of the results and discussions. This ellipse, based on L_{Hk} and L_{Vk}, is used to approximately demarcate the wake core from the outer wake. In subsequent

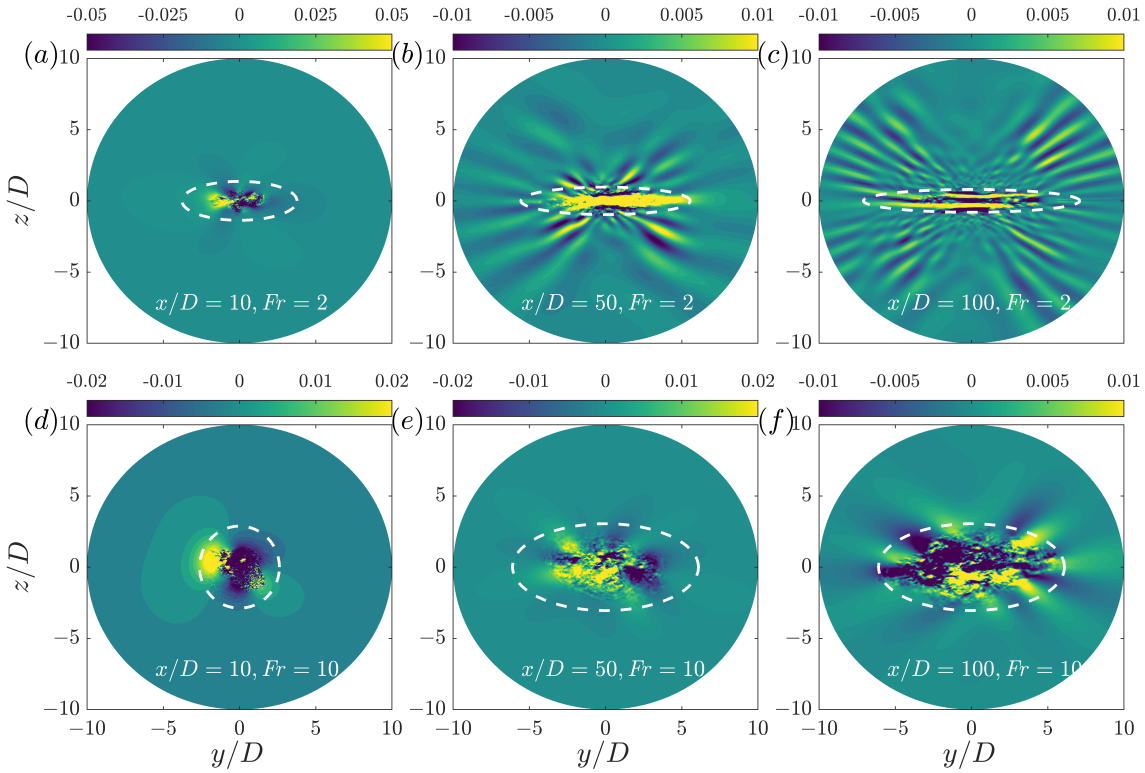

Figure 3.3: Instantaneous snapshots of the fluctuating spanwise velocity u'_y/U_∞ shown for $Fr = 2$ (top row) and $Fr = 10$ (bottom row): (a,d) at $x/D = 10$, (b,e) at $x/D = 50$, and (c,f) at $x/D = 100$. Dashed close curve in white shows wake core.

sections, this definition of the wake core will prove to be useful for the interpretation of some SPOD results.

At $Fr = 2$, an appreciable effect of buoyancy is already present in the near wake as shown in figure 3.3(a) for $x/D = 10$, which corresponds to $Nt_2 = 5$ in buoyancy time units. At the same streamwise location, the $Fr = 10$ wake still has a circular cross-section with an imprint of the $m = 1$ azimuthal mode which was found to be energetically important in the unstratified wake (Nidhan et al. (2020)). As both the wakes evolve downstream, buoyancy has a progressively increasing effect on the the wake core as well as the surrounding outer wake. By $x/D = 50$, vertically flattened wake cores can be observed in figure 3.3(b,d) for both the wakes, more so at $Fr = 2$ than at $Fr = 10$. It is also worth noting that the wake core of $Fr = 2$ consists of distinct layers by $x/D = 50$. The $Fr = 2$ wake also shows a significant amount of IGW activity in the outer region, i.e. outside the ellipse in figure 3.3(b). Farther downstream at $x/D = 100$, the u'_y field of $Fr = 2$ (figure 3.3(c)) shows IGWs occupying a significant portion of the outer wake with the wake core being further flattened and comprising an increased number of horizontally oriented layers. The $Fr = 10$ wake core also starts showing appreciable IGW activity in the ambient by $x/D = 100$ ($Nt_{10} = 10$), as shown in figure 3.3(f).

3.5 Characteristics of SPOD eigenvalues and eigenspectra

We start the discussion of SPOD modes by evaluating their overall contribution to fluctuation energy and by their eigenspectra. There are significant effects of buoyancy as elaborated below.

3.5.1 Cumulative modal contribution to fluctuation energy

Figure 3.4 shows the variation of cumulative energy ($\xi(n)$) as a function of SPOD modal index (n) at four downstream locations: $x/D = 20, 40, 80$, and 100. To calculate $\xi(n)$, the energy

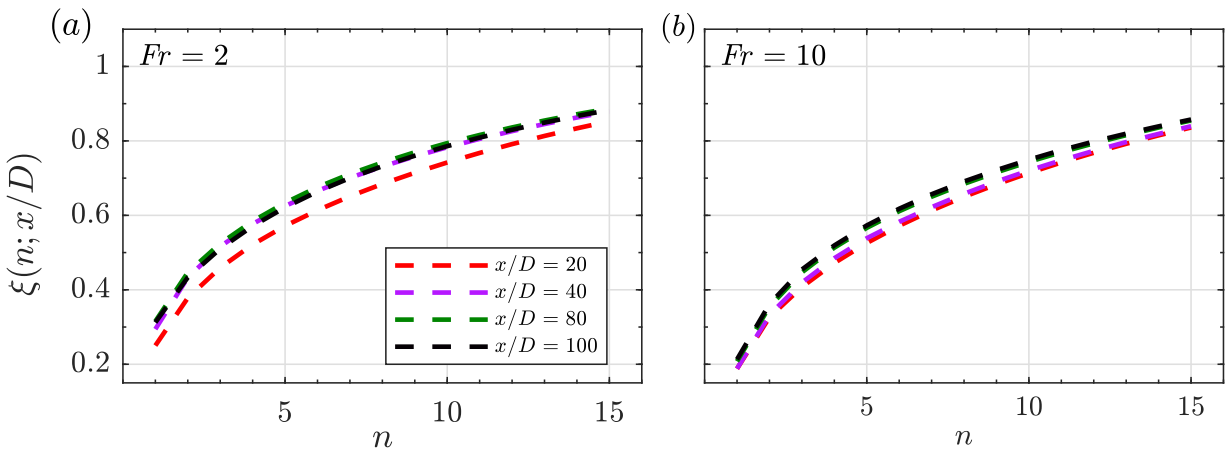

Figure 3.4: Variation of the cumulative energy, $\xi(n)$, as a function of modal index n for (a) $Fr = 2$ and (b) $Fr = 10$ wakes, shown till $n = 15$ SPOD modes.

across all resolved frequencies St at each modal index up to n is summed and normalized by the total energy as follows:

$$\xi(n;x/D) = \frac{\sum_{i=1}^{n} \sum_{St} \lambda^{(i)}(f;x/D)}{\sum_{i=1}^{N_{blk}} \sum_{St} \lambda^{(i)}(f;x/D)}, \tag{3.15}$$

where N_{blk} is the total number of SPOD modes at a given St. Comparison among the various x/D curves shows that the energy captured by leading SPOD modes in both wakes increases with downstream distance. This behavior is in contrast to the unstratified wake where the relative importance of the dominant SPOD modes decreases with increasing x/D (Nidhan et al., 2020). Although both stratified wakes exhibit an increasing dominance of the leading modes as x/D increases, there is a quantitative difference in that the jump of modal energy fraction from its $x/D = 20$ value is larger for the the $Fr = 2$ wake relative to the $Fr = 10$ wake.

As discussed in the introduction, CS2020 found that the $Fr = 2$ wake traversed the WST, IST and SST regimes during its streamwise evolution and the $Fr = 10$ wake accessed only the WST and IST regimes. Readers are referred to section 3.1 for an introduction to these regimes in stratified turbulence. These transitions also appear in the the evolution of the modal energy content $\xi(n;x/D)$. For example, the $Fr = 2$ wake in figure 3.4(a) shows a transition at $x/D \approx 40$

whereby the $\xi(n)$ curves for $x/D \geq 40$ collapse onto a single profile. This result is consistent with CS2020 who find that $x/D \approx 40$ ($Nt_2 \approx 20$) is the location where the $Fr = 2$ wake wake transitions from IST to SST. The $Fr = 10$ wake was found by CS2020 to stay in the WST regime till $x/D \approx 50$ ($Nt \approx 5$) and thereafter transitioned to the IST regime. For the $Fr = 10$ wake in figure 3.4(b), the $\xi(n)$ curves collapse separately, i.e. there is one curve showing collapse between $x/D = 20$ and 40 which lie in the WST regime, and there is another showing collapse between $x/D = 80$ and 100 which lie in the IST regime. Plots of $\xi(n)$ at other values of x/D (not shown here) confirm that locations with $x/D \leq 50$ collapse on the $x/D = 20, 40$ curve and locations with $x/D \geq 80$ collapse on the $x/D = 80, 100$ curve.

The energy summed over frequencies instead of modal indices is now examined. Figure 3.5 shows the variation of $\xi(St)$ calculated as follows:

$$\xi(St; x/D) = \frac{\sum_{f=-St}^{St} \sum_{i=1}^{N_{blk}} \lambda^{(i)}(f; x/D)}{\sum_{i=1}^{N_{blk}} \sum_{St} \lambda^{(i)}(f; x/D)}. \tag{3.16}$$

Figure 3.5 shows that $\xi(St)$ increases for low-St modes with increasing x/D in both wakes, which is a trend also seen for $\xi(n)$. This is yet another indication of the increasing importance of the coherent modes as buoyancy effects come into play in these stratified wakes. Besides, for both wakes, $\xi(St)$ increases steeply between $St = 0.1$ and 0.2 at all downstream locations. The reason behind this sharp increase will be discussed shortly. Another observation of interest is that almost all the fluctuation energy at large x/D is captured by the modes with $St < 1$ in both wakes.

From $x/D = 20$ to 40, there is a large jump in $\xi(St)$ for the $Fr = 2$ wake in figure 3.5(a). As mentioned previously, $x/D = 40$ also marks the arrival of the $Fr = 2$ wake into the SST regime. Also, the $\xi(St)$ curves collapse for locations $x/D = 80$ and 100. On analyzing other streamwise locations (not shown here), we find that the $\xi(St)$ curves for $x/D \geq 70$ collapse together similar to the previously shown $\xi(n)$ curves of the $Fr = 2$ wake. One difference is that the collapse of

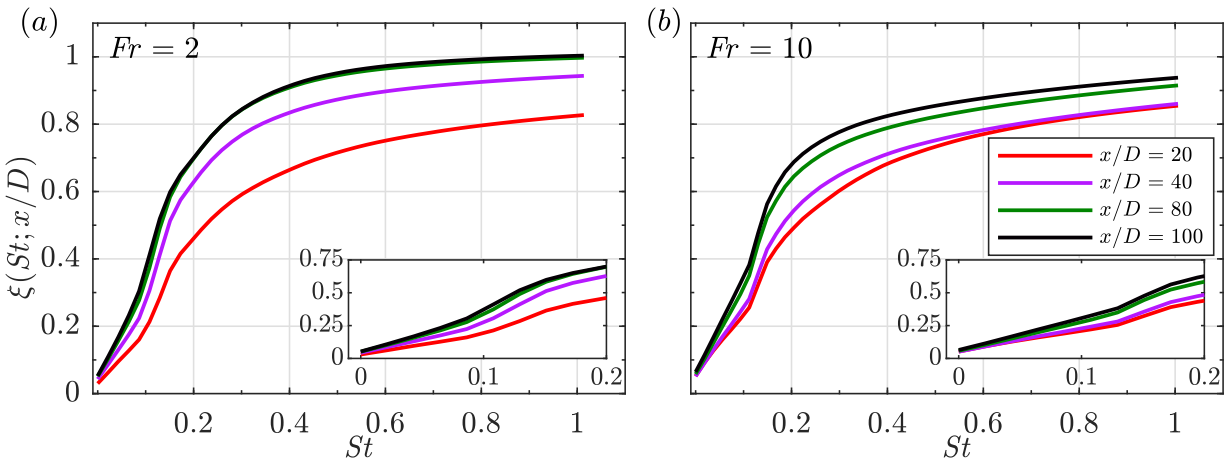

Figure 3.5: Variation of the cumulative fraction of energy, $\xi(St)$, as a function of St for (a) $Fr = 2$ and (b) $Fr = 10$. The plots are shown for $0 \leq St \leq 1$ for both cases. Inset plots show zoomed-in variation of $\xi(St)$ for $0 \leq St \leq 0.2$.

$\xi(n)$ commences closer to the body at $x/D \approx 40$.

Contrary to the $Fr = 2$ wake where the change in $\xi(St)$ from $x/D = 20$ to $x/D = 40$ was large, the corresponding change for the $Fr = 10$ wake (figure 3.5(b)) is small and consistent with an absence of regime change. However, the $Fr = 10$ wake exhibits a significant jump of $\xi(St)$ between $x/D = 40$ and 80, which lie in the WST and IST regime, respectively.

To summarize, figures 3.4 and 3.5 have the following implications. First, the relative importance of the leading SPOD modes increases with x/D for the stratified wakes, which is in stark contrast to their behavior in the unstratified wake (Nidhan et al. (2020)). Second, the trend of increasing dominance of leading SPOD modes is more pronounced for the strongly stratified wake of $Fr = 2$ as compared to $Fr = 10$. Third, transitions between WST, IST and SST regimes discussed by CS2020 for the turbulence statistics are also qualitatively reflected in the energetics of SPOD modes too.

3.5.2 SPOD eigenspectra of $Fr = 2$ and 10 wakes

Figure 3.6 shows the SPOD eigenspectra of the $Fr = 2$ (left column) and $Fr = 10$ (right column) wakes at various downstream locations. The spectrum of the leading SPOD mode

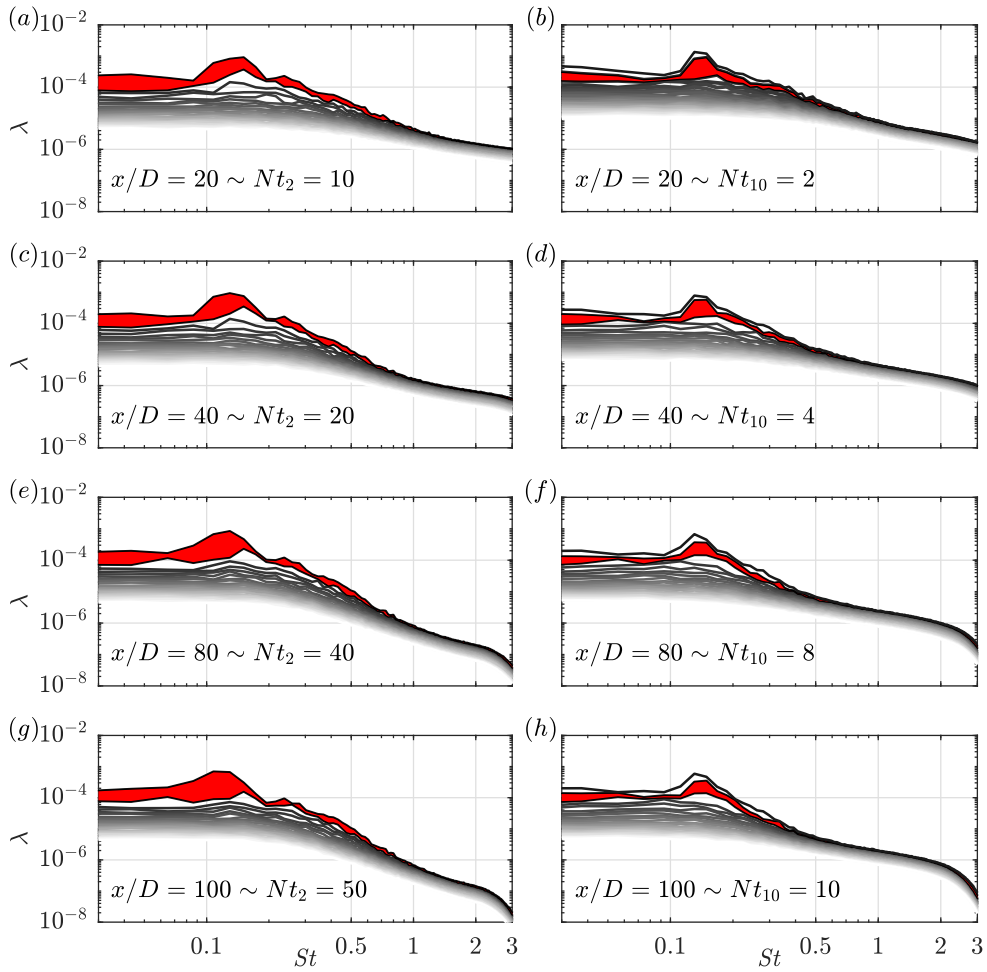

Figure 3.6: SPOD eigenspectra of 25 most energetic modes, $\boldsymbol{\lambda}^{(1)}$ to $\boldsymbol{\lambda}^{(25)}$, for the $Fr = 2$ (left column) and $Fr = 10$ (right column) wakes at four streamwise locations: (a,b) $x/D = 20$, (c,d) $x/D = 40$, (e,f) $x/D = 80$, and (g,h) $x/D = 100$. Dark to light shade corresponds to increasing model index i in $\boldsymbol{\lambda}^{(i)}$.

($\lambda^{(1)}$) shows a distinct spectral peak in the vicinity of $St = 0.13 - 0.15$ at all locations and for both wakes. This pronounced peak is the reason why there was a sharp increase of $\xi(St)$ within $0.1 < St < 0.2$ for both wakes in figure 3.5.

In the $Fr = 10$ wake, the $\lambda^{(1)}$ eigenspectrum at all locations has a distinct peak at $St \approx 0.13$, which is very close to the vortex shedding (VS) frequency of the unstratified wake ($St = 0.135$) at the same Reynolds number (Nidhan et al. (2020)). SPOD eigenspectra at $x/D < 2$ (not presented here) show that this spectral peak has its origin near the wake generator and corresponds to vortex shedding in the $Fr = 10$ wake.

Unlike the $Fr = 10$ wake, the spectral peak in $\lambda^{(1)}$ for the $Fr = 2$ wake shifts slightly from $St \approx 0.15$ at $x/D = 20$ to $St \approx 0.13$ at $x/D = 40$ and onward. At the far wake location of $x/D = 80$, the peak in the $\lambda^{(1)}$ eigenspectrum broadens to reach $St \approx 0.11$. Near-body SPOD eigenspectra (not shown here) for the $Fr = 2$ wake show a prominent peak at $St \approx 0.15$ (slightly larger relative to the unstratified and $Fr = 10$ wakes) just downstream of the recirculation zone at $x/D \approx 2$. Furthermore the pressure spectrum (not presented here) in the immediate proximity of the disk, at $x/D = 0.5$ and $r/D = 0.5$, also peaks at $St \approx 0.15$, indicating that this frequency corresponds to the VS mechanism for the $Fr = 2$ wake. The shift in the spectral peak towards lower St at later x/D is consistent with the sphere-wake study of Spedding (2002a) who report a gradual reduction in the dominant wake St during $40 < Nt < 100$ (see figure 5 of their paper).

In the $Fr = 2$ wake, there is a large gap (demarcated in red) between the $\lambda^{(1)}$ and $\lambda^{(2)}$ spectra for frequencies with $St < 0.2$. Beyond $St \approx 0.2$, values of all $\lambda^{(i)}$ fall sharply. This large difference between $\lambda^{(1)}$ and $\lambda^{(2)}$ implies that the dynamics of the $Fr = 2$ wake is low-rank, i.e. it is dominated by the leading SPOD mode. The sharp drop-off in energy at higher St points to the dominance of low-frequency energetic structures with St in $[0, 0.2]$, specifically around the VS frequency.

In terms of low-rank behavior, the $Fr = 10$ wake shows a peculiar difference from the $Fr = 2$ wake. Although the gap between $\lambda^{(1)}$ and $\lambda^{(2)}$ is significantly less compared to that for

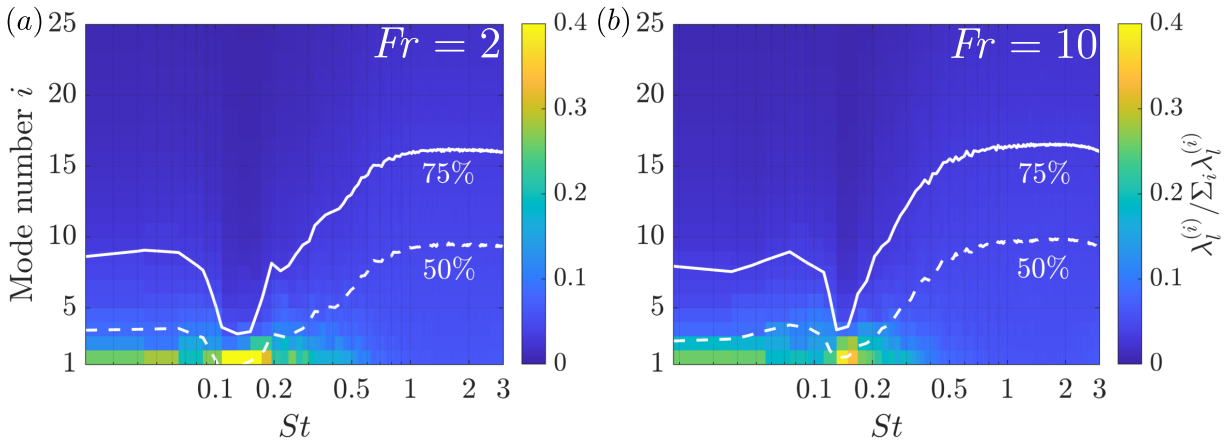

Figure 3.7: Fraction of energy (at a given St) accounted by each SPOD mode as a function of frequency at $x/D = 50$ for: (a) $Fr = 2$ and (b) $Fr = 10$ wakes. The solid and dashed white lines indicate the number of SPOD modes required to retain 75% and 50% of the total fluctuation energy respectively at each frequency.

$Fr = 2$, there is a significant gap between $\lambda^{(2)}$ and $\lambda^{(3)}$ around the VS frequency $St \approx 0.13$, shown in red in the right column of figure 3.6. Furthermore, the variation of $\lambda^{(2)}$ with St is very similar to that of $\lambda^{(1)}$. On further investigation, we find that the SPOD eigenmodes of $\lambda^{(1)}$ and $\lambda^{(2)}$ at the VS frequency have similar spatial structure, but with a rotation in their orientation. We hypothesize that $\lambda^{(1)}$ and $\lambda^{(2)}$ modes at the VS frequency are the manifestation of $m = 1$ and $m = -1$ azimuthal modes in the weakly stratified $Fr = 10$ wake.

Figure 3.7 shows the fraction of energy in each SPOD mode as a function of St for both wakes at a representative location of $x/D = 50$. In both wakes, the leading SPOD mode at the VS frequency capture at least 40% of the total energy contained in the VS frequency. This also holds true for the near ($x/D = 10$) and far ($x/D = 100$) locations in both wakes (not discussed here for brevity). Also, in both, wakes, less than 5 SPOD modes are required to capture 75% of the total energy in the vicinity of the VS frequency, as indicated by the solid white line in figure 3.7.

The key takeaway from figure 3.6 and figure 3.7 is twofold: (i) the VS frequency is the leading contributor to the fluctuating energy content of both $Fr = 2$ and 10 wakes and (ii) its dynamics are primarily governed by a few leading SPOD modes. Previous experimental studies

of Chomaz et al. (1993) and Lin et al. (1992a) have showed the existence of the VS mode in the near wake at moderate stratification using hot-wire measurements (at few select locations) and shadowgraph techniques. The present SPOD analysis enables us to establish the dominance of the VS mode in stratified wakes from near the body to 100 body diameters downstream by providing an ordered set of $\lambda^{(i)}$ eigenvalues for different St.

3.6 The energetics of the vortex shedding (VS) mode

A comparison between SPOD eigenspectra of the stratified wakes (figure 3.6) and the unstratified wake (figure 3 in Nidhan et al. (2020)) reveals that both types of wakes are dominated by vortex shedding which gives rise to a distinct spectral peak in the vicinity of $St \approx 0.13$. For the unstratified wake, besides the VS structure, which appears in the azimuthal mode $m = 1$, a double helix ($m = 2$) mode with a peak at $St \to 0$ is also found to be energetically important (Johansson and George, 2006a, Nidhan et al., 2020). In the stratified wake, as elaborated below, we find that the VS mode is persistent, is linked to unsteady internal gravity waves (IGWs), and is thereby responsible for the accumulation of fluctuation energy outside the wake core.

Stratification qualitatively affects the streamwise evolution of the energy in different frequencies. The evolution of the frequency-binned energy is shown for the stratified wakes in figure 3.8 (a)-(b). For the unstratified case ($Fr = \infty$), the azimuthal modes $m = 1$ and $m = 2$ are shown in figure 3.8(c) and (d), respectively. For the stratified wakes in figures 3.8 (a)-(b), the spectral peak in the vicinity of $St \approx 0.13$ remains prominent for significant downstream distances, especially for $Fr = 2$. A somewhat wide band ($0.1 \leq St \leq 0.2$), centered around $St \approx 0.13$ of the VS mode, is excited for the stratified wakes. Furthermore, this band persists into the far wake. Even at $x/D = 100$, this band has larger energy density than at other frequencies. Such persistence in the energetic dominance of the VS mode (and neighboring frequencies) is absent in the unstratified $Fr = \infty$ case where the energy at the two peaks of: (i) $St = 0.135$ in the $m = 1$

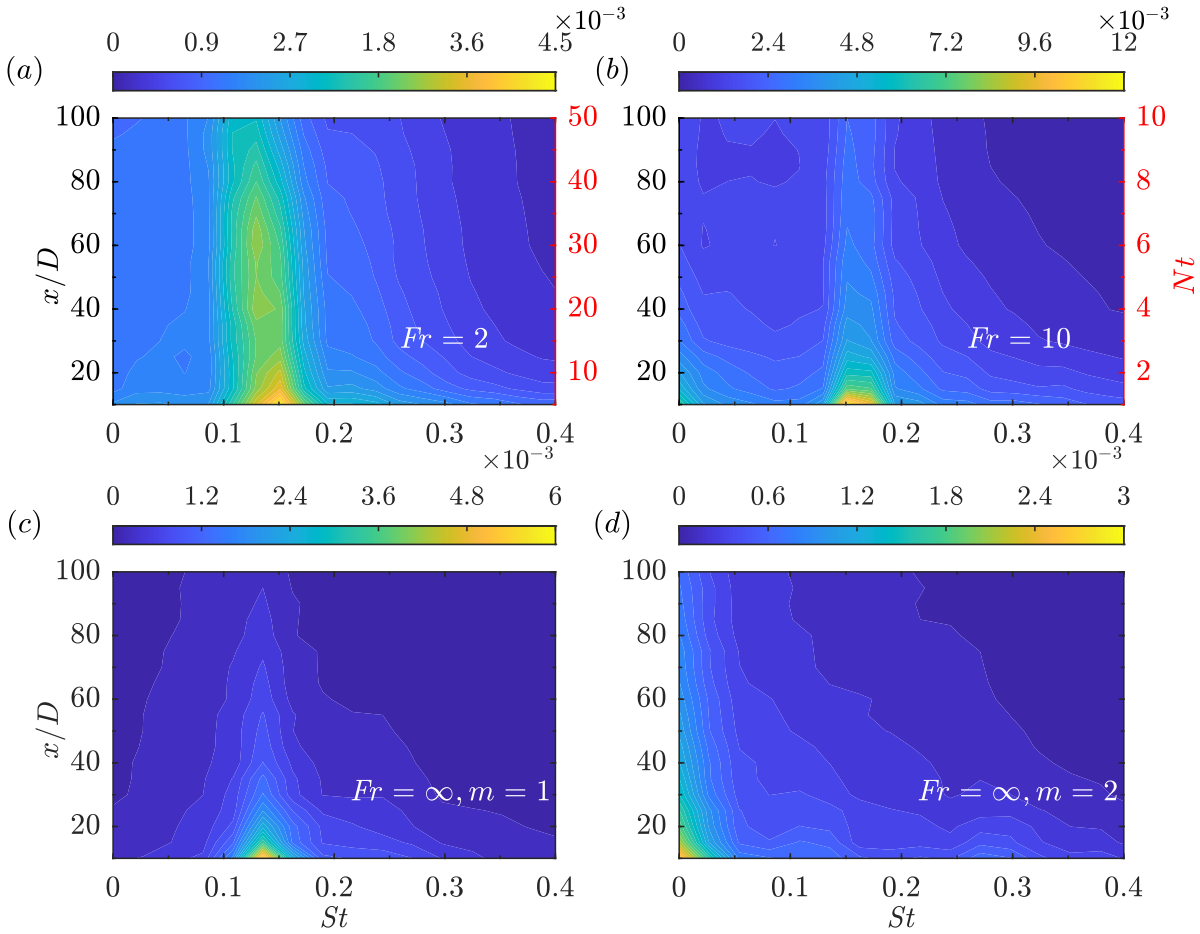

Figure 3.8: $x/D - St$ contour maps showing the variation of total energy in the leading 15 SPOD modes: (a) $Fr = 2$, (b) $Fr = 10$, (c) $Fr = \infty$, $m = 1$ (vortex shedding) mode, and (d) $Fr = \infty$, $m = 2$ (double helix) mode.

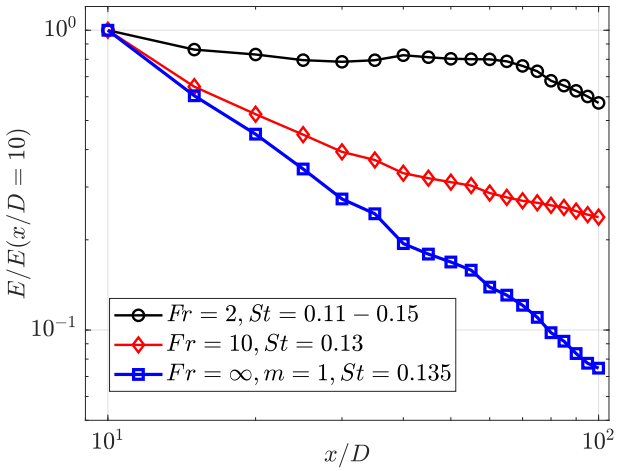

Figure 3.9: Evolution of the energy contained in leading 15 SPOD modes at the vortex shedding frequency is shown for $Fr = 2, 10$, and ∞ wakes. The energy is normalized by its value at $x/D = 10$.

mode (figure 3.8(a)) and (ii) $St = 0$ in the $m = 2$ mode (figure 3.8(b)) declines sharply with increasing x/D.

Figure 3.9 shows the streamwise evolution of energy in the leading 15 SPOD modes and in a frequency band around the VS frequency. The energy in the $Fr = 2$ wake remains almost constant till $x/D = 60$ and starts decaying slowly thereafter. On the other hand, the $Fr = 10$ wake shows an initial decay in the VS mode energy which closely follows that of the $Fr = \infty$ wake till $x/D = 20$. Subsequently, buoyancy effects set in for the $Fr = 10$ wake to slow down the energy decay.

To investigate the reason behind the downstream persistence of the VS spectral peak in stratified wakes, the total energy in the leading 15 SPOD modes is partitioned into two components: (i) energy of the wake core, E_{core} and (ii) energy of the outer wake, E_{outer}. The energy in each of the regions is calculated as:

$$E_{core}(x/D, St) = \sum_{n=1}^{15} \int_{A \in \Omega} \lambda^{(n)}(x/D, St) \Phi_i^{*(n)}(x/D, St) \Phi_i^{(n)}(x/D, St)\, \mathrm{d}A, \tag{3.17}$$

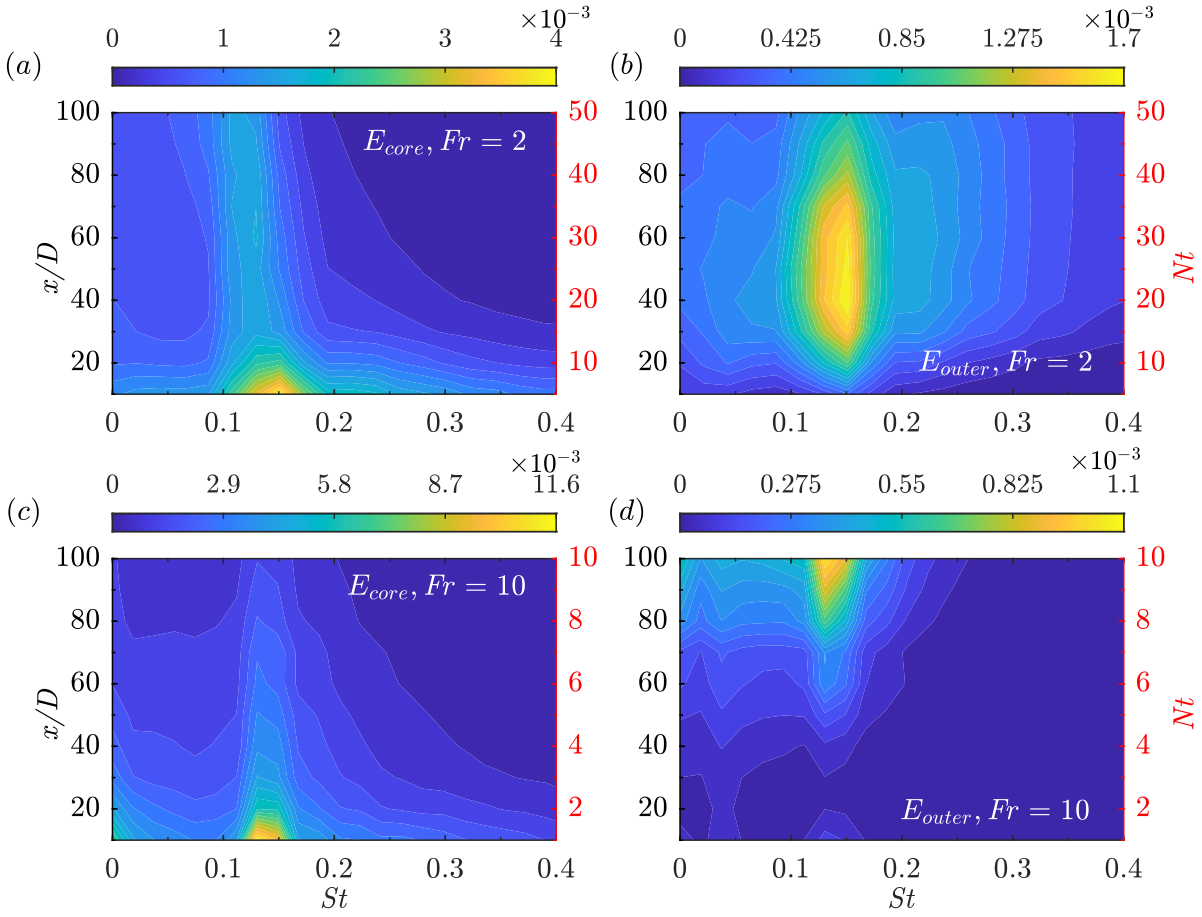

Figure 3.10: Energy partition between core and outer wake: (a) wake core of $Fr = 2$, (b) outer wake of $Fr = 2$, (c) wake core of $Fr = 10$, and (d) outer wake of $Fr = 10$.

$$E_{outer}(x/D,St) = \sum_{n=1}^{15} \int_{A\in\mathcal{H}-\Omega} \lambda^{(n)}(x/D,St)\Phi_i^{*(n)}(x/D,St)\Phi_i^{(n)}(x/D,St)\,\mathrm{d}A, \tag{3.18}$$

where Ω denotes the wake core at a given x/D, as defined in section3.4. $\mathcal{H}$ denotes the area of the circular cross-section bounded by $0 \leq r/D \leq 10$ at a given x/D. Here, $\Phi_i^{(n)}$ corresponds to the n^{th} SPOD eigenmode for a given x/D and St.

The energy in the wake core peaks around the VS-mode frequency, $St \approx 0.12-0.13$, for both wakes (see figure 3.10(a,c)). With increasing x/D (or Nt), the VS signature in the wake core decays for both wakes. The energetics of the outer wake is remarkably different. E_{outer}, which starts off with a small value across all St at $x/D \approx 10$ in the $Fr = 2$ wake, develops a peak at $St \approx 0.15$ at $x/D \approx 20$. Note that this peak is the same as the peak in the SPOD eigenspectrum for the entire wake (figure 3.6(a)). Farther downstream, there is significant energy content in the outer wake for $x/D \approx 16-80$ ($Nt_2 \approx 8-40$) with a spectral peak located at $St \approx 0.13-0.15$. The spectral peak is broad, i.e. nearby frequencies with $0.1 \leq St \leq 0.2$ also have comparable energy levels. For the $Fr = 10$ wake, E_{outer} picks up only beyond $x/D = 60$ ($Nt_{10} = 6$), and thereafter increases progressively in the vicinity of $St \approx 0.13$ till the end of the domain. We also find that the qualitative nature of the variation of energy in the outer wake and wake core found in figure 3.10 does not change when the number of modes over which energy is summed is decreased from 15 to 3 (not presented here for brevity).

In figure 3.11, we sum up the SPOD energies across $St \in [-0.4, 0.4]$ separately for the wake core and the outer wake and compute their percentage contribution to the entire area-integrated fluctuation energy as follows,

$$\chi_{core}(x/D) = \frac{\sum_{|St|=[0,0.4]} E_{core}(St,x/D)}{E_k^T(x/D) + E_\rho^T(x/D)} \times 100, \tag{3.19}$$

$$\chi_{outer}(x/D) = \frac{\sum_{|St|=[0,0.4]} E_{outer}(St,x/D)}{E_k^T(x/D) + E_\rho^T(x/D)} \times 100, \tag{3.20}$$

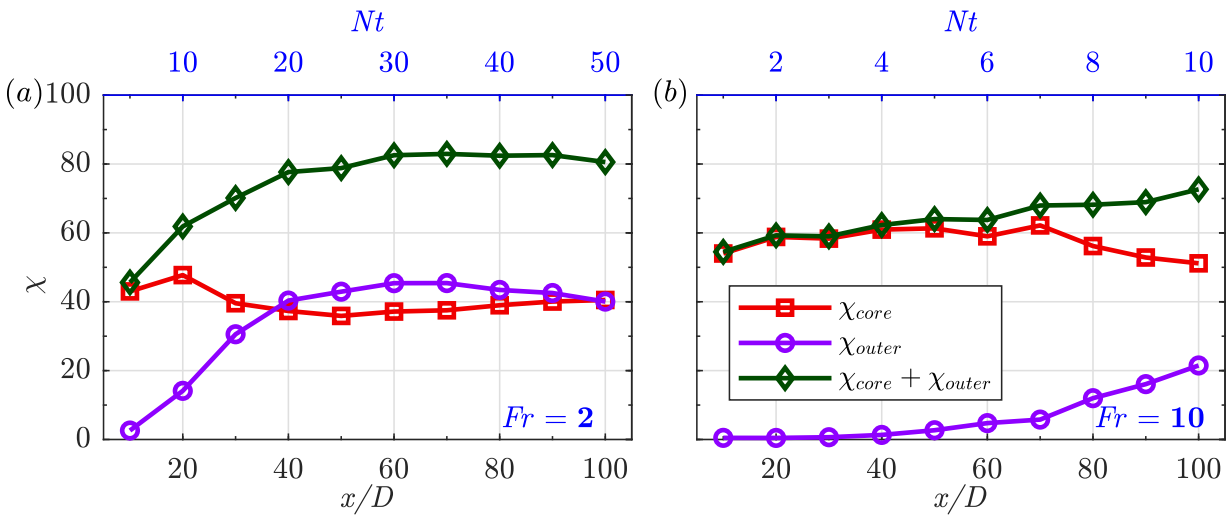

Figure 3.11: Streamwise variation of χ_{core}, χ_{outer}, and $\chi_{core}+\chi_{outer}$: (a) $Fr=2$, (b) $Fr=10$.

where $E_k^T(x/D)$ and $E_\rho^T(x/D)$ are area-integrated TKE and TPE in the circular region of $0 \leq r/D \leq 10$ at the x/D location under consideration. The streamwise evolution of χ_{core} and χ_{outer} are shown in figure 3.11.

For the $Fr=2$ wake (figure 3.11(a)), χ_{outer} increases monotonically until $x/D \approx 60$ followed by a slight decrease. At its peak, χ_{outer} constitutes up to 50% of the total fluctuation energy, becoming even larger than χ_{core}. In the $Fr=10$ wake (figure 3.11(b)), χ_{outer} remains negligible till $x/D=60$, followed by a monotonic increase. The increase in the value of χ_{outer} is accompanied by a decrease in the wake-core contribution. The percentage of total energy captured by the leading 15 SPOD modes and $|St| \in [0, 0.4]$, i.e., $\chi_{wake}+\chi_{outer}$ (shown in green), increases for both wakes from its initial value at $x/D=10$. This reinforces a main finding of this work that stratified wakes display an increased coherence of fluctuation energy as they evolve downstream.

Figure 3.10 suggests that the unsteady IGWs in the outer wake radiate from the VS mode at intermediate to late Nt. Nevertheless, to further establish causation between the unsteady IGW emission and the VS mode, we perform additional SPOD analyses for the $Fr=2$ wake. In these analyses, we replace the fluctuating density field ρ' with the fluctuating pressure field p'. These

SPOD analyses are performed at $x/D = 10, 20, \cdots, 90, 100$. At all locations, the eigenspectra obtained from these modified SPOD analyses show a prominent peak at the VS frequency with a large gap between $\lambda^{(1)}$ and $\lambda^{(2)}$ for $St < 0.2$, qualitatively akin to the left column of figure 3.6.

Using p' along with u_i' enables us to reconstruct the pressure transport term in the radial direction, $\langle p'u_r' \rangle$, which accounts for the energy transferred radially from the wake core to the IGW dominated outer wake region through pressure-work (de Stadler and Sarkar, 2012, Rowe et al., 2020). We reconstruct $\langle p'u_r' \rangle$ contours using leading 15 SPOD modes and frequencies in the range of (i) $St \in [0.1, 0.2]$ and (ii) $St \in [0.1, 0.3]$ as follows:

$$\langle p'u_r' \rangle(x;y,z) = \sum_{St} \sum_{n=1}^{15} \lambda^{(n)}(x;St)\, \Phi_{u_r}^{(n)}(x;y,z,St)\, \Phi_p^{(n)*}(x;y,z,St), \tag{3.21}$$

Figure 3.12 shows the actual (top row) and reconstructed (middle and bottom rows) $\langle p'u_r' \rangle$ at three streamwise locations $x/D = 20, 40$, and 60 for the $Fr = 2$ wake. The actual $\langle p'u_r' \rangle$ shows a strong signature of IGW flux in the outer wake region at all three downstream locations in figure 3.12. We found that the nonlinear transport term was negligible outside the wake core (not shown here). Hence the primary source of the energy transfer to the outer wake is the pressure-work term due to the IGW radiation. The reconstructed $\langle p'u_r' \rangle$ using $St \in [0.1, 0.2]$ (middle row) shows qualitative agreement with the spatial distribution of actual $\langle p'u_r' \rangle$, both in the wake core as well as outer wake region, at all downstream locations. As more frequencies are included (bottom row), adjacent to the VS frequency, the accuracy of reconstruction increases. The key spatial characteristics of $\langle p'u_r' \rangle$ remain similar in both reconstructions, showing that frequencies in the vicinity of the VS frequency satisfactorily capture the key dynamics of unsteady IGW generation.

To further elucidate the causal link between the VS mode and the IGW generation, we plot the $x/D - St$ variation of the integrated $\langle p'u_r' \rangle$ in the outer wake region (similar to 3.18), reconstructed using 3 and 15 SPOD modes (figure 3.13). The evolution of integrated $\langle p'u_r' \rangle$ in the outer wake of the $Fr = 2$ wake is very similar to that of the energy in the outer wake region (figure 3.10(b)). It starts off at a small value at $x/D \approx 10$, develops a broad peak centered at $St \approx 0.15$

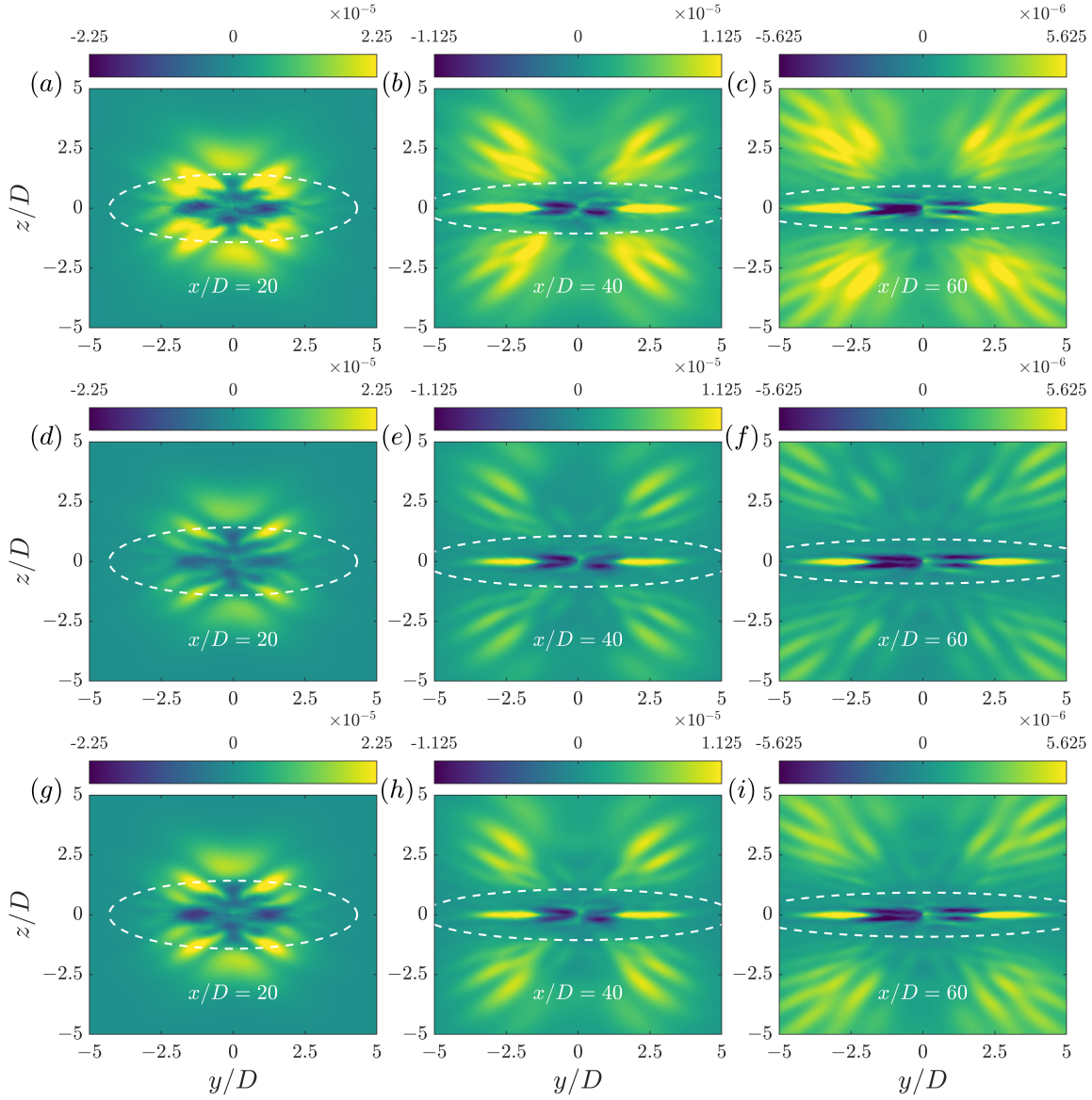

Figure 3.12: Contours of $\langle p'u'_r \rangle$ for the $Fr = 2$ wake obtained from: (i) temporal averaging (top row), reconstruction using leading 15 SPOD modes and (ii) $St \in [0.1, 0.2]$ (middle row) and (iii) $St \in [0.1, 0.3]$ (bottom row). Three streamwise locations $x/D = 20, 40$, and 60 are shown.

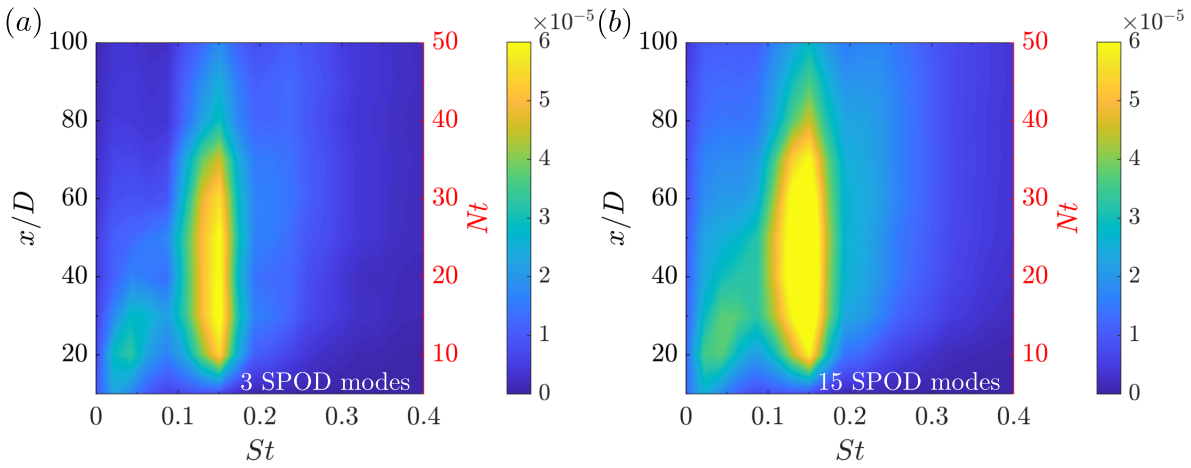

Figure 3.13: $x/D-St$ contour maps showing the variation of integrated $\langle p'u'_r \rangle$ in the outer wake region using: (a) leading 3 SPOD modes and (b) leading 15 SPOD modes for the $Fr = 2$ wake.

between $20 \leq x/D \leq 80$, and gradually starts declining beyond $x/D = 80$. Increasing the number of modes from 3 to 15 makes the active St region broader while intensifying the reconstructed values.

Figure 3.10, 3.12, and 3.13 firmly establish that the VS mode energy radiates out of the wake core instead of being acted on by nonlinear interactions in the turbulent wake responsible for the usual energy cascade. Therefore, unlike their unstratified counterpart, the stratified wakes exhibit a persistent VS spectral peak when the energy in the full domain of influence (denoted by $\mathcal{H}$) of the wake is taken into account as in the SPOD results of figure 3.8(a,b).

3.7 Spatial structure of SPOD eigenmodes

3.7.1 Spatial structure of the VS eigenmode

The spatial structure of the dominant eigenmodes sheds further light on the manner in which buoyancy helps spread unsteady flow perturbation to well outside the turbulent core of the wake. Figure 3.14 shows the real part of the normalized (by L_∞ norm) leading SPOD mode, $\Phi_y^{(1)}(y,z,St;x)/||\Phi_y^{(1)}(y,z,St;x)||_\infty$, of the lateral velocity u_y. The plotted modes correspond to

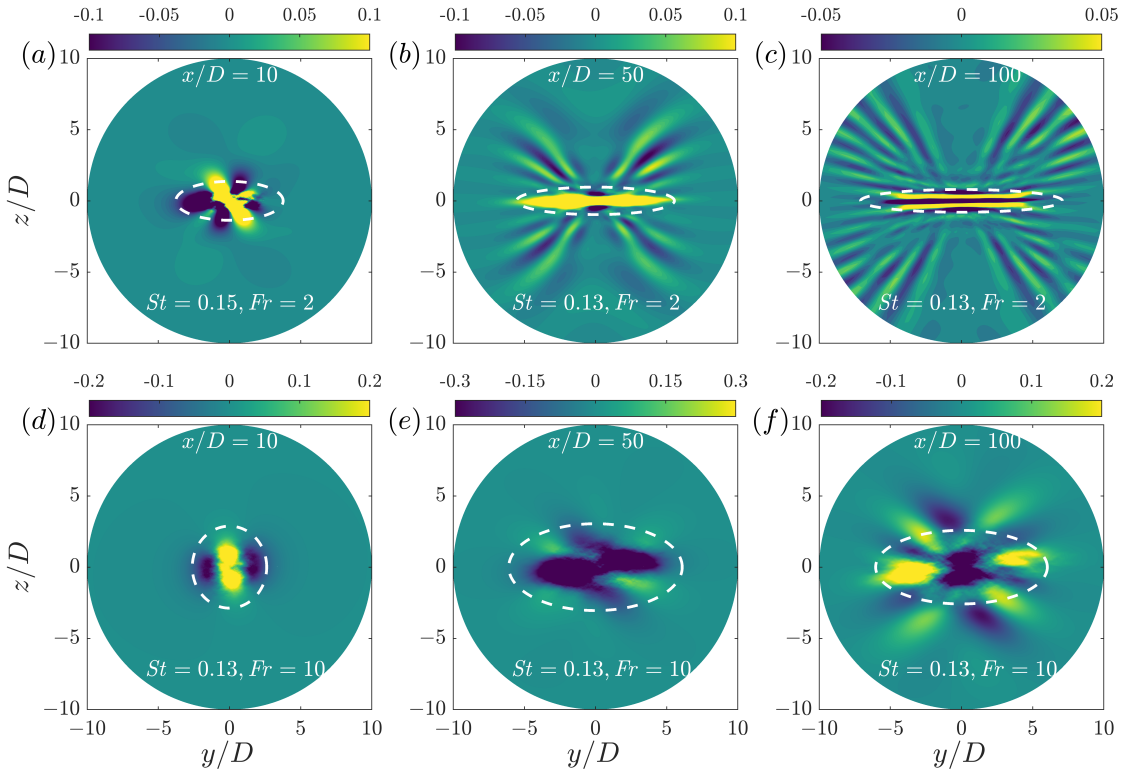

Figure 3.14: Shape of the leading SPOD mode (real part corresponding to $\lambda^{(1)}$) for spanwise velocity, $\Phi_y^{(1)}(y,z,St;x/D)$. At each x/D, the shown mode corresponds to the peak in the eigenspectrum of $\lambda^{(1)}$. Real part of each mode is shown. Dashed closed curve in white shows wake core.

the VS mode, which is at St corresponding to the eigenspectrum peak and are shown for selected values of x/D. The ellipsoid wake core (dashed blue curve) with dimensions $2L_{Hk}$ and $2L_{Vk}$ is also shown. At $Fr = 2$ (upper row), the wake core exhibits flattening from $x/D = 10$ ($Nt = 5$) onward and the eigenmodes in the core show horizontal layering for $x/D \geq 50$. The layering becomes visible in the eigenmodes at $x/D \approx 30$ (not shown here). The region outside the core has little activity at $x/D = 10$ but shows IGW phase lines at $x/D = 50$ and 100. There is a clear and continuous transition of the eigenmode from its layered core to an IGW structure in the outer region at the far downstream locations. The flattening of the wake core and the IGW related spread of the eigenmode is delayed for the $Fr = 10$ wake (bottom row) relative to $Fr = 2$ since equivalent Nt values occur farther downstream.

Comparing figure 3.14(b,c) with figure 3.3(b,c), there are striking similarities in the layered structure of the $Fr = 2$ wake core between the dominant eigenmodes and the instantaneous snapshots at the far downstream locations of $x/D = 50$ and 100. Although SPOD only guarantees that the obtained modes optimally capture the prescribed energy norm of the flow (see section 3.3.1), these modes do generally contain the imprints of actual flow structures, as is the case here. The outer wake shows that distinct IGWs are associated with the wake core structure of dominant eigenmodes at late Nt for both $Fr = 2$ and 10 wakes. For the $Fr = 2$ wake, IGW activity in the outer region of the eigenmodes shown in figure 3.14 is negligible at $x/D = 10$ ($Nt_2 = 5$) while it is readily noticeable at $x/D = 50$ ($Nt_2 = 25$) and $x/D = 100$ ($Nt_2 = 50$). The IGWs are found to be emitted within $30^\circ - 60^\circ$ with the y axis. For $Fr = 10$, the IGWs found at $x/D = 100$ ($Nt_{10} = 10$) are emitted at $\approx 45^\circ$ from the horizontal. A comparison between figure 3.3 and 3.14 reveals that the IGW in the dominant eigenmodes (figure 3.14) represent the IGWs in actual snapshots (figure 3.3) to a satisfactory extent, emphasizing that the VS mechanism is an important IGW generation mechanism in stratified wakes.

The leading VS modes at different locations show asymmetry about the $y = 0$ line, in both $Fr = 2$ (at $x/D = 10$) and $Fr = 10$ (at $x/D = 50$ and 100) wakes. This might be a consequence of

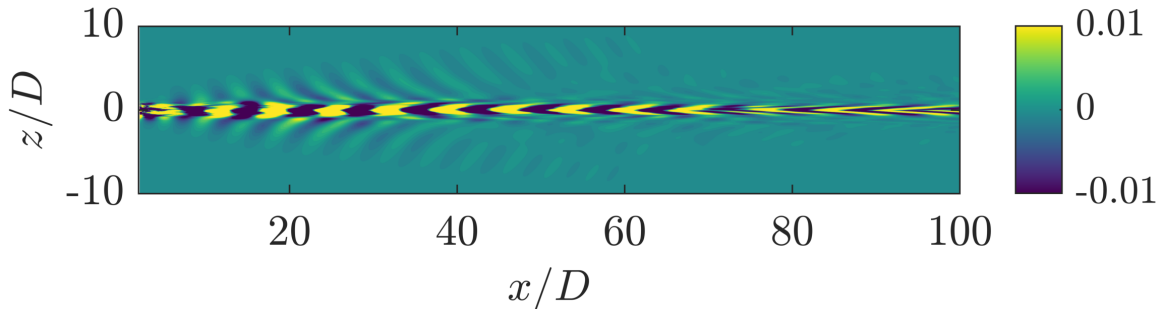

Figure 3.15: Shape of the leading SPOD mode for spanwise velocity, $\Phi_y^{(1)}(x,z,St \approx 0.13; y=0)$ in the center-vertical plane for the $Fr = 2$ wake. Real part of the mode is shown in domain $z,x \in [-10,10] \times [2,100]$.

the presence of a very-low frequency mode (VLF) in the wake (Grandemange et al., 2013, Rigas et al., 2014). For the SPOD, we partitioned the full set of snapshots (spanning $T \approx 700D/U_\infty$) into blocks with $N_{freq} = 512$ entries. This corresponds to time windows of $T = 46D/U_\infty$ and $54D/U_\infty$ for the $Fr = 2$ and 10 wakes respectively. While these durations are sufficient to resolve the VS mode, they are significantly smaller than resolution requirements for the VLF mode which resides at the timescale $T \sim O(10^3 D/U_\infty)$. Hence it is possible that the asymmetry in the leading modes at the VS frequency is a consequence of the VLF mode combined with limited time window of SPOD blocks. Computations with each block spanning $T \sim 1000D/U_\infty$ while desirable, are outside the scope of this work and available computing resources.

To analyze the streamwise coherence of the leading SPOD eigenmode at the VS frequency, we conduct an additional SPOD analysis for the $Fr = 2$ wake, using the fluctuating density and velocity fields, at the center-vertical plane ($y = 0$). Specific details of this SPOD analysis are mentioned towards the end of section 3.3.2. The SPOD eigenspectrum (not shown here for brevity) shows a broad peak at $St \approx 0.13$.

Figure 3.15 shows the spatial structure of the spanwise component of the leading SPOD mode at $St \approx 0.13$. The VS mode appears to be strongly coherent in the streamwise direction with a wavelength of $\lambda/D \approx 1/St_{VS}$. It has two distinctive features: (i) emergence of a well-defined IGW signature beyond $x/D \approx 20$ and (ii) gradual transition of the opposite signed lobes into

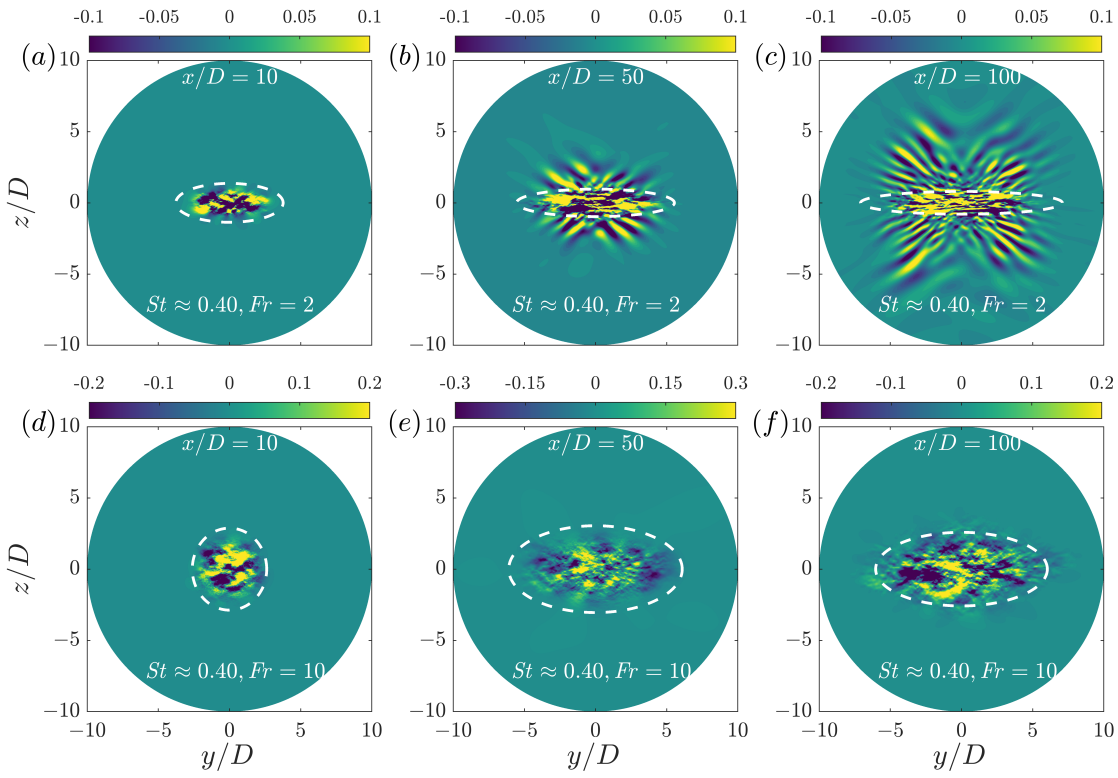

Figure 3.16: Shape of the 15^{th} SPOD mode (real part corresponding to $\lambda^{(15)}$) at $St = 0.40$ for spanwise velocity, $\Phi_y^{(15)}(y,z,St;x/D)$. Dashed closed curve in white shows the wake core.

V-shaped structures as the wake progresses downstream. These structures get progressively thinner and shallower (with respect to x axis) as x/D increases.

3.7.2 Spatial structure of high *St*, high *n* eigenmodes

To contrast the structure of less energetic SPOD eigenmodes with the dominant SPOD eigenmodes, the u_y eigenmode at $n = 15$ and $St = 0.40$ is plotted in figure 3.16 at the same downstream locations of $x/D = 10, 50$, and 100 considered previously. It should be noted that these SPOD modes have low energy, $O(10^{-2})$ that of the dominant SPOD modes. Visual inspection shows that the spatial coherence in the wake core, which is a characteristic of dominant SPOD modes, is lost for the the high-n and high-St modes similar to the result in the snapshot POD study of Diamessis et al. (2010). For both $Fr = 2$ and 10 wakes, $\Phi_y^{(15)}(y,z,St = 0.40)$

in the wake core is dominated by small-scale turbulence. For the $Fr = 2$ wake, the distinct layered structure found in the leading VS eigenmodes at $x/D = 50$ and 100 is absent in the low-energy mode at the same locations. Nevertheless, buoyancy-induced anisotropy is evident at $Nt \geq 5$ in both wakes even in these low-energy modes with high n and St. Moreover, the $\Phi_y^{(15)}(y,z,St \approx 0.40)$ mode also shows IGWs in the outer wake at $x/D = 50$ and 100 in the $Fr = 2$ wake (figure 3.16(b,c)), albeit with smaller wavelength than for the VS mode. Contrary to the $Fr = 2$ wake, the $\Phi_y^{(15)}(y,z,St = 0.4)$ mode for the $Fr = 10$ wake does not show any IGW in figure 3.16(e,f).

3.8 Reconstruction using SPOD modes

In this section, we demonstrate the effectiveness of SPOD modes in reconstructing the following turbulence statistics: (i) turbulent kinetic energy (TKE), $\langle u_i' u_i' \rangle / 2$, (ii) lateral production $\mathcal{P}_{xy} = \langle -u_x' u_y' \rangle \partial \langle U \rangle / \partial y$, and (iii) buoyancy flux $\mathcal{B} = \langle -\rho' u_z' \rangle / Fr^2$. The reconstruction from SPOD modes is performed as follows:

$$\mathrm{TKE}(x;y,z) = \frac{1}{2} \sum_{n=1}^{\Lambda} \sum_{St=-St_r}^{St=St_r} \lambda^{(n)}(x;St)\, \Phi_i^{(n)}(x;y,z,St)\, \Phi_i^{(n)*}(x;y,z,St), \tag{3.22}$$

$$\mathcal{P}_{xy}(x;y,z) = \sum_{n=1}^{\Lambda} \sum_{St=-St_r}^{St=St_r} -\lambda^{(n)}(x;St)\, \Phi_x^{(n)}(x;y,z,St)\, \Phi_y^{(n)*}(x;y,z,St) \frac{\partial \langle U \rangle}{\partial y}, \tag{3.23}$$

$$\mathcal{B}(x;y,z) = \frac{1}{Fr^2} \sum_{n=1}^{\Lambda} \sum_{St=-St_r}^{St=St_r} -\lambda^{(n)}(x;St)\, \Phi_\rho^{(n)}(x;y,z,St)\, \Phi_z^{(n)*}(x;y,z,St). \tag{3.24}$$

In $(3.22) - (3.24)$, the values of Λ and St_r determine the set of modes used for reconstruction. The so-obtained turbulence statistics vary spatially in spanwise and vertical directions for different x/D.

Throughout this section, two sets of low-order truncation are used for reconstruction: (i)

$n \leq 5$, $|St| \leq 0.20$ (R1) and (ii) $n \leq 15$, $|St| \leq 0.40$ (R2). While the R1 truncation primarily takes the VS mode into account for both wakes, R2 also accounts for some of the low-energy modes which reside at relatively higher n and St. It should be noted that R1 and R2 set of modes account for approximately 0.7% and 4.34% of the total SPOD modes in both wakes.

Figure 3.17 compares the reconstructed TKE with its actual value for the $Fr = 2$ wake at $x/D = 20, 50$, and 100. The actual TKE decays in magnitude, expands horizontally, and narrows vertically with increasing x/D. At $x/D = 50$ and 100, the TKE contours display horizontal layering. At all three locations, reconstruction using the R1 set of modes (middle column) gives a fairly accurate estimate of the shape and spatial extent of the TKE contour. The layering at $x/D = 50$ and 100 is also captured by the R1 reconstruction. These layers were also present in the reconstruction using only $n = 1$ and $|St| \leq 0.2$ modes (not shown here), indicating the low-rank nature of layering in stratified wakes. On further increasing $[n, St]$ as in the R2 reconstruction (right column), the overall shape and structural features of the reconstructed TKE remain unchanged, while the magnitude increases, particularly at intense TKE locations, increasing the overall accuracy. It can also be ascertained visually that the accuracy of R1 and R2 increases with downstream distance pointing to the increasing coherence of the wake as it progresses downstream.

Figure 3.18 pertains to the reconstruction of the lateral production $\mathcal{P}_{xy}$ in the $Fr = 2$ wake. We limit ourselves to the lateral component since it dominates its vertical counterpart after the onset of buoyancy induced suppression of vertical turbulent motions (Brucker and Sarkar (2010), de Stadler and Sarkar (2012), Redford et al. (2015)). In the IST and SST regimes of the disk wake, P_{xy} is the dominant component of turbulent production. The actual $\mathcal{P}_{xy}$ (left column) shows two off-axis lobes of intense production primarily located near the horizontal center plane ($z/D = 0$). With increasing x/D, these lobes flatten owing to buoyancy. With respect to the lateral production, the R1 and R2 set of modes capture the spatial distribution accurately for the $Fr = 2$ wake as shown in the middle and right column of figure 3.18, respectively. Although SPOD modes are

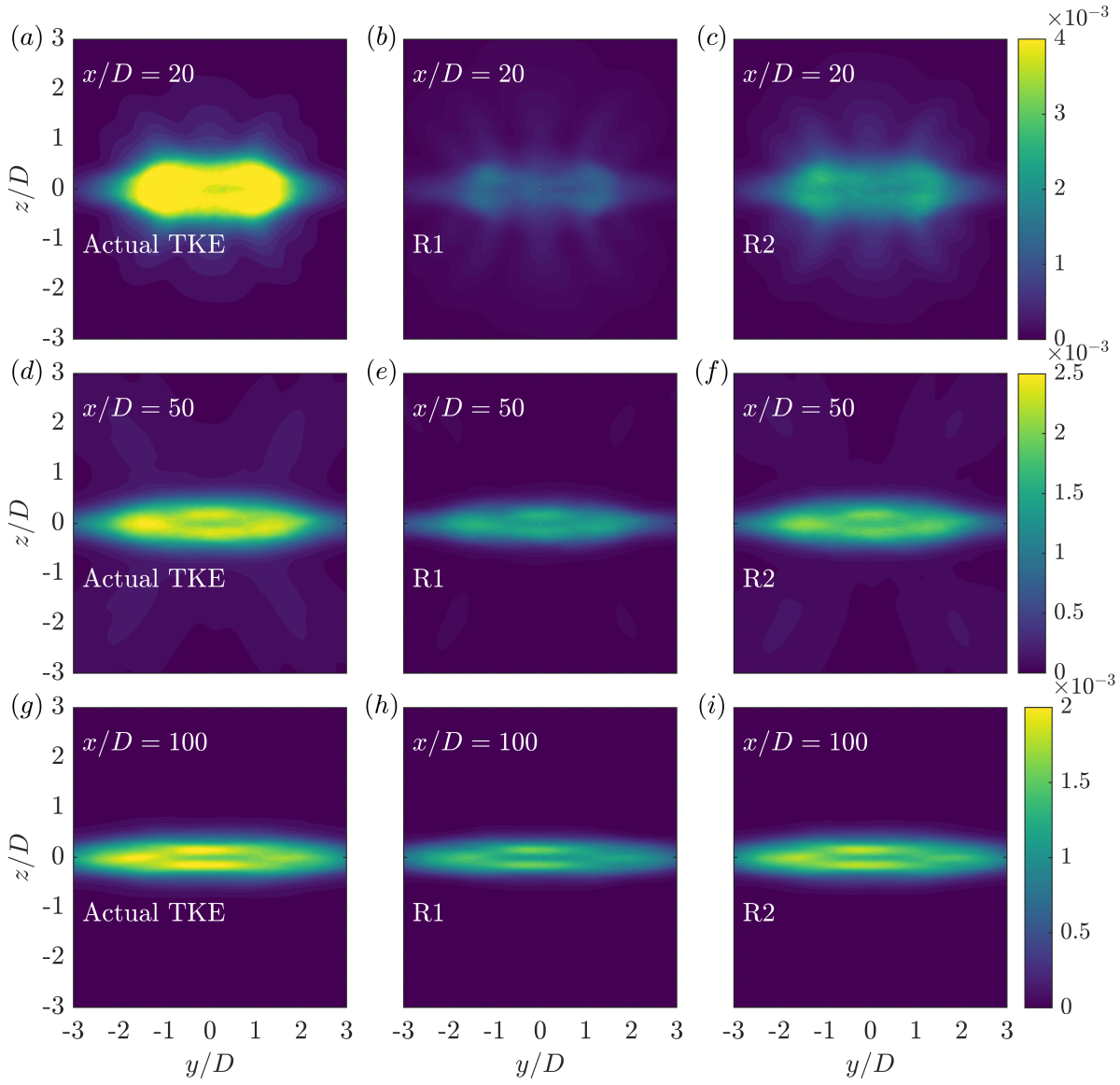

Figure 3.17: Contours of TKE for the $Fr = 2$ wake obtained from temporal averaging (left column), reconstruction from R1 set of modes (middle column), and reconstruction from the R2 set of modes (right column). Three streamwise locations $x/D = 20, 50$, and 100 are shown.

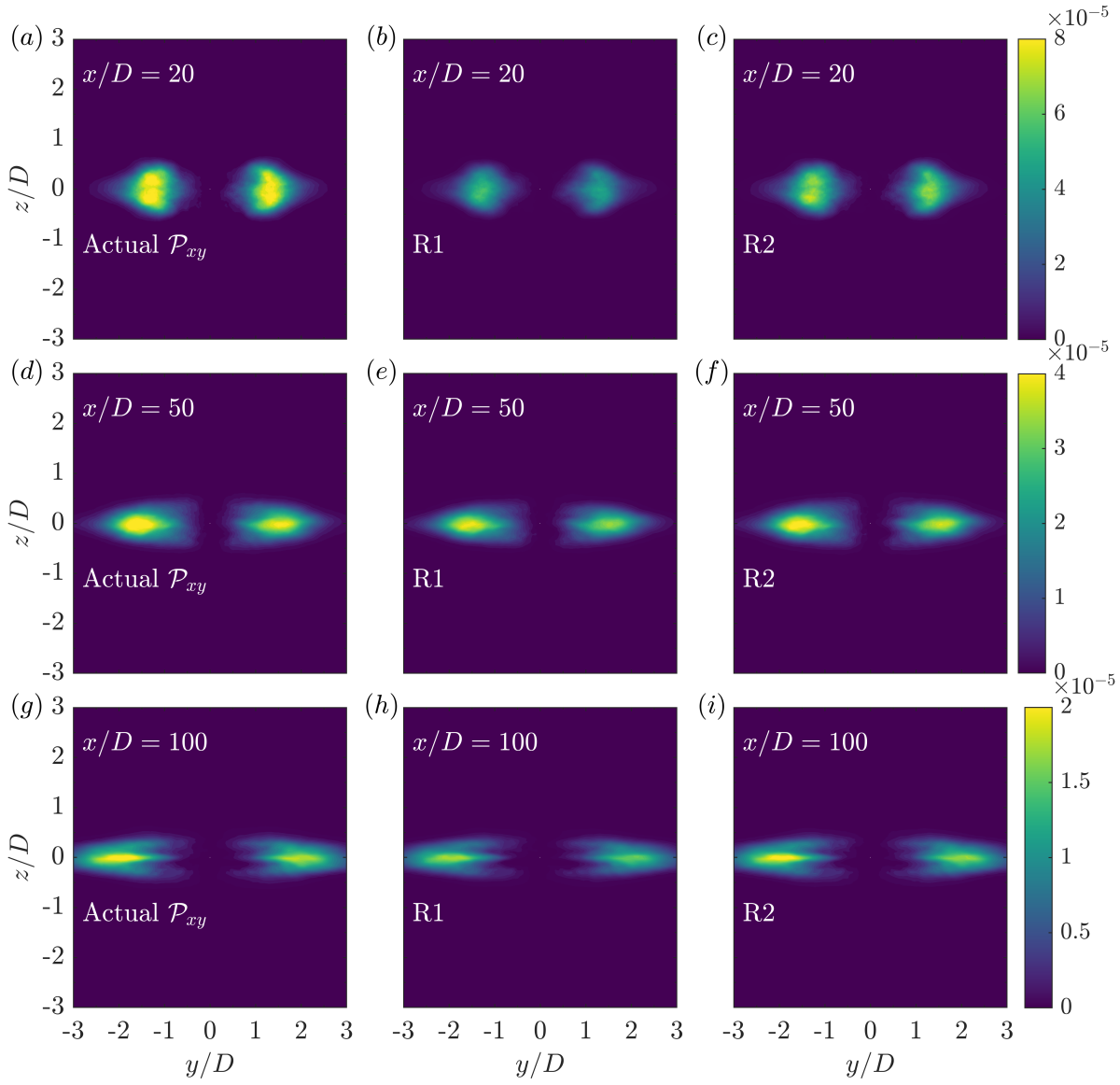

Figure 3.18: Contours of $\mathcal{P}_{xy}$ for the $Fr = 2$ wake obtained from temporal averaging (left column), reconstruction from R1 set of modes (middle column), and reconstruction from R2 set of modes (right column). Three streamwise locations $x/D = 20, 50$, and 100 are shown.

optimal for capturing the area-integrated sum of $\langle u_i' u_i' \rangle$ and $\langle \rho' \rho' \rangle / Fr^2$ by construction, we find that these modes provides an excellent low-order approximation for the production too.

Finally, we explore the effectiveness of buoyancy flux ($\mathcal{B}$) reconstruction in figure 3.19. Unlike TKE and $\mathcal{P}_{xy}$, $\mathcal{B}$ is not a same-signed quantity in the turbulent wake, as can be seen from figure 3.19(a,d,g). The R1 reconstruction of $\mathcal{B}$ (middle column) accurately captures the structural features of $\mathcal{B}$ at all locations: (i) layers of positively and negatively signed $\mathcal{B}$ at $x/D = 50$, 100, and (ii) IGWs in the outer wake which carry significant $\mathcal{B}$ at $x/D = 20$ and 50. On closer inspection, the R1 truncation is found to underpredict the strength of $\mathcal{B}$ in these outer regions with intense buoyancy flux. Including higher St and n modes for reconstruction, as done for R2, significantly improves the quality as shown in the right column.

The reconstruction trends of these statistical quantities are also investigated for the $Fr = 10$ wake, but are not shown here for brevity. Qualitatively, the trends are similar to that of the $Fr = 2$ wake, wherein the R1 set captures the structural features of these quantities very satisfactorily. Further addition of high-n and high-St modes in the R2 truncation improves the quantitative prediction of these statistics, particularly in the region where they are found to be intense in the actual data.

To conclude this section, the streamwise variations of the wake-core-integrated TKE and $\mathcal{P}_{xy}$ for the $Fr = 2$ and $Fr = 10$ wakes are shown in figure 3.20. The corresponding variation for $\mathcal{B}$ is not shown here as it fluctuates between small positive and negative values, unlike TKE and $\mathcal{P}_{xy}$ which decay monotonically with x/D.

For the $Fr = 2$ wake, wake core TKE shows two distinct decay rates: (i) TKE $\sim x^{-1.11}$ in the IST regime spanning $10 \leq x/D \leq 40$ ($5 \leq Nt_2 \leq 20$) and (ii) TKE $\sim x^{-0.30}$ in the SST regime spanning $60 \leq x/D \leq 100$ ($30 \leq Nt_2 \leq 50$). The quality of TKE reconstruction improves monotonically from R1 to R2 at all downstream locations for both wakes, as is observed in figure 3.20(a,b). For $Fr = 2$, the TKE contained in the R1 set of modes stays approximately constant for $x/D \geq 40$ (figure 3.20(a)). It is only after high-St and high-n modes are added, as in R2, that

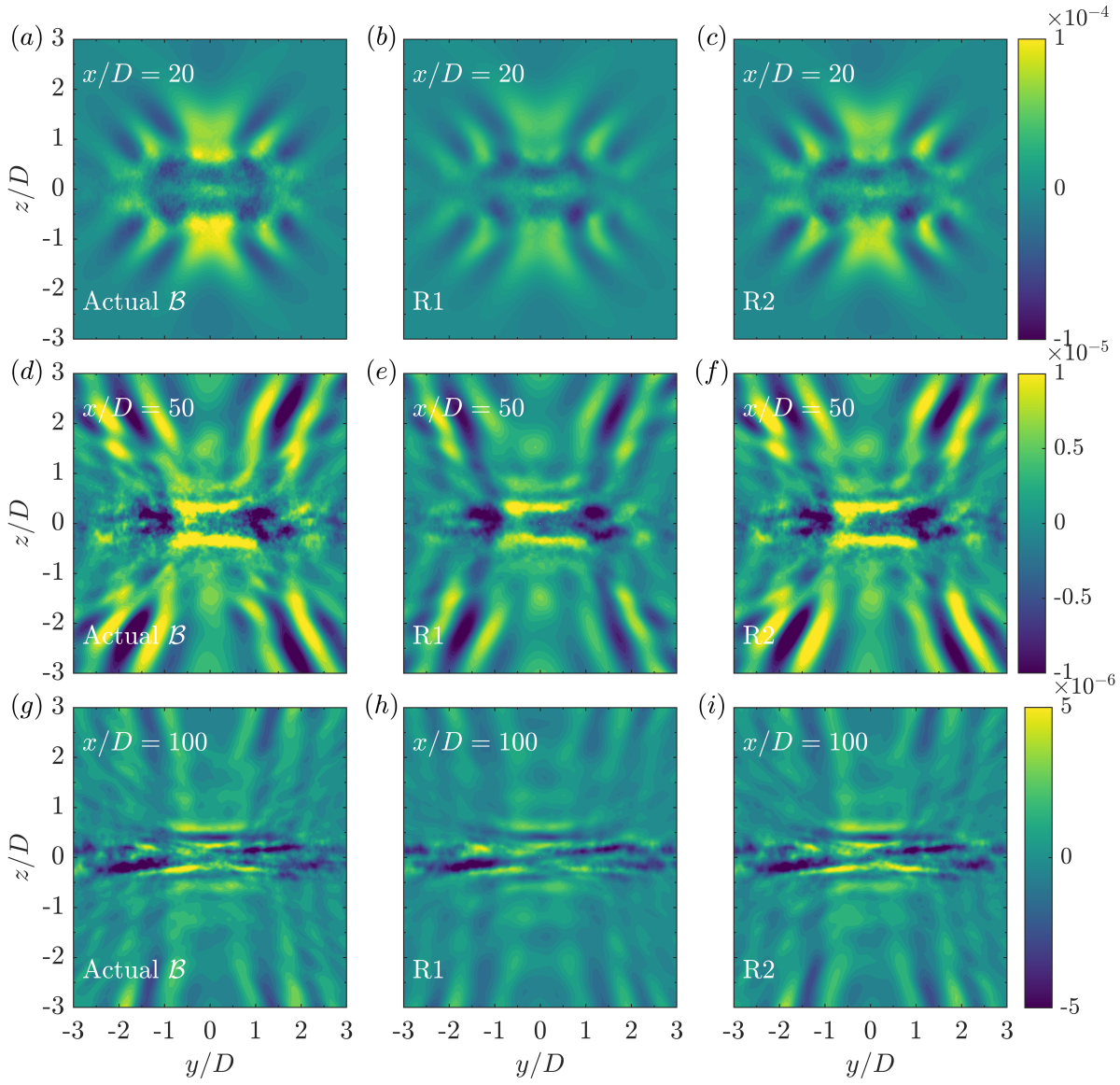

Figure 3.19: Contours of $\mathcal{B}$ for the $Fr = 2$ wake obtained from temporal averaging (left column), reconstruction from R1 set of modes (middle column), and reconstruction from R2 set of modes (right column). Three streamwise locations $x/D = 20, 40$, and 100 are shown.

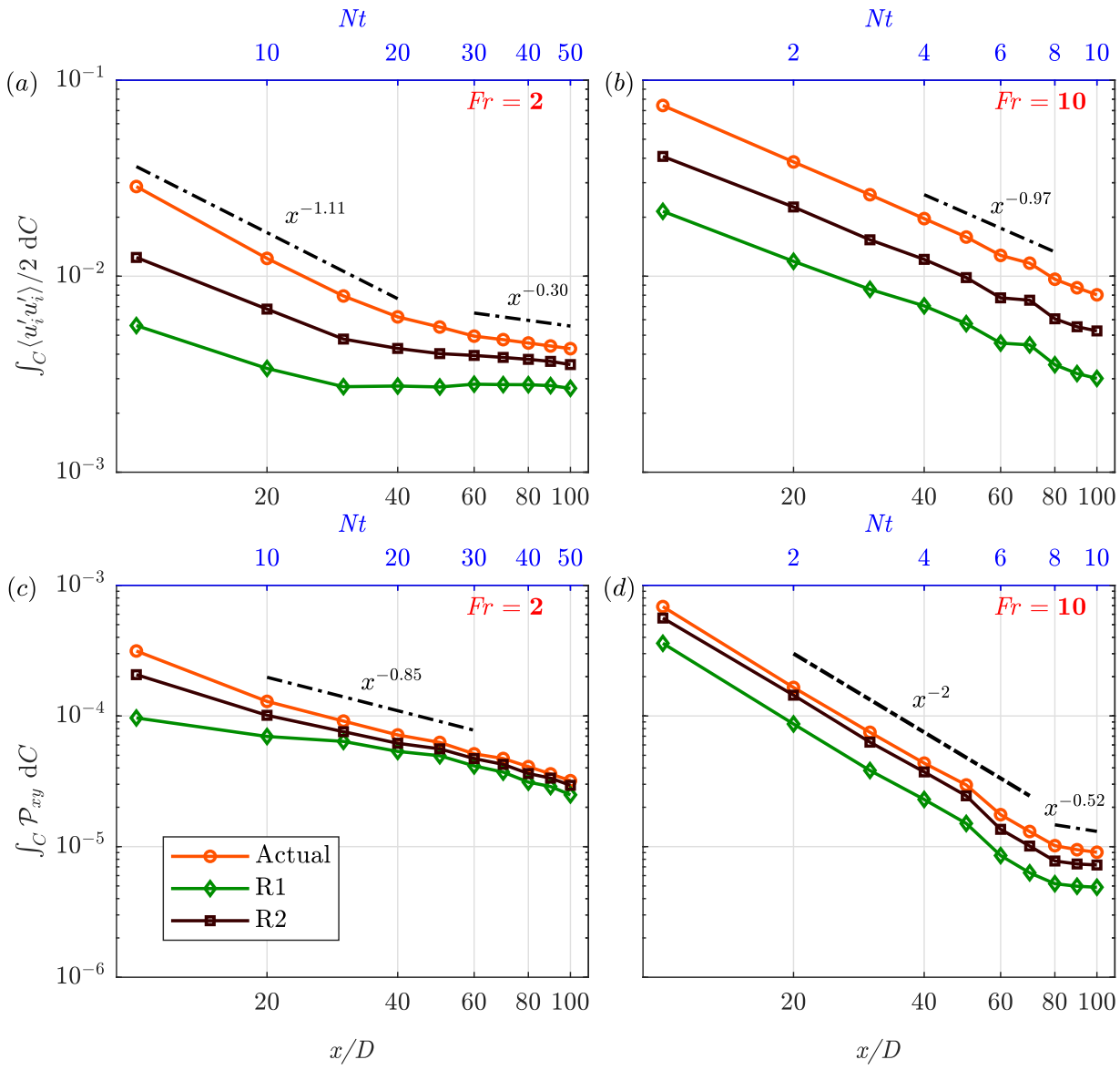

Figure 3.20: Streamwise variation of wake core TKE and $\mathcal{P}_{xy}$ reconstructed from R1 and R2 truncations: (a) TKE for $Fr = 2$, (b) TKE for $Fr = 10$, (c) $\mathcal{P}_{xy}$ for $Fr = 2$, and (d) $\mathcal{P}_{xy}$ for $Fr = 10$. Here, $\int_C (.) \, \mathrm{d}C$ denotes the integration in the wake core.

the reconstructed TKE follows the decay rate of actual TKE. Reconstructed TKE from further lower-order truncations (not shown here), i.e., with lesser n and St than in R1, showed an increase in wake core TKE at large x/D, opposite to the decrease in the actual value. For the $Fr = 10$ wake, reconstruction from low-order truncations decay quite similar to the actual TKE (figure 3.20(b)).

The accuracy of R1 and R2 increase approximately three-folds and two-folds from $x/D = 10$ to 100 for the TKE reconstruction in the $Fr = 2$ wake, suggesting development of low-rank dynamics in the $Fr = 2$ wake. By $x/D = 100$, R1 and R2 modes capture $\approx 63\%$ and $\approx 82\%$ respectively of the wake core TKE for $Fr = 2$. On the other hand, the reconstruction quality of the moderately stratified $Fr = 10$ wake changes only slightly from $x/D = 10$ to 100 for both low-order truncations: (i) TKE in R1 modes changes from $\approx 29\%$ of total TKE at $x/D = 10$ to $\approx 38\%$ at $x/D = 100$ and (ii) TKE in R2 modes change from $\approx 45\%$ to $\approx 55\%$ between $x/D = 10$ and 100.

Figure 3.20(c,d) show the reconstruction trends for wake core $\mathcal{P}_{xy}$ term in the $Fr = 2$ and 10 wakes, respectively, along with its actual variation obtained from temporal averaging (shown in red). The wake core $\mathcal{P}_{xy}$ for $Fr = 2$ decays as $x^{-0.85}$ throughout the spatial domain under consideration (figure 3.20(c)). Both R1 and R2 provide very good reconstruction of $\mathcal{P}_{xy}$ beyond $x/D \approx 30$ and exhibit better approximations relative to that for TKE. With its additional modes, R2 follows the behavior of the actual value of $\mathcal{P}_{xy}$ very closely. The wake core $\mathcal{P}_{xy}$ for the $Fr = 10$ wake shows a faster decay rate of x^{-2} in $10 \leq x/D \leq 70$ (figure 3.20(d)). Beyond $x/D \approx 80$, it decays at a slower rate of $x^{-0.52}$. Similar to the $Fr = 2$ wake, R2 reconstructs the actual wake core $\mathcal{P}_{xy}$ very well.

The visually good reconstruction of $\mathcal{P}_{xy}$ by the R2 set of modes can be quantified for both wakes. At $x/D = 10$ and 100, R2 already accounts for $\approx 66\%$ and $\approx 92\%$ of the actual $\mathcal{P}_{xy}$, respectively, for the $Fr = 2$ wake. For the $Fr = 10$ wake, the R2 set of modes capture $\approx 80\%$ of the actual $\mathcal{P}_{xy}$ at both $x/D = 10$ and 100. The SPOD modes provide a better low-order truncation

for the lateral production as compared to the TKE for both wakes. This is similar to the trend observed by Nidhan et al. (2020) for the unstratified wake at same Re.

3.9 Discussion and conclusions

In this study, we have extracted and analyzed coherent structures in the stratified turbulent wake of a disk using spectral POD (SPOD). Body-inclusive LES databases from Chongsiripinyo and Sarkar (2020) (referred to as CS2020) at $Re = 5 \times 10^4$ and $Fr = 2, 10$ are used in this study. Streamwise distance spanning $10 \leq x/D \leq 100$ is analyzed for both wakes. The obtained SPOD eigenvalues ($\lambda^{(n)}$) are a function of modal index (n), frequency (St), and streamwise distance (x/D). By construction, SPOD modes have the following properties: (i) coherence in both space and time, (ii) optimal capture of the area-integrated total fluctuation energy, summed over kinetic and potential energy components, and (iii) ordering such that the energy content (given by $\lambda^{(n)}$) decreases with increasing n for a given $(x/D, St)$. To the best of the authors' knowledge, this is the first numerical study utilizing SPOD and body-inclusive simulation data together to uncover the dynamics of coherent structures in high-Re stratified wakes.

Q criterion and vorticity visualizations of both $Fr = 2$ and 10 wakes give a qualitative indication of the prevalence of large-scale coherent structures in these wakes. SPOD analysis reveals their dominance, namely, the first five ($n = 1$ to 5) modes, summed across all resolved St, capture around 60% of the total fluctuation energy in both wakes. Likewise, most of the contribution to the total energy comes from SPOD modes with $St < 1$ in both wakes. Contrary to the unstratified wake, the coherence in the stratified wakes increases with x/D. This is observed in both n and St variation of the SPOD eigenvalues, wherein the relative contribution of the low n and St eigenvalues increases with x/D. This increase in coherence is found to be more pronounced in the $Fr = 2$ wake compared to the $Fr = 10$ wake. Interestingly, the transitions between different turbulence regimes (WST, IST, and SST) in these wakes, discussed in detail by

CS2020, are also reflected in the n and St variations of the SPOD eigenvalues.

SPOD eigenspectra of both wakes at downstream locations ranging from the near to the far wake uncover a prominent spectral signature of the vortex shedding (VS) mechanism at $St \approx 0.11 - 0.13$. Both wakes exhibit a low-rank behavior in the vicinity of the vortex shedding frequency at all locations analyzed here, i.e. the leading modes have significantly higher energy content than the sub-optimal modes ($n > 2$). While previous experimental studies of Lin et al. (1992b) and Chomaz et al. (1993) have shown the existence of the VS phenomenon in stratified wakes using qualitative visualizations and measurements of spectra at a few locations, SPOD enables us to objectively isolate and quantify the VS mechanism by providing the optimal decomposition of the two-point two-time cross-correlation matrix.

We also find that the $Fr = 2$ wake exhibits the slowest decay of the energy at the VS frequency, followed by the $Fr = 10$ and ∞ wakes, respectively. To further analyze this trend, the energy in the leading 15 SPOD modes is partitioned between the wake core and outer wake region for $(x/D, St)$ pairs. The outer wake in the $Fr = 2$ case shows significantly elevated energy levels during $8 \leq Nt_2 \leq 40$ ($16 \leq x/D \leq 80$) with a strong spectral peak at the VS frequency. On the other hand, the outer-wake energy at $Fr = 10$ remains negligible till $x/D = 60$ ($Nt_{10} = 6$) and increases monotonically thereafter, again with a spectral peak at $St \approx 0.13$ (the VS frequency). Additional SPOD analyses of the $Fr = 2$ wake using fluctuating pressure and velocity components show that the frequencies in the vicinity of the VS mechanism contribute significantly to energy transfer from the wake core turbulence to the IGWs in the outer wake region, establishing a firm causal link between the VS mode and unsteady IGW generation in stratified wakes. It is also noteworthy that the outer-wake energy constitutes up to 50% of the total cross-section energy at the point where its contribution to the total energy peaks in the $Fr = 2$ wake.

In their recent temporally evolving simulations, Rowe et al. (2020) found that the most energetic IGWs were generated during $10 \leq Nt \leq 25$. They analyzed the instantaneous power extracted from the wake core at high Re and varying Fr. Other works employing a temporal

model for the wake (Abdilghanie and Diamessis (2013), de Stadler and Sarkar (2012))have also found strong IGW activity in the range of $20 \leq Nt \leq 70$. In our SPOD analysis, the results are in qualitative agreement with the findings of these temporal model studies. However, the temporal simulations were not able to capture the vortex shedding mechanism. Also, the IGW energy appears in the outer wake at $Nt = 6-8$ in the present simulation, which is somewhat earlier than in the previous studies. The current results expand our knowledge by establishing that it is the VS mode in bluff-body wakes which links the wake core to the outer region of IGW activity in the NEQ wake, at least up to $x/D = 100$.

The visualizations of spatial structures of the leading SPOD eigenmodes at the VS frequency reveal layering in the wake core of the $Fr = 2$ case beyond $x/D \geq 30$. The layering in the stratified wake core, although consistent with the finding of Spedding (2002b), has notable differences. Spedding (2002b) found that the number of layers increases once the sphere wake reached the Q2D regime at $Nt \approx 50$, contrary to the present results where the increase happens between $Nt_2 = 15$ and 50. Spedding (2002b) also hypothesized that the vertical layers become decorrelated at late times (between $50 < Nt < 100$). In the present results, we see that vertical layers correspond to well-defined coherent structures (coherent in the $y-z$ plane) at late x/D locations, captured in the respective leading SPOD eigenmodes at $St \approx 0.13$, implying that the layering found here connects to the body-generated VS mechanism. We also analyze the leading eigenmode of the VS frequency at the center-vertical ($y = 0$) plane, finding that the VS mode is correlated in the streamwise direction throughout the domain. Far from the disk, it organizes into V-shaped structures which progressively get shallower and thinner. These V-shaped structures were previously identified by Chongsiripinyo et al. (2017) in the instantaneous visualizations of sphere wake at a lower $Re = 3700$. Utilizing SPOD, we show that these structures are a robust feature of the flow even at higher Re and reside at the VS frequency.

We also find that SPOD modes provide an efficient reconstruction of second-order statistics that are important in stratified wakes: (i) TKE, (ii) lateral production ($\mathcal{P}_{xy}$), and (iii) buoyancy

flux ($\mathcal{B}$). The spatial distribution of all three statistics is captured satisfactorily even with a few energetic SPOD modes ($n \leq 5$ and $St \leq 0.2$). Inclusion of additional SPOD modes with higher n and St further increases the accuracy of the reconstruction. Between $Fr = 2$ and 10, we find that reconstruction accuracy is better for the strongly stratified $Fr = 2$ wake. Furthermore, we also find that $\mathcal{P}_{xy}$ shows significantly better reconstruction than TKE. This was also observed in the reconstruction trends of the unstratified wake at the same Re by Nidhan et al. (2020). Thus, similar to the $Fr = \infty$ wake, it is only a significantly small set of SPOD modes in the stratified wake that interact with the mean shear, although a larger set of modes is required to reconstruct TKE. These are primarily the large-scale coherent structures which are captured by SPOD modes in the limit of low n and St.

Overall, SPOD turns out to be a very effective technique in isolating space-time coherent structures and establishing that they have a strong link to various distinctive features of turbulent stratified wakes. SPOD as well as other modal decomposition techniques (e.g., resolvent analysis) have been extensively used in other flow configurations to construct reduced-order models and shed light on various aspects of those flows. However, applications to stratified flows, particularly wakes, are relatively scarce. In the future, further studies of stratified wakes using different modal decomposition techniques will surely help in advancing our understanding of these flows and our ability to efficiently model them.

3.10 Acknowledgments

Chapter 3 is a reprint of the material in the article: S. Nidhan, O. T. Schmidt, and S. Sarkar, “Analysis of coherence in turbulent stratified wakes using spectral proper orthogonal decomposition”, Journal of Fluid Mechanics, 934:A12 (2022). The dissertation author was the primary investigator and author of this work.

Chapter 4

The high-*Re* stratified wake of a slender body and its comparison with a bluff body wake

4.1 Introduction

Due to their low drag coefficients, slender bodies are extensively used in aerospace and naval applications. Multiple studies have described the flow around these bodies focusing on the drag force, the boundary layer, and the flow separation (Chesnakas and Simpson, 1994, Constantinescu et al., 2002, Costis et al., 1989, Fu et al., 1994, Wang, 1970, Wang et al., 1990, Wikström et al., 2004). However, despite their presence in many underwater applications, only a few works have looked into the wake of a slender body (Chevray, 1968, Jiménez et al., 2010, Kumar and Mahesh, 2018) and, only recently, the far wake of a slender body has been studied (Ortiz-Tarin et al., 2021).

The near wake of a slender body with a turbulent boundary layer (TBL) is characterized by having a small recirculation region. The recirculation region is surrounded by a ring of

small scale turbulence that emerges from the boundary layer and does not show strong vortex shedding (Jiménez et al., 2010, Kumar and Mahesh, 2018, Ortiz-Tarin et al., 2021, Posa and Balaras, 2016). As a result, the wake is thin and develops slowly compared to the wake of bluff bodies. These particular features of the slender body high-*Re* near wake lead to interesting effects further downstream: (i) despite having a smaller drag coefficient than bluff bodies, the defect velocity ($U_d = U_\infty - U$) of the slender body wake can be larger than that of a bluff body for a long downstream distance, (ii) the turbulent kinetic energy of the wake shows an off-center radial peak at the location where the turbulent boundary layer separates – instead of a Gaussian profile with a central peak, and (iii) helical instabilities come into play only in the intermediate and far field of the wake. These particularities affect the scaling laws of the wake. In a domain spanning $80D$ the defect velocity, the kinetic energy, and the dissipation do not follow the classic high-*Re* scaling and they decay differently than bluff body wakes (Ortiz-Tarin et al., 2021) exhibiting a non-equilibrium scaling of dissipation (Dairay et al., 2015, Vassilicos, 2015).

The few studies that look into slender body wakes assume that the body moves in an unstratified environment, where the density of the surrounding fluid is constant. However, in a realistic underwater marine environment the effect of density stratification due to salinity and temperature can become relevant. Density stratification suppresses vertical motions, triggers the formation and sustenance of coherent structures, and leads to the radiation of internal gravity waves. More importantly, in a stratified environment, the wake of a submersible lives longer than in an unstratified environment, i.e., it takes more time for the flow disturbance to die out (Spedding, 2014). The study of stratified wakes has been nearly exclusively focused on the flow past bluff bodies (Chomaz et al., 1992, Hanazaki, 1988, Lin and Pao, 1979, Lin et al., 1992b, Orr et al., 2015, Pal et al., 2017) and underwater topography (Baines, 1998, Castro et al., 1983, Drazin, 1961). Here, we study the influence of stratification on the high-*Re* wake of a prolate spheroid with a turbulent boundary layer.

The strength of ambient stratification is measured by the body-based Froude number

$Fr = U_\infty/ND$. This is the ratio between the convective frequency of the flow, U_∞/D – where U_∞ is the freestream velocity and D the diameter of the body – and the buoyancy frequency N. In the wake of ocean submersibles, $Fr \sim O(1-10^2)$. However, since the velocity deficit in the wake $U_d(x)$ decays with the streamwise distance and the wake width $L(x)$ increases, the Froude number defined with local variables $Fr_l = U_d/NL$ decreases as the flow evolves. Thus, even in a weakly stratified environment, eventually all wakes are affected by stratification.

Since the relative strength of stratification increases locally as the flow develops, the evolution of the stratified wake is multistage in nature. Based on the measurements of U_d and L in high-Fr (i.e. initially weak stratification) bluff body wakes, Spedding (1997) identified three regimes in stratified wake evolution based on the power-law decay rates of U_d. These regimes are generally identified by empirically fitting decay rates to U_d in different temporal (or spatial) regions and are as follows:

1. Three-dimensional (3D) regime: Close to the generator, wake decay is similar to the unstratified wake of the corresponding body shape. This is the so-called 3D regime and lasts until the buoyancy time defined by $Nt = Nx/U = x/D \cdot 1/Fr$ approaches $O(1)$, equivalently until $x/D \sim Fr$.

2. Non-equilibrium (NEQ) regime: As the wake evolves, buoyancy effects become progressively stronger. The decay of U_d slows relative to the 3D regime and, furthermore, anisotropy between the vertical and horizontal velocity components increases. Spedding (1997) reported this non-equilibrium (NEQ) region to last for $Nt \approx 2-50$. Later, temporal simulations of Brucker and Sarkar (2010) and Diamessis et al. (2011) found an increase in the span of the NEQ regime at higher Reynolds numbers. $U_d \sim x^{-0.25\pm0.04}$ during the NEQ regime according to Spedding (1997). However, there has been some variability in the observed NEQ decay rate in later studies. Bonnier and Eiff (2002) reported a NEQ regime with $U_d \sim x^{-0.38}$ for $1.5 < Fr < 5$. Brucker and Sarkar (2010) and Diamessis

et al. (2011) reported $U_d \sim Nt^{-1/4}$ during the NEQ regime in their temporal simulations. Chongsiripinyo and Sarkar (2020) found that $U_d \sim x^{-0.18}$ during the NEQ regime of their $Fr = 2$ and 10 disk wakes. For wakes with $Fr \sim O(1)$, the NEQ decay rate is preceded by a pronounced oscillatory modulation in U_d which is linked to lee waves (Chongsiripinyo and Sarkar, 2020, Ortiz-Tarin et al., 2019, Pal et al., 2017).

3. Quasi two-dimensional (Q2D) regime: After the NEQ regime, the stratified wake enters into the quasi two-dimensional regime (Q2D regime). The Q2D regime is characterized by transition in the U_d power law to a significantly increased decay rate, e.g. Spedding (1997) reports a transition to $U_d \sim x^{-3/4}$. In the Q2D regime, the wake progressively organizes into vortices that meander primarily in the horizontal plane (Brucker and Sarkar, 2010, Dommermuth et al., 2002, Gourlay et al., 2001) and take the form of 'pancakes'. Although the wake motion in this regime is primarily in the horizontal plane, there is a variability in the vertical direction in the form of layers (Spedding, 2002a), hence the prefix 'quasi'.

In recent literature, stratified wakes have been characterized using turbulence features (Chongsiripinyo and Sarkar, 2020, Zhou and Diamessis, 2019) instead of the U_d-based criteria of Spedding (1997). These studies are motivated by an attempt to connect buoyancy-related wake transitions to the broader stratified turbulence field.

Notice that the arrival of the wake into each of the three stages in its evolution depends on the value of Nt, which is equivalent to a downstream distance of x/Fr from the wake generator. At high Froude number, the downstream distance required to reach the NEQ and Q2D regions can become very large. Consequently, the size of the computational domain required to access these regimes rapidly becomes computationally unfeasible. To circumvent these limitation temporal simulations were used in the study of Gourlay et al. (2001). Temporal simulations use a reference frame moving with the wake where time correlates with streamwise distance in a fixed reference frame. By assuming that the streamwise development of the flow is slow, periodic boundary

conditions can be used and the equations are advanced in time without the need of introducing the wake generator. This reduces the computational cost significantly. Most of the studies that have contributed to our current understanding of stratified wakes use temporal simulations (Abdilghanie and Diamessis, 2013, Brucker and Sarkar, 2010, de Stadler and Sarkar, 2012, Diamessis et al., 2011, Dommermuth et al., 2002, Gourlay et al., 2001, Redford et al., 2015, Rowe et al., 2020).

The main drawback of the temporal model is the influence of its initialization. Since the flow at the wake generator is not solved, the starting profiles of the mean and turbulence have to be assumed. These simulations lack some specific features that are generated due to the body, e.g., steady lee waves, near-wake buoyancy effects, and the vortical structures shed from the boundary layer. Even when it is tempting to assume that body specific features are lost far from the body, the universality of the wake decay has remained elusive to experiments (Bevilaqua and Lykoudis, 1978, Redford et al., 2012, Wygnanski et al., 1986), even in unstratified wakes. An alternative to temporal simulations are body inclusive simulations that retain the wake generator dependent features at the expense of a higher computational cost and a limited domain size (Chongsiripinyo et al., 2017, Gola et al., 2022, More and Ardekani, 2020, 2021, More et al., 2021, Nidhan et al., 2019, Orr et al., 2015, Pal et al., 2017).

To the best of authors' knowledge, Ortiz-Tarin et al. (2019) performed the first study of a stratified flow past a slender body that investigates the near and intermediate wake dynamics. Their analyses reveal that at $Fr \sim O(1)$ the type of separation and the subsequent wake establishment is strongly dependent on the characteristic frequency of the lee waves and the aspect ratio of the body. When half the wavelength of the steady lee waves ($\lambda = 2\pi Fr$) matches the length of the slender body (L), the separation of the boundary layer is inhibited by buoyancy effects. Based on this condition, a critical Froude number can be defined $Fr_c = L/D\pi$. When $Fr > Fr_c$ stratification suppresses the generation of turbulence in the near wake, when $Fr \approx Fr_c$ buoyancy strongly limits the flow separation and can lead to a relaminarization of the wake at low Reynolds numbers. Finally, when $Fr < Fr_c$, the lee waves enlarge the separation region and there might be an increase

in the turbulence intensities in the wake. When $Fr \approx Fr_c$ the wake is in a resonant state with both the separation and the wake dimensions being strongly modulated by the steady lee waves (Chomaz et al., 1993, Hunt and Snyder, 1980, Ortiz-Tarin et al., 2019).

As mentioned before, the use of body inclusive simulations has one major limitation, i.e., the high computational cost. Due to the high resolution required to solve the boundary layer of the wake generator, the downstream domain is limited and thus the possibility of looking into the far wake gets significantly restricted, particularly at high Re. VanDine et al. (2018) presented a hybrid spatially-evolving model, which builds on the hybrid temporally-evolving model of Pasquetti (2011), and addresses most of the aforementioned problems. The hybrid method uses inflow conditions generated from a well-resolved body-inclusive simulation to perform a separate temporal simulation in the case of Pasquetti (2011) or spatially-evolving simulation in the work of VanDine et al. (2018) without including the body. By doing so, the amount of required points is substantially reduced since the flow near the body does not have to be resolved. This important reduction of the computational cost allows one to extend the domain farther downstream to gain insight in the far wake.

Here, we use a hybrid method that combines a body-inclusive simulation and a spatially evolving body-exclusive simulation to study the stratified high-Re far wake of a slender body for the first time. The Reynolds number is set to $Re = U_\infty D/\nu = 10^5$ and two levels of stratification are used, $Fr = U_\infty/ND = 2$ and 10. The simulation at $Fr = 10$ allows us to study the evolution of a weakly stratified wake in a domain that spans $80D$. Additionally, $Fr = 2$ is chosen because it is close to the critical Froude number for a 6:1 prolate spheroid $Fr_c = (L/D)/\pi = 6/\pi$. At the critical Froude number, the size of the separation region is strongly reduced by the lee waves (Ortiz-Tarin et al., 2019). These choices also allow us to compare our results with the findings of Chongsiripinyo and Sarkar (2020) (hereafter referred as CS20) regarding the stratified wake of a disk.

In CS20, the stratified wake of a disk at $Re = 5 \times 10^4$ is studied at $Fr = 2, 10, 50, \infty$. Apart

from a detailed analysis of the decay rates of the mean and turbulent quantities, CS20 links the general evolution of stratified homogeneous turbulence (Brethouwer et al., 2007, de Bruyn Kops and Riley, 2019) with the evolution of the wake turbulence. As the disk wake evolves, the influence of buoyancy is 'felt' by the turbulent motions at progressively smaller scales. First the mean flow and the large scales and later the r.m.s. velocities are affected by stratification. Simultaneously, the horizontal eddies start gaining energy. Based on the strength of these effects, three distinct stages can be identified: weakly, intermediate and strongly stratified turbulence. In CS20, the transition between these regimes is examined and parameterized using local Froude and Reynolds numbers. Zhou and Diamessis (2019) also examined these transitions and their link with the evolution of stratified homogeneous turbulence using temporal simulations.

The present work is the continuation of Ortiz-Tarin et al. (2021) – referred to as ONS21 – where the unstratified wake of a 6:1 prolate spheroid with a turbulent boundary layer was studied and compared with a large number of simulations and experiments. In our previous study we found that the particularities of the slender body wake, e.g., small recirculation region, low entrainment, large defect velocity, bimodal distribution of the turbulent kinetic energy, among others affect the wake decay significantly. In this study we are analyzing how these features affect the evolution of the stratified wake. We also analyze the simulations of CS20 to closely compare our results with the stratified bluff body wake.

Some of the questions we want to answer are: do the stratified decay laws and their transition points depend on the shape of wake generator? how does the turbulence evolve in stratified slender body wakes and are there difference with bluff body wakes? how does the phase-space evolution of the stratified turbulence compares between bluff and slender body wakes? In broader terms, we attempt to find whether a turbulent stratified wake retains some imprint of the wake generator in the mean and turbulence evolution.

A description of the solver and the methodology is given in §2. The wakes are visualized in §3. The decay of the mean wake properties is analyzed in §4. Finally, the evolution of

the turbulence and the phase-space analysis of the wake are presented in sections §5 and §6, respectively. The study is concluded in §7.

4.2 Methodology

To study the far wake of a slender body at a high Reynolds number we use a hybrid simulation. The hybrid model combines two simulations: body-inclusive (BI) that solves the flow past the wake generator and body-exclusive (BE) that resolves the intermediate and far wakes. Here, we use a spatially-evolving simulation following the procedure validated by VanDine et al. (2018). In the implementation, data from a selected cross-plane in the BI simulation is interpolated on to a new grid and used as an inlet boundary condition for the BE stage. This procedure allows us to alleviate the natural stiffness of the wake problem. Whereas the BI simulation is designed to capture the turbulent boundary layer and the flow separation, the BE simulation resolves the turbulence in the wake. Both the grid size and the time step required to solve the turbulent boundary layer are much smaller than those needed in the intermediate and far wakes. This method leads to significant savings in computational cost without compromising accuracy.

The setup and the solver here are the ones used in ONS2021 with the addition of stratification. Both simulations solve the three-dimensional Navier-Stokes with the Boussinesq approximation in cylindrical coordinates. The solver uses a third-order Runge-Kutta method combined with second-order Crank-Nicolson to advance the equations in time. Second-order-accurate central differences are used for the spatial derivatives in a staggered grid. A wall-adapting local eddy viscosity (WALE) is used to properly capture the turbulent boundary layer dynamics (Nicoud and Ducros, 1999). Both the BI and BE simulations use Dirichlet boundary conditions at the inflow, convective outflow and Neumann at the radial boundary. Similarly to Ortiz-Tarin et al. (2019) a sponge layer is added to the boundaries to avoid the spurious reflection of gravity waves.

An immersed boundary method (Balaras, 2004, Yang and Balaras, 2006) is used to resolve

the flow past a 6:1 prolate spheroid at zero angle of attack. A numerical bump is introduced on the surface of the body to accelerate the transition of the boundary layer to turbulence. The annular bump is located where the surface favorable pressure gradient is nearly zero. This location is found at approximately $0.5D$ from the nose. The radial extent of the bump is $0.002D$ (~ 15 wall units) and the streamwise extent is $0.1D$.

The stratification is set by a linear background density profile characterized by the Froude number, $Fr = U_\infty/ND$, where N is the buoyancy frequency. Three levels of stratification are simulated: $Fr = 2, 10$ and ∞. $Fr = 2$ is close to the critical Froude number $Fr_c = 6/\pi$ for the 6:1 spheroid at which the suppression of turbulence in the wake by stratification is optimal (Ortiz-Tarin et al., 2019). $Fr = 10$ is a moderate level of stratification closer to oceanic values. Finally $Fr = \infty$ is the unstratified case which will be used as a reference (ONS21).

The cylindrical coordinate system is (x, r, θ) with the origin at the body center. For convenience, the Cartesian coordinate system (x, y, z) will also be used, where z is the vertical direction aligned with gravity, y is the spanwise direction, and x is the streamwise direction.

The BI grid is designed to resolve the turbulent boundary layer and the small-scale wake turbulence. The turbulent boundary layer is resolved with $\Delta x^+ = 40$, $\Delta r^+ = 1$, and $r\Delta\theta^+ = 32$. There are 10 points in the viscous sublayer and 130 across the buffer and log layers. The mean velocities and turbulence intensities within the boundary layer were validated against existing studies (Kumar and Mahesh, 2018, Posa and Balaras, 2016) and the law of the wall. Additionally a grid refinement study was performed to guarantee the independence of the statistics to the grid choice.

In the wake, the peak ratio between the grid size and the Kolmogorov length $\eta = (\nu^3/\varepsilon)^{1/4}$, in both BI and BE domains is $\max(\Delta x/\eta) = 7.5$, $\max(\Delta r/\eta) = 6$, and $\max(r\Delta\theta/\eta) = 5$. A figure showing the ratio between the Kolmogorov scale and the grid resolution can be found in ONS21 (figure 2). Additionally, the unstratified wake decay coincides with all the previous existing numerical and experimental works on slender body wakes (see figure 1 of ONS21).

Table 4.1: Parameters of the body-inclusive simulation of prolate 6:1 spheroid. L_x^- and L_x^+ are the upstream and downstream distances from the wake generator.

Case	Re	Fr	L_r	L_θ	L_x^-	L_x^+	N_r	N_θ	N_x
1	10^5	∞	5	2π	8	15	746	512	2560
2	10^5	10	60	2π	20	30	848	512	3072
3	10^5	2	60	2π	20	30	848	512	3072

Table 4.2: Parameters of the body-exclusive simulations. x_e is the extraction location of the BI simulations that is fed as inlet to the BE simulations.

Case	Re	Fr	L_r	L_θ	x_e	L_x	N_r	N_θ	N_x
1	10^5	∞	10	2π	6	80	479	256	4608
2	10^5	10	57	2π	9	90	619	256	4608
3	10^5	2	57	2π	9	90	619	256	4608

The domain size in the stratified cases is large so that internal gravity waves are weak before reaching the sponge region near the walls. The total number of grid points across BI and BE domains is approximately 1.5 billion in the unstratified case and 2 billion in the stratified simulations. Tables 4.1 and 4.2 include the most relevant parameters of BI and BE simulations, respectively. Further details on the grid design can be found in section 2 of ONS21.

Once the flow has reached statistically steady state, the statistics are obtained by temporal averaging, denoted by $\langle\cdot\rangle$. Instantaneous quantities are written with lower case, mean quantities with upper case, and fluctuations with prime. In the stratified cases the average is performed over $270D/U_\infty$, approximately three flow-throughs. In the unstratified simulation flow statistics are obtained through the temporal (over $100D/U_\infty$) as well as azimuthal averaging. Apart from

Table 4.3: Parameters of the disk simulations (CS20).

Case	Re	Fr	L_r	L_θ	L_x^-	L_x^+	N_r	N_θ	N_x
1	5×10^4	∞	15.14	2π	30.19	125.51	364	256	4608
2	5×10^4	10	80	2π	30.19	125.51	529	256	4608
3	5×10^4	2	80	2π	30.19	125.51	529	256	4608

temporal averaging, some statistics are obtained from cross-wake area integration denoted by $\{\cdot\}$. Unless otherwise indicated, the integral is performed over a cross-section of radius $4D$. All the flow statistics presented here die out well before they reach the limit of the integrated region.

Reported velocities and lengths are normalized with the free-stream velocity U_∞ and the body minor axis D, respectively. The normalized streamwise distance from the center of the body x is also measured as a function of the buoyancy frequency and the time. The time in the Nt axis refers to time measured by an observer attached to the mean flow that sees the body move at a speed $-U_\infty$. A Galilean transformation yields $x/Fr = Nt$.

To compare the stratified wake of the 6:1 spheroid with that of a bluff body we use the body-inclusive disk wake simulations of CS20. The solver used in CS20 is the same as the one used here although, instead of using the WALE closure model, CS20 uses a variant of dynamic Smagorinsky. The eddy-viscosity model was changed in the spheroid simulations since WALE was demonstrated to capture the behavior of the turbulent boundary layer with the resolution used in the present wall-resolved LES. Both sets of simulations are very well resolved and have a small subgrid contribution – see ONS21 and CS20 – hence the validity of the comparison. Further details of the simulations can be found in ONS21 and CS20. The main parameters of disk simulations are shown in table 4.3.

4.3 Visualizations

Figure 4.1 shows instantaneous snapshots of the near wake of a spheroid and a disk at $Fr = 2$ and $Fr = 10$. At both Fr, the near wake structure of the two bodies is very different. Compared to the spheroid with turbulent boundary layer (TBL), the disk wake has a large recirculation region ($\sim 2D$), as shown by the red isolines in figure 4.1. This large recirculation region oscillates (Rigas et al., 2014) and generates a vortex shedding structure that is advected downstream (Nidhan et al., 2020). In a spheroid with TBL, the recirculation region is very

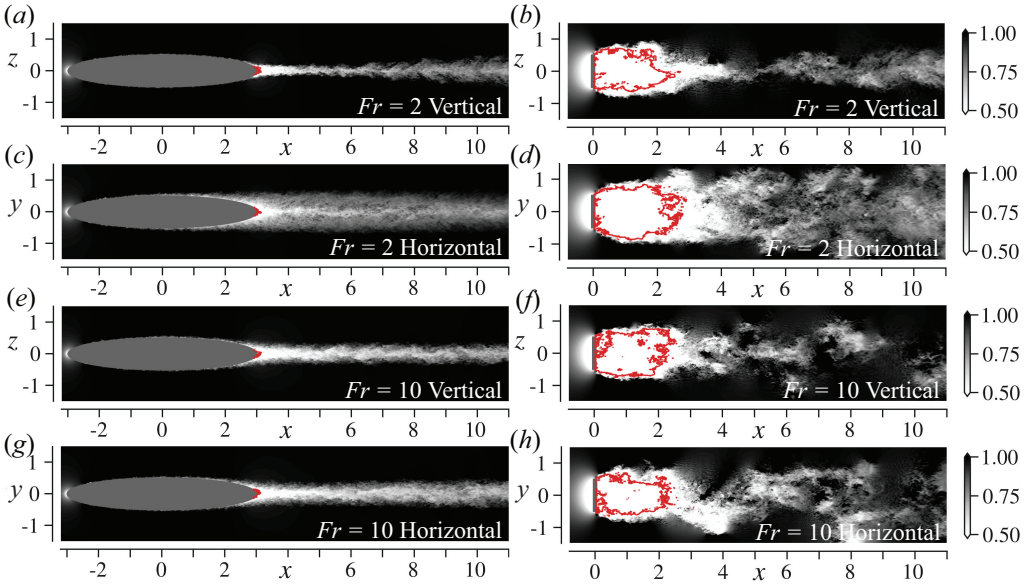

Figure 4.1: Instantaneous contours of streamwise velocity in the near wake for spheroid (left) and disk wakes (right) at $Fr = 2$ and $Fr = 10$ on center-vertical ($y = 0$) and center-horizontal ($z = 0$) planes. Red isolines show the limit of recirculation regions where the streamwise velocity is zero.

small ($\sim 0.1D$) and is surrounded by the small scale turbulence of the boundary layer. As a result, the near wake is highly organized and large scale oscillations are not observed in the near wake (Jiménez et al., 2010, Kumar and Mahesh, 2018, Ortiz-Tarin et al., 2021). Only further downstream, does the wake begin to show a helical structure. This change in the structure of the slender body wake has been found to lead to a change in the decay rate and dissipation scaling in the unstratified wake (ONS21). In the following sections, we will analyze how the differences between the near wake of a disk and that of a spheroid lead to distinct trends of mean and turbulence evolution in a stratified environment. But first, let us describe different snapshots of the spheroid intermediate and far wakes. Snapshots of the disk intermediate and far wakes can be found in CS20.

Figure 4.2 shows an instantaneous visualization of the spheroid $Fr = 2$ wake in the center-vertical and center-horizontal planes. One of the distinctive features of the spheroid wake is that at $Fr \sim O(1)$ the separation of the boundary layer can be strongly modulated by the steady lee waves

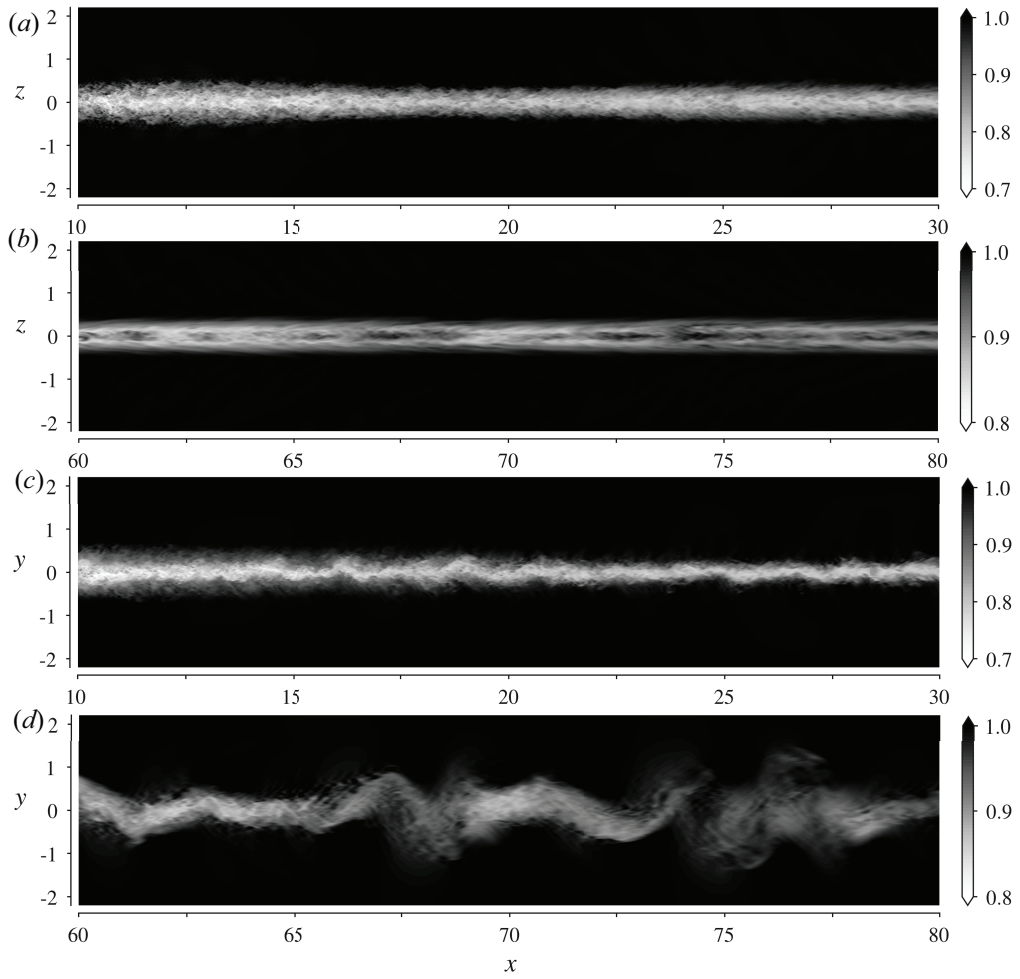

Figure 4.2: Instantaneous contours of streamwise velocity of the spheroid $Fr = 2$ wake in center-vertical (a,b) and center-horizontal planes (c,d).

(Ortiz-Tarin et al., 2019). This interaction between the lee waves and the wake is particularly strong when the Froude number is close to a critical Froude number $Fr_c = AR/\pi$, where AR is the body aspect ratio. When $Fr \approx Fr_c$, half the wavelength of the lee wave ($\lambda/D = 2\pi Fr$) coincides with the length of the body and the size of the separation region is reduced. The flow is then in what is called resonant or saturated lee wave regime, (Chomaz et al., 1992, Hanazaki, 1988). At low Reynolds numbers, this effect can lead to the relaminarization of the turbulent wake (Ortiz-Tarin et al., 2019, Pal et al., 2016). In the present case, figure 4.2(a) reveals that, even at $Re = 10^5$, the wake height is strongly modulated by the waves, although the wake is not relaminarized due to the high Re of the flow. For example, the wake height exhibits oscillations with a wavelength of $\lambda/D = 2\pi Fr = 4\pi$. The modulation of the wake by the waves leads to an unusual configuration in the intermediate wake ($x = 20-40$) where the wake width L_H is smaller than the wake height L_V, figure 4.2(a) and (c). In these figures, sinuous oscillations are observed only in the horizontal plane (figure 4.2d) due to strong stratification. These horizontal sinuous instabilities contrast with the lee wave induced varicose modulation in the vertical plane. As the wake evolves, the $L_H < L_V$ configuration transitions to the expected $L_H > L_V$. In this late region, the small-scale turbulence of the boundary layer has been dissipated and a layered-layer structure is observed in the vertical plane, figure 4.2(b). The qualitative trends of L_H and L_V discussed here are quantified in §4.4.

The main features of the $Fr = 10$ wake can be observed in the instantaneous snapshots of figure 4.3. The near wake, figure 4.3(a,c), is thin and carries the small scale turbulence generated in the boundary layer. Similar to the unstratified wake of ONS21, in the $x < 20$ region, it has a quasi-cylindrical structure. Only after $x \approx 20$, a helical structure develops. In the unstratified wake, the oscillation found at $x \approx 20$ is present until the end of the domain. Here, the $Fr = 10$ wake does not show major oscillations after $x \approx 30$. Stratification restrains the vertical motions in the wake and enhances the horizontal spread as can be seen in the visualization of the late wake, figure 4.3(b,d). Unlike the $Fr = 2$ wake, the horizontal and vertical $Fr = 10$ wake extent grow

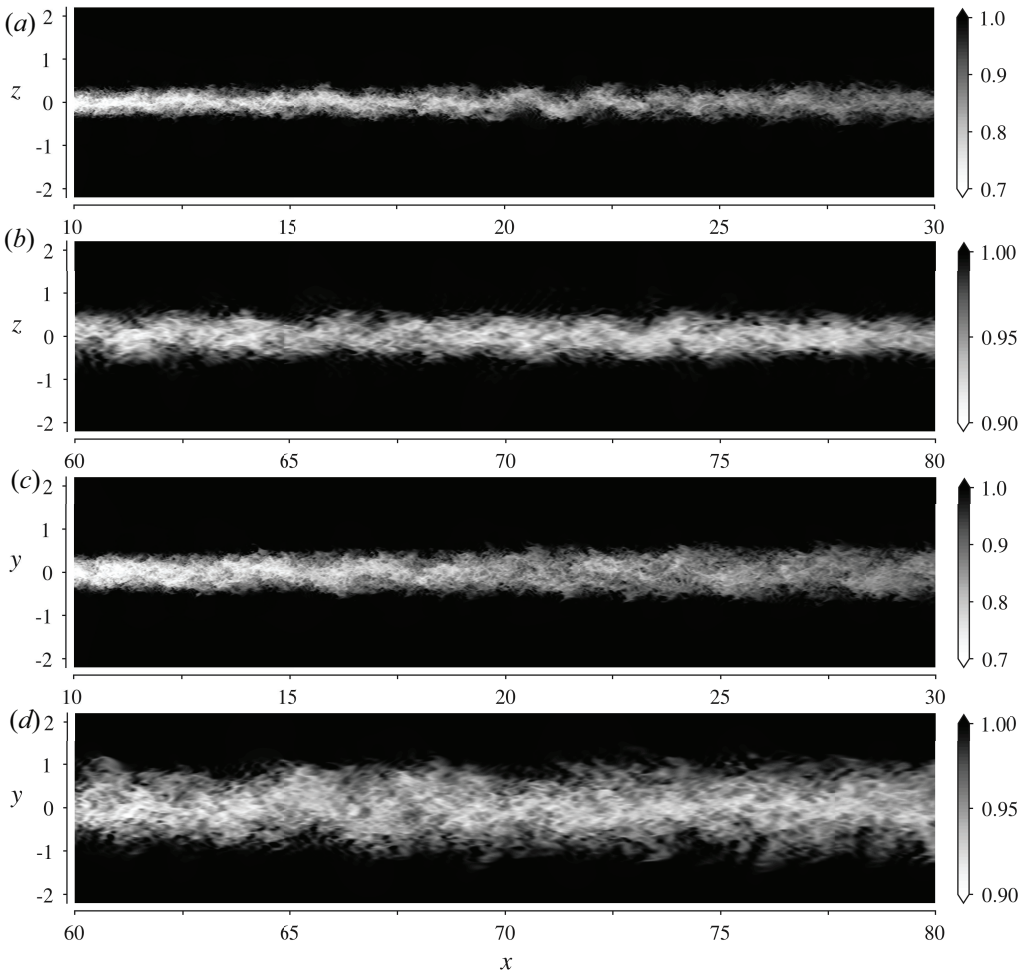

Figure 4.3: Instantaneous contours of streamwise velocity of the spheroid $Fr = 10$ wake in center-vertical (a,b) and center-horizontal planes (c,d).

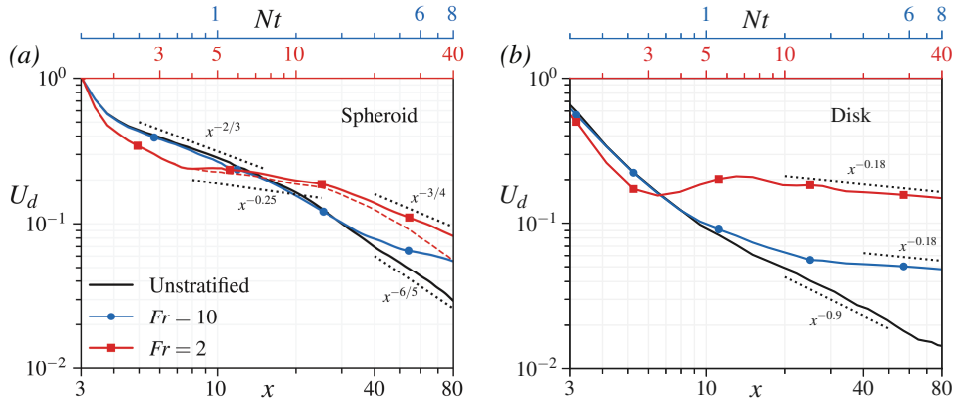

Figure 4.4: Decay of the peak defect velocity in (a) spheroid and (b) disk. The red dashed line in (a) indicates the decay of the $Fr = 2$ centerline defect velocity. For all other cases, centerline and maximum U_d coincide. Note that the origin of the Nt scale is 1.5 for $Fr = 2$ and is 0.3 for $Fr = 10$.

monotonically with increasing downstream distance.

4.4 Evolution of the mean flow in spheroid and disk wakes

4.4.1 Evolution of the mean defect velocity (U_d)

The decay rate of the mean defect velocity $U_d = U_\infty - U$ shows the different stages in the evolution of a wake. In a stratified environment, wakes transverse the 3D, NEQ and Q2D regimes (Spedding, 1997). Figure 4.4 compares the decay of U_d among the unstratified, $Fr = 10$, and $Fr = 2$ spheroid and disk wakes. To facilitate a one-to-one comparison, we present the disk data in the domain $3 \lesssim x \lesssim 80$, coinciding with the domain of the spheroid wake. Since x is measured from the center of the body, the location of $x = 3$ is in the near wake for the disk and is at the terminus of the body for the spheroid. The unstratified spheroid wake (figure 4.4a) shows a transition between the classical high-Re decay $U_d \sim x^{-2/3}$ to $U_d \sim x^{-6/5}$ at $x \approx 20$ coinciding with the development of a helical structure (ONS21). The $Fr = \infty$ disk wake decays as $U_d \sim x^{-0.9}$ from $10 \lesssim x \lesssim 65$ and transitions to the classical high-Re decay of $x^{-2/3}$ afterward (CS20), as shown in figure 4.4(b). Compared to the disk, the $Fr = 10$ and $Fr = \infty$ spheroid wakes have

a higher value of U_d, owing to weaker near-wake entrainment and the slower development of slender body wakes.

In the weakly stratified $Fr = 10$ regime, the defect velocity of the spheroid wake (figure 4.4a) evolves similarly to the unstratified wake until $Nt \approx 3.5$, when the decay rate slows down. However, at the same value of $Fr = 10$ but for the disk wake (figure 4.4b), U_d deviates from the unstratified case at $Nt \approx 1$. Based on U_d, the end of the 3D region and the beginning of the NEQ region of the spheroid wake occurs at $x \approx 30$ whereas in the disk it occurs at $x \approx 10$. We discuss the reason behind this delayed deviation of the spheroid-wake U_d from its unstratified counterpart in §5.

At $Fr = 2$, there are significant differences in U_d evolution between the disk and spheroid wakes. In the $Fr = 2$ spheroid wake, U_d shows an increased decay rate from the beginning. Although not shown here, the wake establishment is affected similarly to the $Fr = 1$ wake of the 4:1 spheroid of Ortiz-Tarin et al. (2019), where there was no 3D regime. The boundary layer evolution on the body and the separation are affected by stratification. At $Nt \approx \pi$, there is a sudden change in the decay rate due to the lee-wave-induced oscillatory modulation (Pal et al., 2017) observed in the $3 \lesssim x \lesssim 10$ region. This oscillatory modulation gets weaker downstream as the lee-wave amplitude decreases with the distance from the source.

At $Nt \approx \pi$, the wake transitions to the NEQ stage where U_d exhibits a slower decay compared to both the preceding stage and the following stage which commences at $Nt \approx 15$. Fitting a power law to the NEQ stage between $x = 6 - 25$ results in a decay with $x^{-0.266}$. This decay is close to the -1/4 decay in the NEQ regime found in the experiments of Spedding (1997) and later in numerical simulations (Brucker and Sarkar, 2010, Diamessis et al., 2011, Pal et al., 2017, Redford et al., 2015). More details about the fitting strategy can be found in ONS21. At $Nt \approx 15$, the spheroid wake transitions to the Q2D regime with a sharper decay and a power-law fit between $x = 30 - 80$ results in $U_d \sim x^{-0.72}$, which is close to the $x^{-0.75}$ behavior established by Spedding (1997) for the Q2D regime. The $Fr = 2$ disk wake shows a very different behavior.

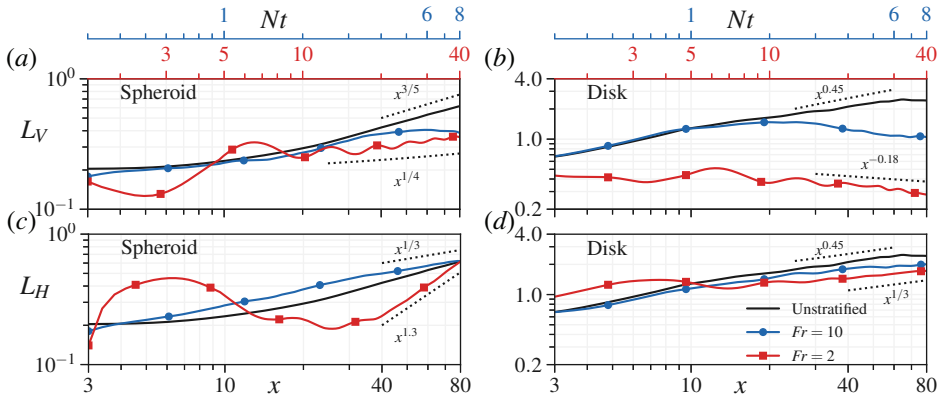

Figure 4.5: Wake dimensions measured using the mean defect velocity U_d for the spheroid (a,c) and disk (b,d) wakes in center-vertical (a,b) and center-horizontal (c,d) planes. The legends are same as in figure 4.4.

Until at least $x = 125$ ($Nt = 62.5$) – the full extent of the computational domain – the disk wake exhibits no transition to the Q2D regime. Instead, after transitioning to the NEQ regime with a power law of $U_d \sim x^{-0.18}$, the disk wake stays in that regime.

Thus, the NEQ regime in the spheroid wake at $Fr = 2$ is significantly shortened compared to the disk wake, with it starting at $Nt \approx \pi$ and ending early at $Nt \approx 15$ when Q2D commences. In the experiments of Spedding (1997), the NEQ regime is reported to last until $Nt \approx 40$. Other temporal studies have found that the span of the NEQ regime depends on the Reynolds number. For example, in temporal simulations, Diamessis et al. (2011) found an increase of the NEQ duration to $Nt \approx 50$ when the Reynolds number increased to $Re = 10^5$. Brucker and Sarkar (2010) found a transition to a Q2D-type power law at $Nt \approx 100$. Only Redford et al. (2015) observed an earlier transition around $Nt \approx 25$. The reasons behind the early arrival of the Q2D regime in the spheroid $Fr = 2$ wake will be discussed in §5.

4.4.2 Evolution of the mean horizontal (L_H) and vertical (L_V) lengthscales

The evolution of the mean wake dimensions in the spheroid and disk wakes is shown in figure 4.5(a,c) and (b,d), respectively. L is defined such that $U_\infty - U(L) = \frac{1}{2}U_d$. The subscripts $\{V,H\}$ indicate that these measures have been taken in the vertical and horizontal planes so that

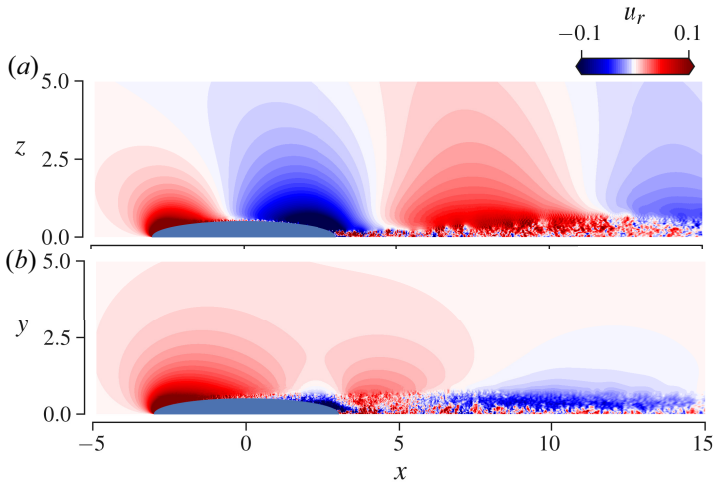

Figure 4.6: Instantaneous radial velocity contours of the $Fr = 2$ spheroid wake in the (a) center-vertical and (b) center-horizontal planes.

they represent the half height and the half width.

The wake of a slender body is generally thinner than its bluff body counterpart. Compared to the disk wake of CS20, the present unstratified wake is smaller by a factor of about 3 – contrast black lines in figure 4.5(a) to (b). The difference in wake size stems from the different near-wake features. Here, the initial non-dimensional wake width is around 0.2 whereas its value for the disk is around 0.7. This observation agrees well with the scaling proposed by Tennekes and Lumley (1972) and used in stratified wake experiments by Meunier and Spedding (2004), where the wake dimensions behind a body with diameter D scale with the drag coefficient $\sqrt{C_D}$. We find that $C_D^{\text{disk}} \approx 1.11$ and $C_D^{\text{spheroid}} \approx 0.13$ resulting in $(C_D^{\text{disk}}/C_D^{\text{spheroid}})^{0.5} \approx 3.2$. Besides the initial dimensions, the near-wake growth rates of the spheroid and disk are also very different. Whereas in the $x = 3-20$ region the spheroid unstratified wake grows as $L \sim x^{0.2}$, the disk wake grows as $L \sim x^{0.45}$. Later, the growth rate of both wakes becomes comparable but the difference in size is already established and dictated by the near wake.

The evolution of the $Fr = 10$ spheroid wake height (L_V) is similar to its unstratified counterpart until $Nt \approx 3.5$ where the growth of L_V slows down. While L_V remains almost constant beyond $Nt \approx 4$, L_H keeps increasing with a growth rate of $\sim x^{1/3}$. In the $Fr = 10$ disk

wake, the deviation from the $Fr = \infty$ case happens at $x \approx 20$ ($Nt \approx 2$). Interestingly, after $Nt \approx 2$, the disk wake shows a continuous decrease in wake height. L_H of both spheroid and disk wakes at $Fr = 10$ closely follow the trend of the corresponding unstratified wake. See figures 4.5(c,d).

The wake dimensions at $Fr = 2$ for both disk and spheroid show oscillations with a wavelength of $\lambda/D = 2\pi Fr$. This reveals the influence of the steady lee waves especially on the wake height, see figure 4.5(a,b). From $Nt = 1 - 15$ the oscillations of L_V and L_H are consistent with the conservation of momentum deficit, i.e., to counteract the contraction of L_V caused by buoyancy, L_H is enhanced. Note that these initial oscillations are of similar amplitude in both disk and spheroid. However, the relative change over the initial wake dimensions is much more pronounced in the spheroid wake (~ 10 times) owing to its initial thinness. The influence of the lee waves on the spheroid $Fr = 2$ wake dimensions is illustrated by radial velocity contours in figure 4.6. The wake width contracts significantly in the region where the vertical velocity of the lee wave induces a rapid increase of wake height. Starting at $Nt = 20$, the width of the spheroid wake shows a rapid growth $L_H \sim x^{1.3}$ corresponding with: (i) the development of the horizontal wavy motions observed in figure 4.2(d) and (ii) the arrival of the Q2D stage with $U_d \sim x^{-3/4}$. The growth of L_V remains constant at a rate of $x^{0.25}$. Both, the very rapid growth of L_H and the sustained increase in L_V of the spheroid wake, are very different from the trends in the $Fr = 2$ disk wake. In the disk wake, we find that, instead of an increase, the vertical height exhibits a decrease ($L_V \sim x^{-0.18}$) at $x \gtrsim 20$. Furthermore, L_H grows at $x^{1/3}$, a moderate rate relative to its rapid growth rate in the disk wake.

4.4.3 Comparison of flow topology between stratified spheroid and disk wakes

The difference between the spheroid and disk with regards to the evolution of mean length scales (L_V and L_H), particularly at $Fr = 2$, points toward qualitative differences in the flow topology. To further characterize these differences in the $Fr = 2$ wake, figure 4.7 shows contours

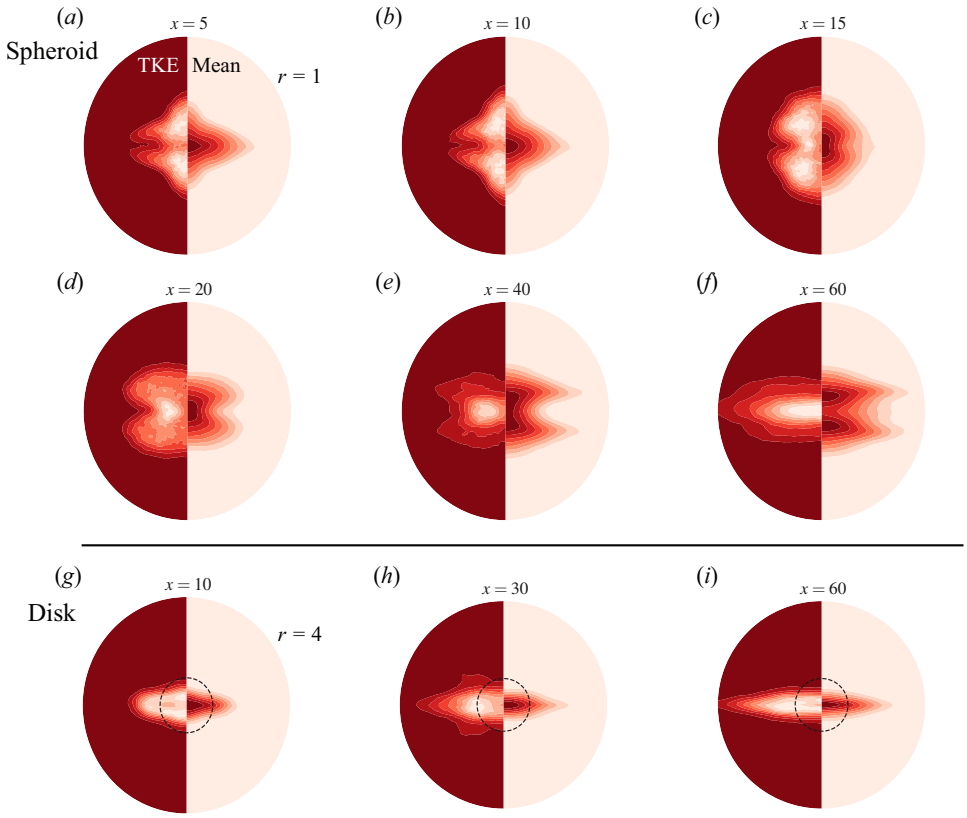

Figure 4.7: $Fr = 2$ wakes of spheroid (a-f) and disk (g-i) at different streamwise locations. Contour limits are between the minimum (red) and maximum (white) values of the respective quantity at a given x with ten levels in between. Radial extent span till $r = 1$ and $r = 4$ for the spheroid and disk contours.

of mean streamwise velocity (U) at different streamwise locations for the spheroid (top two rows) and the disk (bottom row). In each panel of figure 4.7, the right half shows U_x and the left half shows turbulent kinetic energy (TKE), $E_T^K = (\langle u_x'^2 \rangle + \langle u_y'^2 \rangle + \langle u_z'^2 \rangle)/2$.

For the sake of brevity, we have not included contours of the $Fr = 10$ disk and spheroid wakes since their topology is similar – the mean can be well approximated by a vertically-squeezed two-dimensional Gaussian while the TKE evolves from a bimodal (off-center peaks) distribution in the radial direction to a Gaussian at intermediate to late streamwise distances. In the case of the disk, the TKE evolves as a two-dimensional Gaussian right beyond the recirculation region.

We first discuss the disk wake (bottom row). The mean shows a monotonic spread in the horizontal direction and resembles the shape of an ellipse or a two-dimensional Gaussian squeezed in the vertical direction. This shape does not change until the end of the computational domain at $x \approx 125$. The TKE for the disk wake also has a similar vertically squeezed appearance.

Turning to the spheroid wake, we find that its turbulence topology is different from that of the mean. In the region $5 \leq x \leq 15$, TKE shows two off-center peaks reminiscent of the TBL shedding from a slender body (Jiménez et al., 2010, Kumar and Mahesh, 2018, Ortiz-Tarin et al., 2021, Posa and Balaras, 2016) while mean U_x shows a single central peak. At $x = 20$, we see the start of a horizontal contraction of the mean velocity in the central region of the wake and the emergence of a 'butterfly' shape reminiscent of the separation and wake patterns observed in Ortiz-Tarin et al. (2019), where the $Fr_c = 4/\pi \approx 1$ wake of a 4:1 spheroid was studied. Note that in this stage, the wake is thinner than taller, i.e., $L_H < L_V$. At $x \approx 20$, TKE starts transitioning from a bimodal distribution to a single peak near the center-horizontal plane. In the next section, we will analyze how the horizontal contraction of the mean wake between $x = 20$ and $x = 40$ results in an increased horizontal mean shear, resulting in the maximum TKE being produced close to the center-horizontal plane. This leads to a transition in the TKE topology from bimodal distribution to a squeezed-Gaussian distribution at $x \gtrsim 40$. By $x \approx 60$, U has been organized into two distinct layers while TKE is sustained between these two vertically off-center layers. Note

that the multi-layered mean flow structure at late x in the $Fr = 2$ spheroid wake is reminiscent of the layered structure of the Q2D regime Spedding (1997).

Previously, temporal simulations (Brucker and Sarkar, 2010, Gourlay et al., 2001, Redford et al., 2015) have shown that the mean and the turbulence can evolve differently. Indeed, the effect of buoyancy is 'felt' very differently by the large and the small scales in the flow. The general trend is that, in the late wake, the turbulence occupies a smaller and smaller vertical fraction of the mean defect as time passes (Redford et al., 2015). Instead, the finding here for the spheroid wake is the combined effect of having a wake in saturated-lee-wave state and initial off-center peaks of TKE, established by the TBL separation. These characteristics of the flow have not been not captured in temporal simulations since they have not accounted for the wake generator and the steady lee waves.

4.5 Evolution of the turbulent flow in spheroid and disk wakes

The energy of the flow is contrasted between spheroid and disk wake in this section. The turbulent kinetic energy (TKE also denoted as E_K^T), turbulent potential energy (TPE, E_P^T), mean kinetic energy (MKE, E_K^M) and mean potential energy (MPE, E_P^M) are defined as:

$$E_K^T = (\langle u_x'^2 \rangle + \langle u_y'^2 \rangle + \langle u_z'^2 \rangle)/2\,, \qquad E_P^T = \gamma \langle \rho' \rho' \rangle / 2, \tag{4.1}$$

$$E_K^M = (U_d^2 + \langle u_y \rangle^2 + \langle u_z \rangle^2)/2\,, \qquad E_P^M = \gamma \langle \rho_d \rangle^2 / 2, \tag{4.2}$$

where $\gamma = g^2/\rho_o^2 N^2$. In what follows, trends of area-integrated values, denoted by $\{\cdot\}$, of these energy measures are reported. Area-integrated quantities are preferred because the peaks of mean and turbulence in stratified slender wakes are often times off-centered as can be seen in figure 4.7. The integration allows for a uniform comparison across cases. Also note that temporally averaged

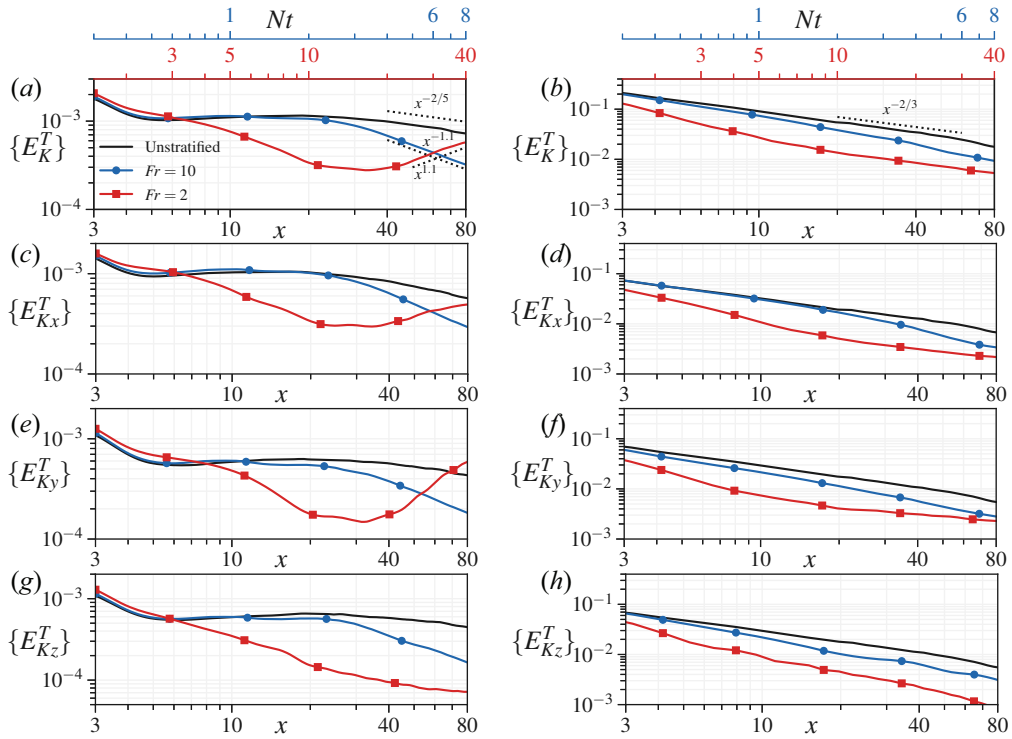

Figure 4.8: Comparison of evolution of TKE between spheroid (left) and disk (right) wakes. (a,b) total TKE, (c,d) streamwise TKE, (e,f) spanwise TKE, and (g,h) vertical TKE.

quantities are denoted by the angled brackets $\langle\cdot\rangle$.

4.5.1 Evolution of TKE, spectra and PE-to-KE ratios

The evolution of the area-integrated TKE of the disk and spheroid wakes is shown in figure 4.8. The most noticeable aspect is that, for all Fr numbers, $\{E_K^T\}$ in spheroid wakes is an order of magnitude smaller than in corresponding disk wakes. Although it is not shown here, we found a similar result for the area-averaged TKE (over an area of $r = 4D$ cross-section), instead of area-integrated TKE.

The decay of the unstratified wake is studied in more detail in ONS21 for the spheroid and CS20 for the disk. In unstratified flow, $\{E_K^T\}$ decays following $\{E_K^T\} \sim x^{-2/5}$ for the spheroid and the disk wake follows $\{E_K^T\} \sim x^{-2/3}$. Note that these fits are empirical. Both decay rates are consistent with the decay of the peak TKE (k) and the growth of wake width (L) under the

self-similarity framework, i.e., $\{E_K^T\} \sim kL^2$. Specifically, in the case of the spheroid $L \sim x^{3/5}$ and $k \sim x^{-8/5}$ (Ortiz-Tarin et al., 2021) and, in the case of the disk, $L \sim x^{1/3}$ and $k \sim x^{-4/3}$ (Chongsiripinyo and Sarkar, 2020).

At $Fr = 10$ and for both the spheroid and the disk, $\{E_K^T\}$ deviates from the unstratified case at between $Nt \approx 1$ and $Nt \approx 3$, see figure 4.8(a,b).Interestingly, while the TKE is affected by stratification in the similar Nt range for both wake generators, the mean flow showed a different behavior. In the disk $Fr = 10$ wake, U_d deviated from its unstratified counterpart at $Nt \approx 1$ while, in the spheroid, this change occurred later at $Nt \approx 3$. The onset of deviations from the unstratified case will be explained in more detail in the following subsections.

At $Fr = 2$, there is a striking influence of the wake generator on the evolution of TKE. Whereas in the disk wake, the TKE decays monotonically, the far wake of the spheroid displays a rapid increase.

The disk wake shows a monotonic decay in $\{E_T^K\}$ and its individual components throughout $3 < x < 80$. Compared to the horizontal components, $\{E_{Tz}^K\}$ shows a sharper decay after $Nt \approx 10$ and turbulence anisotropy progressively increases. In the spheroid $Fr = 2$ wake, $\{E_T^K\}$ decays rapidly until $Nt \approx 10$. However, after $Nt \approx 10$, the decay slows down and is followed by a period of sustained growth starting at $Nt \approx 20$ and lasting until the end of the domain. The region of TKE growth coincides with the development of the large scale horizontal motions observed in figure 4.2(d) and the rapid growth of L_H shown in figure 4.5(c). It also coincides with the accelerated decay rate of U_d starting at $Nt \approx 20$.

Notice that right before the start of the rapid increase of TKE, the $Fr = 2$ wake has a configuration where $L_H < L_V$ (figure 4.7d). The horizontal response of the flow to the strong lee waves is what sustains this configuration. It is only after their strength subsides that the control on the wake is released to allow the horizontal wavy motion to develop. The rapid development of this motion coincides with the rapid increase in horizontal TKE, namely $\{E_{Ky}^T\}$ and $\{E_{Kx}^T\}$ as seen in figure 4.8(c,e). To the best of the authors' knowledge this is the first wake study, resolving

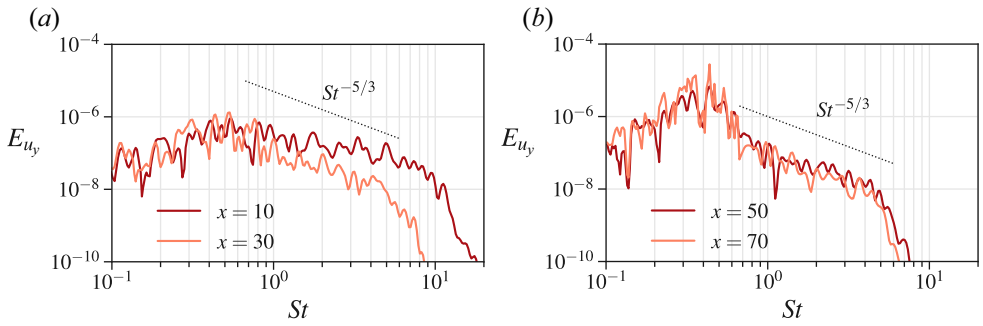

Figure 4.9: Energy spectra of the $Fr = 2$ spheroid wake computed with the spanwise velocity fluctuations at the centerline at (a) $x = 10, 30$ and (b) $x = 50, 70$.

the flow at the body, that observes an increase of fluctuation energy with downstream distance instead of its usual decrease.

To further quantify the horizontal wavy motions observed in figure 4.2(d), the energy spectra of the spanwise velocity are computed at the centerline. These spectra are compared between locations before (figure 4.9a) and after (figure 4.9b) the start of the the TKE increase associated with the Q2D regime. The spectra before $x < 40$ do not show preferential energization of the low frequencies. This finding is consistent with the visualizations in figure 4.2 where the intermediate wake does not show any sign of large scale motions. Beyond $x = 40$, however, spectra show a strong peak at Strouhal number $St = fD/U_\infty \approx 0.35$ (figure 4.9b). This value of Strouhal number agrees with the approximate wavelength of structures in figure 4.2(d), where the wavelength $\lambda/D \approx 1/St$. To summarize, the arrival of the Q2D regime in the $Fr = 2$ wake is accompanied by a strong increase in TKE (figure 4.8a) and the appearance of large scale motions in the center-horizontal plane (figure 4.2d and 4.9b).

In the $Fr = 2$ disk wake, the vortex shedding mode at $St = fD/U_\infty \approx 0.13 - 0.14$ is dominant throughout the whole domain. The horizontal meanders, which are prevalent in the spheroid wake, are absent in the disk wake at least until the end of the domain at $x/D = 125$.

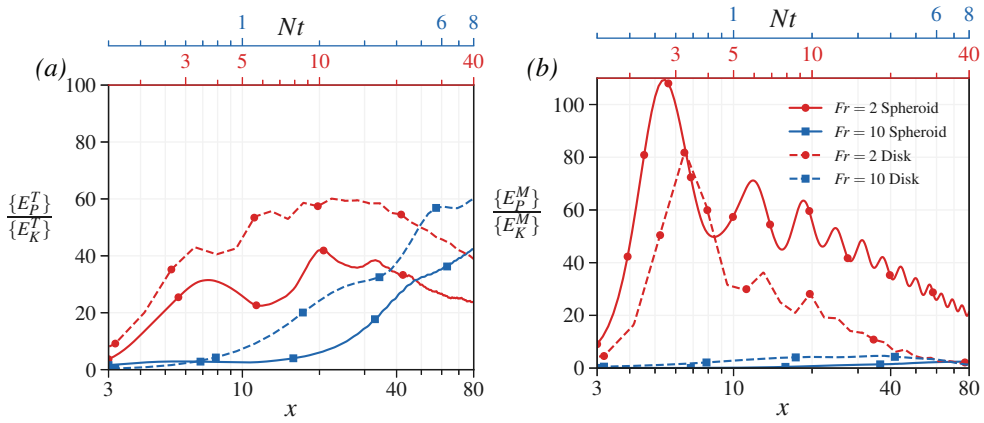

Figure 4.10: Ratio of area-integrated (a) turbulent potential energy to turbulent kinetic energy and (b) mean potential energy to mean kinetic energy in stratified spheroid and disk wakes.

Since the vortex shedding mode, its long-lasting effect on the wake, and its internal wave field are described in detail by Nidhan et al. (2022b), we do not discuss these aspects further.

The spheroid wake has significantly lower TKE content relative to the disk wake and also a different distribution of the mean momentum. The content of potential energy relative to that of kinetic energy is also of interest. Figure 4.10 shows the ratio of area-integrated potential energy (PE) to kinetic energy (KE). Both fluctuating (4.10a) and mean (figure 4.10b) components are shown at $Fr = 2$ and 10 for both wake generators.

At $Fr = 10$, the turbulent PE-to-KE ratio increases steadily in both disk and spheroid cases indicating an increasing influence of buoyancy on turbulence (figure 4.10a). In the $Fr = 2$ wakes, the turbulent PE-to-KE ratio peak around $x \approx 30$ in both cases and decay afterward. By the end of the measurement region at $x = 80$, the turbulent PE-to-KE ratios are similar across $Fr = 2$ and 10 wakes. Thus, stratification and body shape do not qualitative affect the ability of turbulence to stir the density field in the intermediate and far wake. Quantitatively, the TPE-to-TKE ratios are somewhat higher for the disk relative to the spheroid for both wakes.

The mean PE-to-KE ratios in the $Fr = 10$ wakes (figure 4.10b) are minuscule compared to their turbulent counterparts. At $Fr = 2$, the mean-based ratio is much larger, particularly close to the wake generators, pointing towards a strong influence of the steady lee waves. Both disk

and spheroid mean-based ratios oscillate with a characteristic lengthscale corresponding to the wavelength of steady lee waves at $Fr = 2$. It is particularly revealing as to how much larger is the magnitude of $\{E_P^M\}/\{E_K^M\}$ in the spheroid wake compared to the disk, as it explains why the spheroid flow is so strongly modulated by the lee waves. It is worth noting that comparison of the absolute value of MPE between the disk and the spheroid reveals that it is the disk that has the larger MPE, an order of magnitude larger. The amplitude of the lee wave generated by the disk is larger than that of the spheroid by about a factor of 2.

4.5.2 Analyses of the spheroid TKE budget terms

To quantitatively understand the origin of TKE increase in the $Fr = 2$ spheroid wake, we look into the different terms of the TKE transport equation:

$$U_i \frac{\partial E_K^T}{\partial x_i} + \frac{\partial T_i}{\partial x_i} = P - \varepsilon + B \,, \tag{4.3}$$

where P is the turbulent production, ε is the turbulent dissipation and B denotes the turbulent buoyancy flux. These quantities are defined by:

$$P = -\langle u_i' u_j' \rangle \frac{\partial U_i}{\partial x_j}, \quad \varepsilon = 2\nu \langle s_{ij}' s_{ij}' \rangle - \langle \tau_{ij}'^s s_{ij}' \rangle \,, \quad B = -\frac{g}{\rho_0} \langle \rho' u_z' \rangle \,, \tag{4.4}$$

where $s_{ij} = (\partial_j u_i + \partial_i u_j)/2$ is the strain-rate tensor and $\tau_{ij}^s = -2\nu_s s_{ij}$ is the subgrid stress tensor. The contribution of the subgrid term to the TKE transport equation is found to be small.

The turbulent production is a source of TKE and a sink in the MKE equation. The turbulent buoyancy flux transfers energy between TKE and TPE and the turbulent dissipation is a sink of TKE. Along with the sinks and sources of energy, there is a term responsible for the spatial redistribution of TKE, the turbulent transport,

$$T_i = \frac{1}{2} \langle u_i' u_j' u_j' \rangle + \langle u_i' p' \rangle - 2\nu \langle u_j' s_{ij}' \rangle - \langle u_j' \tau_{ij}'^s \rangle \,. \tag{4.5}$$

The turbulent transport redistributes energy, primarily in the y-z plane, and its contribution to the area-integrated budget is negligible.

The production term in equation (4.3) can be further expanded as follows:

$$P = -\langle u_x' u_j' \rangle \frac{\partial U_x}{\partial x_j} - \langle u_y' u_j' \rangle \frac{\partial U_y}{\partial x_j} - \langle u_z' u_j' \rangle \frac{\partial U_z}{\partial x_j}. \tag{4.6}$$

For the stratified wakes at hand, $U_y, U_z << U_x$. Hence equation (4.6) can be further simplified as below:

$$P = -\langle u_x' u_x' \rangle \frac{\partial U_x}{\partial x} - \langle u_x' u_y' \rangle \frac{\partial U_x}{\partial y} - \langle u_x' u_z' \rangle \frac{\partial U_x}{\partial z}. \tag{4.7}$$

In a wake developing in the x direction, P is primarily dominated by the transverse shear terms since $|\partial U_x/\partial y|, |\partial U_x/\partial z| >> |\partial U_x/\partial x|$. Hence in the discussions on $\{P\}$ to follow, we focus on the transverse terms, namely $P_{xy} = \langle u_x' u_y' \rangle \partial_y U_x$ and $P_{xz} = \langle u_x' u_z' \rangle \partial_z U_x$.

Figure 4.11 shows the evolution of the area-integrated terms in the TKE transport equation of the spheroid wake. We do not present the TKE transport terms of the disk wakes here as they are presented and discussed in great detail in CS20. We first discuss the trends of the area-integrated production, $\{P\}$, and its components in $Fr = 2$ and 10 spheroid wakes. This is followed by a discussion of the area-integrated dissipation, $\{\varepsilon\}$. Thereafter, the variation of $\{P\}/\{\varepsilon\}$ sheds light on why an increase in TKE is observed in the $Fr = 2$ spheroid wake for $x > 30$.

$\{P\}$ in the $Fr = 10$ spheroid wake decays at a rate comparable to its unstratified counterpart until $Nt \approx 3$ when it starts to deviate (figure 4.11a). U_d in the $Fr = 10$ spheroid wake also starts deviating around $Nt \approx 3$ (figure 4.4a). At $Nt \approx 3$, the contribution of $P_{xz} = \langle u_x' u_z' \rangle \partial_z U_x$ starts declining due to a reduction in $\langle u_x' u_z' \rangle$ (not shown here for brevity). At $Nt \approx 4.5$, the contribution of the lateral production P_{xy} exceeds that of the vertical production P_{xz}.

The reduction of $\{P_{xz}\}$ in the $Fr = 10$ wake coincides with the transition of U_d to a

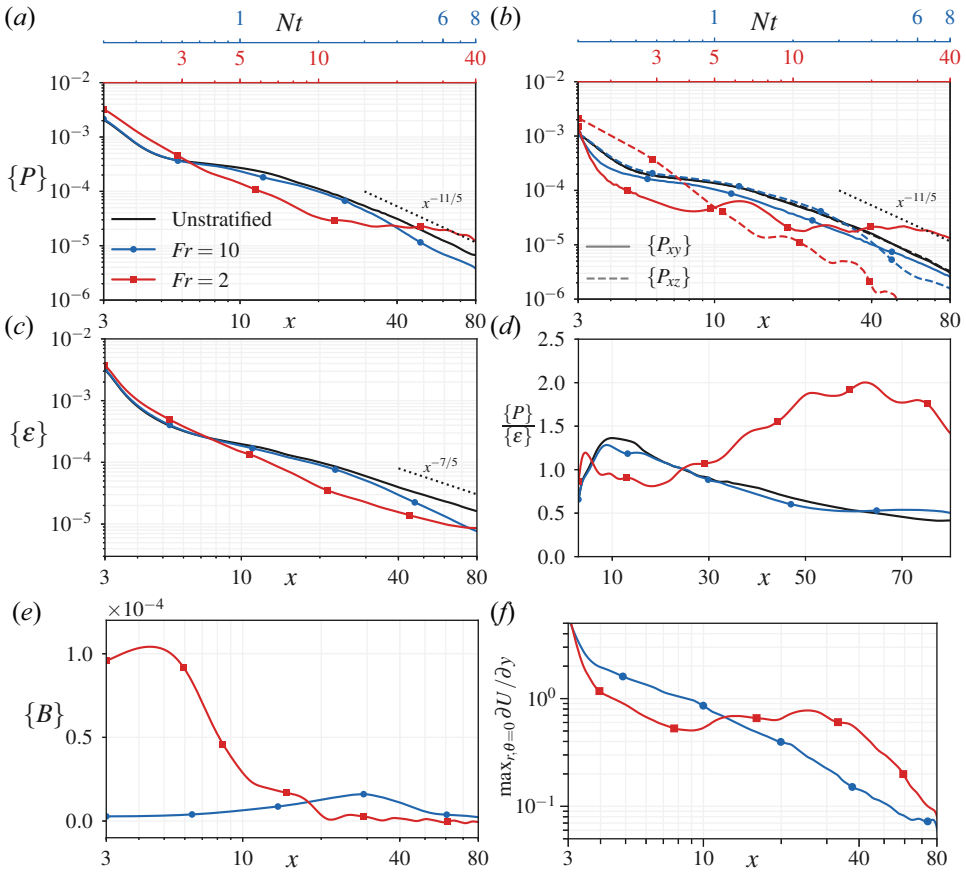

Figure 4.11: Spheroid wakes. (a) Area-integrated production. (b) Main components of the turbulent production. (c) Area-integrated dissipation. (d) Ratio between area-integrated production and dissipation. (e) Area-integrated buoyancy flux. (f) Maximum value of mean horizontal shear $\partial U_x/\partial y$.

slower decay rate. In figure 4.11(b), we note that $\{P_{xz}\}$ starts decaying faster than its unstratified counterpart between $3 < Nt < 4$ (or $30 < x < 40$). In figure 4.4(a), we see that this the location where U_d of the $Fr = 10$ spheroid wake starts deviating from the $Fr = \infty$ spheroid wake. At the same location that $\{P_{xz}\}$ starts decaying rapidly, there is a maximum in the buoyancy flux $\{B\}$ (figure 4.11e) and a slowdown in the growth of L_V (figure 4.5a). Buoyancy is starting to affect the wake decay.

The initial value of $\{P\}$ in the $Fr = 2$ wake is higher than in the unstratified case. The distinct separation pattern and the vertical contraction of the mean flow (figure 4.5a) lead to an increase in the vertical shear and hence $\{P_{xz}\}$, see red dashed lines in figure 4.11(b). This initially high value of $\{P_{xz}\}$ rapidly decays as L_V increases, leading to a reduction in the vertical shear. Note that the beginning of the U_d-based NEQ regime at $Nt \approx \pi$ also coincides with this reduction of $\{P_{xz}\}$. However, the mechanism at $Fr = 2$ is different from that of the $Fr = 10$ wake. Whereas at $Fr = 10$, the reduction of $\langle u_x' u_z' \rangle$ causes the decay of $\{P_{xz}\}$, at $Fr = 2$ the decay of $\langle u_x' u_z' \rangle$ is accompanied by a sudden reduction of $\partial_z U_x$ (not shown here). The reduction in vertical shear is driven by the expansion of L_V due to lee wave modulation in figure 4.5(a).

As the modulation of the wake by the lee waves continues, the horizontal production is enhanced by the strong reduction in L_H (figure 4.5c) in the NEQ region during $7 < x < 20$. The value of $\{P_{xy}\}$ overtakes $\{P_{xz}\}$ at $Nt \approx 5$. The magnitude of $\{P_{xy}\}$ remains nearly constant until the end of the domain. Figure 4.11(f) shows the maximum of the horizontal mean shear $(\partial U_x/\partial y)$, i.e., $\max_{(r,\theta=0)} \partial U_x/\partial y$, in the central streamwise-horizontal plane for both wakes. The mean shear in the $Fr = 2$ wake increases in the region $10 < x < 30$, exactly in the region where the TKE decay starts plateauing (see figure 4.8a). The enhanced mean horizontal shear at $Fr = 2$ prevents the horizontal production from decaying monotonically unlike $Fr = 10$.

Figure 4.11(c) shows the evolution of $\{\varepsilon\}$ as a function of x for $Fr = \infty, 10$ and 2 spheroid wakes. In the $Fr = 10$ case, the decay of ε is similar to that of the unstratified wake until $Nt \approx 3$ after which the decay rate increases slightly. The $Fr = 2$ wake dissipation shows a sharper decay

until $x \approx 20$. After $x \approx 20$, the decay rate appears to be closer to the $Fr = \infty$ decay rate of $x^{-7/5}$ (Ortiz-Tarin et al., 2021).

Since the turbulent dissipation keeps decreasing monotonically in the $Fr = 2$ spheroid wake (figure 4.11c), while the production tends to asymptote for $x > 30$ (figure 4.11a), the value of $\{P\}/\{\varepsilon\}$ becomes greater than 1 in the $Fr = 2$ spheroid wake, see figure 4.11(d), explaining the rapid increase of TKE beyond $x \approx 30$. Note that the $\{P\}/\{\varepsilon\}$ ratio oscillates with the characteristic wavelength of the lee waves revealing the strong influence of wave-related buoyancy effects on the energetics of the $Fr = 2$ wake.

One of the features of the arrival of the NEQ regime reported in previous studies is the radiation of internal gravity waves (Abdilghanie and Diamessis, 2013, de Stadler and Sarkar, 2012, Rowe et al., 2020). In these spheroid wakes, we find that the integrated wave flux remains negligible compared to the other terms in the TKE budget and hence is not shown here. The small magnitude of the turbulent wave flux is consistent with the findings of Meunier et al. (2018) who found that the magnitude of the wake-generated waves depends on the body drag coefficient – and the 6:1 spheroid has a very low drag compared to bluff bodies.

4.5.3 Early arrival of the Q2D regime in the $Fr = 2$ spheroid wake

Remember that the Q2D regime in stratified wakes is characterized by a faster decay of the mean defect velocity ($U_d \sim x^{-3/4}$) and the organization of wake into distinct layers in the vertical direction. Due to the strong effects of buoyancy, the fluid motions are primarily confined to the horizontal plane. However, the vertical variations in the velocity profiles still exist during the Q2D regime, primarily in the form of layered structures.

A key difference between the $Fr = 2$ disk and spheroid wakes is the early arrival of the Q2D regime in the spheroid wake. Whereas in the disk wake, CS20 did not observe a transition to the Q2D in a domain that extended up to $x = 125$ ($Nt = 62.5$), here we observe a transition at $x \approx 40$ ($Nt \approx 20$). The early transition in the spheroid wake is a consequence of the strong

modulation of the intermediate wake by buoyancy, an effect that occurs for bodies with large aspect ratio (L/D) and, specifically, when Fr is near its critical value $Fr_c = L/D\pi$.

Figure 4.5(c) shows that L_H in the $Fr = 2$ spheroid wake contracts in the region $5 < x < 30$ as a response to the expansion of L_V (figure 4.5a) by steady lee waves. This phenomenon leads to the 'butterfly' shaped structure of mean U_x (figure 4.7(d,e)) which was also observed at a lower Reynolds number, $Re = 10^4$ in Ortiz-Tarin et al. (2019). In that study, which was performed at $Re = 10^4$, the spheroid wake at critical Fr_c relaminarized. Here, at a higher $Re = 10^5$, the flow response at the resonant state is quite different. The constriction of L_H leads to an enhancement in the mean horizontal shear shown in figure 4.11(f). This enhancement significantly slows down the decay of horizontal production (figure 4.11b). While ε continues to decay, $\{P\}/\{\varepsilon\}$ becomes > 1 leading to an increase of TKE for $x > 40$ (figure 4.8a). In figure 4.7(d-f), we also see the maximum TKE location moving to the wake axis from its off-center location in the near wake. It is worth noting that the enhanced $\{P\}$ that acts as a source of TKE is a sink for the mean energy. The sharp increase in TKE leads to a faster decay of U_d, and the $Fr = 2$ wake transitions to the Q2D regime early on, at $x \approx 40$.

In the disk wake, L_H is initially $3-4$ times larger than in the spheroid wake. While the lee wave modulation of L_H is present in the disk wake as well (figure 4.5d), its amplitude relative the original value of L_H is quite small. Hence the horizontal mean shear (not shown here) and the horizontal production in the $Fr = 2$ disk wake continue to decay unlike in the spheroid wake.

The arrival of the Q2D regime in the spheroid wake is also accompanied by distinctive features of the Q2D regime reported in previous literature. Figure 4.2(d) shows lateral meanders in the late $Fr = 2$ wake similar to the lateral meanders in temporal simulations in the literature (Brucker and Sarkar, 2010, Diamessis et al., 2011), albeit the temporal-simulation meanders occur much later in Nt units. As noted during the discussion of spectra, the waviness in the late wake has a characteristic frequency $St \approx 0.35$. The mean wake in the Q2D regime has a layered topology (figure 4.7f) as reported by Spedding (2002b) and Chongsiripinyo et al. (2017).

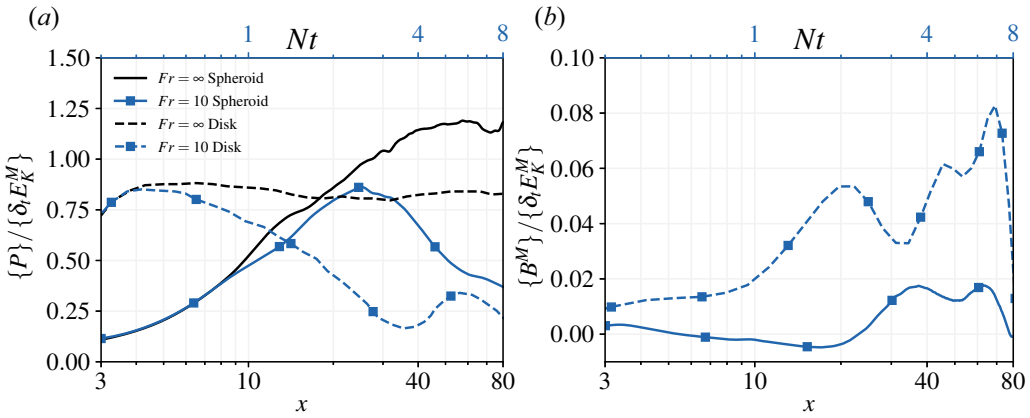

Figure 4.12: Area-integrated (a) production and (b) buoyancy flux in the disk and spheroid $Fr = 10$ wakes. The unstratified wake ($Fr = \infty$) production is also shown in (a). The terms are normalized by the Lagrangian rate of change of their corresponding mean kinetic energy $\{\delta_t E_K^M\} = \{E_K^M\}U_\infty/x$.

The turbulence state in the Q2D regime is characterized by weak vertical fluctuations $u_z' << u_h'$ (Spedding, 1997) with $\{E_{Kz}^T\}/\{E_{Kh}^T\} < 0.1$ at $x > 60$ – where subscript h denotes the horizontal component of the fluctuations. Since the Q2D regime of the spheroid wake is in a relatively early phase, pancake vortices do not appear until the end of the simulation domain, $x = 80$.

4.5.4 Late transition to the NEQ regime in the $Fr = 10$ spheroid wake

At $Fr = 10$, the main difference between the disk and spheroid wakes is the location at which U_d deviates from the unstratified counterpart, i.e., the transition point to the NEQ regime. In the spheroid wake this transition occurs around $Nt \approx 3$, whereas in the disk it occurs at $Nt \approx 1$, compare the $Fr = 10$ curves between figure 4.4 (a) and (b). The beginning of the NEQ regime is marked by a slowdown in the decay rate of U_d in the stratified wake as compared to its unstratified counterpart. The NEQ regime is also characterized by the progressively increasing anisotropy between the horizontal and vertical components of TKE.

To understand better how this transition occurs we look into the mean kinetic energy (MKE) transport equation. The TKE transport equation was given in equation (4.3). In a similar fashion, the MKE transport equation is given by:

$$U_i \frac{\partial E_K^M}{\partial x_i} + \frac{\partial T_i^M}{\partial x_i} = -P - \varepsilon^M + B^M \,, \tag{4.8}$$

where superscript M denotes the mean counterparts of terms in equation (4.3).

Figure 4.12(a) shows the area-integrated production $\{P\}$ normalized by the Lagrangian change of the MKE ($\{E_K^M\}U_\infty/x$) in the disk and spheroid wakes at $Fr = \infty$ and 10. Likewise, figure 4.12(b) shows the normalized area-integrated mean buoyancy flux $\{B^M\}$. Normalization by the Lagrangian change of MKE allows us to quantify the individual importance of each budget term to the change of MKE .

Broadly, the mean and turbulence quantities in stratified wakes deviate from their unstratified counterparts as a result of buoyancy. In the MKE transport equation, buoyancy can affect (a) the turbulence production P as an indirect effect and (b) the MKE $\leftrightarrow$ MPE transfer, through the mean buoyancy flux B^M. In both the disk and spheroid $Fr = 10$ wakes, we find that the contribution of the mean buoyancy flux to the MKE transport is significantly smaller than the contribution of the production, particularly for $x \lessapprox 40$. Now turning to the area-integrated production in figure 4.12(a), we find that the production at $Fr = 10$ displays a strong reduction from the $Fr = \infty$ wake later in the spheroid at $x \approx 30$ ($Nt \approx 3$) compared to the disk where a similar strong reduction occurs at $x \approx 10$ ($Nt \approx 1$). This explains the late transition of the spheroid wake to the NEQ regime, i.e. U_d deviates from unstratified behavior later ($Nt \approx 3$) for the spheroid than the $Nt \approx 1$ transition point for the disk.

The decreased production in the $Fr = 10$ wakes of both bodies is a consequence of the decreased $\langle u_x' u_z' \rangle$ correlation (not shown here for brevity) in stratified turbulent shear flows. In stratified wakes, this buoyancy effect has been observed experimentally by Spedding (2002b) and numerically by Brucker and Sarkar (2010). The deviation between production of the $Fr = 10$ and ∞ wakes (figure 4.11a) is indeed caused by a reduction in its $\{P_{xz}\}$ component, see blue dashed lines in figure 4.11(b).

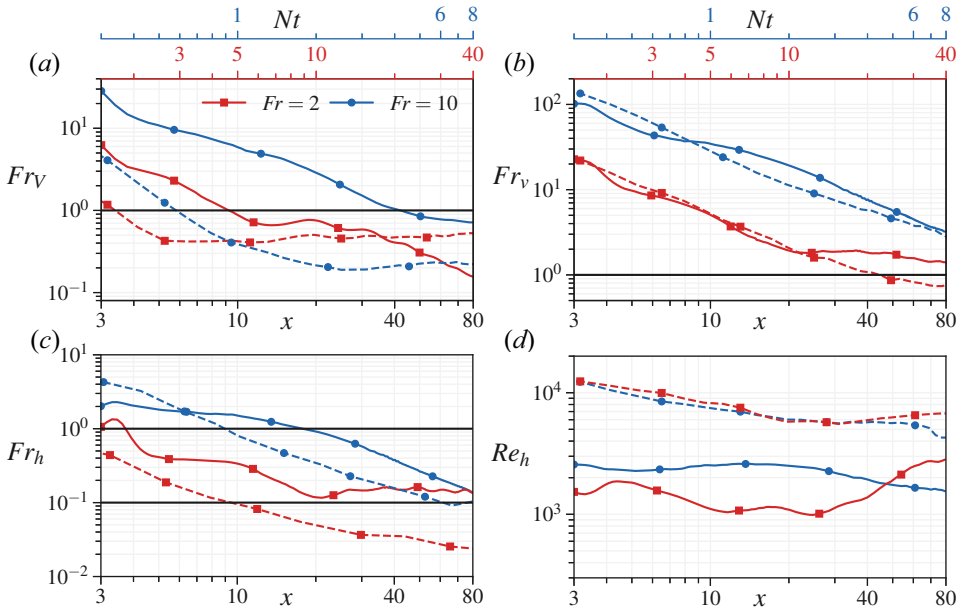

Figure 4.13: Evolution of the spheroid (solid lines) and disk (dashed lines) wakes: (a) local vertical mean Froude number Fr_V, (b) local vertical turbulent Froude number Fr_v, (c) local horizontal turbulent Froude number Fr_h, and (d) local horizontal Reynolds number.

4.6 Evolution of the local flow state and its trajectory in the phase space

In previous sections, we showed how the spheroid and the disk wake do not transition between the 3D, NEQ and Q2D regimes at the same Nt. In this section, we examine the evolution of key local non-dimensional numbers describing the mean and fluctuating state to explore their roles. These non-dimensional numbers are local, streamwise-varying measures of stratification (Froude number) and the dynamical range of inertially dominated scales (Reynolds number). We also plot the trajectory of each wake in the Froude-Reynolds phase space.

The mean vertical Froude number (Fr_V) and the turbulent vertical and horizontal Froude numbers (Fr_v, Fr_h) are defined as

$$Fr_V = \frac{U_d}{2NL_V}, \qquad Fr_v = \frac{u'_h}{Nl_v}, \qquad Fr_h = \frac{u'_h}{NL_{Hk}}, \tag{4.9}$$

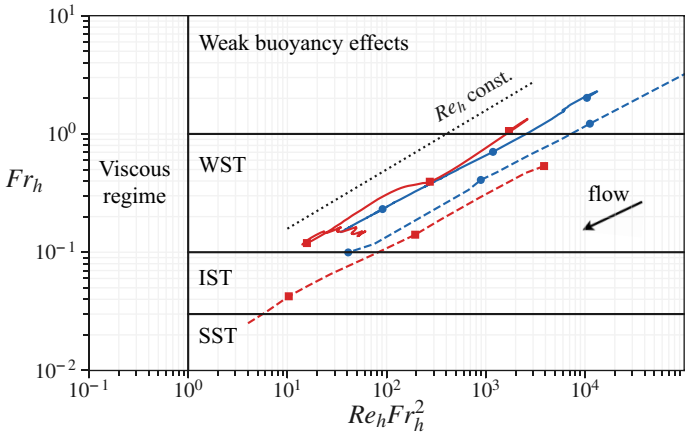

Figure 4.14: Description of the trajectories of spheroid (solid lines) and disk (dashed lines) wakes in $Fr_h - Re_h Fr_h^2$ phase space. Here, $Fr = 2$ and $Fr = 10$ are shown in red and blue, respectively. Dotted black line shows a $Re_h =$ const. line in phase space.

where $u_h' = (\langle u_x'^2 \rangle + \langle u_y'^2 \rangle)^{1/2}$ is the r.m.s. of the horizontal fluctuations and $l_v^2 = \langle u_x'^2 + u_y'^2 \rangle / \langle (\partial_z u_x')^2 + (\partial_z u_y')^2) \rangle$ is a vertical turbulent length scale (Riley and DeBruynKops, 2003).

The mean Froude number is defined consistently with the global Froude number ($Fr = U_\infty / ND$), this is, with the wake full height $2L_V$. The turbulent Froude numbers are defined with turbulence length scales in the energy-containing range. Since the horizontal turbulent integral length scale (l_h) is not easy to compute in a spatially evolving flow, we use the TKE-based horizontal half wake width (L_{Hk}) as a surrogate following CS20. L_{Hk} at a downstream location x is calculated by $E_K^T(y = L_{Hk}, z = 0, x) = 0.5 E_K^T(y = 0, z = 0, x)$.

The mean vertical Froude number Fr_V (figure 4.13a) becomes $O(1)$ in both disk and spheroid wakes at the location at which the decay of U_d slows down signaling the beginning of the NEQ regime, marked by $Nt \approx 1$ for the disk and $Nt \approx 3$ for the spheroid. For the $Fr = 2$ cases, Fr_V in the spheroid wake starts dropping faster beyond $x \approx 40$ – the streamwise location where the wake transitions from NEQ to Q2D regime.

The turbulent Froude numbers play an analogous role to those based on the mean. When their values become $O(1)$, turbulence starts being affected by buoyancy. Fr_v is defined using l_v which has a significance to shear instability. Defined with l_v, Fr_v is proportional to $Ri^{-1/2}$, where

Ri is the Richardson number of the fluctuating shear (Riley and DeBruynKops (2003), CS20). When Fr_v becomes $O(1)$ (figure 4.13b) is also when the spanwise and vertical components of the TKE start showing anisotropy of the turbulence stress tensor and $E^T_{Ky} > E^T_{Kz}$ as shown in figure 4.8 for the $Fr = 2$ wakes. See also figure 8 of CS20.

The avid reader will notice that the four $Fr_v = u'_h/Nl_v$ curves could collapse if plotted against Nt instead of x. Indeed, these curves collapse in the (Fr_v, Nt) plot for $1 < Nt < 10$ and the factor of 5 present between the curves in figure 4.13(b) is simply the ratio of buoyancy frequency N between $Fr = 2$ and $Fr = 10$. This result points to the fact that the spheroid and disk wakes are at a sufficiently high Re so that there is a range of small-scale wake turbulence with dynamics relatively unaffected by the large scales and, therefore, by neither the shape of the wake generator nor buoyancy. u'_h/l_v is a quantity that reflects such dynamics and thus, on dimensional grounds, evolves as $u'_h/l_v \sim t^{-1}$ so that $Fr_v = u'_h/Nl_v \sim (Nt)^{-1}$. We note that buoyancy does affect large scale wake features, which are affected by the body particularities – hence the lack of collapse in Fr_V. The values of the buoyancy Reynolds number $Re_b = \varepsilon/\nu N^2$ and the Reynolds of the Taylor micro-scale $Re_\lambda = \sqrt{k}\lambda/\nu$ where $\lambda^2 = 15\nu u'^2_x/\varepsilon$ (not included here for brevity) are very similar in magnitude for both disk and spheroid wakes at the two levels of stratification. This finding is consistent with the initial collapse of Fr_v when plotted against Nt.

In figure 4.13(c), the $Fr = 10$ wakes of both disk and spheroid reach $Fr_h \sim O(1)$ at $x \approx 10 - 20$, the location at which the $\{E^T_K\}$ starts deviating from its unstratified counterpart (figure 4.8(a,b)). In the $Fr = 2$ spheroid wake, $Fr_h < 1$ throughout the domain and $\{E^T_K\}$ deviates from the unstratified decay from the very beginning in both disk and spheroid wakes. Overall, we find that $Fr_h \sim O(1)$ is a good indicator of the deviation of $\{E^T_K\}$ from the unstratified counterpart. In contrast, $Fr_v \sim O(1)$ marks the location at which turbulence anisotropy between the vertical and the spanwise components starts growing. Figure 4.13(d) shows the evolution of turbulence Reynolds number, $Re_h = u'_h L_{Hk}/\nu$ with u'_h being the intensity of horizontal turbulent fluctuations. The value of Re_h (figure 4.13d) changes slowly as the wake evolves, remaining at $O(10^4)$ for the

disk wake and at $O(10^3)$ for the spheroid wake.

A consolidated view of the evolution of the state of fluctuations is provided in phase space (Brethouwer et al., 2007, Chongsiripinyo and Sarkar, 2020, de Bruyn Kops and Riley, 2019, Zhou and Diamessis, 2019). In the phase-space portrait, one axis measures the buoyancy effect on the large scales through the turbulent Froude number (Fr_h) and the other axis is a measure of Reynolds number that is not Re_h but one which accounts for buoyancy in addition to inertia. Ozmidov-scale eddies are the largest eddies unrestrained by buoyancy. The Ozmidov scales $l_o = (\varepsilon/N^3)^{1/2}$ and $u_o = (\varepsilon/N)^{1/2}$ lead to the definition of $Re_b = u_o l_o/\nu = \varepsilon/\nu N^2$ as the so-called buoyancy Reynolds number. Another convenient measure of Reynolds number, which does not require explicit computation of the turbulent dissipation rate, is the buoyancy-weighted Reynolds number, $Re_h Fr_h^2$ (Billant and Chomaz, 2001, Riley and DeBruynKops, 2003). The Reynolds numbers based on buoyancy tend to decrease with downstream distance as buoyancy progressively increases in importance and limits the range of scales which are susceptible to 3D turbulent motions. As long as $Re_h Fr_h^2 > O(1)$, viscous effects do not dominate.

Following CS20, figure 4.14 shows the evolution all four wakes in the $Re_h Fr_h^2 - Fr_h$ phase space, where $Re_h = u_h' L_{Hk}/\nu$, u_h' being the intensity of horizontal turbulent fluctuations. The flow evolves in the direction of the arrow from a state where buoyancy effects are weak (almost negligible) to a region characterized by the presence of stratified turbulence. Within the state of stratified turbulence, three different regimes can be demarcated: weakly, intermediately, and strongly stratified turbulence (WST, IST, and SST). Unlike the case of freely decaying turbulence, the mean velocity is also important here. Therefore, CS20 elected to distinguish between WST (where buoyancy begins to affect the mean velocity) and IST (where the turbulence anisotropy begins to be affected) as we do here. The SST regime is one where buoyancy effects on the large scales is very strong ($Fr_h \ll 1$) but nevertheless the value of $Re_h Fr_h^2$ is sufficiently large so that viscous effects are not dominant at the large scales.

The slope in the $Re_h Fr_h^2 - Fr_h$ plane is similar for both disk and spheroid wakes in the

weak buoyancy and WST stages. The slope almost follows a line of constant Re_h, marked by a dashed line, signaling the slow evolution of Re_h compared to that of Fr_h. However, there are significant differences in the way the spheroid wakes transverse the phase space. The spheroid wake starts out thinner than the disk wake, leading to larger local Froude numbers. Also, despite the body-based Re being larger in the spheroid wake by a factor of two, the turbulence intensity in the disk wake is higher, hence the Re_h difference observed in figure 4.13(d). This difference in Re_h can be seen in the horizontal offset between the disk and spheroid lines in the phase-space representation.

Despite the larger spheroid body-based Reynolds number – $Re = 10^5$ instead of $Re = 5 \times 10^4$, turbulence in the spheroid wake is unable to access either the the IST regime or the SST regime while the disk wake is able to access these regimes of stratified turbulence. Furthermore, the increase in TKE, which is not observed in the $Fr = 2$ disk wake, reverses the trajectory of the $Fr = 2$ spheroid wake. To the authors' best knowledge, a reversing trend of phase-space trajectory has not been seen before in the stratified turbulence literature. These differences reveal that the phase space evolution, at least for $Fr \leq 10$, depends on the features of the wake generator, e.g., its aspect ratio or the type of BL separation.

Based on the phase-space portrait alone, one may hastily conclude that stratified slender body wakes always experience a weaker buoyancy effect relative to bluff bodies. This is true for the $Fr = 10$ case, at least for the limited Nt simulation time, in terms of the relative amount of TPE (figure 4.10) and the vertical scale (L_V) deviation from the unstratified case – note that both are smaller in the spheroid wake than in the disk. However, we have also shown that for the $Fr = 2$ spheroid wake, compared to the disk wake, there is a much earlier onset of the Q2D regime. The mean and turbulence quantities are highly intertwined and the strong modulation of the mean flow by steady lee waves of the high aspect-ratio spheroid in the $Fr = 2$ case ultimately leads to an early entry into the Q2D regime. Hence, it is not entirely accurate to say that the slender body wakes are weakly affected by stratification. The present work calls for a need to

generalize the parameter space of $\{Re, Fr\}$ in turbulent shear flows to account for the mean flow field (also possibly its instabilities) to build a more comprehensive understanding of buoyancy effects in shear flows. In the case of wakes, the shape of the body generator is brought into play through the mean flow as shown here.

4.7 Discussion and final remarks

The high-Reynolds number stratified wake of a slender body has been studied using a high-resolution hybrid simulation. The wake generator is a 6:1 prolate spheroid with a tripped turbulent boundary layer, the diameter-based Reynolds number is $Re = 10^5$ and the Froude numbers, namely $Fr = U_\infty/ND = \{2, 10, \infty\}$, take moderate to large values. By comparing the spheroid wake with the disk wake of Chongsiripinyo and Sarkar (2020) (referred to as CS20), we are able to study the influence of the wake generator - slender versus bluff - in the establishment and evolution of stratified wakes.

The near wake of the 6:1 prolate spheroid with a turbulent boundary layer is characterized by a small recirculation region ($\sim 0.1D$). The recirculation region is surrounded by small-scale turbulence that emerges from the boundary layer and the flow does not show strong vortex shedding at the body(Jiménez et al., 2010, Kumar and Mahesh, 2018, Ortiz-Tarin et al., 2021, Posa and Balaras, 2016). As a result, the wake is much thinner and develops slower than the wake of a bluff body like the disk, which has a large recirculation region ($\sim 2D$) and vortex shedding from the body (Nidhan et al., 2020). These body-dependent features of the near wake were recently shown to affect the decay of the far wake in environments without density stratification (Ortiz-Tarin et al., 2021). In the present stratified simulations also we find substantial differences in the decay of the disk and spheroid wake. Particularly, we find that the starting locations of the non-equilibrium (NEQ) and the following quasi-2D (Q2D) regions of wake deficit velocity depend on the wake generator.

At $Fr = 2 \approx (L/D)/\pi$, the wake of a 6:1 prolate spheroid is in a resonant state. The half wavelength of the lee waves is equal to the body length and, as a result, the flow separation and the wake are strongly modulated by the waves. Whereas previous works had described this regime in laminar-separation configurations of a sphere (Chomaz et al., 1993, Hanazaki, 1988) and a 4:1 spheroid (Ortiz-Tarin et al., 2019), the present results show that the influence of the waves persists even at high Reynolds numbers and with the separation of a turbulent boundary layer. At $Fr = 2$, the flow and the turbulence in the spheroid wake evolve very differently from the disk wake. Both the lack of strong shedding in the near wake (Ortiz-Tarin et al., 2021) and the strong modulation of the mean flow by the lee waves, lead to a wake with vertical and horizontal profiles of mean velocity that depart strongly from Gaussian. These features are not observed in the disk wake at $Fr = 2$, which shows a vertically-squeezed Gaussian topology and a weak imprint of lee waves on the wake dimensions.

At $Fr = 2$, both disk and spheroid wakes transition to the NEQ regime at $Nt \approx \pi$. However the transition to the Q2D regime - with enhanced wake decay relative to the NEQ regime - is very different; whereas the spheroid wake transitions at $Nt \approx 15$, the disk wake does not access the Q2D regime in a domain that spans $Nt \approx 60$. Other bluff bodies, e.g., the towed sphere (Spedding, 1997) show transition to the Q2D regime at $Nt \approx 50$, a location which is also delayed with respect to the spheroid wake. The early transition to the Q2D regime of the spheroid wake is driven by its strong modulation – horizontal contraction and expansion of the wake width – in response to the vertical contraction and expansion by the lee waves. This modulation has a particularly strong effect on the slender wake of a spheroid where the horizontal contraction is a large fraction of the wake width. The early start of the Q2D regime in the spheroid wake is accompanied by a sustained increase of turbulent kinetic energy (TKE), driven by an increase of the horizontal mean shear which acts on the turbulence of the separated boundary layer. The TKE increase is limited to the horizontal velocity with the spanwise component being strongest, having almost an order of magnitude larger energy than the vertical. Although coherent vortical structures and

spanwise flapping are seen in the horizontal motion, pancake eddies are incipient and not fully formed at the end of the domain, $x/D = 80$.

At $Fr = 10$ also, there are differences between the disk and the spheroid wakes. Particularly in the spheroid wake, the beginning of the NEQ stage occurs later, at $Nt \approx 3$ instead of $Nt \approx 1$ ($x \approx 30$ instead of $x \approx 10$). The difference in the start of the NEQ can be attributed to the value of the local mean Froude number $Fr_V = U_d/2NL_v$. As noted previously, the spheroid wake is thinner than the disk wake, the mixing in the near wake is weaker, and as a result the defect velocity in the intermediate wake is larger. These features increase the value of the spheroid wake local Froude number and delay the onset of the buoyancy effect that gives rise to the NEQ regime. Additionally, the analysis of the mean kinetic energy (MKE) transport terms shows that the onset of buoyancy effect on the mean flow of both the disk and spheroid $Fr = 10$ wakes is associated with the decreased energy transfer from MKE to TKE.

Taking the unstratified case as a base line, the effect of buoyancy in the spheroid $Fr = 10$ wake is observed earlier (at $Nt \approx 1$) on the decay of the TKE than its effect (at $Nt \approx 3$) on the decay of U_d. In the spheroid wake at $Fr = 10$, the transfer from TKE to TUE is responsible for the enhanced decay of TKE at $Nt \approx 1$. On the other hand, the decrease in turbulent production at a farther downstream distance (compared to the disk $Fr = 10$ wake) in the spheroid $Fr = 10$ wake is responsible for the slowed decay of the mean defect velocity at $Nt \approx 3$. The decrease in the production is caused by a reduction in the $\langle u'_x u'_z \rangle$ correlation (Brucker and Sarkar, 2010, Spedding, 2002a).

Meunier and Spedding (2004) compared the evolution far into the stratified wake, up to $x \approx 8000$, among several body shapes that also included a 6:1 prolate spheroid and a circular disk. The body Reynolds number was $Re = 5000$ and their diameter based Froude numbers were $Fr = 4$ and 16. When normalized using $D_{\text{eff}} = D\sqrt{C_D/2}$ instead of D, the evolution of the peak defect velocity of different wake generators exhibited approximate collapse for $Nt \gtrapprox 50$ (see their figure 5b) with a Q2D decay rate of $\sim x^{-0.75}$. Similarly, the wake width in the horizontal

of different shapes approximately collapsed for $x/D_{\text{eff}} > 400$ to exhibit a growth rate of $\sim x^{0.35}$. Since their 6:1 spheroid data starts from $x/D \approx 100$ (see their figure 5a), a direct comparison is not possible with our simulations that end at at $x/D = 80$.

In regard to the mean defect decay, a major difference between Meunier and Spedding (2004) and our results is that the transition to Q2D power-law behavior appears earlier, around $Nt \approx 15$, in the $Fr = 2$ spheroid wake relative to the the $Fr = 2$ disk wake which does not transition to the Q2D decay rate until the end of the domain at $Nt = 62.5$. The value of $Re = 10^5$ in the spheroid wake is larger here and it is possible that the features that we have linked to the early onset of the Q2D stage for the spheroid $Fr = O(1)$ wake, i.e., the instability that leads to horizontal meanders and also the enhanced TKE production, are inhibited by viscous damping at the lower Re of the experiments.

The present simulations, both of the disk and the spheroid, do not extend into the very far wake regime reached by their experiments. Future hybrid simulations or experimental work at higher Re that probe the very far wake would clearly be useful. At any given Re and Fr, it will also be of interest to look at how tripping affects the wake evolution for the different body shapes.

The simulations show that the buoyancy timescale Nt alone is not sufficient to determine the state of the wake decay for both generators. However, we find that the value of the local turbulent and mean Froude numbers can be a good proxy to describe some aspects of the wake state. For both disk and spheroid wakes, $Fr_V = U_d/2NL_v$ becomes $O(1)$ at the location at which the decay of U_d slows down; $Fr_h = u_h'/NL_{Hk} \sim O(1)$ marks the location at which the area-integrated TKE of the stratified wake starts deviating from the unstratified case; and $Fr_v = u_h'/Nl_v \sim O(1)$ signals the location at which anisotropy between the different TKE components starts growing.

The buoyancy-weighted Reynolds number ($Re_h Fr_h^2$) has been used widely in stratified flow as a convenient surrogate for the buoyancy Reynolds number ($Re_b = \varepsilon/\nu N^2$) since it displays

similar trends during the flow evolution and the two quantities can be shown to be proportional using classical inviscid scaling of the turbulent dissipation rate. The surrogacy is true for the stratified wakes considered here except for the spheroid $Fr = 2$ wake after its entry into the stage of Q2D wake decay. The horizontal fluctuation energy, therefore Fr_h, increases owing to horizontal meanders and flapping of the flow. However, ε continues to decrease, albeit at a reduced rate relative to the NEQ regime. The value of $Re_b = O(10)$ is not high in the Q2D regime realized here at $Fr = 2$. It remains to be seen if, in the Q2D regime at even higher body-based Reynolds number, the equivalence between $Re_h {Fr^2}_h$ and Re_b is recovered and whether the unusual upward trajectory seen here in $\{Fr_h, Re_h Fr_h^2\}$ phase space is also seen in $\{Fr_h, Re_b\}$ space. The duration of the upward trajectory in phase space until the eventual downward shift toward the viscous regime is also of interest.

The differences between bluff body (disk) and slender body (6:1 spheroid) wakes illustrate the difficulty of finding a universal scaling for the high-*Re* stratified wake. The initial magnitude of U_d for different wake generators and levels of stratification can be roughly scaled with the global *Fr* and the body drag coefficient (Meunier and Spedding, 2004). However, the start and the duration of the NEQ regime cannot be assumed to be independent of the wake generator. We find that rather than a particular Nt, the local mean Froude number is a good proxy for the onset of the NEQ regime in the mean defect velocity and the values of local turbulent Froude number provide guidance for the behavior of TKE, e.g., the onset of buoyancy effect as well as the location at which the ratio of vertical to horizontal TKE starts decreasing. We are unable to connect Froude number to the Q2D regime transition of the wake. More numerical and experimental work spanning different wake generators, different sources of turbulence including freestream turbulence, and longer downstream distances will be instrumental in building a comprehensive picture of the effect of initial/boundary conditions on subsequent wake evolution.

4.8 Acknowledgments

Chapter 4 is a reprint of the material in the article: J. L. Ortiz-Tarin, S. Nidhan, and S. Sarkar, “The high–Re stratified wake of a slender body and its comparison with a bluff body wake”, submitted to Journal of Fluid Mechanics. The dissertation author was the co-primary investigator and co-first author of this work.

Chapter 5

Wake of a slender body at a moderate angle of attack in stratified and homogeneous environments

5.1 Introduction

Despite their widespread presence in applications, slender body flows have received significantly less attention compared to the flows past bluff bodies. There are some particularities that make the study of slender body flows especially challenging. In a numerical simulation, resolving the boundary layer (BL) of a long body is computationally more expensive than resolving the BL of a blunt body. Additionally, in experimental studies, slender bodies can take up a significant portion of the measurement section and, since they normally generate thin wakes, they are potentially harder to probe and measure.

The first experimental study of flow past a slender body dates back to Chevray (1968) who investigated the wake of a 6:1 prolate spheroid at $Re = 4.5 \times 10^5$. The wake measurements spanned a streamwise distance of $x/D = 18$. Han and Patel (1979) conducted an experimental

study of flow past a 4.3:1 spheroid at different angles of attack (α) at $Re \approx 2 \times 10^4$. They primarily focused on the flow separation pattern, identifying two regimes as α was changed: (i) closed or bubble separation and (ii) open or free-vortex type separation. Wang et al. (1990) extended the study of Han and Patel (1979) to prolate spheroids with aspect ratios of 2:1, 3:1, and 4:1 for a wide range of α in the range $[0^\circ, 90^\circ]$. Experimental studies have also been performed at higher *Re* with tripped BL by Fu et al. (1994) and Chesnakas and Simpson (1994). Jiménez et al. (2010) and Ashok et al. (2015a) studied the high *Re* wake of a DARPA SUBOFF at $\alpha = 0^\circ$ and in pitch configurations, respectively. While Jiménez et al. (2010) focused on the self-similarity and scalings in the near to intermediate wake, Ashok et al. (2015a) characterized the wake asymmetries induced due to the pitch configuration.

Numerical simulations have also been used to study slender body flows. Constantinescu et al. (2002) and Wikström et al. (2004) conducted RANS and LES studies of flow past a 6:1 prolate spheroid at $Re = 4.2 \times 10^6$ and $\alpha = 10^\circ$, 20°. Tezuka and Suzuki (2006) carried out a three-dimensional stability analysis study for the flow past a 4:1 spheroid for varying α. For $\alpha \neq 0^\circ$, as *Re* was increased, they found transition from a symmetric to an asymmetric flow configuration in the longitudinal center-plane. The flow asymmetry at nonzero angle of attack was later studied in more detail using DNS by Jiang et al. (2015). In the last few years, the wake of a DARPA SUBOFF has also been studied through LES by Kumar and Mahesh (2018), Posa and Balaras (2016) at $Re \sim O(10^5)$. Ortiz-Tarin et al. (2021) was the first study of an unstratified slender body flow that probed far wake statistics, extending to $x/D = 80$.

The LES study by Ortiz-Tarin et al. (2019) is the first to take background stratification into account for the study of slender body flows. Their high-resolution LES study was conducted for a 4:1 spheroid at zero angle of attack, $Re = 10^4$ and $Fr = \infty, 3, 1$ and 0.5. They analyzed the laminar BL evolution, force distribution, and the near- and far-field characteristics of the steady lee waves. Recently Ortiz-Tarin et al. (2021, 2022a,b) conducted hybrid simulations to investigate the far wake of a slender 6:1 spheroid at zero angle of attack in unstratified and stratified environments.

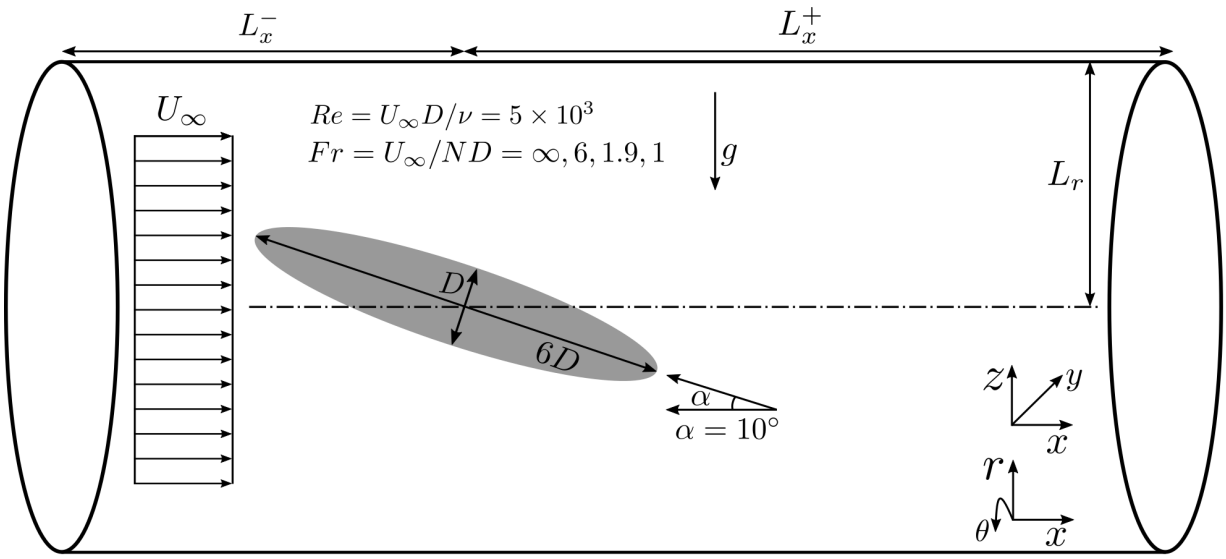

Figure 5.1: Schematic of the flow configuration in the cylindrical solver. L_x^-, L_x^+ and L_r refer to the upstream, downstream and radial domain distance, respectively. *Re*, *Fr* and α correspond to the diameter-based Reynolds number, diameter-based Froude number and angle of attack, respectively.

In recent years, there has also been an increased focus on experimentally characterizing the stratified wakes at non-zero incidence, e.g., Ohh et al. (2022), Ohh and Spedding (2021), owing to their immense importance in hydrodynamic applications. In the current work, we build upon their work studying the effect of varying *Fr* on the flow past a 6:1 spheroid placed at a moderate angle of attack ($\alpha = 10^\circ$). We analyze the effect of stratification on: (i) the variation of C_p, C_f, (ii) the forces on the body, (iii) the flow separation, (iv) the mean wake and streamwise vorticity dynamics, and (v) the unsteady structures and spectra in the wake. We also present a brief analysis of forces on the body at $\alpha = 0^\circ$ for comparison with $\alpha = 10^\circ$ cases. To the best of our knowledge, this is the first study exploring the characteristics of an inclined slender body flow in stratified environments, both on the body as well as in the wake.

5.2 Numerical Methodology

Figure 1 shows the schematic of the simulation set-up wherein a 6:1 prolate spheroid, with major and minor axis given by $L = 6D$ and D respectively, is placed at an angle of attack α in a cylindrical computational domain. Non-dimensional filtered Navier-Stokes equations under the Boussinesq approximation are solved, in conjunction with the continuity and density diffusion equation, to simulate the flow past a prolate spheroid:

(i) continuity,

$$\frac{\partial u_i}{\partial x_i} = 0, \tag{5.1}$$

(ii) momentum,

$$\frac{\partial u_i}{\partial t} + \frac{\partial (u_i u_j)}{\partial x_j} = -\frac{\partial p}{\partial x_i} + \frac{1}{Re}\frac{\partial}{\partial x_j}\Big[\Big(1 + \frac{\nu_s}{\nu}\Big)\frac{\partial u_i}{\partial x_j}\Big] - \frac{1}{Fr^2}\rho'\delta_{i3}, \tag{5.2}$$

(iii) density diffusion,

$$\frac{\partial \rho}{\partial t} + \frac{\partial (\rho u_j)}{\partial x_j} = \frac{1}{RePr}\frac{\partial}{\partial x_j}\Big[\Big(1 + \frac{\kappa_s}{\kappa}\Big)\frac{\partial \rho}{\partial x_j}\Big]. \tag{5.3}$$

Equations 5.1-5.3 are solved to obtain non-dimensional velocity u_i, density ρ, and pressure p as the flow evolves. Following the Boussinesq approximation, ρ is decomposed as follows:

$$\rho(x_i,t) = \rho_0 + \rho_b(x_i) + \rho'(x_i,t), \tag{5.4}$$

where ρ_0 corresponds to the base density, $\rho_b(x_i)$ is the background density variation and $\rho'(x_i,t)$ is the density fluctuation. For linear stratification, $\partial\rho_b(x_i)/\partial z = C$, where C is a constant. It is assumed that $\rho_b/\rho_0 << 1$ and $\rho'/\rho_0 << 1$, which lead to the simplified continuity and momentum equations as shown in equations 5.1 and 5.2 respectively.

The following parameters are used for the non-dimensionalization: (i) free-stream velocity

U_∞ for u_i, (ii) minor axis length D for x_i, (iii) dynamic pressure $\rho_0 U_\infty^2$ for p, (iv) D/U_∞ for time t, (v) $-DC$ for density, (vi) kinematic viscosity ν for the subgrid kinematic viscosity ν_s, and (vii) molecular diffusivity κ for the subgrid molecular diffusivity κ_s.

The non-dimensionalization procedure leads to the following non-dimensional parameters: (i) Reynolds number $Re = U_\infty D/\nu$, (ii) Froude number $Fr = U_\infty/ND$, where N is the buoyancy frequency given as $N = \sqrt{-gC/\rho_0}$, and (iii) Prandtl number $Pr = \nu/\kappa$. In our simulations, we keep the Re and Pr fixed at values of 5000 and 1 respectively while varying the Fr and fixing angle of attack α at 10°. Various parameters of different simulation cases are presented in table 5.1.

The 6:1 prolate spheroid is represented in the computational domain using immersed boundary method (IBM) of Balaras (2004), Yang and Balaras (2006). The governing equations given from equation 5.1-5.3 are solved in cylindrical coordinates for the pressure p, density ρ, and three velocity components, u_r, u_θ, u_x. Here, r, θ, and x correspond to the radial, azimuthal, and axial directions respectively. These directions along with the Cartesian coordinate system are also shown in figure 5.1. Second-order finite difference schemes are used to calculate the spatial derivatives while the temporal marching is performed using a fractional step method which combines the Crank Nicolson method with the low-storage Runge-Kutta scheme (RKW3). The pressure Poisson equation in the predictor step is solved using a direct solver (Rossi and Toivanen (1999)). The kinematic subgrid viscosity ν_s and density diffusivity κ_s are obtained using the dynamic Smagorinsky model given by Germano et al. (1991). For a detailed description of the solver employed here, readers can refer to Chongsiripinyo and Sarkar (2020), Pal et al. (2017).

At inlet, an uniform inlet velocity boundary condition, $[u_x, u_r, u_\theta] = [U_\infty, 0, 0] = \mathbf{U}$, is prescribed for velocity components. The outlet boundary condition for velocities corresponds to the Orlanski-type convective boundary condition (Orlanski (1976)). The pressure p is set to zero at the inlet boundary. On the rest of the boundaries (outlet and radial), a Neumann boundary condition is used for pressure. For stratified cases, a Robin boundary condition is used at radial

Table 5.1: Simulation parameters at $\alpha = 10^\circ$.

Case	Re	α	Fr	L_r	L_θ	L_x^-	L_x^+	N_r	N_θ	N_x
1	5000	10°	∞	22	2π	12	48	718	256	2560
2	5000	10°	6	53	2π	30	53	1000	128	3584
3	5000	10°	1.9	53	2π	30	53	1000	128	3584
4	5000	10°	1	53	2π	30	53	1000	128	3584

boundary satisfying $\partial\rho/\partial z = C$. This means that the density variation far away from the wake generator is unperturbed. On the body surface, a no-slip condition is prescribed for velocity and the normal gradients of pressure and density are set as zero. To avoid reflection of internal gravity waves from the boundaries, a sponge layer for velocity and density is used at the inlet, outlet, and radial boundaries of the form $\phi(\mathbf{x})(\mathbf{u}-\mathbf{U})^2$ and $\phi(\mathbf{x})(\rho-\rho_b)^2$. Here, ρ_b corresponds to the background density state.

At $\alpha = 0^\circ$, we simulate the wakes until a downstream distance of $x/D = 30$. The radial extent of the domain is $r/D = 17$ and 53 for unstratified and stratified cases, respectively. The grid point distribution for $\alpha = 0^\circ$ cases are as follows: $N_r = 1000$ and 910 for stratified and unstratified cases, respectively, N_θ = 128, and $N_x = 3584$. They are not presented in the form of a table here for brevity.

5.3 Body forces at $\alpha = 0^\circ$

Figure 5.2(a) and (b) show the variation of the pressure coefficient $C_p = (P - P_\infty)/0.5\rho U_\infty^2$ and skin-friction coefficient $C_f = Re^{0.5}|\tau_x|/0.5\rho U_\infty^2$, respectively, for different values of Fr at $\alpha = 0^\circ$. In the reported C_f, the raw skin friction coefficient is multiplied by $Re^{0.5}$ to obtain an $O(1)$ value. The $\theta = 0^\circ$ and 90° labels correspond to the horizontal $x-y$ and vertical $x-z$ plane, respectively. An averaging time window of $30D/U_\infty$ is used to obtain these results.

For $Fr \geq 1.9$ cases (figure 5.2(a)), the drop of pressure and its recovery primarily occur towards the beginning and the end of the body, respectively. For $-2 \lessapprox x/D \lessapprox 1$, C_p remains

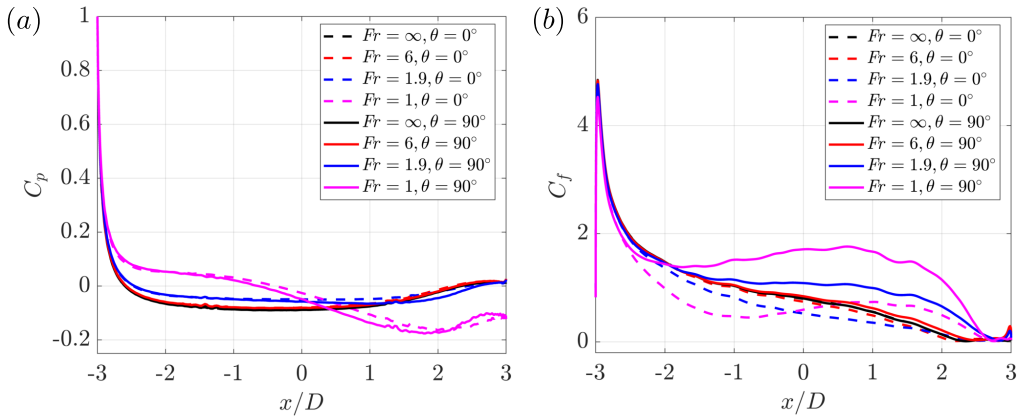

Figure 5.2: Variation of (a) pressure coefficient C_p and (b) skin-friction coefficient C_f for different Fr at $\alpha = 0°$. The $\theta = 0°$ and 90° curves correspond to variations on the surface in the horizontal and vertical plane, respectively. Plotted value of C_f is $Re^{0.5}$ times the friction coefficient.

approximately constant for $Fr \geq 1.9$. On the other hand, C_p in $Fr = 1$ case shows a monotonic decay till $x/D \approx 2$ and a slight recovery for $x/D \gtrapprox 2$, indicating strong effect of buoyancy on the flow over the body. For $Fr \geq 1.9$, C_p variations are qualitatively very similar. The differences between $Fr = \infty$ and the critical Fr_c curves are less pronounced in the 6:1 spheroid ($Fr_c = 1.9$) than what was observed in the 4:1 spheroid ($Fr_c \approx 1$) as reported by Ortiz-Tarin et al. (2019). Anisotropy between horizontal and vertical plane C_p curves appears at $Fr = 1.9$ and increases slightly at $Fr = 1$. Pressure visualizations (not shown here) confirm that the low pressure region in the tail of the spheroid (in the vertical plane) at $Fr = 1$ is imposed by the steady lee-wave field, indicating a strong influence of buoyancy on the flow at this value of Fr.

Figure 5.2(b) shows the variation of C_f for different Fr at $\alpha = 0°$. Similar to the behavior of C_p, the variation of C_f for $Fr = 6$ and ∞ are very similar. The flow separates at $x/D = 2.34$ for the unstratified flow (marked by $C_f \to 0$). This value is in excellent agreement with the result of Patel and Kim (1994). $Fr = 1.9$ shows elevated and suppressed levels of C_f in vertical and horizontal planes, respectively, compared to $Fr = 6$ and ∞. At $Fr = 1$, C_f in the vertical plane further increases compared to $Fr = 1.9$. Moreover, in the horizontal plane as well, $Fr = 1$ shows higher C_f than $Fr = \infty$ and 6 for $x/D \gtrapprox 0.5$. Increased C_f in the vertical plane for $Fr = 1$ and 1.9

Table 5.2: Drag coefficients (C_d) and corresponding pressure (C_d^p) and friction contributions (C_d^f) for $\alpha = 0^\circ$ at different Fr.

$\alpha = 0^\circ$, Fr	C_d	C_d^f	C_d^p	$\Delta C_d = C_d - C_d(\infty)$
$Fr = \infty$	0.24	0.22	0.02	0
$Fr = 6$	0.26	0.23	0.03	0.02
$Fr = 1.9$	0.32	0.25	0.07	0.08
$Fr = 1$	0.52	0.29	0.23	0.28

is a consequence of thinner BL over the body (not shown here for brevity) compared to $Fr = 6$ and ∞. In the horizontal plane, for $Fr = 1$ (compared to $Fr = \infty$), BL thickens between $x/D \approx -2$ to 0 and gets thinner beyond $x/D \approx 1$, explaining the trend of C_f in the horizontal plane for $Fr = 1$.

Table 5.2 presents $C_d = F_d/(0.5\rho_o U_\infty^2 A)$ for different Fr at $\alpha = 0^\circ$. Here, $A = \pi D^2/4$. There is a monotonic increase in C_d, C_d^p, and C_d^f with increasing stratification levels. Friction contributes more to the drag than pressure (except at $Fr = 1$), as expected for a slender body flow. However, compared to flow past a 4:1 spheroid (Ortiz-Tarin et al., 2019), we find that the effect of stratification on the overall drag, quantified by $\Delta C_d = C_d - C_d(\infty)$, is weaker in the 6:1 spheroid. Between $Fr = \infty$ and $Fr = 1.9$, C_d changes by $\approx 33\%$ in the present case while there was a 100% increase in the 4:1 spheroid. This smaller increase in C_d for 6:1 spheroid is primarily due to a smaller increase in C_d^p at $Fr_c = 1.9$ (compared to $Fr = \infty$), unlike in the 4:1 prolate spheroid. It is only when $Fr = 1$ that we see a sharp jump in C_d^p leading to a $\approx 100\%$ increase in C_d, consistent with the differences we observe in C_p curves (figure 5.2a) between $Fr = 1$ and $Fr \geq 1.9$ cases.

It is a well-established observation that the amplitude of steady lee-waves decreases with increasing value of Fr in the $Fr \geq 1$ regime for a variety of wake generators, including 6:1 prolate spheroid (Bonneton et al., 1993, Meunier et al., 2018). Specifically, Meunier et al. (2018) found that the lee-wave amplitude for a 6:1 spheroid (based on $\partial w/\partial z$) decayed as Fr^{-2}. On the other hand, it should be noted that the definition of critical Fr_c given by Ortiz-Tarin et al. (2019) is based purely on kinematic considerations, i.e., by equating half-wavelength of the lee-wave to

the length of the body. As a result, $Fr_c = L/\pi D$ increases linearly with the aspect ratio. Thus, for the 6:1 spheroid, we see a weaker effect of stratification on the drag at its critical value of $Fr_c = 6/\pi = 1.9$ compared to the 4:1 spheroid for which $Fr_c = 4/\pi = 1.27$ is lower. That the lee wave field in the $Fr = 1.9$ case is weaker than in the $Fr = 1$ case is also confirmed also by quantification of the pressure field, not shown here for brevity.

5.4 Body forces at $\alpha = 10^\circ$

Introducing even a moderate angle of attack, namely $\alpha = 10^\circ$, significantly changes the characteristics of flow on the body, reflected by significantly different trends of C_p, C_f and force coefficients in $\alpha = 10^\circ$ flows compared to their $\alpha = 0^\circ$ counterparts. In what follows, we discuss the trends of above-mentioned quantities when $\alpha = 10^\circ$ and $Fr = \infty, 6, 1.9$, and 1. For $\alpha = 10^\circ$, a time averaging window of approximately $50D/U_\infty$ is used.

5.4.1 Coefficient of Pressure C_p

Figure 5.3(a-h) show the pressure contours on the leeside and windside of the body. We also present the variation of C_p along $y = 0$ line on the leeside and windside in figure 5.3(i,j), respectively. C_p obtained from potential flow solution is also presented for comparison in figure 5.3(i,j). On both sides, the agreement between the potential solutions and LES simulations is excellent till $x/D \approx 1$. Beyond $x/D \approx 1$ LES simulations deviate from potential solutions, presumably due to the three-dimensionality of BL evolution and effects of flow separation. Pressure drop on both sides primarily happens near to the nose of the body and in the ascending order of Fr, i.e., the pressure drop in the nose for $Fr = 1 > 1.9 > 6 > \infty$ (figure 5.3(i)). It is also worth noting that the $Fr = 6$ and ∞ cases show asymmetry in the leeside pressure contours about the $y = 0$ plane as shown in figure 5.3(a,c).

On the leeside, for $Fr \geq 1.9$ cases, pressure recovers continuously, albeit slowly, after

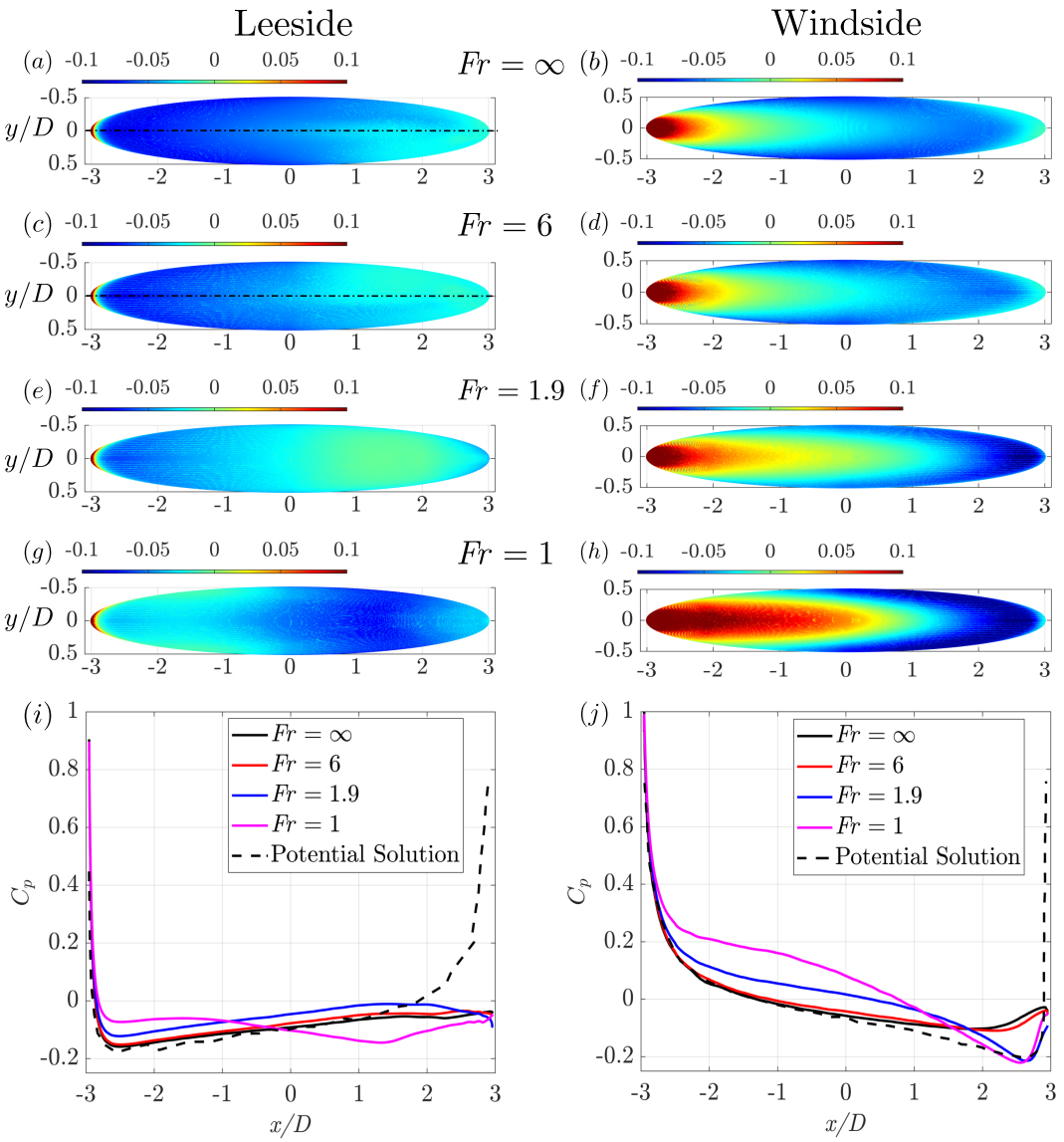

Figure 5.3: Pressure contours on the leeside (a,c,e) and windside (b,d,f) of the spheroid shown for all simulated Fr at $\alpha = 10^{\circ}$. Also shown is the variation of C_p (i, j) on the leeside and windside of the body surface in the $y = 0$ plane. Potential solution for C_p in dashed line from Piquet and Queutey (1992).

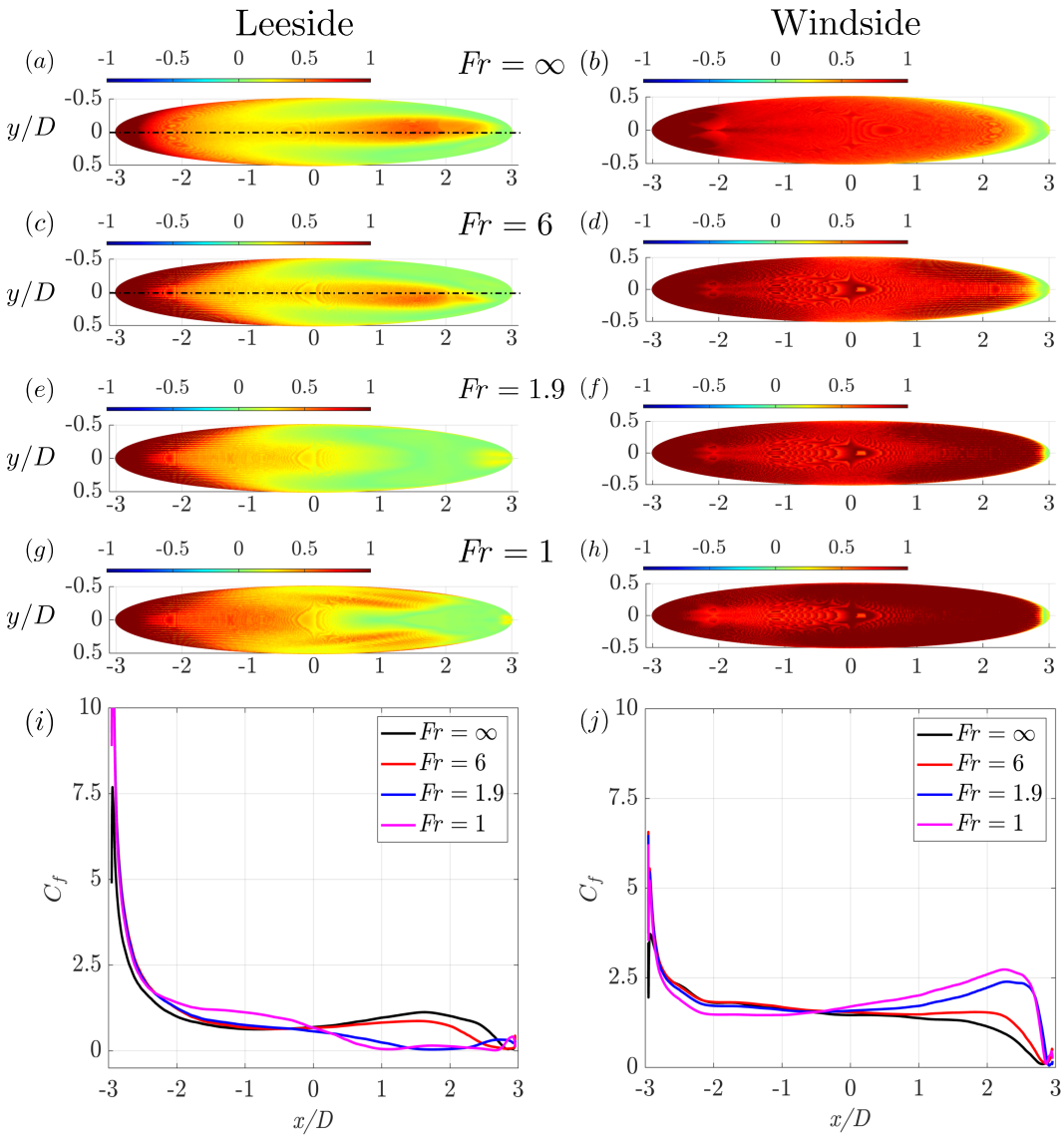

Figure 5.4: Contours of $Re^{0.5}|\tau_x|$ (a-h) on the leeside and windside of the spheroid for all Fr at $\alpha = 10°$. Dashed lines in (a) and (c) correspond to $y = 0$. Variation of C_f (i, j) on the leeside and windside of the body at $y = 0$ plane.

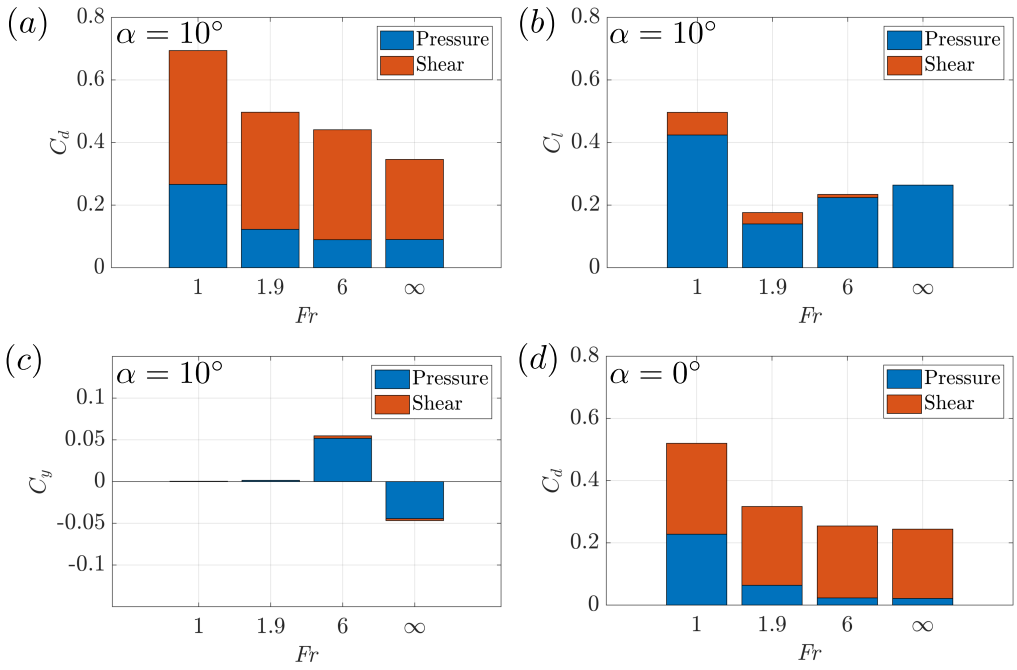

Figure 5.5: Force coefficients decomposed between pressure and shear contribution: (a) coefficient of drag C_d, (b) coefficient of lift C_l, (c) lateral force C_y at $\alpha = 10°$, and (d) C_d at $\alpha = 0°$.

the initial drop in the nose (figure 5.3i). On the contrary, pressure in the $Fr = 1$ case, which shows the lowest initial drop (from the stagnation value at the nose) of all cases in the fore of the body ($x/D < 0$) drops below that of the remaining cases for $x/D > 0$. This is evident both from contours (figure 5.3g) and C_p plots (figure 5.3i). Mean pressure contours in the vicinity of the spheroid (not shown here for brevity), reveal a strong low-pressure region on the entirety of the leeside. This low-pressure region is imposed by the steady lee wave field at $Fr = 1$. The differences between the unstratified case and strongly stratified cases ($Fr = 1.9$ and 1) are even more pronounced on the windside compared to the leeside of the spheroid. Beyond $x/D \approx 2$, C_p of $Fr = 1.9$ and 1 fall significantly below those of $Fr = \infty$ and 6 (figure 5.3j), followed by a sharp recovery towards the end. The contours in figure 5.3(b,d,f,h) confirm this trend of higher and lower pressure at the head and tail, respectively, for the $Fr = 1$ and 1.9 cases compared to $Fr \geq 6$.

5.4.2 Coefficient of Friction C_f

Figure 5.4(a-h) show the contours of scaled shear stress $Re^{0.5}|\tau_x|$ on the leeside (left) and windside (right) for all cases at $\alpha = 10^\circ$. In figure 5.4(i,j), we present the variation of C_f on the spheroid surface and in the $y = 0$ plane on both sides. Similar to the pressure contours, a distinct asymmetry is present on the leeside of $Fr = \infty$ and 6 flows as shown figure 5.4(a,c), to be discussed in more detail in the next subsection.

The shear stress contours show that flow separation primarily happens on the leeside at $\alpha = 10^\circ$ across all Fr. The region of separated flow can be identified by the region of $|\tau_x| \to 0$, marked in green in figure 5.4 contours. For $Fr = \infty$ and 6, flow separates primarily from the two lateral sides on the lee of the body (figure 5.4(a,c)). There is a central region near $y = 0$ which remains attached until nearly the tail. In the $Fr = 1.9$ case, separation occurs from the sides as well as the central region around the $y = 0$ plane (figure 5.4e) while in the $Fr = 1$ case, separation primarily happens in the central region (figure 5.4g) and not at the sides. Thus, it can be inferred that the stratification level strongly influences the flow separation even at the moderate non-zero angles of attack of this study.

In the vertical-center plane ($y = 0$), C_f varies similarly for all Fr on both sides (figure 5.4(i,j)) till $x/D \approx 0$. On the leeside (figure 5.4i) and for $x/D \geq 0$, the $Fr = \infty$ and 6 cases show higher C_f than the strongly stratified cases of $Fr = 1.9$ and 1. On the windside, beyond $x/D \approx 1$, $Fr \leq 1.9$ cases show elevated C_f as compared to $Fr \geq 6$ (figure 5.4j). This region of elevated surface shear in the $Fr = 1.9$ and 1 flows coincides with the region of steep pressure drop observed at $x/D > 1$ (figure 5.3j).

5.4.3 Force Coefficients

Figure 5.5(a,b,c) present the force coefficients ($C_i = F_i/0.5\rho U_\infty^2 A$) at $\alpha = 10^\circ$, decomposed between pressure and friction contributions. Here C_x, C_y and C_z correspond to drag (C_d), lateral

force, and lift (C_l) on the body, respectively. We first discuss C_d and C_l and follow by noting the unusual characteristics of C_y for $\alpha = 10^\circ$. Figure 5.5(d) also shows C_d for $\alpha = 0^\circ$ for reference. In $\alpha = 0^\circ$ cases, $C_l \approx 0$ and $C_y \approx 0$ at all Fr indicating no asymmetry in the flow over body.

For all Fr, C_d, C_d^f and C_d^p (figure 5.5a) at $\alpha = 10^\circ$ increase relative to the zero degree angle of attack ((figure 5.5d). Similar to $\alpha = 0^\circ$, there is a weak monotonic increase in C_d till $Fr = 1.9$ and a large jump thereafter at $Fr = 1$. This jump primarily comes from an approximately 100% increase in C_d^p from $Fr = 1.9$ to $Fr = 1$. Figure 5.3(g,h) show that the pressure contours at $Fr = 1$ are quite different from those of $Fr \geq 1.9$. The tail and nose on the leeside and windside, respectively, are at a lower and higher pressure (compared to $Fr \geq 1.9$ cases) which leads to an enhanced C_d^p. For C_l, primary contributor is the pressure rather than shear, as expected for a moderate angle of attack. It is interesting to note that C_l decreases till $Fr = 1.9$ and then increases significantly at $Fr = 1$ case, resulting from an increase in C_l^p. The reason for this increase is the large difference between the leeside and windside pressure in $Fr = 1$ flow as shown in figure 5.3(g,h).

Figure 5.5(c) shows that $C_y \neq 0$ for $Fr = \infty$ and 6 at $\alpha = 10^\circ$. For $Fr = \infty$, $C_y \approx -0.05$ and for $Fr = 6$, $C_y \approx 0.05$. This value is approximately 12% of the streamwise drag force in both cases. Intuitively, C_y should be equal to zero due to reflectional symmetry in the configuration about the $y = 0$ plane. Non-zero C_y implies lateral asymmetry in the flow on the body. Pressure and friction contours in figure 5.3(a,c) and 5.4(a,c), respectively, show that this is indeed the case and the asymmetry originates on the leeside of the body at $x/D \gtrapprox 1$ (the $y = 0$ intersection of the body surface is shown to better identify this lateral asymmetry). No asymmetry is present on the windside flow over the spheroid. When the value of Fr is decreased to 1.9, $C_y \to 0$. Further decrease to $Fr = 1$ also results in $C_y = 0$. This indicates that the flow asymmetry is suppressed as the stratification is increased. Figure 5.3(e,g) and figure 5.4(e,g) also confirm that for $Fr = 1.9$ and 1, no asymmetry is visually evident on the leeside of the spheroid. Hence, two important findings from the analysis of C_y are: (i) the weakly stratified ($Fr = 6$) and unstratified ($Fr = \infty$) flow

exhibit lateral asymmetry and (ii) this asymmetry is suppressed as the strength of stratification is increased, i.e., at $Fr = 1.9$ and 1.

Our finding regarding lateral asymmetry in the unstratified case is in accord with previous studies on flow past slender bodies (Ashok et al., 2015a,b, Jiang et al., 2015, Tezuka and Suzuki, 2006). It is also interesting to note that the C_y of $Fr = \infty$ and $Fr = 6$ are similar in magnitude but flipped in sign. We hypothesize that the $Fr = \infty$ and $Fr = 6$ flows might be locked in two different reflectional-symmetry-breaking states, with each state being equally probable. There can be a switching between these two states at a very large timescale. The existence of a long time scale for switching between different reflection-symmetry-breaking states have been extensively researched in flow past three-dimensional blunt bodies (Dalla Longa et al., 2019, Grandemange et al., 2013, Rigas et al., 2014). Interestingly, Jiang et al. (2015), who also found lateral asymmetry in their flow (6:1 spheroid at $\alpha = 45^\circ$), did not find a switch even after $600D/U_\infty$. We aim to investigate the characteristics of the intermediate to far wake, besides looking at near-body flow. Hence, running the simulations for $T \sim 1000D/U_\infty$ would be prohibitively expensive and out of scope of the current work.

5.5 Mean wake field in $\alpha = 10^\circ$ cases

5.5.1 Mean wake velocity and lengthscales

After describing the mean flow field over the body, we move to the description of the mean wake at near and intermediate distances. Figure 5.6 shows the mean defect velocity U_d contours across all Fr and streamwise locations $x/D = 3, 10, 20$ and 30.

For the unstratified case and $Fr = 6$, the asymmetry, observed in the pressure and shear profiles on the body, leaves its imprint on the ensuing near wake as well (see figure 5.6(a,b,e,f)). The reversal of the asymmetry between the $Fr = \infty$ and $Fr = 6$ cases is also observed in the contours at $x/D = 3$ and 10. At $Fr = 1.9$ and 1, U_d contour is symmetric across $y/D = 0$ plane.

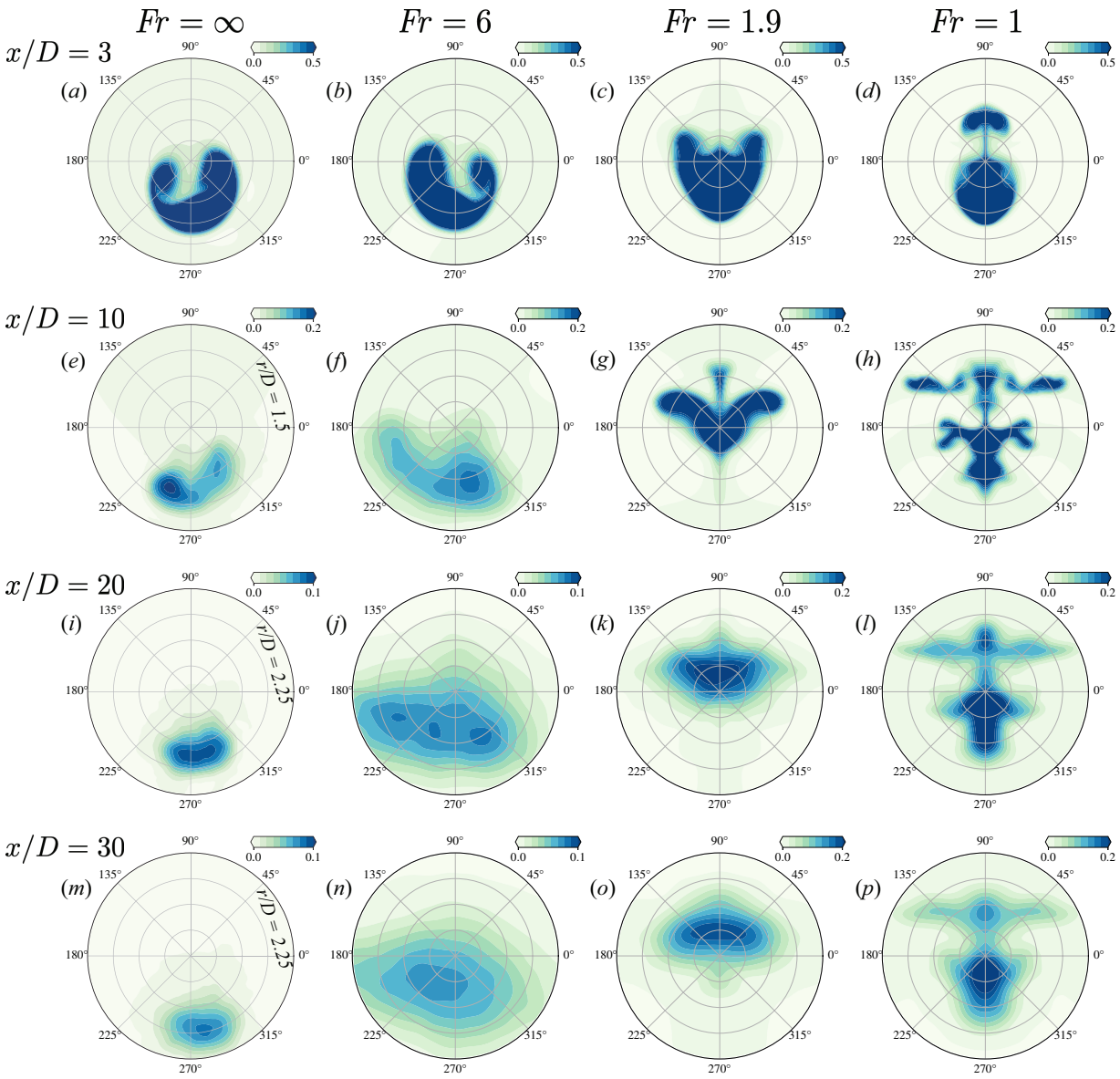

Figure 5.6: Mean defect velocity (U_d) contours at $x/D = 3, 10, 20$ and 40 (row-wise) for $Fr = \infty, 6, 1.9$ and 1 (column-wise). The radial domain is $r/D = 1$ unless explicitly mentioned (see $x/D = 10, 20, 40$ for the $Fr = \infty$ wake).

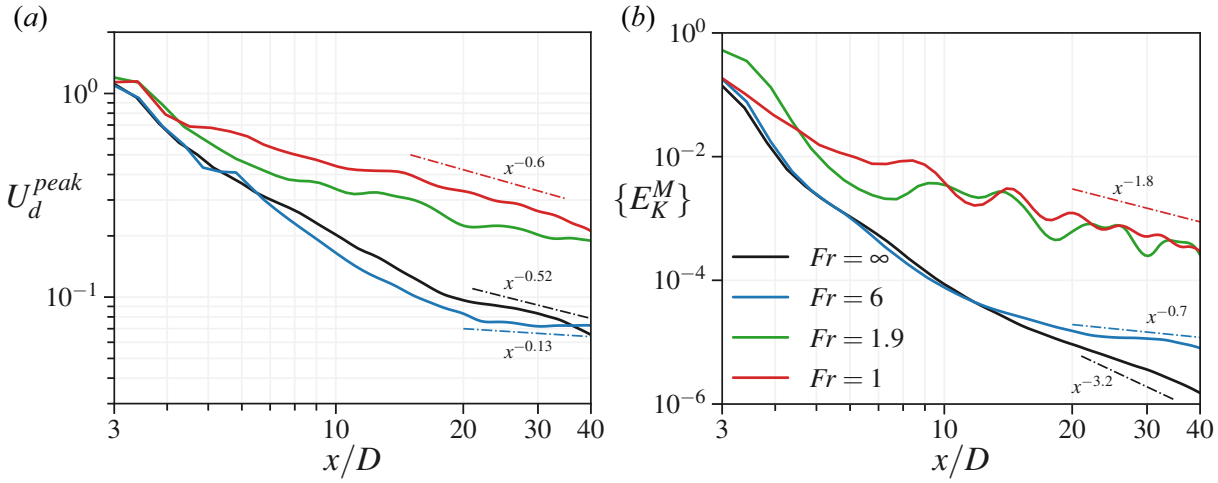

Figure 5.7: (a) Decay of the mean defect velocity peak, U_d^{peak}, and (b) area-integrated mean kinetic energy, $\{E_K^M\}$, decay for $\alpha = 10^\circ$ cases.

A double-lobed structure of U_d appears at $Fr = 1$, figure 5.6(d). These two lobes are connected by a thin thread lying on the $y/D = 0$ plane.

As the wake evolves downstream, the initial asymmetry causes both $Fr = \infty$ and $Fr = 6$ wakes to be displaced from the $y/D = 0$ line (figure 5.6(i,j,m,n)). The unstratified wake continuously drifts away from the centerline. Due to the inhibiting effect of buoyancy in the vertical direction, the extent of veering away from the centerline is contained in the $Fr = 6$ wake. By $x/D = 30$, the wake center appears to settle at a slightly negative vertical location in the $Fr = 6$ wake (figure 5.6(j,n)). In the $Fr = 1.9$ case, U_d shows an oscillation in the vertical direction initially, compare figure 5.6(c) to 5.6(k). Unlike the $Fr = \infty$ and 6 cases, the wake center remains on the $y/D = 0$ line. The two lobes in the $Fr = 1$ maintain their integrity until $x/D = 30$. Both these lobes spread in the horizontal direction as x/D increases. Figure 5.6 shows that differences in the initial flow separation have a lasting impact on the mean wake profiles of the simulated cases. By $x/D = 30$, there are significant qualitative differences across these cases.

Figure 5.7(a) shows the decay of peak mean defect, U_d^{peak} as a function of x/D for all four cases. The magnitude of U_d^{peak} follows the following order: U_d^{peak} for $Fr = 1 > Fr = 1.9 > Fr = 6 > Fr = \infty$ beyond $x/D \approx 6$. The unstratified wake transitions from a faster decay rate

to $\sim x^{-0.52}$ from $x/D \approx 20$ onward. Around the same time, the decay of $Fr = 6$ slows down significantly to $\sim x^{-0.13}$, signaling the increasing dominance of stratification. U_d^{peak} in $Fr = 1.9$ and $Fr = 1$ cases show a decay rate of $U_d^{peak} \sim x^{-0.6}$ for $x/D > 15$. Figure 5.7(b) shows the decay of area-integrated mean kinetic energy, $\{E_K^M\} = \int_C (U_d^2 + \langle u_y \rangle^2 + \langle u_z \rangle^2 \mathrm{dC}$, of simulated cases. Cross-section areas of radii $r/D = 2$ and $r/D = 3.5$ are used for the stratified cases and the unstratified case, respectively. These radii ensure that the wakes lie inside the domain of integration for all x/D. The MKE of $Fr \sim O(1)$ wakes is higher than the $Fr = \infty$ and $Fr = 6$ cases by almost two orders of magnitude. Unlike the decay of U_d^{peak}, lee-wave induced oscillations are visible in both $Fr = 1.9$ and 1 wakes. The area-integrated energy in both $Fr \sim O(1)$ wakes is of comparable magnitude throughout the domain. The unstratified wake and $Fr = 6$ wake $\{E_K^M\}$ values remain close till $x/D \approx 13$ after which the decay rate of $Fr = 6$ wake slows down significantly compared to the unstratified wake.

Figure 5.6 makes it clear that wakes of the prolate spheroid at an angle of attack need not be centered at the $r/D = 0$ line and evolve in a complex fashion, both in terms of wake lengthscales and center. Figure 5.8 presents the evolution of wake center and lengthscale in the spanwise and vertical direction as a function of x/D. Following Brucker and Sarkar (2010) and de Stadler and Sarkar (2012), these quantities are calculated as follows:

$$Y^C = \frac{\int y U_d^2 \mathrm{dA}}{\int U_d^2 \mathrm{dA}}, \qquad Z^C = \frac{\int z U_d^2 \mathrm{dA}}{\int U_d^2 \mathrm{dA}} \tag{5.5}$$

$$L_y^2 = \frac{\int (y - Y^C)^2 U_d^2 \mathrm{dA}}{\int U_d^2 \mathrm{dA}}, \qquad L_z^2 = \frac{\int (z - Z^C)^2 U_d^2 \mathrm{dA}}{\int U_d^2 \mathrm{dA}} \tag{5.6}$$

Figure 5.8(a,b) shows the evolution of the wake center in the horizontal and vertical direction, respectively, as a function of downstream distance. It becomes clear that all four wakes evolve in a very different manner. The unstratified wake veers away in both y/D and z/D coordinates as the flow evolves, more so in the z (vertical) direction than the y (horizontal)

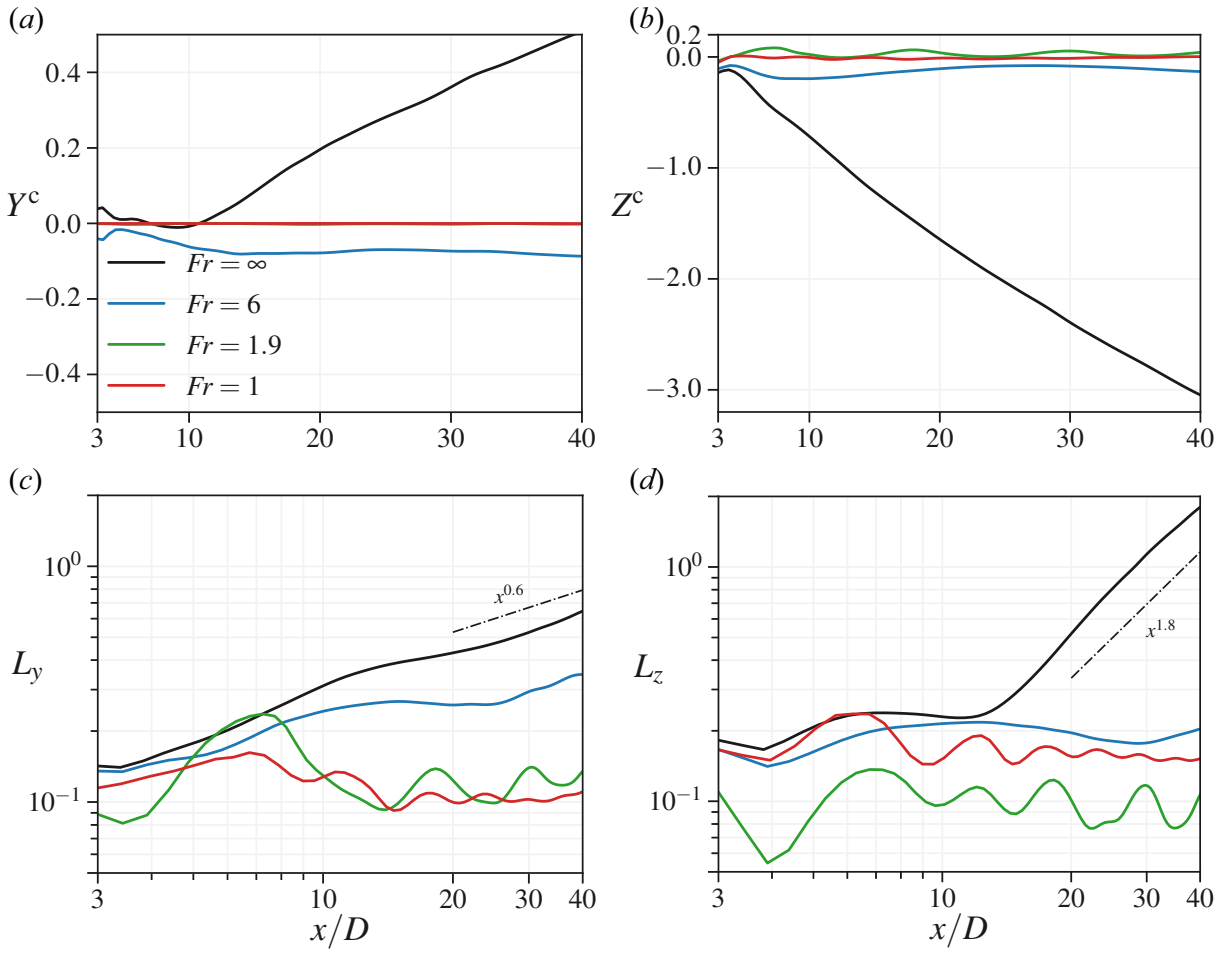

Figure 5.8: Evolution of wake center in the (a) horizontal (Y^c) and (b) vertical (Z^c) directions. Evolution of wake (a) horizontal (L_y) and (b) vertical (L_z) lengthscales.

direction. Though both the unstratified wake and the $Fr = 6$ wake start from the body in a very similar fashion (figure 5.6(a,b)), their further development, in terms of the wake center, deviate very early on. Y^C for the $Fr = 6$ wake asymptotes to a value of ≈ -0.09 (figure 5.8a) while Z^C (figure 5.8b) stays very close to the zero value. Readers with a keen eye can also notice a very weak oscillation of wavelength $\lambda/D = 2\pi Fr$ in the Z^C of the $Fr = 6$ wake. Y^C of the $Fr = 1.9$ and 1 wake remain zero throughout their evolution, see figure 5.8(a). In the vertical direction, the $Fr = 1.9$ wake shows a lee-wave induced oscillation in the Z^C trend (figure 5.8b). It is quite interesting to note that the Z^C of the $Fr = 1$ wake also stays close to zero, implying that the vertical coordinate centers of the two lobes in figures 5.6(d,h,l,p) balance each other out.

Figure 5.8(c,d) show the evolution of horizontal (L_y) and vertical (L_z) lengthscale, respectively. L_y of $Fr = \infty$ and 6 wakes evolve in a similar fashion, albeit L_y of the $Fr = 6$ wake is consistently smaller than the unstratified wake. The other two cases show an initial contraction of L_y between $7 < x/D < 15$ and a very weak increase thereafter. Contrary to L_y, L_z evolution between the $Fr = \infty$ and 6 wake is quite different. While the unstratified wake has a growth of $L_z \sim x^{1.8}$ beyond $x/D \approx 10$, the $Fr = 6$ wake vertical lengthscale increases only slightly between $x/D = 3$ and 40. The $Fr \sim O(1)$ wakes, on the other hand, show a slight reduction in L_z. All three stratified cases have an imprint of lee-wave-induced oscillation in L_z trends.

5.5.2 Mean streamwise vorticity field in the wake

Next, we investigate the dynamics of streamwise vortices developing over the body and in the wake in this subsection. Figure 5.9 shows the instantaneous streamwise vorticity ω_x at locations $x/D = 0, 1, 2$ and 2.75 as the flow develops over the body. We present the view at these four locations from left and right to focus on the structure of both the negative and positive vorticity, respectively.

In the $Fr = \infty$ and 6 cases, the vortex filaments can be seen as early as $x/D = 0$ (figure 5.9(a,b,c,d)). By $x/D = 1$, they develop identically, maintaining the symmetry about the vertical

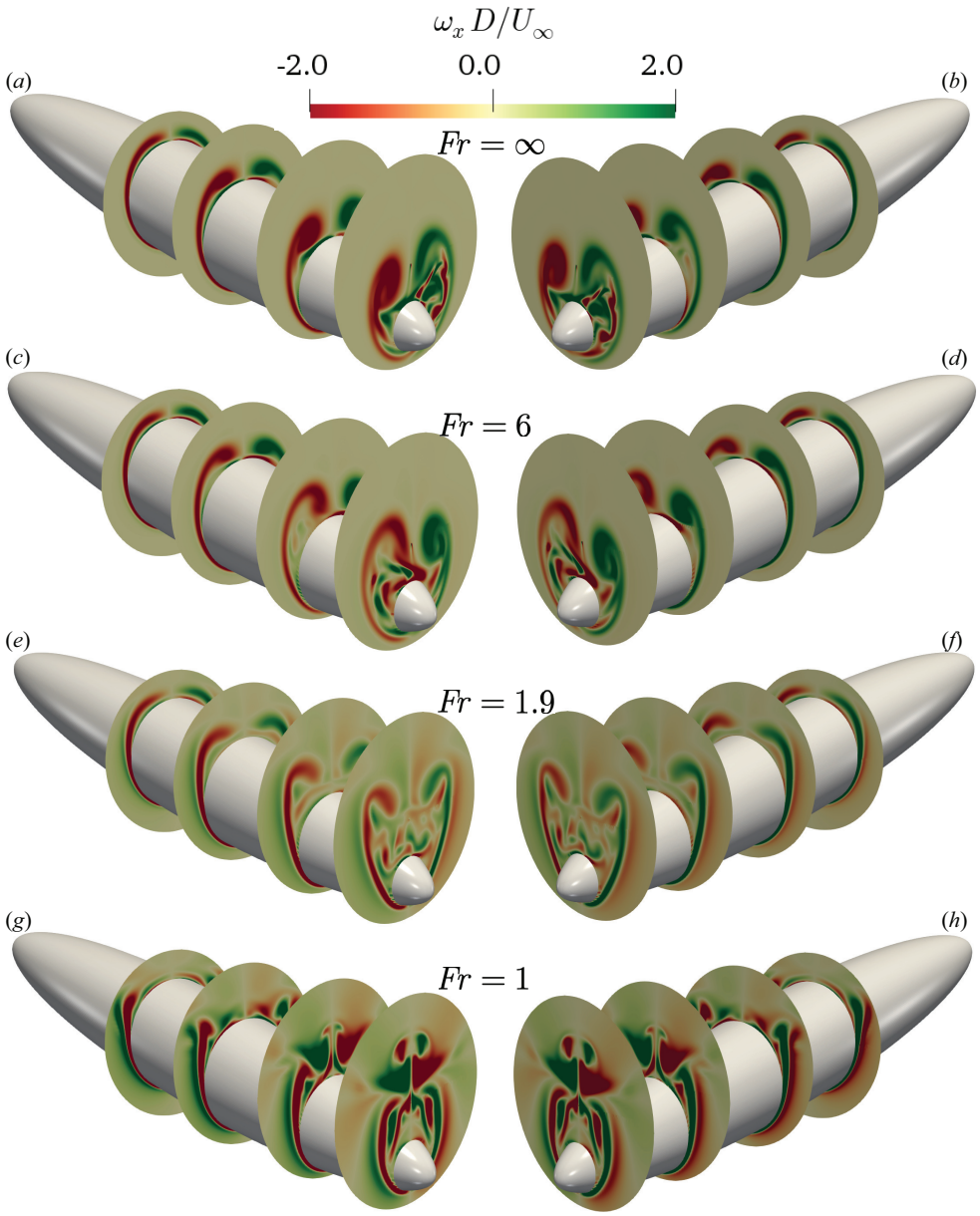

Figure 5.9: Instantaneous streamwise vorticity (ω_x) on the spheroid at $x/D = 0, 1, 2$ and 2.75 for all Fr at $\alpha = 10^\circ$. Left and right views are shown.

centerplane through the spheroid. At $x/D = 2$, we can observe asymmetry developing between these two vortices, as one side rolls up earlier than the other. Between the unstratified and the $Fr = 6$ case, the side that rolls up earlier is interchanged, i.e., positive vortex filament for the unstratified wake (figure 5.9b) and the negative vortex filament (figure 5.9c) for the $Fr = 6$ wake. By $x/D = 2.75$, the difference in the evolution of the two filaments is even more stark (figure 5.9(a,b,c,d)).

As the stratification strength increases to $Fr = 1.9$, we see that the asymmetry in the left and right filament is suppressed (figure 5.9(e,f)). The shape of the vortex filaments also changes qualitatively, i.e., at $Fr = 1.9$ these filaments are thinner and longer (in the vertical direction) than the ones at $Fr = \infty$ or 6. Stratification starts affecting the evolution of the vorticity as early as $x/D = 1$, compare figure 5.9(b,d) to figure 5.9(f). At $Fr = 1$, the vorticity field gets more complex. The roll-up is inhibited compared to the $Fr = 1.9$ case. Besides that, the region away from the spheroid also contains streamwise vorticity, unlike in the $Fr = 1.9$ flow (compare $x/D = 2.75$ slice between the last and third row in figure 5.9).

Moving away from the body, we track the evolution of the vorticity field into the wake. Figure 5.10 shows the contours mean streamwise vorticity Ω_x from $x/D = 3$ to 30 for all four cases. Figure 5.10(a,e,i,m) show the evolution of Ω_x for the $Fr = \infty$ wake. As the flow evolves, it is interesting to note that the two vortices maintain their spatial integrity, similar to high-Re studies on DARPA SUBOFF by Ashok et al. (2015a). On the contrary in the $Fr = 6$ wake, Ω_x field at $x/D = 20$ and 30 does not contain the distinct imprint of the two vortices that left the body. At further low stratification levels of $Fr = 1.9$ and 1, Ω_x field is quite complicated beyond $x/D = 10$. These wakes are strongly modulated by the presence of internal gravity waves that also carry vorticity. The wake vorticity and the IGW vorticity interact in a complex fashion making it difficult the discern the fate of the shed vortices from the contours alone, unlike the $Fr = \infty$ wake.

Figure 5.11 presents the clockwise and counterclockwise circulation ($\Gamma = \int_A \Omega_x \mathrm{dA}$) as a function of x/D for all four wakes. Similar to other area-integrated statistics, the area-integration

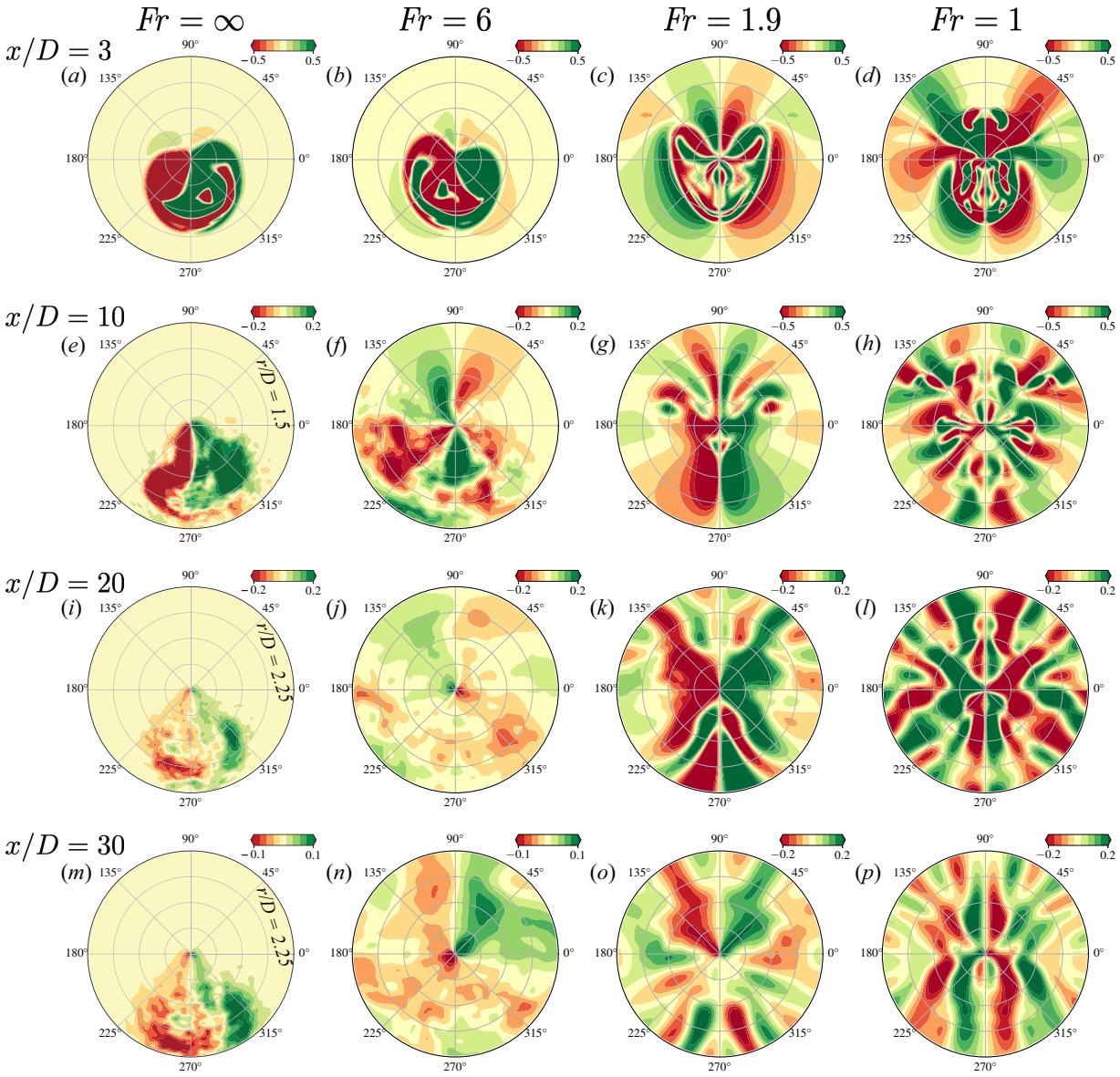

Figure 5.10: Mean streamwise vorticity (Ω_x) contours at $x/D = 3, 10, 20$ and 30 (row-wise) for $Fr = \infty, 6, 1.9$ and 1 (column-wise). The radial domain is $r/D = 1$ unless explicitly mentioned (see $x/D = 10, 20, 30$ for the $Fr = \infty$ wake).

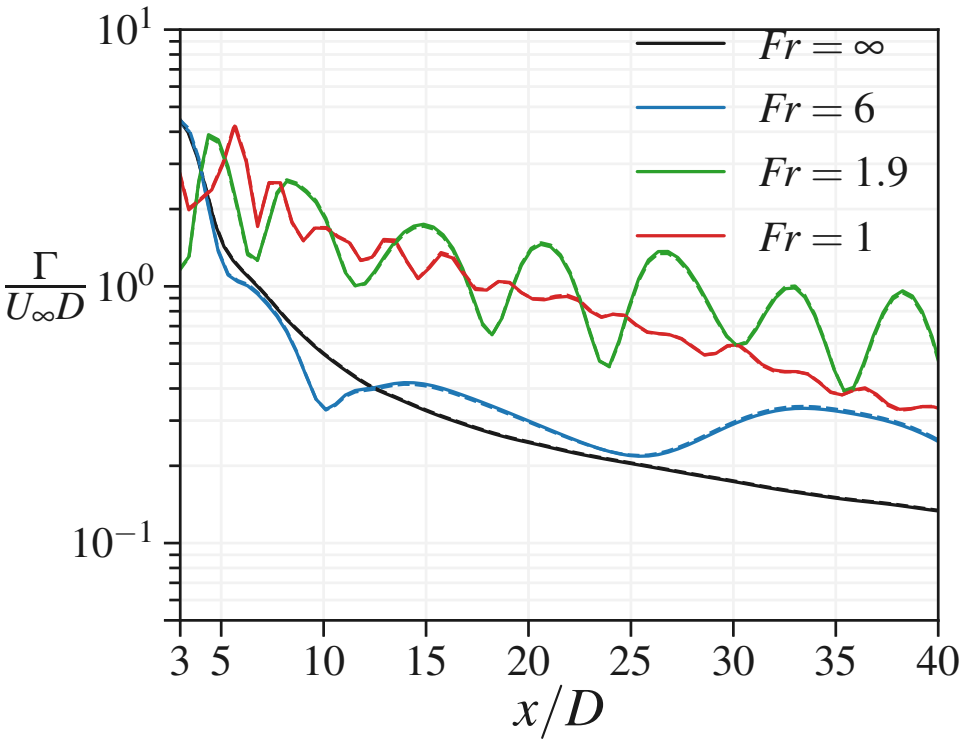

Figure 5.11: Mean circulation at a streamwise cross-section of x/D for all Fr at $\alpha = 10^\circ$. Positive and negative circulations are shown with solid and dashed lines, respectively.

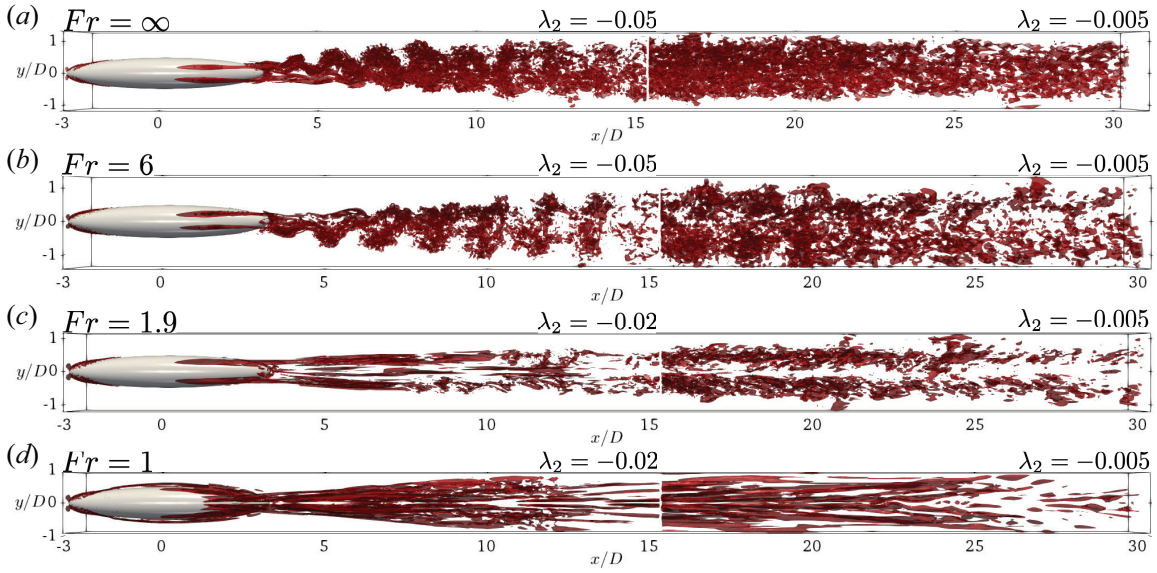

Figure 5.12: Top view of instantaneous λ_2 criterion for (a) $Fr = \infty$, (b) $Fr = 6$, (c) $Fr = 1.9$, and $Fr = 1$ cases. λ_2 thresholds are different for $x/D < 15$ and $x/D > 15$ to elucidate the near wake and the intermediate wake features, respectively.

is performed over a circular cross-section of radii $r/D = 3.5$ and $r/D = 2$ for the unstratified case and the stratified cases, respectively. The net circulation is zero over the area of integration across all four cases. Γ in $Fr = \infty$ and 6 wakes are similar in magnitude and lie below that of $Fr = 1$ and 1.9 wakes. Oscillations in the Γ trends for stratified wakes are approximately half the wavelength of the steady lee waves. In stratified cases, we see that the IGWs carry significant vorticity. The source of vorticity production in these waves is the baroclinic torque that goes as $\nabla\rho.\nabla p/\rho_o^2$. Since the baroclinic torque is a product of two terms both of which have the same wavenumber corresponding to the steady lee wave, it has a wavelength half of that of the steady lee waves. As a result, Γ, that consists of significant contribution from these waves show oscillation wavelength half of that of the steady lee waves.

5.6 Visualizations and spectra in the wake

Figure 5.12 shows the iso-contours of instantaneous λ_2 criteria for all four flow fields. The iso-contour threshold is different for the $x/D \lessapprox 15$ and $x/D \gtrapprox 15$ locations for all four cases to enhance the structures in the near as well as the intermediate wake of the body. At both $Fr = \infty$ and $Fr = 6$ wakes, we see a very distinct signature of vortex shedding structures being shed from the body. As found beforehand in the pressure, shear, and vorticity contours, these vortex shedding structures are asymmetrical as well. When one goes to locations $x/D \gtrapprox 15$, it becomes difficult to discern these structures from the naked eye in figure 5.12(a,b). At lower $Fr = 1$ and 1.9 (figure 5.12(c,d)), the near wake instantaneous λ_2 structures are layered. These layers then subsequently break down into small-scale structures as the wake evolves.

To further quantify the spectral characteristics of these structures in the wake, we present the spectra of probes ranging from the near to the intermediate wake locations in all four cases in figure 5.13. Figure 5.13(a,b) presents spectra in the unstratified and $Fr = 6$ wakes. At all the four locations presented, we see a spectral peak at $St \approx 0.62$ and $St \approx 0.57$ in $Fr = \infty$ and $Fr = 6$, respectively. These St correspond to the vortex shedding frequency in these wakes. Near the body, the small scales, e.g., $St > 1$, have very different energy content owing to asymmetry in both cases (compare the dashed lines to the solid lines). As the wake evolves further, this difference is attenuated. For $Fr = 1.9$ (figure 5.13(c)), the vortex shedding frequency peak is not present. Instead, a low-frequency signal appears at $x/D = 3$ around $St \approx 0.1$. At further downstream locations as well, this peak is present, however significantly weaker than at $x/D = 3$. Visualizations (not shown here) show that this frequency is associated with an unsteady oscillation in the near wake. At further lower $Fr = 1$, neither $St \approx 0.6$ nor $St \approx 0.1$ is present in the near wake (see solid and dashed maroon lines in figure 5.13(d)). When one looks at $x/D > 10$ locations, there are spectral peaks in the vicinity of $St = [0.6, 0.9]$. We hypothesize that these peaks are associated with the breaking down of layers into small structures.

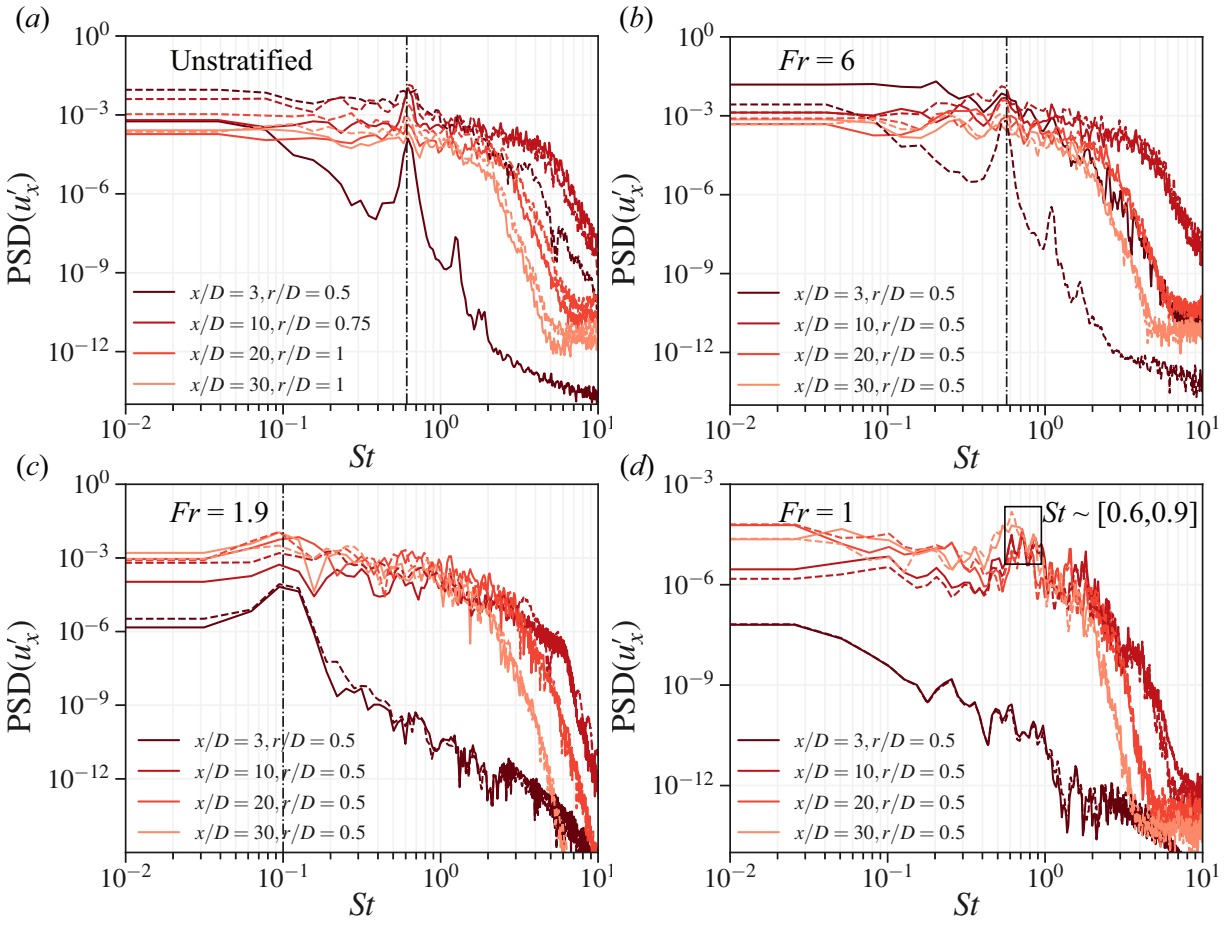

Figure 5.13: Power spectral density of streamwise velocity fluctuations (u'_x) across the four simulated cases. (a) $Fr = \infty$, (b) $Fr = 6$, with solid and dashed lines corresponding to $\theta = 225°$ and $\theta = 315°$. (c) $Fr = 1.9$, (d) $Fr = 1$, with solid and dashed lines corresponding to $\theta = 0°$ and $\theta = 180°$.

5.7 Conclusions

Large-eddy simulations (LES) are performed to study the characteristics of flow over a 6:1 spheroid placed at an angle of attack $\alpha = 10^\circ$. We present results at $Re = 5000$ and $Fr = \infty, 6, 1.9,$ and 1. Additionally, flows past a 6:1 spheroid at the same (Re, Fr) combinations but at $\alpha = 0^\circ$ are simulated to provide a basis for comparison. We find that the buoyancy effect introduced by stratification strongly modulates the pressure and friction forces on the body. The critical Froude number (Ortiz-Tarin et al., 2019) given by $Fr_c = L/\pi D$ is defined kinematically by equating the body length to the half-wavelength of the generated lee wave. For the 6:1 spheroid, the effect of stratification on C_p, C_f, and C_d is more pronounced at $Fr = 1$ than at the critical Froude number $Fr_c \approx 1.9$. For both $\alpha = 0^\circ$ and 10° cases, C_d monotonically increases with decreasing Fr. At $\alpha = 10^\circ$, a distinct lateral asymmetry is visible in the C_p and C_f contours for $Fr = 6$ and ∞ cases. This gives rise to a non-zero lateral force whose magnitude is approximately 12% of the streamwise drag at $\alpha = 10^\circ$. Further increasing the stratification kills the asymmetry at $Fr = 1.9$ and 1. At $\alpha = 10^\circ$, we also find that the flow separation over the body is strongly dependent on the value of Fr. At $Fr = 6$ and ∞, the flow separates from the lateral sides on the lee of the body while at $Fr = 1$, the flow separates predominantly near the vertical center plane $y = 0$.

In the ensuing wake, we find that the flow separation patterns have a lasting impact on the wake dynamics, at least until $x/D \approx 40$ for $\alpha = 10^\circ$ cases. The mean wake defect U_d of the $Fr = \infty$ wake continues to drift away from the centerline while the $Fr = 6$ wake is inhibited significantly from drifting. As the Fr decreases further to $O(1)$, the wake remains close to the centerline and is modulated by the steady lee waves both in U_d (the defect velocity) and wake lengthscales. The mean streamwise vorticity (Ω_x) contours show that while the unstratified wake maintains its structural integrity until $x/D = 40$, Ω_x in the stratified cases is quite complex, a consequence of the interaction of the wake vorticity field with the vorticity of the steady lee waves. Spectra and visualizations reveal the vortex shedding mechanism being present for $Fr \geq 6$

cases. At lower *Fr*, the vortex shedding is not observed in the spectra and other spectral features corresponding to different phenomena appear.

5.8 Acknowledgments

Chapter 5 is being prepared for publication titled: S. Nidhan, J. L. Ortiz-Tarin, and S. Sarkar, "Wake of a slender body at a moderate angle of attack in stratified and homogeneous environments". Parts of chapter 5, with slight modifications, also appear in the conference proceeding titled: S. Nidhan, J. L. Ortiz-Tarin, and S. Sarkar, " Flow past an inclined spheroid in homogeneous and stratified environments", 12th International Symposium on Turbulence and Shear Flow Phenomena, Osaka, Japan (Virtual). The dissertation author is the primary investigator and author of this work.

Chapter 6

Conclusions

As mentioned in the foregoing, the dissertation has been divided into two parts. The conclusions specific to each chapter are present at the end of each chapter. Here, a big picture summary of both the themes of the work is given.

6.1 Modal analysis of bluff body wakes

In chapters 2 and 3, the turbulent wake of a disk at $Re = 5 \times 10^4$ in homogeneous and stratified conditions, respectively. For the stratified wakes, body-based Froude numbers of $Fr = 2$ and 10 were analyzed. Spectral proper orthogonal decomposition (SPOD) was used to distill the coherent structures from the LES database of Chongsiripinyo and Sarkar (2020). The statistically steady nature of a spatially developing wake and the presence of distinct frequency signatures make turbulent wake datasets especially suitable for the SPOD analysis.

In the unstratified wake, owing to the azimuthal homogeneity, fluctuations are first decomposed in azimuthal modes (m). Thereafter, SPOD is performed at different x/D locations to decompose the turbulent flow into modes quartets. These modes are functions of streamwise distance (x/D), modal index (n), Strouhal number (St), and azimuthal wavenumbers (m). SPOD reveals the presence of two very distinct large-scale structures in the flow that persist at least

until $O(100D)$ downstream distance. These two structures are (a) the vortex shedding (VS) mode at $n = 1, m = 1, St = 0.135$ and (b) the double helix (DH) mode, $n = 1, m = 2, St \to 0$. In the beginning, the VS mode dominates but the DH mode overtakes as the wake progresses (after $x/D \approx 40$). Scaling analyses reveal fundamental differences in the way the eigenvalues and eigenmodes of these two different modes scale as x/D increases. Furthermore, TKE and Reynolds stress reconstructions are also performed at different x/D locations to assess the contribution of different modes to the second-order moments.

In stratified wakes, owing to the azimuthal inhomogeneity, flow snapshots at different x/D locations are directly decomposed into $(St, n, x/D)$ modes. The VS mode is the most dominant mode in both $Fr = 2$ and $Fr = 10$ wakes. Compared to the unstratified wake, we find that the large-scale coherence lasts longer in the stratified wakes, more so in the $Fr = 2$ wake than in the $Fr = 10$ wake. Partitioning the energy at any cross-section into the wake core and outer wake region reveals that this sustenance of large-scale coherence is a consequence of unsteady internal gravity waves (IGWs) being emitted from the wake core to the outer wake. Further, reconstruction of the pressure wave flux term using the SPOD modes confirms the causal link between the VS mode and the IGW generation. We find that at least for $Fr \geq 2$, the VS mode is the most dominant source of the unsteady IGW generation. Similar to the unstratified wake, TKE and Reynolds stress reconstruction trends are analyzed for the stratified wakes as well.

The one key takeaway message from both chapters 2 and 3 is that the turbulent wakes at high *Re* are still characterized by the dominance of the large-scale structures in the flow, more so than other sister shear flows like turbulent jets or wall-bounded flows. These large-scale structures can modulate other crucial phenomena in these wakes, e.g., the generation of IGWs in the stratified wakes. The current dissertation focuses on analyzing flow physics using SPOD. Future studies can aim at the low-order modeling of these flows using SPOD (or other data-driven techniques). For example, reconstructing back the flow field from the SPOD modes (Nekkanti and Schmidt, 2021), one can modify the SPOD modes and initialize a hybrid simulation similar

to VanDine et al. (2018). In this fashion, several important questions can be tackled: (a) What happens to the IGW characteristics when one removes the VS contribution in the stratified wakes and let the flow evolve downstream? (b) How do the turbulence statistics and SPOD modes change if we remove the VS mode in the unstratified wake and let the flow evolve? (c) Can one mimic a high *Re* wake by initializing the simulation with a large-scale contribution obtained from a cheaper low *Re* wake simulation and the small-scale contribution modeled using flow-enrichment techniques (Ghate et al., 2020)?

6.2 Large eddy simulations of slender body wakes

In chapters 4 and 5, the focus was on the characterization of slender body wakes. First, we study the turbulent stratified wakes of a prolate 6:1 spheroid at a body-based Reynolds number of 10^5 and $Fr = 2$, 10. The slender wake is compared to the disk wake at $Re = 5 \times 10^4$ and $Fr = 2, 10$ (Chongsiripinyo and Sarkar, 2020). Second, the stratified wake of a prolate 6:1 spheroid placed at a moderate angle of attack $\alpha = 10^\circ$ and $Re = 5000$ is analyzed for varying levels of stratification $Fr = \infty, 6, 1.9$ and 1. A scarcity of studies on the slender body wakes in stratified conditions, despite their widespread importance, is the motivation for our study.

In chapter 4, the hybrid simulations of slender body stratified wakes at high *Re* reveal a significant difference between the wake of a slender body (6:1 spheroid) and a bluff body (circular disk). A key difference is found in terms of the arrival locations (in non-dimensional buoyancy time Nt) of various mean wake regimes (3D, NEQ, and Q2D). At $Fr = 2$, strong modulation of the wake by lee waves results in the early arrival of the Q2D-like decay regime at $Nt \approx 15$. Contrary to the spheroid, the disk $Fr = 2$ wake does not enter the Q2D regime at least until $Nt = 62.5$. In the $Fr = 10$ case, we see a delay in the arrival of the NEQ regime in the spheroid wake (at $Nt \approx 3$) compared to the disk wake (at $Nt \approx 1$). This phenomenon was analyzed under the light of the MKE and TKE budget terms, revealing that the decrease in the turbulent production at

a farther downstream distance in the spheroid wake is responsible for the late NEQ transition. Thereafter, the wake evolution of spheroid and disk was compared in terms of the evolution of local non-dimensional numbers.

In chapter 5, we perform large eddy simulations of flow past a 6:1 spheroid at $Re = 5000$ and four different stratification levels ranging from the unstratified case to $Fr = 1$. A key finding is the presence of lateral asymmetry in the mean as well as statistics of the fluctuating fields at $Fr = 6$ and $Fr = \infty$. The asymmetry strength is similar in magnitude but is reflected across the $y/D = 0$ centerplane between the two cases, implying the possibility of a steady or very low-frequency unsteady bifurcation at these two Fr. As the stratification strength is further increased, we find that the flow on the body as well as in the wake becomes symmetric, leading to the result that the stratification kills the asymmetry. Another important finding is that in the unstratified case, the vortex pair that is shed from the body, maintains its spatial integrity until $x/D = 40$ while the vortex pair in stratified wakes (specifically $Fr = 1.9$ and 1) interact with the surrounding lee wave field, leading to a very complex Ω_x distribution. As a result, a direct connection between the initial streamwise vortex pair and its late presence (at $x/D = 40$) is not discernible from the contours alone at stronger Fr. Even for the lower $Fr = 6$ case, the streamwise vortex pair differs substantially from its unstratified counterpart within a few body lengths from its trailing edge. Further visualizations and flow spectra are also shown delineating specific differences among the four cases.

The key takeaway from the second part of the dissertation is that finding a universal framework for stratified turbulent wakes across various controlling parameters like body shape, angle of attack, Re, Fr, etc. is a daunting task at best and an elusive goal at worst. Both our studies show that slight changes in the initial conditions leave a lasting impact on the wake evolution. The universality in the wake evolution might be achieved only at far downstream locations (Redford et al., 2012). Thus in author's opinion, a feasible way to build our understanding of these flows is to first create an extensive wake database across different controlling parameters. Thereafter it

is imperative to perform detailed analyses of the quantities of interest, e.g., coherent structures, first-order moments, second-order moments, forces on the body, etc. As more analyses and databases come to light, one can hope that different classes of wakes will show similar behavior, pointing towards possible universality among the wakes of those specific classes. This modified notion of universality, i.e., looking at different classes of wakes instead of clubbing all the various turbulent wakes under one big umbrella, can then inform the design decision for engineering and geophysical applications.

Bibliography

Abdilghanie, A. M. and Diamessis, P. J. (2013). The internal gravity wave field emitted by a stably stratified turbulent wake. J. Fluid Mech., 720:104–139.

Abreu, L. I., Cavalieri, A. V. G., Schlatter, P., Vinuesa, R., and Henningson, D. S. (2020). Spectral proper orthogonal decomposition and resolvent analysis of near-wall coherent structures in turbulent pipe flows. J. Fluid Mech., 900.

Achenbach, E. (1974). Vortex shedding from spheres. J. Fluid Mech., 62(2):209–221.

Arndt, R. E. A., Long, D. F., and Glauser, M. N. (1997). The proper orthogonal decomposition of pressure fluctuations surrounding a turbulent jet. J. Fluid Mech., 340:1–33.

Ashok, A., Van Buren, T., and Smits, A. (2015a). Asymmetries in the wake of a submarine model in pitch. J. Fluid Mech., 774:416–442.

Ashok, A., Van Buren, T., and Smits, A. J. (2015b). The structure of the wake generated by a submarine model in yaw. Exp Fluids, 56(6):123.

Baines, P. G. (1998). Topographic Effects in Stratified Flows. Cambridge University Press.

Balaras, E. (2004). Modeling complex boundaries using an external force field on fixed Cartesian grids in large-eddy simulations. Comput. Fluids, 33(3):375–404.

Bearman, P. W. (1984). Vortex shedding from oscillating bluff bodies. Annu. Rev. Fluid Mech., 16(1):195–222.

Berger, E., Scholz, D., and Schumm, M. (1990). Coherent vortex structures in the wake of a sphere and a circular disk at rest and under forced vibrations. J. Fluids Struct., 4(3):231–257.

Bevilaqua, P. M. and Lykoudis, P. S. (1978). Turbulence memory in self-preserving wakes. J. Fluid Mech., 89(3):589–606.

Billant, P. and Chomaz, J. (2001). Self-similarity of strongly stratified inviscid flows. Phys. Fluids, 13(6):1645–1651.

Bonnet, J. P., Cole, D. R., Delville, J., Glauser, M. N., and Ukeiley, L. S. (1994). Stochastic estimation and proper orthogonal decomposition: Complementary techniques for identifying structure. Exp. Fluids, 17(5):307–314.

Bonneton, P., Chomaz, J. M., Hopfiliger, E., and Perrier, M. (1996). The structure of the turbulent wake and the random internal wave field generated by a moving sphere in a stratified fluid. Dyn. Atmospheres Oceans, 23(1-4):299–308.

Bonneton, P., Chomaz, J. M., and Hopfinger, E. J. (1993). Internal waves produced by the turbulent wake of a sphere moving horizontally in a stratified fluid. J. Fluid Mech., 254:23–40.

Bonnier, M. and Eiff, O. (2002). Experimental investigation of the collapse of a turbulent wake in a stably stratified fluid. Phys. Fluids, 14(2):791–801.

Brandt, A. and Rottier, J. (2015). The internal wavefield generated by a towed sphere at low Froude number. J. Fluid Mech., 769:103–129.

Brethouwer, G., Billant, P., Lindborg, E., and Chomaz, J.-M. (2007). Scaling analysis and simulation of strongly stratified turbulent flows. J. Fluid Mech., 585:343–368.

Brucker, K. A. and Sarkar, S. (2010). A comparative study of self-propelled and towed wakes in a stratified fluid. J. Fluid Mech., 652:373–404.

Cannon, S., Champagne, F., and Glezer, A. (1993). Observations of large-scale structures in wakes behind axisymmetric bodies. Exp Fluids, 14(6):447–450.

Castro, I. P., Snyder, W. H., and Marsh, G. L. (1983). Stratified flow over three-dimensional ridges. J. Fluid Mech., 135:261–282.

Chesnakas, C. J. and Simpson, R. L. (1994). Full three-dimensional measurements of the cross-flow separation region of a 6:1 prolate spheroid. Exp. Fluids, 17:68–74.

Chevray, R. (1968). The turbulent wake of a body of revolution. ASME J. Basic Eng., 90:275–284.

Chomaz, J. M., Bonneton, P., Butet, A., Perrier, M., and Hopfinger, E. J. (1992). Froude number dependence of the flow separation line on a sphere towed in a stratified fluid. Phys. Fluids, 4(2):254–258.

Chomaz, J. M., Bonneton, P., and Hopfinger, E. J. (1993). The structure of the near wake of a sphere moving horizontally in a stratified fluid. J. Fluid Mech., 254:1–21.

Chongsiripinyo, K., Pal, A., and Sarkar, S. (2017). On the vortex dynamics of flow past a sphere at Re = 3700 in a uniformly stratified fluid. Phys. Fluids, 29(2):020704.

Chongsiripinyo, K. and Sarkar, S. (2017). Effect of stratification on the turbulent wake behind a sphere at Re = 10,000. In Tenth International Symposium on Turbulence and Shear Flow Phenomena (TSFP10), July 6-9, 2017, Swissotel, Chicago-IL, USA.

Chongsiripinyo, K. and Sarkar, S. (2020). Decay of turbulent wakes behind a disk in homogeneous and stratified fluids. J. Fluid Mech., 885:A31.

Chu, T. and Schmidt, O. T. (2021). A stochastic SPOD-Galerkin model for broadband turbulent flows. Theor. Comput. Fluid Dyn.

Citriniti, J. H. and George, W. K. (2000). Reconstruction of the global velocity field in the axisymmetric mixing layer utilizing the proper orthogonal decomposition. J. Fluid Mech., 418:137–166.

Constantinescu, G. S., Pasinato, H., Wang, Y. Q., Forsythe, J. R., and Squires, K. D. (2002). Numerical investigation of flow past a prolate spheroid. J. Fluids Eng., 124(4):904–910.

Constantinescu, G. S. and Squires, K. D. (2003). LES and DES investigations of turbulent flow over a sphere at Re = 10,000. Flow Turbul. Combust, 70(1-4):267–298.

Costis, C. E., Telionis, D. P., and Hoang, N. T. (1989). Laminar separating flow over a prolate spheroid. J. Aircr., 26(9):810–816.

Dairay, T., Obligado, M., and Vassilicos, J. C. (2015). Non-equilibrium scaling laws in axisymmetric turbulent wakes. J. Fluid Mech., 781:166–195.

Dalla Longa, L., Evstafyeva, O., and Morgans, A. S. (2019). Simulations of the bi-modal wake past three-dimensional blunt bluff bodies. J. Fluid Mech., 866:791–809.

Davoust, S., Jacquin, L., and Leclaire, B. (2012). Dynamics of $m = 0$ and $m = 1$ modes and of streamwise vortices in a turbulent axisymmetric mixing layer. J. Fluid Mech., 709:408–444.

de Bruyn Kops, S. M. and Riley, J. J. (2019). The effects of stable stratification on the decay of initially isotropic homogeneous turbulence. J. Fluid Mech., 860:787–821.

de Stadler, M. B. and Sarkar, S. (2012). Simulation of a propelled wake with moderate excess momentum in a stratified fluid. J. Fluid Mech., 692:28–52.

Delville, J., Ukeiley, L., Cordier, L., Bonnet, J. P., and Glauser, M. (1999). Examination of large-scale structures in a turbulent plane mixing layer. Part 1. Proper orthogonal decomposition. J. Fluid Mech., 391:91–122.

Diamessis, P., Gurka, R., and Liberzon, A. (2010). Spatial characterization of vortical structures and internal waves in a stratified turbulent wake using proper orthogonal decomposition. Phys. Fluids, 22(8):086601.

Diamessis, P. J., Spedding, G. R., and Domaradzki, J. (2011). Similarity scaling and vorticity structure in high-Reynolds-number stably stratified turbulent wakes. J. Fluid Mech., 671:52–95.

Dommermuth, D. G., Rottman, J. W., Innis, G. E., and Novikov, E. A. (2002). Numerical simulation of the wake of a towed sphere in a weakly stratified fluid. J. Fluid Mech., 473:83–101.

Drazin, P. G. (1961). On the steady flow of a fluid of variable density past an obstacle. Tellus, 13(2):239–251.

Fu, T. C., Shekarriz, A., Katz, J., and Huang, T. T. (1994). The flow structure in the lee of an inclined 6:1 prolate spheroid. J. Fluid Mech., 269:79–106.

Fuchs, H. V., Mercker, E., and Michel, U. (1979). Large-scale coherent structures in the wake of axisymmetric bodies. J. Fluid Mech., 93(1):185–207.

George, W. K. (1989). The self-preservation of turbulent flows and its relation to initial conditions and coherent structures. Advances in turbulence, 3973.

Germano, M., Piomelli, U., Moin, P., and Cabot, W. H. (1991). A dynamic subgrid-scale eddy viscosity model. Phys. Fluids, 3(7):1760–1765.

Ghate, A. S., Ghaisas, N., Lele, S. K., and Towne, A. (2018). Interaction of small scale Homogenenous Isotropic Turbulence with an Actuator Disk. In 2018 Wind Energy Symposium, Kissimmee, Florida. American Institute of Aeronautics and Astronautics.

Ghate, A. S., Towne, A., and Lele, S. K. (2020). Broadband reconstruction of inhomogeneous turbulence using spectral proper orthogonal decomposition and Gabor modes. J. Fluid Mech., 888:R1.

Gilreath, H. E. and Brandt, A. (1985). Experiments on the generation of internal waves in a stratified fluid. AIAA J., 23(5):693–700.

Glauser, M. N. and George, W. K. (1987). An orthogonal decomposition of the axisymmetric jet mixing layer utilizing cross-wire velocity measurements. Sixth Symp. on Turbulent Shear Flows, Toulouse, France.

Glauser, M. N., Leib, S. J., and George, W. K. (1987). Coherent structures in the axisymmetric turbulent jet mixing layer. In Turbulent Shear Flows 5, pages 134–145. Springer.

Gola, D., Nidhan, S., Ortiz-Tarin, J. L., Pham, H., and Sarkar, S. (2022). Disk wakes in nonlinear stratification. arXiv preprint arXiv:2208.12442.

Gordeyev, S. V. and Thomas, F. O. (2000). Coherent structure in the turbulent planar jet. Part 1. Extraction of proper orthogonal decomposition eigenmodes and their self-similarity. J. Fluid Mech., 414:145–194.

Gordeyev, S. V. and Thomas, F. O. (2002). Coherent structure in the turbulent planar jet. Part 2. Structural topology via POD eigenmode projection. J. Fluid Mech., 460:349–380.

Gourlay, M. J., Arendt, S. C., Fritts, D. C., and Werne, J. (2001). Numerical modeling of initially turbulent wakes with net momentum. Phys. Fluids, 13(12):3783–3802.

Grandemange, M., Cadot, O., Courbois, A., Herbert, V., Ricot, D., Ruiz, T., and Vigneron, R. (2015). A study of wake effects on the drag of Ahmed's squareback model at the industrial scale. J. Wind Eng. Ind. Aerodyn., 145:282–291.

Grandemange, M., Gohlke, M., and Cadot, O. (2013). Turbulent wake past a three-dimensional blunt body. Part 1. Global modes and bi-stability. J. Fluid Mech., 722:51–84.

Han, T. and Patel, V. C. (1979). Flow separation on a spheroid at incidence. J. Fluid Mech., 92(4):643–657.

Hanazaki, H. (1988). A numerical study of three-dimensional stratified flow past a sphere. J. Fluid Mech., 192:393–419.

Hellstrom, L. H. O., Marusic, I., and Smits, A. J. (2016). Self-similarity of the large-scale motions in turbulent pipe flow. J. Fluid Mech., 792:R1.

Holmes, P. and Lumley, J. L. and Berkooz, G. and Rowley, C. W. (2012). Turbulence, coherent structures, dynamical systems and symmetry. Cambridge University Press.

Hunt, J. C. R. and Snyder, W. H. (1980). Experiments on stably and neutrally stratified flow over a model three-dimensional hill. J. Fluid Mech., 96:671–704.

Hunt, J. C. R., Wray, A. A., and Moin, P. (1988). Eddies, streams, and convergence zones in turbulent flows. Tech. Rep. CTR, 14(2).

Iqbal, M. O. and Thomas, F. O. (2007). Coherent structure in a turbulent jet via a vector implementation of the proper orthogonal decomposition. J. Fluid Mech., 571:281–326.

Jeong, J. and Hussain, F. (1995). On the identification of a vortex. J. Fluid Mech., 285:69–94.

Jiang, F., Gallardo, J. P., Andersson, H. I., and Zhang, Z. (2015). The transitional wake behind an inclined prolate spheroid. Phys. Fluids, 27(9):093602.

Jiménez, J. M., Hultmark, M., and Smits, A. J. (2010). The intermediate wake of a body of revolution at high Reynolds numbers. J. Fluid Mech., 659:516–539.

Johansson, P. B. V. and George, W. K. (2006a). The far downstream evolution of the high-Reynolds-number axisymmetric wake behind a disk. Part 1. Single-point statistics. J. Fluid Mech., 555:363.

Johansson, P. B. V. and George, W. K. (2006b). The far downstream evolution of the high-Reynolds-number axisymmetric wake behind a disk. Part 2. Slice proper orthogonal decomposition. J. Fluid Mech., 555:387.

Johansson, P. B. V., George, W. K., and Gourlay, M. J. (2003). Equilibrium similarity, effects of initial conditions and local Reynolds number on the axisymmetric wake. Phys. Fluids, 15(3):603–617.

Johansson, P. B. V., George, W. K., and Woodward, S. H. (2002). Proper orthogonal decomposition of an axisymmetric turbulent wake behind a disk. Phys. Fluids, 14(7):2508.

Jovanović, M. R., Schmid, P. J., and Nichols, J. W. (2014). Sparsity-promoting dynamic mode decomposition. Phys. Fluids, 26(2):024103.

Katul, G. G. and Parlange, M. B. (1995). Analysis of Land Surface Heat Fluxes Using the Orthonormal Wavelet Approach. Water Resour. Res., 31(11):2743–2749.

Kim, I. and Pearlstein, A. J. (1990). Stability of the flow past a sphere. J. Fluid Mech., 211:73–93.

Kumar, P. and Mahesh, K. (2018). Large-eddy simulation of flow over an axisymmetric body of revolution. J. Fluid Mech., 853:537–563.

Leib, S. J., Glauser, M. N., and George, W. K. (1984). An application of Lumley's orthogonal decomposition to the axisymmetric jet mixing layer. Proc. 9th Rolla Symp.

Lesshafft, L., Semeraro, O., Jaunet, V., Cavalieri, A. V. G., and Jordan, P. (2019). Resolvent-based modeling of coherent wave packets in a turbulent jet. Phys. Rev. Fluids, 4(6):063901.

Lin, J. and Pao, Y. (1979). Wakes in stratified fluids. Annu. Rev. Fluid Mech., 11(1):317–338.

Lin, Q., Boyer, D. L., and Fernando, H. J. S. (1992a). Turbulent wakes of linearly stratified flow past a sphere. Phys. Fluids A: Fluid Dynamics, 4(8):1687–1696.

Lin, Q., Lindberg, W. R., Boyer, D. L., and Fernando, H. J. S. (1992b). Stratified flow past a sphere. J. Fluid Mech., 240:315.

Lumley, J. L. (1967). The structure of inhomogeneous turbulent flows. Atmospheric Turbulence and Radio Wave Propagation, pages 166–178.

Lumley, J. L. (1970). Stochastic Tools in Turbulence. Academic Press.

McKeon, B. J. and Sharma, A. S. (2010). A critical-layer framework for turbulent pipe flow. J. Fluid Mech., 658:336–382.

Meunier, P., Le Dizès, S., Redekopp, L., and Spedding, G. R. (2018). Internal waves generated by a stratified wake: experiment and theory. J. Fluid Mech., 846:752–788.

Meunier, P. and Spedding, G. (2004). A loss of memory in stratified momentum wakes. Phys. Fluids, 16(2):298–305.

More, R. V. and Ardekani, A. M. (2020). Motion of an inertial squirmer in a density stratified fluid. J. Fluid Mech., 905.

More, R. V. and Ardekani, A. M. (2021). Hydrodynamic interactions between swimming microorganisms in a linearly density stratified fluid. Phys. Rev. E, 103(1):013109.

More, R. V., Ardekani, M. N., Brandt, L., and Ardekani, A. M. (2021). Orientation instability of settling spheroids in a linearly density-stratified fluid. J. Fluid Mech., 929.

Muralidhar, S. D., Podvin, B., Mathelin, L., and Fraigneau, Y. (2019). Spatio-temporal proper orthogonal decomposition of turbulent channel flow. J. Fluid Mech., 864:614–639.

Natarajan, R. and Acrivos, A. (1993). The instability of the steady flow past spheres and disks. J. Fluid Mech., 254:323–344.

Nekkanti, A. and Schmidt, O. T. (2020). Modal analysis of acoustic directivity in turbulent jets. AIAA J., 59(1):228–239.

Nekkanti, A. and Schmidt, O. T. (2021). Frequency–time analysis, low-rank reconstruction and denoising of turbulent flows using spod. J. Fluid Mech., 926.

Nekkanti, A. and Schmidt, O. T. (2022). Gappy spectral proper orthogonal decomposition. arXiv preprint arXiv:2206.06494.

Nicoud, F. and Ducros, F. (1999). Subgrid-scale stress modelling based on the square of the velocity gradient tensor. Flow Turbul. Combust., 62:183–200.

Nidhan, S., Chongsiripinyo, K., Schmidt, O. T., and Sarkar, S. (2020). Spectral proper orthogonal decomposition analysis of the turbulent wake of a disk at Re = 50 000. Phys. Rev. Fluids, 5(12):124606.

Nidhan, S., Ortiz-Tarin, J. L., Chongsiripinyo, K., Sarkar, S., and Schmid, P. J. (2019). Dynamic Mode Decomposition of Stratified Wakes. In AIAA Aviation 2019 Forum, Dallas, Texas. American Institute of Aeronautics and Astronautics.

Nidhan, S., Ortiz-Tarin, J. L., and Sarkar, S. (2022a). Flow past an inclined spheroid in homogeneous and stratified environments. In Tenth International Symposium on Turbulence and Shear Flow Phenomena (TSFP12), July 19-22, 2022, Osaka, Japan (Online).

Nidhan, S., Schmidt, O. T., and Sarkar, S. (2022b). Analysis of coherence in turbulent stratified wakes using spectral proper orthogonal decomposition. J. Fluid Mech., 934.

Nogueira, P. A. S., Cavalieri, A. V. G., Jordan, P., and Jaunet, V. (2019). Large-scale streaky structures in turbulent jets. J. Fluid Mech., 873:211–237.

Obligado, M., Dairay, T., and Vassilicos, J. C. (2016). Nonequilibrium scalings of turbulent wakes. Phys. Rev. Fluids, 1(4):044409.

Oertel Jr, H. (1990). Wakes behind blunt bodies. Annu. Rev. Fluid Mech., 22(1):539–562.

Ohh, C., Oliver, M., and Spedding, G. (2022). Asymmetric stratified wakes. Bulletin of the American Physical Society.

Ohh, C. and Spedding, G. (2021). Coherent structures in the stratified near-wake of an inclined 6: 1 prolate spheroid. In APS Division of Fluid Dynamics Meeting Abstracts, pages E30–006.

Orlanski, I. (1976). A simple boundary condition for unbounded hyperbolic flows. J. Comput. Phys., 21(3):251–269.

Orr, T. S., Domaradzki, J. A., Spedding, G. R., and Constantinescu, G. S. (2015). Numerical simulations of the near wake of a sphere moving in a steady, horizontal motion through a linearly stratified fluid at Re = 1000. Phys. Fluids, 27(3):035113.

Ortiz-Tarin, J. L., Chongsiripinyo, K. C., and Sarkar, S. (2019). Stratified flow past a prolate spheroid. Phys. Rev. Fluids, 4(9):094803.

Ortiz-Tarin, J. L., Nidhan, S., and Sarkar, S. (2021). High-Reynolds number wake of a slender body. J. Fluid Mech., 261:333–374.

Ortiz-Tarin, J. L., Nidhan, S., and Sarkar, S. (2022a). The high-Re far wake of a slender body and the effects of density stratification. arXiv preprint arXiv:2202.13287.

Ortiz-Tarin, J. L., Nidhan, S., and Sarkar, S. (2022b). The high-Re stratified wake of a slender body and its comparison with a bluff body wake. arXiv preprint arXiv:2208.11218.

O'Neill, P. L., Nicolaides, D., Honnery, D., and Soria, J. (13-17 December, 2004). Autocorrelation Functions and the Determination of Integral Length with Reference to Experimental and Numerical Data. Proceedings of the 15th A.F.M.C. Australasian Fluid Mechanics conference, page 4.

Pal, A., Sarkar, S., Posa, A., and Balaras, E. (2016). Regeneration of turbulent fluctuations in low-Froude-number flow over a sphere at a Reynolds number of 3700. J. Fluid Mech., 804:R2.

Pal, A., Sarkar, S., Posa, A., and Balaras, E. (2017). Direct numerical simulation of stratified flow past a sphere at a subcritical reynolds number of 3700 and moderate froude number. J. Fluid Mech., 826:5–31.

Pasquetti, R. (2011). Temporal/spatial simulation of the stratified far wake of a sphere. Comput. Fluids, 40(1):179–187.

Patel, V. and Kim, S. (1994). Topology of laminar flow on a spheroid at incidence. Comp. Fluids, 23(7):939–953.

Pickering, E., Rigas, G., Schmidt, O. T., Sipp, D., and Colonius, T. (2021). Optimal eddy viscosity for resolvent-based models of coherent structures in turbulent jets. J. Fluid Mech., 917.

Piquet, J. and Queutey, P. (1992). Navier-stokes computations past a prolate spheroid at incidence - I. Low incidence case. Comp. Fluids, 21:599–625.

Pope, S. B. (2000). Turbulent flows. Cambridge University Press, UK.

Posa, A. and Balaras, E. (2016). A numerical investigation of the wake of an axisymmetric body with appendages. J. Fluid Mech., 792:470–498.

Puthan, P., Pawlak, G., and Sarkar, S. (2022a). High drag states in tidally modulated stratified wakes. J. Phys. Oceanogr., 52(6):1033–1048.

Puthan, P., Pawlak, G., and Sarkar, S. (2022b). Wake vortices and dissipation in a tidally modulated flow past a three-dimensional topography. J. Geophys. Res. Oceans, 127(8):e2022JC018470.

Puthan, P., Sarkar, S., and Pawlak, G. (2021). Tidal synchronization of lee vortices in geophysical wakes. Geophys. Res. Lett., 48(4):e2020GL090905.

Redford, J. A., Castro, I. P., and Coleman, G. N. (2012). On the universality of turbulent axisymmetric wakes. J. Fluid Mech., 710:419–452.

Redford, J. A., Lund, T. S., and Coleman, G. N. (2015). A numerical study of a weakly stratified turbulent wake. J. Fluid Mech., 776:568–609.

Reed, A. M. and Milgram, J. H. (2002). Ship wakes and their radar images. Annu. Rev. Fluid Mech., 34:469.

Rigas, G., Oxlade, A. R., Morgans, A. S., and Morrison, J. F. (2014). Low-dimensional dynamics of a turbulent axisymmetric wake. J. Fluid Mech., 755:R5.

Riley, J. and DeBruynKops, S. M. (2003). Dynamics of turbulence strongly influenced by buoyancy. Phys. Fluids, 15(7):2047–2059.

Rodriguez, I., Borell, R., Lehmkuhl, O., Perez Segarra, C. D., and Oliva, A. (2011). Direct numerical simulation of the flow over a sphere at $Re = 3700$. J. Fluid Mech., 679:263–287.

Rossi, T. and Toivanen, J. (1999). A Parallel Fast Direct Solver for Block Tridiagonal Systems with Separable Matrices of Arbitrary Dimension. SIAM J. Sci. Comput., 20(5):1778–1793.

Rowe, K. L., Diamessis, P. J., and Zhou, Q. (2020). Internal gravity wave radiation from a stratified turbulent wake. J. Fluid Mech., 888:A25.

Rowley, C. W. and Dawson, S. T. M. (2017). Model Reduction for Flow Analysis and Control. Annu. Rev. Fluid Mech., 49(1):387–417.

Schmid, P. J. (2010). Dynamic mode decomposition of numerical and experimental data. J. Fluid Mech., 656:5–28.

Schmid, P. J. (2022). Dynamic mode decomposition and its variants. Annu. Rev. Fluid Mech., 54:225–254.

Schmidt, O. T. and Colonius, T. (2020). Guide to spectral proper orthogonal decomposition. AIAA Journal, 58(3):1023–1033.

Schmidt, O. T., Towne, A., Colonius, T., Cavalieri, A. V. G., Jordan, P., and Bres, G. A. (2017). Wavepackets and trapped acoustic modes in a turbulent jet: coherent structure eduction and global stability. J. Fluid Mech., 825:1153–1181.

Schmidt, O. T., Towne, A., Rigas, G., Colonius, T., and Bres, G. A. (2018). Spectral analysis of jet turbulence. J. Fluid Mech., 855:953–982.

Semeraro, O., Jaunet, V., Jordan, P., Cavalieri, A. V., and Lesshafft, L. (2016). Stochastic and harmonic optimal forcing in subsonic jets. In 22nd AIAA/CEAS Aeroacoustics Conference, Lyon, France. American Institute of Aeronautics and Astronautics.

Sirovich, L. (1987). Turbulence and the dynamics of coherent structures. I. Coherent Structures. Q. Appl. Maths, 45(3):561–571.

Spedding, G. R. (1997). The evolution of initially turbulent bluff-body wakes at high internal Froude number. J. Fluid Mech., 337:283–301.

Spedding, G. R. (2002a). The streamwise spacing of adjacent coherent structures in stratified wakes. Phys. Fluids, 14(11):10.

Spedding, G. R. (2002b). Vertical structure in stratified wakes with high initial Froude number. J. Fluid Mech., 454:71–112.

Spedding, G. R. (2014). Wake Signature Detection. Ann. Rev. Fluid Mech., 46(1):273–302.

Taira, K., Brunton, S. L., Dawson, S. T. M., Rowley, C. W., Colonius, T., McKeon, B. J., Schmidt, O. T., Gordeyev, S., Theofilis, V., and Ukeiley, L. S. (2017). Modal analysis of fluid flows: An overview. AIAA J., 55(12):4013–4041.

Taira, K., Hemati, M. S., Brunton, S. L., Sun, Y., Duraisamy, K., Bagheri, S., Dawson, S. T. M., and Yeh, C. (2020). Modal analysis of fluid flows: Applications and outlook. AIAA J., 58(3):998–1022.

Taneda, S. (1978). Visual observations of the flow past a sphere at Reynolds numbers between 10^4 and 10^6. J. Fluid Mech., 85(1):187–192.

Tennekes, H. and Lumley, J. L. (1972). A first course in turbulence. MIT press.

Tezuka, A. and Suzuki, K. (2006). Three-Dimensional Global Linear Stability Analysis of Flow Around a Spheroid. AIAA Journal, 44(8):1697–1708.

Thomareis, N. and Papadakis, G. (2018). Resolvent analysis of separated and attached flows around an airfoil at transitional Reynolds number. Phys. Rev. Fluids, 3(7):073901.

Thompson, M. C., Leweke, T., and Hourigan, K. (2021). Bluff bodies and wake–wall interactions. Annu. Rev. Fluid Mech., 53:347–376.

Tomboulides, A. G. and Orszag, S. A. (2000). Numerical investigation of transitional and weak turbulent flow past a sphere. J. Fluid Mech., 416:45–73.

Towne, A., Schmidt, O. T., and Colonius, T. (2018). Spectral proper orthogonal decomposition and its relationship to dynamic mode decomposition and resolvent analysis. J. Fluid Mech., 847:821–867.

Townsend, A. A. R. (1976). The structure of turbulent shear flow. Cambridge University Press.

Tseng, Y., Meneveau, C., and Parlange, M. B. (2006). Modeling flow around bluff bodies and predicting urban dispersion using large eddy simulation. Environ. Sci. Technol., 40(8):2653–2662.

Tutkun, M., Johansson, P. B. V., and George, W. K. (2008). Three-Component Vectorial Proper Orthogonal Decomposition of Axisymmetric Wake Behind a Disk. AIAA Journal, 46(5):1118–1134.

Uberoi, M. S. and Freymuth, P. (1970). Turbulent energy balance and spectra of the axisymmetric wake. Phys. Fluids, 13(9):2205–2210.

Ukeiley, L., Cordier, L., Manceau, R., Delville, J., Glauser, M., and Bonnet, J. P. (2001). Examination of large-scale structures in a turbulent plane mixing layer. Part 2. Dynamical systems model. J. Fluid Mech., 441:67–108.

VanDine, A., Chongsiripinyo, K., and Sarkar, S. (2018). Hybrid spatially-evolving DNS model of flow past a sphere. Comput Fluids, 171:41–52.

Vassilicos, J. C. (2015). Dissipation in turbulent flows. Annu. Rev. Fluid Mech., 47(1):95–114.

Wang, K. C. (1970). Three-dimensional boundary layer near the plane of symmetry of a spheroid at incidence. J. Fluid Mech., 43:187–209.

Wang, K. C., Zhou, H. C., Hu, C. H., and Harrington, S. (1990). Three-dimensional separated flow structure over prolate spheroids. Proc. R. Soc. London, Ser. A: Mathematical and Physical Sciences, 429(1876):73–90.

Welch, P. (1967). The use of fast fourier transform for the estimation of power spectra: a method based on time averaging over short, modified periodograms. IEEE Trans. Audio Electroacoust., 15(2):70–73.

Wikström, N., Svennberg, U., Alin, N., and Fureby, C. (2004). Large eddy simulation of the flow around an inclined prolate spheroid. J. Turbul., 5(29).

Wygnanski, W., Champagne, F., and Marasli, B. (1986). On the large-scale structures in two-dimensional, small-deficit, turbulent wakes. J. Fluid Mech., 168:31–71.

Xiang, X., Chen, K. K., and Spedding, G. R. (2017). Dynamic mode decomposition for estimating vortices and lee waves in a stratified wake. Exp. Fluids, 58(5):56.

Yang, J. and Balaras, E. (2006). An embedded-boundary formulation for large-eddy simulation of turbulent flows interacting with moving boundaries. J. Comput. Phys., 215(1):12–40.

Yang, J., Liu, M., Wu, G., Zhong, W., and Zhang, X. (2014). Numerical study on coherent structure behind a circular disk. J. Fluids Struct., 51:172–188.

Yeh, C. and Taira, K. (2019). Resolvent-analysis-based design of airfoil separation control. J. Fluid Mech., 867:572–610.

Yun, G., Kim, D., and Choi, H. (2006). Vortical structures behind a sphere at subcritical Reynolds numbers. Phys. Fluids, 18(1):015102.

Zhou, Q. and Diamessis, P. J. (2016). Surface manifestation of internal waves emitted by submerged localized stratified turbulence. J. Fluid Mech., 798:505.

Zhou, Q. and Diamessis, P. J. (2019). Large-scale characteristics of stratified wake turbulence at varying Reynolds number. Phys. Rev. Fluids, 4(8):084802.